Surface modification of oxide nanoparticles using phosphonic acids : characterization, surface dynamics, and dispersion in sols and nanocomposites

Céline Schmitt

▶ To cite this version:

Céline Schmitt. Surface modification of oxide nanoparticles using phosphonic acids : characterization, surface dynamics, and dispersion in sols and nanocomposites. Material chemistry. Université Montpellier, 2015. English. NNT : 2015MONTS083 . tel-01630576

HAL Id: tel-01630576
https://theses.hal.science/tel-01630576

Submitted on 7 Nov 2017

THÈSE
Pour obtenir le grade de
Docteur

Délivré par **l'Université de Montpellier**

Préparée au sein de l'école doctorale
Sciences Chimiques BALARD

Et des unités de recherche
Institut Charles Gerhardt,
équipe Chimie Moléculaire et Organisation du Solide
et
Laboratoire Charles Coulomb
département Matière Molle et Verres

Spécialité : Chimie et Physico-Chimie des Matériaux

Présentée par Céline SCHMITT

Surface modification of oxide nanoparticles using phosphonic acids: characterization, surface dynamics, and dispersion in sols and in nanocomposites

Soutenue le lundi 30 novembre 2015 devant le jury composé de

M^{me} Sylvie BEGIN-COLIN, Professeur, IPCMS-Strasbourg	Rapporteur
M. Thomas HELLWEG, Professeur, Université de Bielefeld	Rapporteur
M. Emmanuel BEYOU, Professeur, IMP-Lyon	Président du jury
M. Hubert MUTIN, Directeur de Recherche, ICGM-Montpellier	Directeur de thèse
M. Julian OBERDISSE, Directeur de Recherche, L2C-Montpellier	Directeur de thèse
M^{me} Anne-Caroline GENIX, Maître de Conférences, L2C-Montpellier	Co-encadrant
M. Johan ALAUZUN, Maître de Conférences, ICGM-Montpellier	Invité

"You never fail until you stop trying."

Albert Einstein

Pour Guillaume…

Glossary

AIBA: 2,2’-Azobis (2-methylpropionamide) dihydrochloride
APTMS: 3-aminopropyltrimethoxysilane
BDS: Broadband Dielectric Spectroscopy
C_3PA: n-propyl phosphonic acid
C_5PA: n-pentyl phosphonic acid
C_8PA: n-octyl phosphonic acid
C_{12}PA: n-dodecyl phosphonic acid
C_{18}PA: n-octadecyl phosphonic acid
CAPA: 6-phosphonohexanoic acid
CTAB: cetyl trimethyl ammonium bromide
DEPA: (2-(2-(2-hydroxy-ethoxy)-ethoxy)-ethyl) phosphonic acid
DLS: Dynamic Light Scattering
DTMS: decyltrimethoxysilane
EA: ethylacrylate
FTIR: Fourier Transform InfraRed spectroscopy
HLB: hydrophilic-lipophilic balance
ICP-OES: Inductively Coupled Plasma Optical Emission Spectroscopy
L200S: Levasil L200S/30, commercial colloidal dispersion of alumina-coated nanoparticles
LS101: Lotus Synthesis 101, commercial colloidal dispersion of titania nanoparticles
MAS: Magic Angle Spinning
MEK: methylethyl ketone
NC(s): nanocomposite(s)
NHSG: non-hydrolytic sol-gel
NMR: Nuclear Magnetic Resonance
NP(s): nanoparticle(s)
PA(s): phosphonic acid(s)
PBuA: polybutyl acrylate
PC: Plasmachem PL-TiO-10p, commercial colloidal dispersion of titania nanoparticles
PD: polydispersity of polymer chain lengths
PEA: polyethyl acrylate
PEO: polyethylene oxide
PMMA: polymethyl methacrylate
PPA: phenyl phosphonic acid
PS: polystyrene
PZC: point of zero charge
QENS: Quasi-Elastic Neutron Scattering
RMC: reverse Monte Carlo
SAM(s): self-assembled monolayer(s)
SAS: Small Angle Scattering
SANS: Small Angle Neutron Scattering
SAXS: Small Angle X-rays Scattering
tBuPA: tert-butyl phosphonic acid
TEM: Transmission Electron Microscopy
TEOS: tetraethoxysilane
TGA: thermogravimetric analysis
VdW: Van der Waals
XRD: X-Rays Diffraction

Outline

General introduction

In 1925, Richard Adolf Zsigmondy (Germany) received the Nobel Prize in Chemistry “for his demonstration of the heterogeneous nature of colloidal dispersions”. The following year, Theodor Svedberg (Sweden) also received the Nobel Prize “for his work on dispersed systems”. Nowadays, colloidal dispersions, including nanoparticle colloidal sols, are largely used in the industry, from paints to cosmetics. Even though these systems have been widely investigated and are now well understood, they are still under study, and the key point remains the understanding and control of the interactions between the dispersed objects and with the dispersion medium.

Mastering these interactions leads to a control of the state of aggregation of the objects. This can be achieved in different ways, for example by modifying electrostatic interactions or by modifying the surface of the objects by adsorption of organic molecules or macromolecules. In the case of nanoparticles (NPs), the use of colloidal sols is of high interest, as it allows avoiding the use of dried NPs. Manipulating dry NPs powders is controversial due to safety concerns about the toxicity of nanoparticles, as inhalation is considered the main source of exposure to nanoparticles. Consequently, the development of surface modification methods directly in the colloidal state is needed.

Over the last few decades, polymer nanocomposites have been found promising for a wide variety of applications, e.g. one of the best-known example is car tires in which silica nanoparticles are dispersed in the polymer rubber. The properties of such materials, e.g. mechanical properties, depend both on the size of the nanoparticles and on their state of dispersion in the polymer matrix.

The purpose of this PhD work is to develop in a first step surface functionalization methods of oxide nanoparticles in colloidal sols in order to control the dispersion of nanoparticles in the sols and in polymer nanocomposites derived from these sols. In a second step this dispersion will be evaluated using advanced characterization methods like small-angle scattering measurements.

In order to tune the interactions of nanoparticles, and thus their dispersion, the NP surface has been modified by grafting organic molecules. As a wide variety of oxide nanoparticle sols are conveniently prepared in aqueous medium, we aimed to develop methods allowing the NP surface modification directly in the aqueous sols. However, the commonly used silanization route is hardly applicable in water. Consequently, we chose to use phosphonic acids to modify the nanoparticles surface, as these molecules can be grafted in water on a wide variety of oxide nanoparticles.

The outline of this PhD dissertation is the following.

Chapter I - Bibliography

This part defines the different topics addressed in this study, and gives a brief literature survey concerning these notions. The first part deals with nanoparticles, e.g. oxide NPs and colloidal dispersions. The second part gives different surface modification ways with small organic molecules, and focused on silanes and phosphonic acids surface modification. The third part concerns the state of dispersion of oxide NPs in solvent, and how to modify the nanoparticles aggregation state. The last part highlights different possibilities for incorporating nanoparticles in a polymer matrix and the characterization of the dispersion state in the obtained nanocomposites.

Chapter II - Methods and materials

This chapter describes the principle of the three main characterization methods used in this work, i.e. Dynamic Light Scattering, Small-Angle Scattering, and Broadband Dielectric Spectroscopy. In a second part, the raw materials are characterized: the different nanoparticles, the phosphonic acids, and the synthesized latexes. The experimental protocols are also given in this chapter.

Chapter III - Impact of grafting of phosphonic acids on nanoparticles interactions and stability in aqueous solutions

In this chapter, we study the surface modification of alumina-coated silica nanoparticles with different phosphonic acids. First, a characterization of the modified NPs is given, and then the stability of the obtained colloidal dispersion is investigated. Finally, the dispersion state of the modified nanoparticles is studied as a function of the surface modification for different nature of the phosphonic acids and grafting density.

Note that the main part of the results presented in this chapter were published in reference [1].

Chapter IV - Spatial arrangement and interfacial dynamics of the dried nanoparticles

The aim of this chapter is to provide a study of the structure and interfacial dynamics of the raw and PA-grafted nanoparticles in the dry state, i.e. in powders. As we want to incorporate them in a polymer matrix, the interfacial characteristics are an unavoidable topic. The first part focuses on the spatial arrangement of the dried NPs as a function of the grafting density. The second part consists in a dielectric study of the surface dynamics of the raw and surface modified NPs in the dried state, and also for different hydration levels.

Chapter V - Surface-modified NPs/PEA nanocomposites

In this chapter, the raw and surface modified NPs are incorporated in a poly(ethyl acrylate) matrix by a latex route. The impact of different parameters (NP volume fraction, grafting density, and nature of the grafted phosphonic acids) on the nanoparticles state of dispersion in the polymer matrix are studied by Small-Angle Neutron Scattering.

Chapter VI - Simultaneous phase transfer and surface modification of TiO_2 NPs using alkylphosphonic acids

Titania nanoparticles are surface modified using phosphonic acids, and transferred in an organic phase. The different transfer parameters are investigated. In a second part, the PA-grafted nanoparticles are characterized. Then, their state of dispersion in the organic phase is investigated by Dynamic Light Scattering and Small-Angle Scattering. Finally, the modified NPs are dried and redispersed in several organic solvents.

Note that the main part of the results presented in this chapter were published in reference [2].

Chapter I - Bibliography

I - Nanoparticles

Nanoparticles (NPs) are particles of any shape with at least one dimension in the 1 to 100 nm range.[3] Due to their size, the nanoparticles may have other properties than the corresponding bulk material, e.g. in terms of mechanical behavior[4], phase transition temperature[5], magnetic behavior[6], electronic[7] or optical properties[8]. Concerning hydrodynamic properties of NPs suspended in solvents, the small size of NPs implies a "Stokesian" behavior, i.e. the inertia forces are negligible. Also, as the specific surface area of a spherical NP is increasing in 1/size, small-size NPs involves a high surface-to-volume ratio, and thus a high interfacial energy.

1 - Oxide nanoparticles

Oxide nanoparticles offer a large variety of properties and structures, and have numerous (potential) applications, for instance, in energy storage and conversion, biomedicine, catalysis and photocatalysis.[9, 10] The most widespread oxides NPs are silica (SiO_2), and titania (TiO_2) NPs.

a - SiO_2 nanoparticles

Silica NPs are cheap, have a high hardness and good chemical stability.[11] According to these properties, they have many fields of application: for example electronics, paper, textile, polishing, catalysis, cements, or coatings. They are often used as fillers to improve the mechanical properties of composite materials, e.g. in car tires and shoe soles. In the industry, SiO_2 NPs play also the role of adsorbent agent, additives to control rheology, catalytic supports, or binders in paints.[11-13]

SiO_2 NPs can be synthesized under two forms: aggregated powders and colloidal dispersions. The powders are mostly issued from precipitation methods and flame processes. Both methods are widely used to produce commercial quantities of silica NPs. In 1971, Ulrich reported a flame hydrolysis method to obtain SiO_2 nanoparticles by combustion of $SiCl_4$.[14] This high-temperature method leads to powder of aggregated SiO_2 NPs of approximately 50 nm. The synthesis of fumed silica from silanes or other silicate residues is also possible.[15] Precipitated silica is produced by precipitation from a solution containing silicate salts, for instance by addition of H_2SO_4.

Concerning the dispersions, sols of silica spherical NPs are generally synthesized by sol-gel process in basic medium or in reverse micro-emulsions.[16] In 1968, Stöber et al. proposed an innovative synthesis by a sol-gel route based on the hydrolysis and condensation of tetraethoxysilane (TEOS) in ethanol with ammonia as a catalyst.[17] This method leads to the formation of monodisperse and electrostatically stabilized silica particles with diameters ranging from 50 nm to 1 µm. Many other studies were published using this method and varying synthesis parameters to obtain different size-range, polydispersities, and reactive functions on the NPs surface. For instance, Arriagada and Osseo-Asare have been studying the synthesis of silica NPs in reverse micro-emulsions since the nineties.[18] This process allows obtaining NPs with a narrow size distribution dispersed in apolar medium, however the removal of surfactant after synthesis is cumbersome.

b - TiO_2 nanoparticles

TiO_2 NPs are the most studied metal oxide nanoparticles.[19] The most common crystal phases are anatase and rutile (tetragonal), and brookite (orthorhombic). These nanoparticles have a high refractive index (2.5 - 2.6), they are thus widely used as pigments and fillers in paints, coatings, and in the paper industry. Unlike SiO_2, TiO_2 is a semi-conductor, which opens up several applications. TiO_2 strongly absorbs UV, and is largely used in sunscreens. TiO_2 anatase is a good photocatalyst, which is used extensively as a heterogeneous photocatalyst and in self-cleaning coatings. For the applications as pigments in paints, this photo-catalytic activity is not desirable (because of film deterioration), and needs to be reduced by coating with silica or alumina.[20] TiO_2 is used in energy conversion, for instance in dye-sensitized solar cells.[21] TiO_2 NPs can also be used in other fields of applications such as catalysis, optical industry, gas sensing, or environmental application.[19, 22]

As for SiO_2 NPs, titania NPs can be obtained by flame methods, e.g. by pyrolysis of $TiCl_4$.[15] The resulting powder consists of aggregated NPs. The size of the particles depends on the process parameters. For instance, Formenti and co-workers reported NPs sizes between 15 and 150 nm depending on gas velocity or on the flow rate of $TiCl_4$ in the burner.[23]

Various other ways of synthesis can be used to obtain titanium dioxide nanoparticles: for instance, hydro- and solvothermal processes, oxidation methods, or chemical vapor deposition[24]; but the most versatile way to prepare well-dispersed titanium dioxide NPs with controlled size and even shape is the sol-gel process. Either conventional sol-gel, based on hydrolysis and condensation of titanium alkoxides [25, 26] or non-hydrolytic sol-gel (NHSG), based on the reaction of Ti precursors with organic oxygen donors such as alcohols or ethers.[19] The conventional sol-gel process presents different drawbacks that can be avoided by NHSG: low rates of conversion, particle agglomeration and poor crystallinity of the obtained particles. Moreover, NHSG offers a convenient way to synthesize TiO_2 nanoparticles with an excellent control of size and shape, by varying the experimental parameters.

2 - Colloidal dispersion

a - Definition

A colloidal dispersion is a homogeneous mixture of two phases, the stability of which is ensured by Brownian motion. The dispersed phase has a typical size between 1 nm and 1 µm. In some cases, the stability of a colloidal dispersion is ensured by the use of stabilizing agents, for instance surfactants. Depending on the nature of both the dispersion and the dispersed phase, colloidal systems can be subdivided in different categories as shown in table 1.1.

Table 1.1: Classification of colloidal dispersions.

		Dispersed phase		
		Gas	**Liquid**	**Solid**
Continuous phase	**Gas**	X	Liquid aerosol	Solid aerosol
	Liquid	Foam	Emulsion	Sol
	Solid	Solid foam	Gel	Solid sol

The colloidal dispersions studied in chapters III and VI are alumina-coated silica and titania sols, i.e. NPs dispersed in a solvent, either water or an organic solvent. In chapter V, the nanocomposites are prepared by mixing a NPs sol and a latex, which is a water-based mixture of polymer particles stabilized in water by surfactants: a latex is a sol.

b - Interactions governing colloidal dispersions of nanoparticles

As commented above, the stability of colloidal dispersions is due to thermal agitation, but also to the interactions between NPs. These interactions can be either attractive or repulsive. The attractive forces are attributed to Van der Waals (VdW) forces: dipole-dipole, dipole-induced dipole and London forces (instantaneous induced dipole-induced dipole). The repulsive forces are of two kinds: electrostatic and steric.

Electrostatic repulsions can have different origins:

- Charged groups at the surface of colloids. In the case of oxide NPs in water, the -OH surface groups can be either protonated at low pH or deprotonated at high pH, leading to $-OH_2^+$ or $-O^-$ surface groups, respectively.
- Adsorbed molecules or ions. For instance, latexes synthesized using ionic surfactants are charged due to these surfactants.

In both cases, these charged surface groups interact with the counterions present in the solution, which surround (are adsorbed onto the surface of) the charged particles, the thickness of the counterion cloud being described by the Debye screening length. These two layers (charges of the particle and the counterions) form the electrical double layer of the nanoparticle. Differences in the ionic concentrations between two particles with respect to the bulk solution generate an osmotic pressure, resulting in a repulsive force between the particles.[27]

Colloidal dispersions of silica NPs are commercially available. The theoretical isoelectric point of silica, also named “point of zero charge” (PZC), is at pH 2.[28] This point corresponds to the conditions for which the electrical charge density is zero.[29] Close to this point, there is no electrostatic repulsion between NPs. Accordingly, silica NPs form stable sols in water at basic pH (8 - 10), because of the negatively charged nanoparticles.

It is also possible to find commercial “cationic silica sols”, stable at low pH (ca 4). NPs in these sols are actually silica NPs coated with an alumina layer, which display a PZC of about 7 - 8. However, sols of silica NPs in acid solution also exist. Regarding titanium dioxide NPs dispersions, commercial sols stabilized at low pH (< 2) by positive charges are sold.

Steric repulsions are due to the presence of bulky organic groups at the surface of the colloids. The most common example consists in polymer chains grafted onto the nanoparticles surface.

According to the DLVO (Derjaguin, Landau, Verwey, Overbeek) theory, the stability of a dispersion depends on the sum of the repulsive and attractive forces, which the particles experience by approaching one another.[30, 31] If the attractive VdW interactions predominate, the total (interaction) energy decreases monotonically when the interparticle distance decreases, resulting in fast coagulation of the particles. If the double-layer repulsions are high enough, the total energy shows a maximum (an energy barrier) and no secondary minimum, leading to stable NPs suspension. For intermediate repulsion forces, the total energy exhibits a maximum and a secondary minimum. In that case, the suspension is kinetically stable, if the second minimum is deep enough, see figure 1.1.

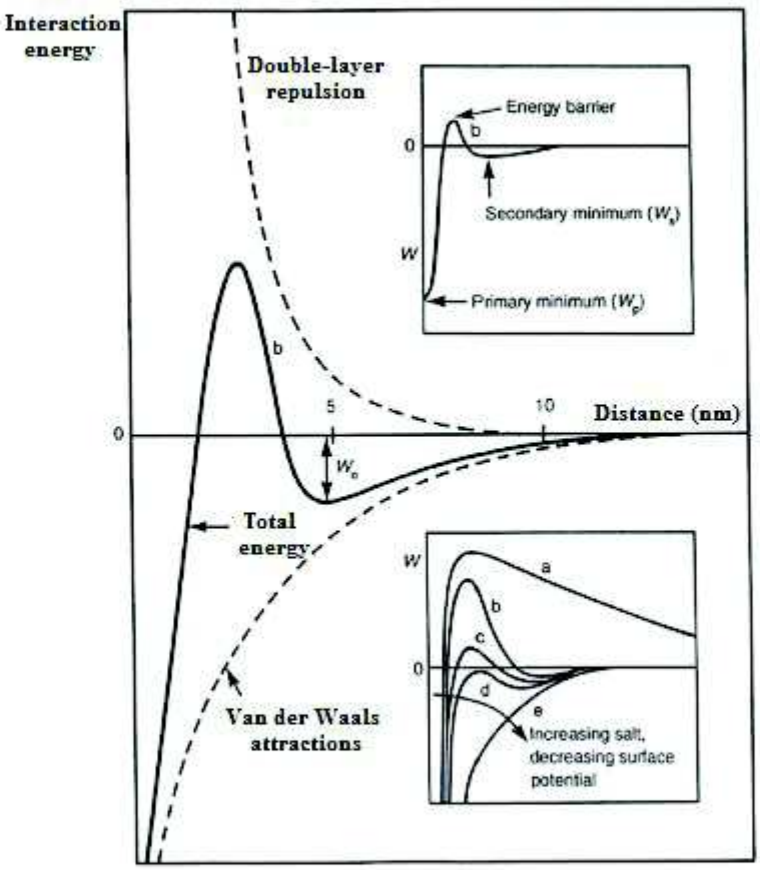

Figure 1.1: Evolution of the interaction energy with the distance between nanoparticles according to the DLVO theory, which consists in summing the repulsive and attractive forces.[27]

In the case of hydrophobic NPs (or inorganic NPs modified by hydrophobic organic groups), Van der Waals attractive interactions between surface groups become significant and may lead to aggregation in aqueous medium if steric repulsions are not high enough. Therefore, it is necessary to evaluate the hydrophobicity of molecules, which can be estimated using the "hydrophilic-lipophilic balance" (HLB).[32] This empirical value provides information about the emulsifying or solubilization properties of a surfactant, as given in table 1.2.

Table 1.2: Correlation between HLB values and emulsifying properties.

Range of HLB values	Associated property of the molecule
3 - 6	Water in Oil emulsifier
7 - 9	Wetting agent
8 - 18	Oil in Water emulsifier
13 - 15	Detergent
15 - 18	Solubilization

Different methods of calculation were proposed. Davies attributes a value, named "group number", to each function or part of the molecule. In its model, the HLB is given by:

$$\mathrm{HLB_{Davies}} = 7 + \sum \text{group numbers} \qquad \text{(eq.1.1)}$$

A selection of group numbers is given in the table 1.3.

Table 1.3: Chosen group numbers.

Chemical group	Group number [32, 33]
$-CH_2-$ or $-CH_3$	- 0.475
$-O-CH_2-CH_2-$	+ 0.33
-OH	+ 1.9
-COOH	+ 2.1
$-PO(OH)_2$	+ 13.3

Note that this value gives an indication of the properties of a molecule, but no information about the stability of the obtained emulsion. In the case of unstable colloidal dispersions, the destabilization processes are numerous. The main destabilization processes for nanoparticles dispersions in a solvent are:

- sedimentation and creaming: nanoparticles settle down or up due to their difference of density with respect to the solvent
- flocculation: particles aggregate in suspension

For emulsions, other destabilization processes must be taken into account:

- coalescence: several droplets merge to form a single bigger droplet
- phase inversion
- Ostwald ripening: small droplets release molecules which feed larger droplets

In this section, we saw that a major concern in the study of colloidal solutions is the identification of the different interactions, e.g. in order to control stability or dispersion of the NPs. The stability of a colloidal dispersion can be predicted by the DLVO theory. We were focusing mainly on raw nanoparticles. In the next part, we will give examples on how to modify the surface of these NPs.

II - Surface modification of oxide NPs

Grafting organic molecules on inorganic surfaces allows controlling the surface/interface properties in many applications, for example adhesion, corrosion, sensing, or catalysis. The most studied molecules are the so-called “silanes”, which are used to modify oxide surfaces (cf. section II-1), and thiols, which are used to modify coinage metal surfaces, e.g. Au, Ag, Cu, etc.[34-36]

In the case of nanoparticles, surface modification is used for instance to modify the affinity of NPs with solvents or polymeric matrixes, in order to promote compatibility or homogeneity in composite materials.[37] Surface modification of NPs is also used to prevent aggregation or to induce self-assembly.[38, 39]

Different families of molecules can be used to modify oxide NPs, depending on the nature of the oxide. In the case of silica, the most suited compounds are the organosilanes, which form stable, covalent Si-O-Si bonds with the surface. In the case of metal oxides such as TiO_2, organosilanes, organophosphorus acids, carboxylic acids, sulfonates, catechols, or amines are used.[36]

The surface modification of TiO_2 NPs with carboxylic acids was reported by different groups. For instance, Ojamäe and collaborators modified the surface of rutile TiO_2 NPs with different carboxylic acids.[40] Note that this type of surface modification is not covalent: upon adsorption onto the metal oxide surface, carboxylic acids dissociate and form a surface salt with a surface metal cation.[41]

Surface modification with catechols - the general chemical formula of which is given in figure 1.2 - was also used to modify metals, metal oxides, mica, or silica.[42] For example, Li et al. studied the adsorption of catechols on TiO_2 substrates.[43] They concluded on the possibility of catechols to form two different full-coverage structures on titania involving monodentate or mixed mono- and bidentate bonding. Catechols can also easily form self-assembled monolayers (SAMs).[36, 42]

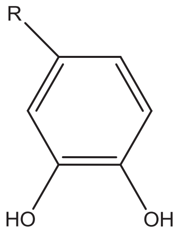

Figure 1.2: General formula of a catechol molecule. R is a substituent, for instance an alkyl chain.

Adsorption of amines on metal oxide surfaces is also possible, but is rarely used as a surface modification method. For instance, Nakayama and Hayashi used both carboxylic acid and hexylamine to modify the surface of TiO_2 NPs to allow NPs dispersion in organic solvents.[44] According to them, these two components capped both Bronsted (Ti-OH) and Lewis (Ti^+) acid sites. Raza and co-workers studied the surface modification of titania NPs with different type of grafts: carboxylate, phosphonate, sulfate and amine.[45] They highlighted that phosphonates and carboxylates were grafted with strong interactions with the surface (covalent interaction for phosphonate, and coordination for carboxylates), whereas amines and sulfates interact electrostatically with the surface.

A last example of molecules that are used to modify the surface of titanium dioxide is sulfonates. Ramakrishna and Ghosh capped TiO_2 NPs with dodecylbenzenesulfonate to allow their dispersion in organic solvents.[46]

In the case of oxide NPs, the most commonly used coupling molecules are organosilanes and phosphonic acids. We will now focus on these two types of compounds.

1 - Silanes

Organosilanes are the most widespread grafted molecules.[36] They can be used in many domains as adhesion promoters or coupling agents[47], for instance to modify the surface of silica particles in rubbers. The main advantage of this surface modification is (in principle) the rapid formation of covalent M-O-Si-C bonds between the grafts and the support (M = Si or a metal atom), and the possibility to form highly stable self-assembled monolayers.[41] The chemical formula of organosilanes is $R_nSiX_{(4-n)}$ with n = 1, 2, or 3. R is an organic group linked to Si by a Si-C bond, which is stable toward hydrolysis, and X a hydrolysable organic group, in most cases ethoxy, methoxy, or chloro. These molecules can be grafted onto many oxide surfaces, for example, SiO_2, Al_2O_3, and TiO_2. However, in the case of multifunctional organosilanes (e.g. $R\text{-}SiX_3$), during surface modification with these molecules, there is a competition between hetero- and homocondensation reactions.

Heterocondensation: Si-OH + M-OH → Si-O-M + H_2O

Homocondensation: Si-OH + Si-OH → Si-O-Si + H_2O

The competition between these two reactions governs the nature and homogeneity of the grafted layer. It depends on the water content of the medium, the temperature and the nature of the support.[48, 49] In absence of water, only partial monolayers are formed. A small amount of water is required to form a dense monolayer, which may be seen as a polysiloxane layer linked to the surface by Si-O-M bonds. As the water content increases, homocondensation may lead to the formation of 3-dimensional polysiloxane layers, up to tens of nanometer thick.[50, 51] These cases are presented in figure 1.3.

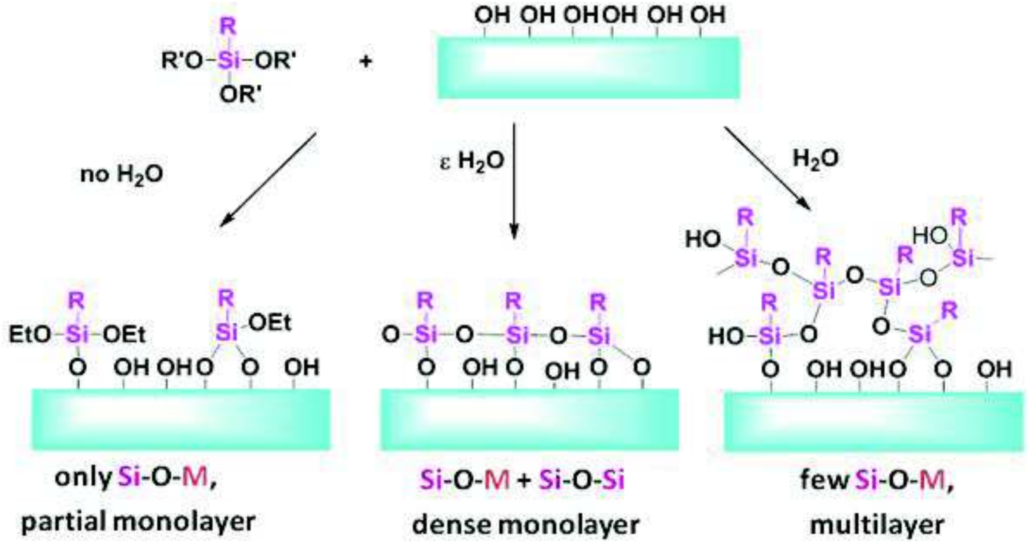

Figure 1.3: Schematic representation of the structure of organotrialkoxysilane layers for different water contents of the grafting medium.[52]

As a consequence, grafting is usually performed in organic medium with a strict control of the water content in the solvent and adsorbed onto the surface. McGovern et al. showed the influence of organic solvent on the grafting density of one organosilane (octadecyltrichlorosilane).[53] For example, surface modification in toluene or in benzene leads to the densest silane films in comparison with e.g. pentane, carbon tetrachloride, or cyclohexane. This is due to the fact that these solvents are able to remove a significant amount of water from the substrate surface. In addition, most organosilanes are not water soluble. This, as well as the risk of anarchic homocondensation, makes the grafting of organosilanes in aqueous medium difficult. Therefore, Choi and co-workers synthesized organosilane-modified silica directly in water by forming an emulsion of the immiscible used organo-silanes in the aqueous medium.[54] Greenwood et al. found that silica sols could be efficiently grafted by slow addition of pre-hydrolyzed γ-glycidoxypropyltrimethoxysilane.[55]

Considering the low solubility of organosilanes in water, as well as their high sensitivity to hydrolysis, we chose phosphonic acids to modify our NPs in water.

2 - Phosphonic acids

Organophosphorus acids such as phosphonic acids and their derivatives (salts and esters) are widely used to control surface and interface properties, especially to modify metal oxide surfaces.[56] These compounds have a good affinity for many different substrates, like metal oxide substrates such as titania, alumina, iron oxides, or indium-tin oxide, as well as metallic substrates with a (native) oxide surface layer such as titanium, titanium alloys, aluminium, aluminium alloys, iron, stainless steel, magnesium alloys, and cobalt-chromium alloys.[52, 56, 57]

We will focus here on phosphonic acids (PAs) with a chemical formula $R\text{-}PO(OH)_2$. As it is a diacid, depending on the pH, two different anions can be formed in solution by deprotonation of the molecule: $RPO_2(OH)^-$ or RPO_3^{2-}. Depending on the nature of the PA, the pKa vary: for instance, the methylphosphonic acid presents pKa values at -2.2 and 7.5.[58] In addition, the P=O oxygen is a good Lewis base. Consequently, PAs can easily bind with oxide surfaces (see figure 1.4):

- by coordination of the P=O with a metal Lewis acid site present at the surface.
- by condensation between a P-OH group and a surface hydroxyl group:

$M\text{-}OH + P\text{-}OH \rightarrow M\text{-}O\text{-}P + H_2O$ where M is a metal or a silicon atom.

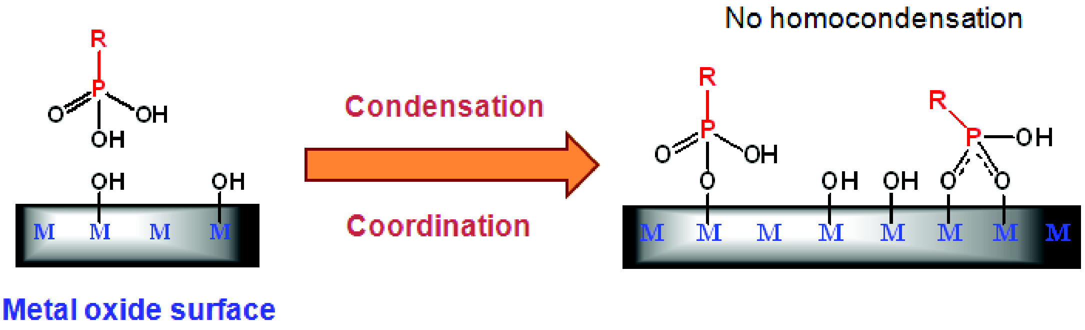

Figure 1.4: Schematic representation of the grafting of phosphonic acids on a metal oxide surface.

It is noteworthy that under mild conditions, there is no formation of P-O-P bonds (homocondensation), which favors the formation of monolayers.[59] However, the absence of lateral polymerization by homocondensation may limit the mechanical and chemical stability of the surface layer.

PAs can bind to a metal oxide by different ways, they can form up to three M-O-P bonds (see figure 1.5). These grafting modes depend on the nature of the grafting, the nature of the surface, and the grafting conditions.

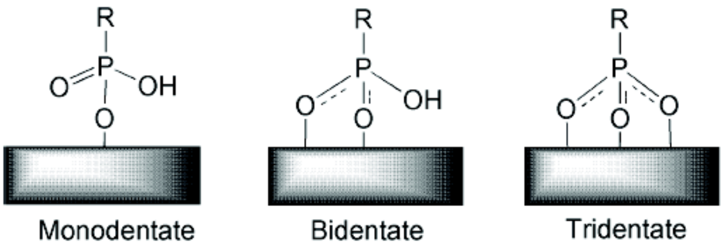

Figure 1.5: Different binding modes of phosphonic acid with a metal oxide surface.[52]

To study these grafting modes, different analyses can be performed, as recently reviewed.[56, 57] Randon and co-workers studied the grafting of phosphoric (H_3PO_4) and alkylphosphonic acids on zirconia and titania membranes.[60] Using infrared spectroscopy, they concluded that the acids were linked to the zirconia surface in a tridentate way, the same grafting mode is expected for the titania surface. However, IR spectroscopy did not allow to deduce bidentate or monodentate grafting modes. Guerrero et al. reported on the titania surface modification by phenylphosphonic acid and esters. Based on XRD, ^{31}P MAS NMR and diffuse reflectance FTIR spectroscopy measurements, they proposed that this surface modification mainly involves tridentate binding modes.[59, 61] In the case of surface modification of alumina with the same PA, according to the absence of residual P-OH bonds on the IR spectra, they also concluded on the formation of tridentate binding modes.[62]

However, a drawback of the use of PAs is the possible dissolution-precipitation of the metal oxide with the phosphonic acid. This reaction leads to the formation of a crystalline phase of metal phosphonate (see figure 1.6).

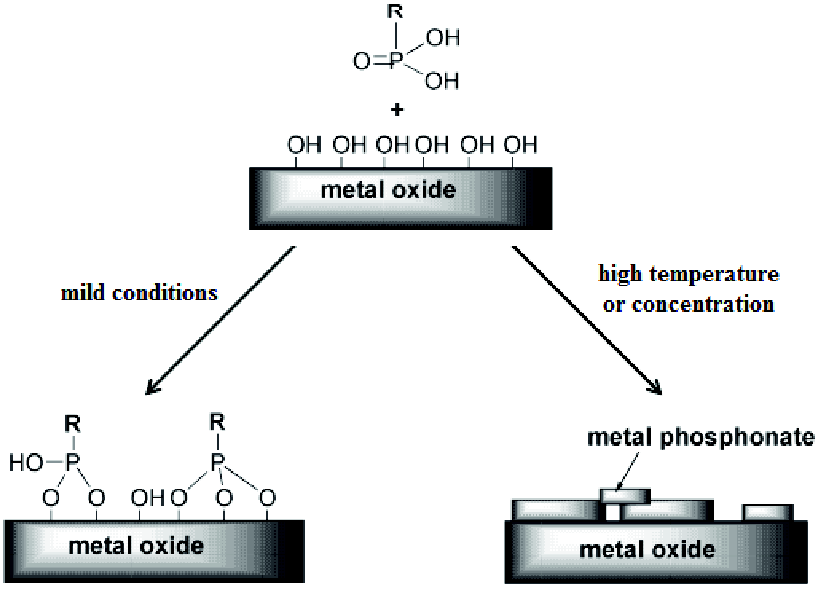

Figure 1.6: Competition between surface modification and dissolution-precipitation of a phosphonic acid with a metal oxide surface depending on the experimental conditions.[52]

For instance, Gao and collaborators reported on the formation of such a metal phosphonate crystalline phase for the surface modification of ZrO_2, TiO_2 and Al_2O_3 with octadecylphosphonic acid depending on the experimental conditions.[63] Excess of acidic pH, high grafting temperatures, or long reaction times favor dissolution precipitation. The formation of a metal phosphonate phase was evidenced by the presence of either a sharp peak in solid-state ^{31}P CP-MAS spectra, or characteristic peaks in XRD pattern.

More recently, Lafond et al.[64] and Brodard et al. [65] studied the binding modes of phosphonic acids in titanium phosphonate solids by ^{17}O solid-state NMR.[64] However, the natural abundance of ^{17}O is very low, and the synthesis of ^{17}O-enriched phosphonic acids is mandatory.

PAs bearing long-alkyl chains (>C8) are able to auto-assemble, and thus to form SAMs. These monolayers are defined by Ulman as an ordered, two-dimensional assembly of molecules, which are adsorbed at the surface of a solid.[41] This assembly is formed by interactions between the adsorbed molecules and the surface, and also between adsorbed molecules. PA SAMs layers were grafted onto different surfaces: for instance, Van Alsten published a method to graft alkylphosphonic acid SAMs on metal surfaces, e.g. on steel or aluminium.[66] Gao et al. studied octadecylphosphonic acids monolayers on metal oxide surfaces, for example zirconated silica.[67] They concluded on the formation of a well-ordered SAM according to FTIR, solid-state ^{13}C and ^{31}P MAS NMR spectra. Woodward and collaborators grafted octadecylphosphonic acids on mica surface and characterized the obtained SAMs with both Atomic Force Microscopy (AFM), and contact angle measurements.[68] Brukman et al. used hydrogenated and fluorinated PAs to form SAMs on different aluminium oxide surfaces, and characterized them by AFM, too.[69] In particular, many studies were done on the formation of SAMs on titania surfaces.[70-74]

It is important to note that Si-O-P bonds are not stable against hydrolysis, contrary to M-O-P bonds (M = Ti, Zr, Al, etc.). This difference in stability has been used to selectively modify patterned SiO_2-TiO_2 substrates and mixed oxide supports. [75]

Silica substrates can be grafted by PAs in aqueous media only when the silica surface is modified by a layer of metal oxide (Ti, Zr, or Al). Therefore, we used alumina-coated silica NPs in our study. In this case, the surface modification is due to the formation of Al-O-P bonds, which are stable in aqueous medium. Such a surface modification has been described by Lassiaz et al. [76]

Even though the surface modification of metal oxide aqueous sols with PAs is feasible, very few studies were published on this topic. Pautrot-d'Alençon et al. modified CeO_2 sols stabilized by acetate groups using 2-carboxyethylphosphonic acid, ethylphosphonic acid, and phosphonoacetic acid in order to tune the acidic character of their surface.[77] Rehor and collaborators studied the adsorption/desorption of a phosphonic acid (or a bis-phosphonic acid) bearing a lanthanide(III) complex on TiO_2 nanoparticles in colloidal suspensions stabilized by polyvinylalcohol.[78]

To summarize, in comparison with other grafts, especially with silanes, the main advantages of phosphonic acids are that the surface modification of metal oxides is possible in water and that homocondensation does not occur. Accordingly, they are used in various domains and for different applications, such as adhesion promotion, electronic devices, nanomaterials, photovoltaic cells, biomaterials, biosensors, catalysis, or corrosion inhibitors.[57]

III - State of dispersion of oxide nanoparticles in solvent

In parts I and II, we described the different interactions present in colloidal dispersions of oxide NPs, and how to modify the surface of these NPs. These notions are very important for studying and understanding the NPs dispersion in solution. We will now focus on different ways to measure and control the NPs state of aggregation in solution.

The control of NPs dispersion in solutions is crucial in different domains, e.g. in water treatment, composite materials, electronics, or diagnostics. For instance, Keller et al. studied the dynamics of aggregation of different metal oxides NPs, like TiO_2, in different aqueous media by dynamic light scattering (DLS), UV Visible, and electrophoretic measurements.[79] The aim of this study was to understand the stability and mobility of different metal oxide NPs in environmental conditions. There are plenty of parameters, which can be varied to control the dispersion. Thus, it is important to be able to evaluate, and to measure the NPs state of dispersion in solution, i.e. the "structure" of NPs in solution.

1 - Aggregation of nanoparticles

Depending on the interactions between NPs, nanoparticles can be individually dispersed, or form aggregates of strongly bound NPs, or loosely linked agglomerates, see figure 1.7.

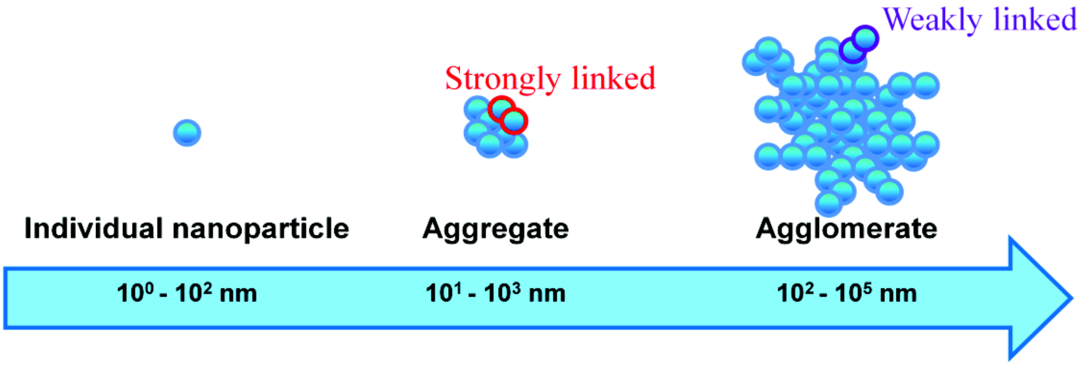

Figure 1.7: Aggregation and agglomeration of nanoparticles.

In order to characterize such arrangements, different parameters are useful:

- the radius of gyration, R_g (see definition in chapter II)
- the aggregation number, N_{agg}
- the fractal dimension of aggregates, D_f.

The aggregation number corresponds to the number of NPs constituting an aggregate. It is defined by the ratio between the volume of all the NPs in one aggregate ("dry volume") and the volume of one individual NP. The fractal dimension gives information about the mass distribution of NPs in an aggregate. This value is comprised between 1 (linear aggregate) and 3 (dense aggregate). D_f values for different geometrical objects are given in figure 1.8.

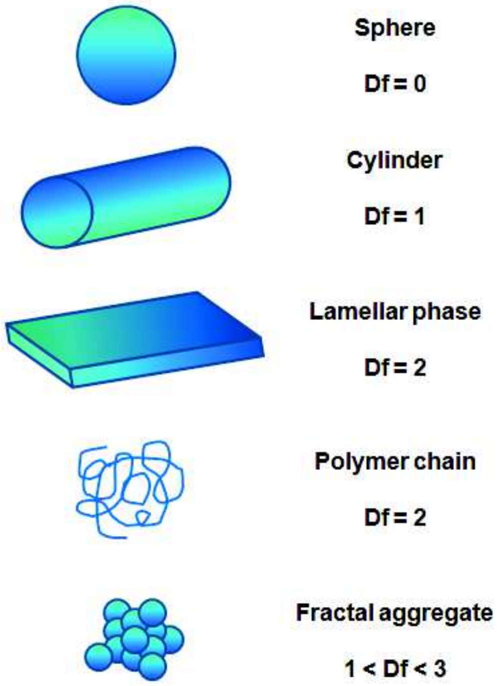

Figure 1.8: Examples of fractal dimension for different geometrical objects.

The fractal dimension is linked to the aggregation number by:

$$N_{agg} = \left(\frac{R_{agg}}{R_{NP}}\right)^{Df} \qquad \text{(eq.1.2)}$$

with R_{agg}, the aggregate radius, and R_{NP}, the NP radius.[80]

2 - Impact of ionic strength and pH of the medium

Different parameters can be varied to tune the interactions between nanoparticles in aqueous medium. Changing the pH or the ionic strength of the solution leads to a modification of the electrostatic repulsions between NPs, and thus to different aggregation states.

Generally, the aggregate size increases when the pH is approaching the point of zero charge, due to the decrease of the electrostatic repulsions. The increase of salt content in the solution also leads to an increase of the aggregate size, because of the screening of the NPs charge, leading to a decrease of the electrostatic repulsions.

There are numerous examples in the literature of such studies. Behrens et al. used the DLVO theory to predict and explain latex aggregation with different pH and salt concentrations in water.[81] Wijnen and co-workers studied the influence of different parameters, in particular pH and ions, on the aggregation of aqueous silica gels by SAXS.[82] Fitting the SAXS curves allowed them to determine the size of the primary silica NPs, and to follow the size and fractal dimension of the aggregates. Knoblich and Gerber also used SAXS to study the evolution of the fractal dimension of aggregates in SiO_2 sols as a function of the solution pH.[83] French et al. published an article on the influence of both the pH and ionic strength on the kinetics of TiO_2 NPs aggregation.[84] They followed the evolution of the hydrodynamic radius of aggregates over the time using DLS. Another example is given by Jiang and collaborators, who focused on TiO_2 NPs dispersions, and varied different parameters, including pH, ionic strength of the solution, and coating of the NPs with polymer.[85] They systematically measured the hydrodynamic size of aggregates by DLS, and followed the evolution of zeta potential with the salt concentration in the solution. They discriminated aggregation due to the NPs synthesis method from the aggregation related to physico-chemical parameters (e.g. salt concentration) by following the evolution of NPs aggregation under sonication: only the aggregates due to physico-chemical parameters are broken during sonication.

3 - Impact of grafting hydrophilic polymer chains

To avoid aggregation in aqueous media, when electrostatic repulsions are not sufficient, the main possibility is to provide steric repulsions. Steric stabilization consists in avoiding the NPs to come close enough to each other to aggregate irreversibly. In practice, long non-ionic chains are grafted or adsorbed on the NPs surface (as seen in part II).

Grafting polyethylene oxide (PEO) chains on silica NPs to improve their stability in aqueous solvents was described by many groups. This surface modification can be performed by “grafting-to” and “grafting-from” methods.[86-88] Simple physisorption of PEO chains has also been used, for instance by Napper and Netschey, who induced steric stabilization of polyvinyl acetate NPs by adsorption of PEO-like surfactants.[89]

Stabilization with other polymer chains is also well-described in the literature. For instance, Deiss and co-workers reported on the stabilization of TiO_2 nanoparticles in aqueous medium with adsorbed polyacrylamide on the NPs surface.[90] Auroy et al. studied the grafting of polydimethylsiloxanes on the surface of silica NPs. The siloxanes allowed to add steric stabilization and to disperse the NPs in different organic phases by centrifugation-redispersion cycles.[91]

Note that steric stabilization in organic solvents is described, too. For instance, El Harrak and collaborators grafted polystyrene (PS) chains on SiO_2 NPs in dimethylacetamide.[92] During all the surface modification steps (grafting of the initiator, and "grafting-from" polymerization), they kept the NPs well-dispersed and followed the colloidal stability by light and small-angle neutron scattering (SANS).

The grafting of hydrophobic polymer chains on NPs, in order to incorporate them in a polymer matrix, will be treated in part IV.

4 - Impact of grating small organic molecules

Another way to play with the state of aggregation in solution is to modify the NP surface with small organic grafts. This can induce VdW interactions and/or hydrogen bonding between grafts, modification in the NPs surface charge, and/or add steric repulsions.

For instance, Bagwe and co-workers studied the impact of different surface groups on silica NP dispersions by DLS coupled with zeta potential analysis.[93] They highlighted the fact that playing with the ratio of protonable (e.g. amino) or deprotonable (e.g. phosphonate) surface groups allowed controlling the zeta-potential of NPs, and thus the state of aggregation. Indeed, the addition of methyl phosphonate on amine-modified silica NPs reduced the aggregate size by increasing the negative charge of NPs, and thus electrostatic repulsions. Starck and Ducker proposed a method to control aggregation between two different organic-coated silica NPs with pH.[94] The first type of silica NPs was coated with a carboxylic acid layer and the second with an ethylene oxide layer. The aggregation can be induced by pH variation, because of the changes of hydrogen bonding between ethylene oxide and carboxylic acid grafts.

Moreover, surface modification with hydrophobic organic groups is commonly used to stabilize NPs sols in organic medium. For instance, Iijima et al. modified the surface of titanium dioxide NPs with decyltrimethoxysilane (DTMS) and 3-aminopropyltrimethoxysilane (APTMS).[95] Depending on the ratio of both grafts, the redispersion of modified NPs was successfully obtained in toluene (100% DTMS) or in a mix of toluene and methanol.

Note that another way to disperse particles was reported by Herman and Walz.[96] They used highly-charged nanoparticles to stabilized weakly-charged silica micrometer-sized particles. The small highly-charged nanoparticles are adsorbed onto the surface of the bigger ones and increase the electrostatic repulsions between them. They quantified the NP zeta-potential evolution with the pH of the solution, and performed optical turbidity measurements to follow the stability or flocculation of the NPs in time. They also measured the aggregate sizes by DLS.

5 - Conclusion

In this part, we have reviewed progress in the monitoring and control of the aggregation state of oxide NPs in solution. The aggregation state can be conveniently tuned by varying physico-chemical parameters of the solution (pH, ionic strength, nature of ions), or by surface modification of the NPs.

Characterization is usually done by DLS (to obtain the hydrodynamic radius of aggregates), by SANS or SAXS (to measure the size of primary NPs and aggregates, and the fractal dimension of aggregates), or by turbidity measurements. In the next part, we will focus on the incorporation of oxide NPs in a polymer matrix, and the control of the NPs aggregation state in the nanocomposite.

IV - Nanoparticles incorporation in a polymer matrix and study of dispersion

According to the IUPAC definition, a composite is a multicomponent material made of different non gaseous phases.[97] In the case of nanocomposites (NCs), at least one of the phases has one dimension in the nanometer range. We are focusing here on polymer nanocomposites, i.e. the continuous phase - the matrix - is a polymer, and more precisely on NPs based polymer nanocomposites. Contrary to traditional filled materials, low loadings of NPs (1 - 5%vol) can lead to significant modification of the macroscopic properties, like the enhancement of mechanical, thermal, flame retardant, or conductive properties of the nanocomposite in comparison with the neat polymer.[98] Such properties strongly depend on the dispersion state of the NPs in the material, and the challenge is to be able to control the NPs dispersion in order to tune these properties. The use of low filler fractions can offer different advantages: for example, reduced weight of the final material, better optical properties, or easier processing. Accordingly, polymer-NPs nanocomposites have many fields of applications: automobile industry, coatings, or electronic.[99]

1 - Incorporation of oxide nanoparticles in a hydrophobic polymer matrix

Unmodified oxide NPs are hydrophilic, they are thus more compatible with hydrophilic polymers, such as polyacrylic acid or PEO. If the polymer is soluble in water, the NC can be obtained directly by mixing a colloidal dispersion of NPs with an aqueous solution of polymer, and then evaporation of the water.[100]

However, in most cases, the polymer matrix is hydrophobic,[101] and direct mixing of NPs in a polymer solution is rarely sufficient to avoid demixion. Thus, different other strategies can be used to incorporate the oxide NPs in the polymer:

- mechanical incorporation;
- in-situ synthesis of NPs;
- in-situ polymerization;
- modification of the polymer with the surface-active groups;
- coprecipitation, also called rapid precipitation method;
- surface modification of NPs;
- aqueous latex route.

Mechanical incorporation in solid phase can be done by different methods: for example, extrusion, internal mixing, or external mixing. This method is often used in the industry. The dispersion state of NPs is closely linked to the elaboration parameters: for instance, temperature and rotation speed play an important role.[102]

In-situ incorporation consists in synthesizing directly one of the components in solution. Thus, NPs can be synthesized in a solution containing the polymer or in the molten polymer (reactive extrusion). For instance, Wahba et al. prepared silica-rubber NCs by in situ sol-gel synthesis of silica

NPs in a polymer solution.[103] The second possibility is to perform an in-situ polymerization, i.e. to conduct the polymerization in a solution containing the NPs, an initiator and the monomer.[104, 105]

The coprecipitation method consists in dissolving a polymer in a solvent, in which the nanoparticles are dispersed, and to add the dispersion drop wise in a poor solvent of the polymer, inducing the precipitation of both NPs and polymer to form the nanocomposite.[106] However, this method involves finding a good solvent of the polymer, in which the nanoparticles are well-dispersed.

We will now focus on the surface modification of nanoparticles and on the use of a latex route, which are the two methods used in this thesis.

a - Surface modification of nanoparticles

As mentioned previously, surface modification of NPs is one of the strategies used to improve or control the dispersion of NPs in a polymer matrix, in order to modify its properties. In most cases, the purpose is to make the NPs hydrophobic and increase the compatibility of the NPs and the polymer. However, modifying the NPs surface changes both the NP-polymer interactions and the NP-NP interactions.

- Polymer grafted on the nanoparticles surface

Different surface modifications with polymer chains have been studied. One possibility consists in linking the polymer to the NPs, using “grafting-to” or “grafting-from” approaches. In the “grafting-to” method, end-functionalized polymer chains are grafted on the NPs surface. In the “grafting-from method”, the polymerization reaction is conducted from the surface of the NPs, on which a polymerizable unit (or an initiator) is grafted. For example, Carrot et al. synthesized core-shell silica-polymer NPs by the “grafting-from” method and characterized them by SANS.[107] Auroy and co-workers modified silica NPs using polydimethylsiloxane chains terminated by an OH group, allowing transfer of the NPs from their initial polar medium to various organic solvents.[91]

Encapsulation provides another way to obtain polymer-coated NPs. This method is based on an emulsion polymerization process. The monomers are adsorbed on the NPs surface, and then the polymerization takes place in the adsorbed layer, to finally form polymer-coated NPs. However, this method has several drawbacks: depending on the experimental conditions, individual or multiple NPs can be covered by the same shell, and isolated polymer particles can be formed.[108]

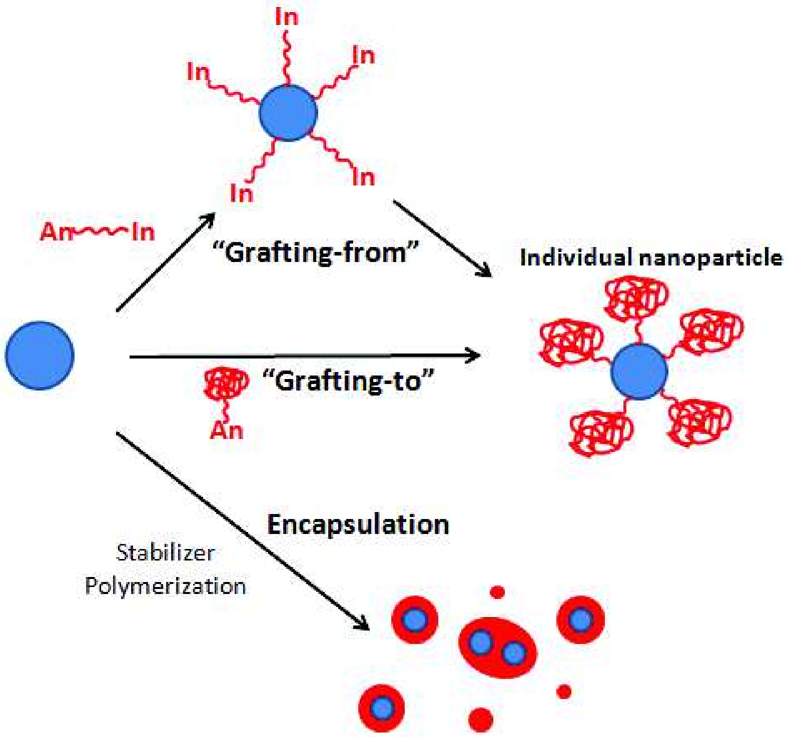

Figure 1.9: Different ways to obtain polymer-modified nanoparticles. **An**=Anchoring group; **In**=initiator. Adapted from reference [108].

The advantages of surface modification with long-polymer chains are manifolds. First, the increase of hydrophobicity of the NPs ensures a better dispersion in the hydrophobic matrix. Secondly, the possible entanglement of the grafted polymer chains with the matrix chains improves the interfacial interactions between NPs and the matrix.[109]

- Small organic molecules grafted on the nanoparticles surface

Different types of surface modification of oxide NPs were described in part II. We will focus here only on the surface modification with small organic molecules, in order to incorporate NPs in a polymer matrix. To cite a few examples, the use of silanes as coupling agent is commonly reported. Palimi et al. used 3-aminopropyltrimethoxysilane to modify and disperse Fe_2O_3 NPs in a polyurethane matrix.[110] In a review, Kango and collaborators give various other examples of surface modification of metal oxide NPs to incorporate them in polymer matrixes: for instance, TiO_2, Al_2O_3, ZnO, or Fe_3O_4, all modified with silanes.[111] Nakayama and Hayashi reported the surface modification of TiO_2 NPs by propionic acid and hexylamine, and the dispersion of these NPs in a polymer matrix.[112] They described the obtained NCs as highly transparent, and characterize this transparency by UV-Visible spectroscopy.

b – Raw nanoparticles/latex system

Aqueous ways to elaborate NCs are also possible with hydrophobic polymers, using a latex suspension, which is a dispersion in water of small polymer particles, usually stabilized by surfactants. The principle consists in mixing directly the aqueous colloidal suspension of NPs with the latex suspension. The NC is then formed by evaporation of the water. Rharbi and co-workers published the first study of silica-polymer NCs elaborated with this method, and reported on the dispersion of NPs in the NC under deformation.[113]

In such systems, different parameters can strongly affect the dispersion of the NPs in the NC. For instance, Oberdisse and collaborators studied the impact of physico-chemical parameters of the NPs colloidal solution. The NCs were made by mixing a colloidal silica NPs suspension and a core-shell polymethyl methacrylate (PMMA)-polybutyl acrylate (PBuA) latex. They highlighted the influence of NPs size, volume fraction, pH of the precursors solutions, and added salt on the structure and on the rheological and mechanical properties[114, 115] of the resulting NCs.[116]

The latex characteristics can also play an important role on the state of dispersion in the NC. The latex film formation mechanism is well-described (see figure 1.10).[117] As said before, the film formation is induced by water evaporation: the solution is concentrated until the polymer beads get in contact. At this stage there is no more water, but the film formation is not ended. During annealing, the polymer beads are deforming and coalescing, and the polymer chains interdiffuse. This interdiffusion is quite-well understood for neat latexes[118-120], and can strongly impact the structure of the final NC[121].

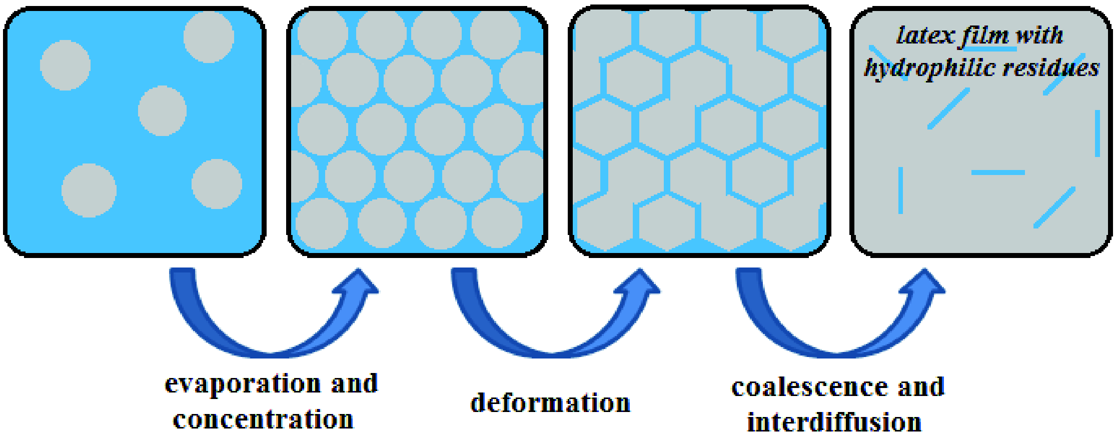

Figure 1.10: Latex film formation mechanism.

Consequently, drying and annealing conditions of the mixed solutions need to be well-controlled.

2 - Characterization of nanoparticles dispersion in nanocomposites

As said previously, the properties (especially the rheological and mechanical behavior) of the resulting NC material are linked to its structure, i.e. to the state of dispersion of the NPs in the NC. Consequently, to understand the structure-properties relation and to tune the properties of the NC, it is important to be able to characterize the structure of the NPs in the polymer matrix. Different methods have been described in the literature, including AFM or tomography.[122, 123] We will focus here on electron microscopy and Small-Angle Scattering (SAS) techniques, which are the most used techniques.

The first method is the direct observation by electron microscopy, e.g. Scanning Electron Microscopy (SEM) and Transmission Electron Microscopy (TEM). These techniques allow obtaining 2D-images of the NPs in the polymer matrix. The advantage is the simplicity of the method: no need of heavy data treatments or simulations. But, due to the small area covered by the images, it is difficult to have a representative picture of the NC. Thus, statistically relevant 3D dispersions of the NPs in the polymer matrix are difficult to obtain by these methods. To cite examples, Kim et al. reported on alumina NPs/polyethylene terephthalate NCs.[124] They followed the evolution of NPs state of dispersion with the degree of mixing by TEM. Palimi and co-workers modified the surface of Fe_2O_3 NPs with a silane (aminopropyltrimethoxysilane, APTMS) and dispersed them into a polyurethane matrix.[110] From the SEM images, they concluded on the better dispersion of surface modified NPs in the NC.

Small-Angle X-rays (SAXS) and Neutron Scattering techniques (SANS) are particularly useful to determine the NPs structure in the polymer matrix owing to the range of distances accessible. In addition, these techniques are non-destructive and allow monitoring the dispersion during formulation steps or under deformation. As described in Chapter II, the scattered intensity is directly proportional to the structure factor of the NPs. This allows quantifying the degree of dispersion of the NPs fillers by fitting and simulating the structure factor. However, the interpretation remains difficult, thus these techniques are often coupled with TEM measurements.

Concerning unmodified NPs dispersed in hydrophobic polymer matrixes, several SAS studies highlighted the impact of various parameters on the NPs structure in the NC. For instance, Jouault and co-workers studied the influence of silica NPs size, and the nature of the polymer matrix (PS or PMMA) on the dispersion, and thus on the mechanical properties of the NCs.[125] By coupling SAXS and TEM measurements, they observed a better dispersion for small silica NPs (radius = 6 nm) than for larger ones (radius = 14 nm). They noted a structure transition between low- and highly-filled NCs, corresponding to the formation of a connected network between the NPs in the NC, which leads to a high enhancement of mechanical properties. Janes et al. studied by TEM and SAXS the influence of the sample thermal history on silica NPs structure in a polymethyl acrylate matrix.[126] They could provide evidence for structural reorganization with annealing: stronger annealing leading to higher aggregation.

Oberdisse and co-workers investigated the aggregation state of NPs in NCs prepared by the latex route, by coupling SAS and TEM measurements.[114, 127, 128] In particular, they confirmed that the aggregation of NPs (aggregate size and number of particles in the aggregate) increased when:

- the NP volume fraction increased: due to a higher probability of contact and, thus to aggregation;

- the pH of the precursors aqueous dispersions decreased: leading to a decrease of the electrostatic charge of NPs;

- the molecular weight of the polymer chains decreased: due to the matrix viscosity decrease, which favor the mobility of NPs, and thus their aggregation.

For polymer-grafted NPs, different parameters have an impact on the NP dispersion state: including the grafting density, the length of the grafted chains, or the ratio of grafted-to-matrix chain mass.[129] For instance, in a silica-rubber system obtained by mechanical mixing in solid phase, Baeza and collaborators evidenced by SAXS and TEM measurements, that for a constant mass of polymer, the structure was impacted by the ratio of graftable to non-reactive polymer chains. The higher the ratio, the smaller the NPs aggregate.[130] However, for the highest contents of graftable chains, the structure did not evolve anymore, probably because of the saturation of the NPs surface. In another article, they demonstrated that two different NCs with the same grafting density display the same filler structure.[131] Indeed, in both samples, the same amount of graftable polymer chains and total mass of polymer were introduced. Although the chain length was different (thus implying a different rheology in the mixer), the structures of the obtained NC were identical. Finally, Chevigny et al.

studied by SAXS and TEM the influence of the ratio between grafted and matrix polymer chain lengths on the dispersion of PS-grafted silica NPs in a PS matrix.[132]

Note that SANS experiments also allow accessing the chain conformation of the grafted chains and the chains in the polymer matrix. Indeed, as it is an isotope-sensitive method, variation of the ratio of hydrogenated to deuterated polymer chains allows matching the NPs contrast, in order to see only the contribution of the polymer chains to the scattered intensity (see chapter II). For instance, the impact of the drying and annealing conditions on the structure of polymer chains in silica-latex NCs were studied by this way.[121]

Chapter II - Methods and materials

I - Dynamic Light Scattering (DLS)

1 - Principle

Dynamic Light Scattering (DLS) allows obtaining size information of colloidal suspensions of NPs or aggregates of nanoparticles.[133-135] It is a common technique to analyze NPs with ligands.[136] The principle is to follow the Brownian motion which is due to thermal agitation of particles by analyzing the resulting fluctuations of scattered light as described below. The size of the objects is expressed through the hydrodynamic radius, R_H. This radius corresponds to the radius of a sphere of same diffusion coefficient D and is given by the Stokes-Einstein law:

$$R_H = \frac{k_B T}{6\pi\eta D} \qquad \text{(eq.2.1)}$$

where $k_B = 1.3806\ 10^{-23}\ \mathrm{J\ K^{-1}}$ is the Boltzmann constant, T the temperature of the solution (in K), and η the viscosity of the solution (in Pa s). Agglomeration leads to an increase of the size of objects and thus of R_H. Thereby, DLS allows following the aggregation state of nanoparticles in suspension.[137]

In practice, the diffusion coefficient is measured by the fluctuations of light scattered by the sample which is illuminated by a monochromatic and coherent light source, a laser. The scattered light is then collected by a photomultiplicator at fixed or variable angle and analyzed. It reflects the structure of the suspension in terms of nanoparticle shapes and positions. The latter evolve due to Brownian motion, and so does the scattered light, which can be described by the decay of an auto-correlation function. The auto-correlation function gives us the probability to find a particle at the same place at the time t and after a short duration τ. This function can be deduced from the time-dependent intensity I(t,q):

$$g_2(\tau, q) - 1 = \frac{\langle I(t,q) I(t+\tau,q)\rangle}{\langle I(t,q)\rangle^2} - 1 \qquad \text{(eq.2.2)}$$

with $q = \frac{4\pi n \sin\left(\frac{\theta}{2}\right)}{\lambda}$, the scattering vector, with n the refractive index of the solution, θ the angle between the incident light and the detector, and λ the wavelength of the laser. The smaller the particles are, the faster they are moving, and the faster the auto-correlation decays to zero as a function of τ. In case of polydisperse objects, the probability decrease is described by the superposition of several functions.

In order to extract size and polydispersity from the auto-correlation function, different models are proposed. During this work, only the “cumulants fit” was used. This fit considers only one relaxation time, τ. The normalized auto-correlation function can be written:

$$g_2(\tau, q) - 1 = \left[\exp(-\overline{D} q^2 \tau)\left(1 + \frac{\overline{D^2} - \overline{D}^2}{2} q^4 \tau^2\right)\right]^2 \qquad \text{(eq.2.3)}$$

where $\overline{D}$ is the average diffusion coefficient, and $\overline{D^2}$ is the average of its square.

In our case, we consider a log-normal distribution of sizes, where the nth moment of the radius can be written:

$$\overline{R^n} = R_0^n \exp\left(\frac{n^2\sigma^2}{2}\right) \qquad \text{(eq.2.4)}$$

with σ the polydispersity of the distribution, defined by: $\sigma^2 = \frac{\overline{D^2} - \bar{D}^2}{\bar{D}^2}$

The apparent radius, R_{app}, of the object is given by:

$$R_{app} = \frac{\overline{R^6}}{\overline{R^5}} = R_0 \exp(5.5\,\sigma^2) = \frac{k_B T}{6\pi\eta\bar{D}} \qquad \text{(eq.2.5)}$$

with $\sigma^2 = \overline{R^2} - \bar{R}^2$.

2 - Experimental set-up

DLS measurements were done with a home-made set up at 90°. The laser used was a cobalt Samba with a power of 150 mW and a wavelength λ = 532 nm. The correlator is a Brookhaven BT9000. The solutions were diluted with solvent prior to analysis and measured directly in the dilution tubes. The data treatment is based on cumulants fit, detailed previously.

II - Small Angle Scattering techniques (SANS, SAXS)

1 - Principle

In Small Angle Scattering (SAS) experiments, a beam of X-rays (SAXS) or neutrons (SANS) is shuttled through a sample.[133, 138, 139] The sample, especially its heterogeneities, scatters the incident beam in all directions without change of energy (elastic scattering), and the scattered waves interfere. The resulting signal is collected at different angles by a 2D-detector, as illustrated in figure 2.1.

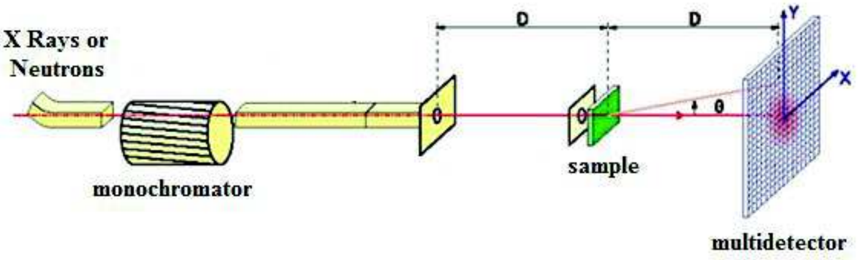

Figure 2.1: Small-angle scattering experiment.

It is more common to represent the evolution of the scattered intensity with the scattering vector q than with the angle between the incident and the scattered beam, θ. The norm of the scattering vector is defined by: $q = \frac{4\pi \sin\left(\frac{\theta}{2}\right)}{\lambda}$ with λ the wavelength of the beam.

The scattered intensity can be expressed by:

$$I(q) = \Delta\rho^2\, \phi\, V\, P(q)\, S(q) = I_0\, P(q) S(q) \qquad \text{(eq.2.6)}$$

with Δρ the scattering contrast (see section "Contrast"), ϕ the volume fraction of objects in the medium, V the volume of the object, P(q) the form factor, and S(q) the structure factor.

The form factor P(q) is related to the shape of the objects: size and shape. In the case of a sphere, the normalized form factor can be expressed as:

$$P(q) = \left(3\frac{\sin(qR) - qR\cos(qR)}{(qR)^3}\right)^2 \qquad \text{(eq.2.7)}$$

with R the radius of the sphere.

The structure factor S(q) depends on the spatial arrangement of the objects, thus also on the interactions between them, and is defined by:

$$S(q) = \frac{1}{N}\left\langle \sum_{j=1}^{N} \sum_{k=1}^{N} e^{i\vec{q}(\vec{Rj} - \vec{Rk})} \right\rangle \qquad \text{(eq.2.8)}$$

where N is the number of objects and R_j the positions of the centers-of-mass of the objects. Consequently, in a diluted medium, there are no interactions between objects, and S(q) = 1. Such a measurement allows deducing only the contribution of the form factor P(q).

2 - Contrast

The nature of the sample influences the scattered intensity, especially through its contrast. The contrast is defined by the difference of scattering length density, ρ, between the object and the dispersion medium, in our case, between the NPs and the solvent or the polymer matrix. Moreover, each atom scatters differently depending on its scattering length, b, which impacts the scattering length density:

$$\rho = \frac{\rho_m N_A}{M} \sum_i n_i b_i \qquad \text{(eq.2.9)}$$

with ρ_m the mass density, N_A the Avogadro number, M the molecular weight, b_i the scattering length of the atom, and n_i the number of atoms. The main scattering length densities of our components are given in table 2.1

In SAXS experiments, the beam interacts with the electron cloud of the atoms. In this case, the scattering length is given by:

$$b_i = Z_i b_e \qquad \text{(eq.2.10)}$$

where Z_i is the atomic number of the atom and b_e = 2.85 10^{-13} cm, the scattering length of an electron.

In neutron scattering experiments, the situation is different as the beam interacts with the nuclei of the atoms. Consequently, each nucleus has its own scattering length. Therefore, SANS experiments are nuclei- and thus isotope-sensible. This property allows performing contrast variation experiments. The principle consists in varying the deuterated/hydrogenated fraction of the dispersion medium, i.e. to vary the contrast of the solvent or polymer for "switching off" one part of the sample. This variation is used, for instance, to study core-shell nanoparticles or chain conformations of polymers.[121, 140]

Table 2.1: SANS and SAXS densities of scattering length of our components and solvents.

Component	ρ^{SANS} **(cm^{-2})**	ρ^{SAXS} **(cm^{-2})**
L200S	$3.67\ 10^{10}$	$1.91\ 10^{11}$
LS101	$2.78\ 10^{10}$	$2.80\ 10^{11}$
PC	$2.88\ 10^{10}$	$2.84\ 10^{11}$
H2O	$-5.58\ 10^{9}$	$9.51\ 10^{10}$
D2O	$6.34\ 10^{10}$	
CHCl3	$2.36\ 10^{10}$	$1.23\ 10^{11}$
CDCl3	$3.15\ 10^{10}$	
C_8PA	$1.4\ 10^{9}$	***
C_{12}PA	$3\ 10^{8}$	***
C_{18}PA	$-6\ 10^{8}$	***
PEA	$1.01\ 10^{10}$	***
PMMA	***	$1.08\ 10^{11}$
PS	***	$9.6\ 10^{10}$

3 - Asymptotical behavior

a - Guinier

The Guinier law is an empirical model valid in the small-angle domain, i.e. for qR << 1. It enables the determination of the size of objects in dispersion, if there are no interactions between them (S(q) = 1), no matter their shape. If these conditions are fulfilled, the form factor can be written:

$$P(q) = \exp\left(\frac{-q^2 {R_g}^2}{3}\right) \qquad \text{(eq.2.11)}$$

where R_g is the radius of gyration, defined by:

$$R_g{}^2 = \frac{1}{N} \sum_i^N r_i^2 \qquad \text{(eq.2.12)}$$

with r_i the distance between scattering molecules and the center-of-mass of the object. For homogenous spheres, the relationship between the geometrical radius, R, and the radius of gyration, R_g, is:

$$R_g = \sqrt{\frac{3}{5}} R \qquad \text{(eq.2.13)}$$

b - Porod

The Porod law describes the scattering curve in the high-q domain. It can be applied to two-phase systems with a contrast $\Delta\rho \neq 0$ and a sharp interface between them. The Porod asymptotical behavior fits:

$$I(q) = \frac{A}{q^{6-D_S}} \qquad \text{(eq.2.14)}$$

with D_s the fractal dimension associated to the surface of the scattering objects. For a perfectly smooth surface, $D_S = 2$, and $I(q) \propto q^{-4}$. In this case: $A = 2\pi\Delta\rho^2 \frac{S}{V}$ where $\Delta\rho$ is the contrast between scattering objects and the continuous medium, and S/V the cumulated specific surface area of the scattering objects.

4 - Reverse Monte Carlo simulation

For a 3D-visualization of particle configurations compatible with the experimentally obtained scattered intensity, a reverse Monte Carlo (RMC) algorithm was applied to I(q).[141-144] It is based on the experimental size distribution of spheres, and assumes homogeneous interacting spheres with excluded volume.[145] The basic design of the algorithm is outlined in reference [146].

In the case of surface modified L200S suspensions, the size of the cubic simulation box was set to about 1570 nm, filled to 0.2 %vol with ca. 2400 NPs.

5 - Experimental

Measurements were performed in different facilities: Laboratoire Léon Brillouin (LLB, Saclay - France) and Heinz Maier-Leibnitz Zentrum (MLZ, Munich - Germany) for SANS; Synchrotron Soleil (Saclay - France) and European Synchrotron Radiation Facility (ESRF, Grenoble - France) for SAXS. Colloidal solutions were measured in 1.5 mm thick capillaries and 1 mm Hellma cuvettes for SAXS and SANS, respectively. Nanocomposites were measured by SANS between two aluminium layers, in order to maintain the nanocomposites shape.

The scattering cross section per unit sample volume $d\Sigma/d\Omega$ (in cm^{-1}) – which we term scattered intensity I(q) – was obtained by using standard procedures including background subtraction and calibration. In order to enable comparison in between scattering data from different radiations, the neutron spectra have been systematically rescaled to the X-ray contrast.

The different configurations are given in appendix 1.

III - Broadband Dielectric Spectroscopy (BDS)

1 - Principle

Broadband Dielectric Spectroscopy measurements provide relevant information concerned with the dynamics (relaxations) of a material.[147, 148] This is possible due to the fluctuation of the dipolar moment upon different molecular processes. The principle is to place a sample between two disk-shaped electrodes (to form a capacitor) and to follow the evolution of the material impedance (related to both the capacity and conductivity) at different temperatures and frequencies under an external electric field, which is sinusoidal to reduce electrode polarization phenomena.

For a material composed of permanent dipoles, the application of a sinusoidal electric field constrains the dipoles' orientation. At high frequency, the degree of orientation is only partial, because dipoles fail to follow the variations of orientation. A decrease of the degree of orientation leads to a decrease of the dielectric permittivity ε. As a consequence, at low enough frequencies, all dipoles are oriented and the dielectric permittivity reaches a plateau corresponding to the dielectric constant of the sample.

It is convenient to represent the sample as a combination of a capacitor and a resistance, with both impedances given by:

$$Z_R = \frac{d}{\sigma_{dc}\, S} \quad \text{for the resistance} \qquad \text{(eq.2.15a)}$$

$$Z_C = \varepsilon\varepsilon_0 \frac{S}{d} = \varepsilon C_0 \quad \text{for the capacitor} \qquad \text{(eq.2.15b)}$$

where S is the electrode area, σ_{dc} the conductivity, d the distance between electrodes, ε the relative permittivity, ε_0 the permittivity in vacuum, and C_0 the capacity of the system without sample. In the general case, the system is well represented by the association of these two components in parallel. The impedance in a sinusoidal electric field is related to the applied current by:

$$Z^* = \frac{U}{I'} + i\,\frac{U}{I''} \qquad \text{(eq.2.16a)}$$

$$\frac{1}{Z^*} = \frac{1}{Z_R} + \frac{1}{Z_C} \qquad \text{(eq.2.16b)}$$

Under sinusoidal electric field, the permittivity becomes *ε*(ω) = ε'(ω) - i ε"(ω)*, the complex dielectric permittivity of the sample, with $\omega = 2\pi f$. The combination of the previous relations yields:

$$Z' = \frac{1}{\left(\frac{\sigma_{dc}}{\varepsilon_0} + \varepsilon''\omega\right) C_0} \qquad \text{(eq.2.17a)}$$

$$Z'' = \frac{1}{C_0 \varepsilon' \omega} \qquad \text{(eq.2.17b)}$$

2 - Models of dielectric relaxations

From a quantitative point of view, all dielectric phenomena, which are leading to a variation of permittivity, can be described by the Havriliak-Negami (HN) equation:[149]

$$\varepsilon^*(\omega) = \varepsilon'(\omega) - i\,\varepsilon''(\omega) = \varepsilon_\infty + \frac{\Delta\varepsilon}{[1+(i\omega\tau)^\alpha]^\gamma} \qquad \text{(eq.2.18)}$$

where $\Delta\varepsilon = \varepsilon_S - \varepsilon_\infty$ is the dielectric strength or dielectric relaxation amplitude; τ, the relaxation time, describes the dynamics of the system; ε' refers to the stored energy and ε" is proportional to the dissipated energy in the system; ε_S is the low-frequency permittivity or static permittivity; and ε_∞ is the high-frequency permittivity.

α and γ parameters in (eq.2.18) relate to a symmetric and asymmetric broadening of the distribution of relaxation times. When α = γ = 1, the process follows the Debye model. The relaxation can be described with a single characteristic time. When γ = 1 and α ≠ 1, the expression corresponds to the Cole-Cole extension of the Debye model, respectively.

3 - Relaxation time

As said previously, BDS measurements provide information about the dynamics of a system. One of the main characteristics is the distribution of relaxation times characterized by the maximum relaxation time, $\tau_{max} = \frac{1}{2\pi f_{max}}$ where f_{max} corresponds to the frequency of maximum loss.

In general, the temperature dependence of this typical time can be described by an Arrhenius equation:

$$\tau\,(T) = \tau_0 \exp\left(-\frac{E_a}{kT}\right) \qquad \text{(eq.2.19)}$$

with E_a the activation energy and k the Boltzmann constant. For components with a glass-transition behavior, $\ln \tau = f\left(\frac{1}{T}\right)$ is not linear. The evolution of the relaxation time is then given by the Vogel-Fulcher-Tamman (VFT) equation[150-152]:

$$\tau\,(T) = \tau_0 \exp\left(\frac{B}{T-T_0}\right) \qquad \text{(eq.2.20)}$$

with B a temperature factor, and T_0 the VTF-temperature.

4 - Ionic conductivity

The ionic conductivity of the sample, σ_{dc}, contributes[153] to the low-frequency increase of the imaginary part of permittivity. ε" is proportional to $\frac{\sigma_{dc}}{\varepsilon_0\,\omega}$. Note that there is no impact of the conductivity on the real part of permittivity ε'.

5 - Measurements

The BDS measurements were done on a Novocontrol Alpha Analyzer system in a frequency range between 10^{-2} and 10^{7} Hz. The samples - approximately 130 mg of washed and dried powders - were placed between two gold-coated electrodes of diameter 3 cm. The electrodes were surrounded by a Teflon ring in order to minimize deshydratation. During the measurements, samples were kept under a constant nitrogen flow. Complementary experimental details are given in appendix 5.

In order to study the dynamics of water molecules, the hydration of the powders were varied by keeping them in hermetic boxes of fixed relative humidity (RH). By using saturated salt solutions of LiCl, $MgCl_2$, K_2CO_3, and NaCl, the RH was set to 11%, 33%, 43%, and 75%, respectively.[154]

IV - Characterization of alumina-covered silica nanoparticles

In the chapters III, IV and V, the raw nanoparticles used are commercial, named Levasil 200S/30 (L200S) and were a gift from Akzo Nobel. This product consists in a stable aqueous suspension of silica NPs covered with an aluminium oxo-hydroxide layer, at pH 3.8, with 30 wt% solid content.

1 - Size of nanoparticles

A form factor measurement of L200S NPs by SAXS in dilute suspensions (0.2 %vol) is shown in figure 2.2. The fit indicates that the form factor is compatible with a log-normal size distribution of NP radii (R_0 = 7.4 nm, σ = 0.38).

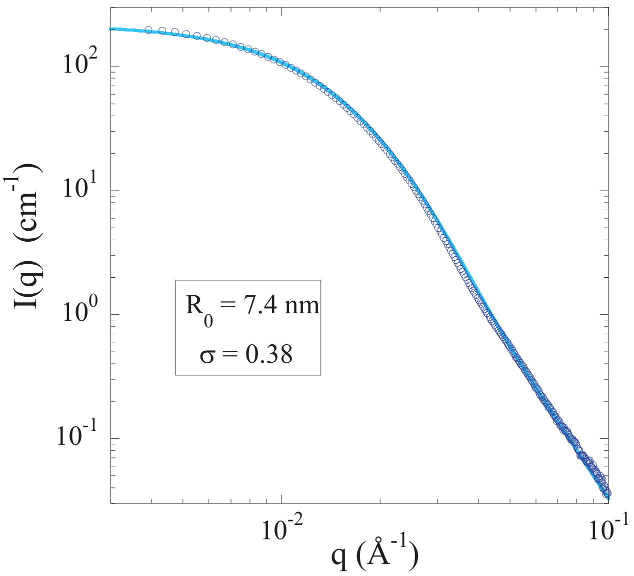

Figure 2.2: Scattered intensity I(q) of colloidal alumina-coated silica L200S at 0.2 %vol in water. The line is the description by the form factor of spheres taking into account a log-normal polydispersity.

The log-normal distribution is shown in the figure 2.3. This highly polydisperse distribution was confirmed by DLS measurements, which give an apparent hydrodynamic radius of R^{DLS} = 18.9 nm and σ = 0.4. Note that the apparent hydrodynamic radius of polydisperse hard spheres can be estimated from the moments of the size distribution derived from SAXS, $<R^6>/<R^5>$, which gives 16.4 nm, in reasonable agreement, with the DLS result. We have also estimated the average radius by TEM over 500 beads, the obtained histogram and the result are shown in figure 2.3. To summarize, the particle size is well-described by a log-normal distribution deduced from SAXS and agrees with the sizes seen by other techniques.

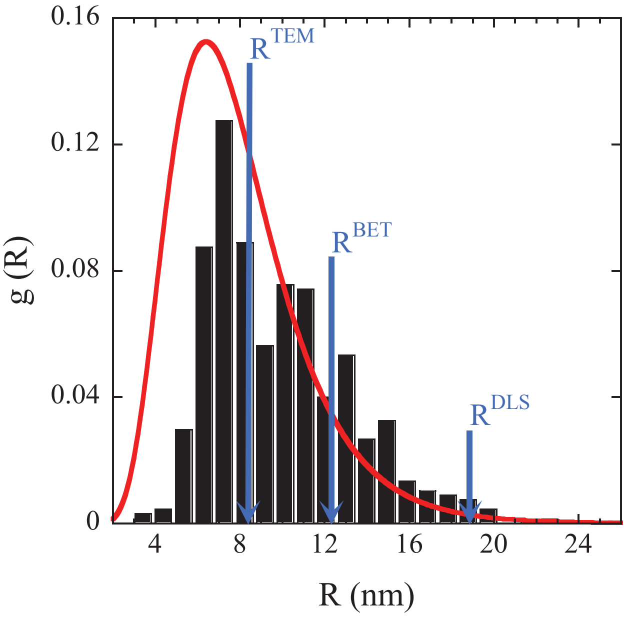

Figure 2.3: Normalized nanoparticles size distribution g(R) obtained by fitting to the form factor. Histogram obtained by measuring the size of approx. 500 NPs on TEM images. Arrows indicate the characteristic radii from TEM, BET, and DLS.

2 - Specific surface area and density

In order to evaluate the specific surface area, S_{spe}, and the density of the NPs, the colloidal solution was dried minimum 12 hours at 120°C under vacuum and degassed overnight at 150°C under vacuum and then put under inert gas. The nanoparticles density is 2.2 g/cm^3, which corresponds approximately to silica density. The adsorption-desorption of nitrogen at 77K gives us a specific surface area of 110.9 m²/g. The isotherms are given in figure 2.4.

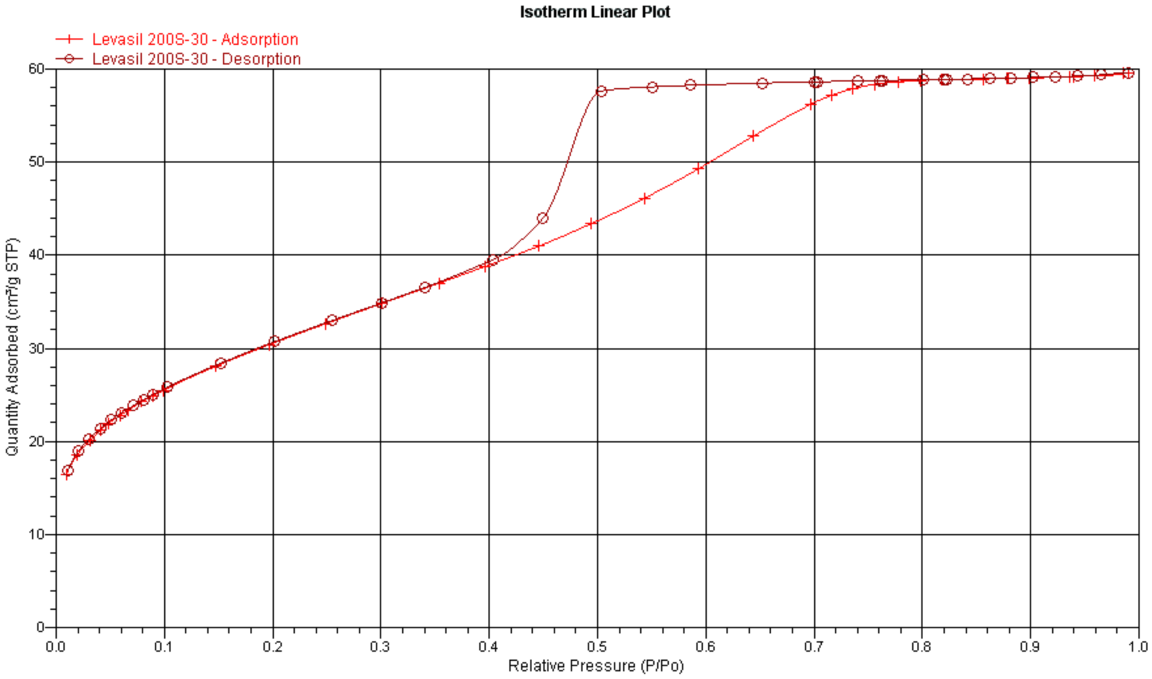

Figure 2.4: Adsorption and desorption isotherms of dried L200S NPs.

3 - Alumina layer

In order to evaluate the amount of the aluminium oxo-hydroxide surface layer, we made some elemental analysis using Inductively Coupled Plasma Optical Emission Spectroscopy (ICP-OES). These measurements give an aluminium content of the dried nanoparticles of 3.9 wt%. Using the BET specific surface area given previously (110.9 m²/g), the surface density of Al-atoms was found to be typically 7.9 nm^{-2}, allowing for the grafting of a dense monolayer of phosphonic acid. Note that this value is in the same range that the Al-OH density at the surface of the (0 1 0) face (the most exposed face) of γ-AlOOH (9.3 Al-OH/nm^2).[155]

4 - Charge of the nanoparticles in solution

Zetametry gave pH-dependent zeta-potentials decreasing from +55 to +35 mV for pH values varying from 4.4 to 6.8 for L200S (see figure 2.4). This positive net charge proves the presence of the alumina-like coating at the surface of the silica NPs (which would otherwise be negatively charged in this pH range) and provides electrostatic stabilization of the initial colloidal solutions. For comparison, the evolution of the zeta-potential of silica NPs (Ludox TM40) is also represented on the figure 2.5 below.

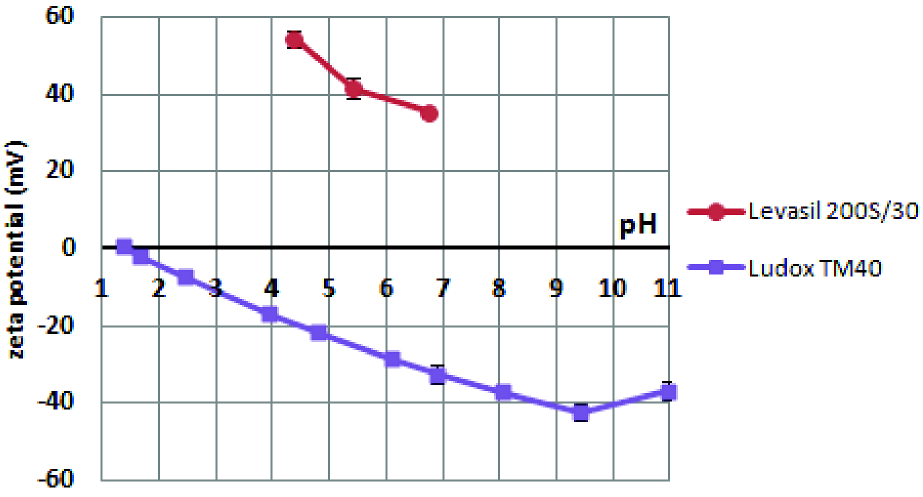

Figure 2.5: Zeta potential of silica (Ludox TM40) and alumina-covered silica (Levasil 200S/30).

5 - Thermogravimetric analysis (TGA)

The average of four different TGA runs of NP powders dried before analysis at 120°C gave a weight loss of 5.8% between 200°C and 800°C under air flow (50 mL/min), as shown in figure 2.6, which is attributed to the condensation of hydroxyl groups.

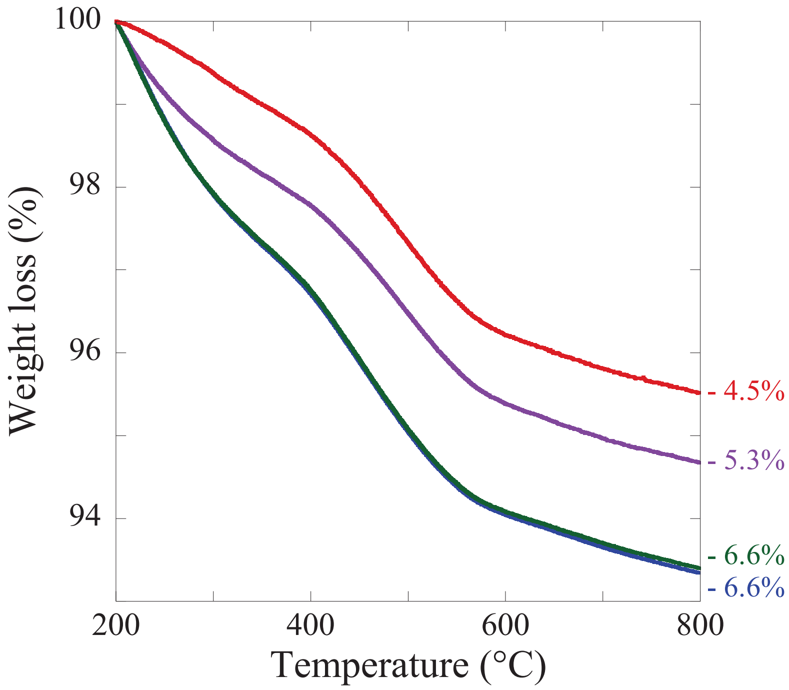

Figure 2.6: Mass loss of L200S given by four TGA measurements of raw and dried NPs.

The main characteristics of the L200S NPs are summed up in the table 2.2 given bellow.

Table 2.2: Main properties of alumina-coated silica NPs Levasil 200S/30.

Al wt% (ICP-OES)	3.9
R^{DLS}	19 $\pm$ 1 nm σ = 0.4
R^{TEM}	8.3 $\pm$ 2.8 nm
R (SAXS)	7.4 nm, σ = 0.38
S_{BET}	110 m²/g
Density	2.22 g/cm^3
Zeta potential at pH 4.4	55 $\pm$ 2 mV

V - Phosphonic acids

The main phosphonic acids (PAs) used for surface modification are n-octadecyl, n-dodecyl, n-octyl, n-pentyl, and n-propyl phosphonic acid (denoted C_{18}PA, C_{12}PA, C_8PA, C_5PA, and C_3PA, respectively), 6-phosphonohexanoic acid (CAPA), and (2-(2-(2-hydroxy-ethoxy)-ethoxy)-ethyl)phosphonic acid (DEPA).

C_3PA and C_5PA were synthesized in the laboratory in the following way. 49.8 g (0.3 mol) of triethylphosphite was gradually added via syringe into a flask containing 0.24 mol of 3-bromopropane (29.5 g) or 5-bromopentane (36.2 g), which was attached to a reflux condenser, a bubbler, and a septum. After thorough mixing, the reaction was refluxed for 12 h in a 150 – 160°C oil bath under argon to continuously remove the bromoethane away. After the cooling, the reaction mixture was distilled under reduced pressure (0.05 mbar) to give 23.8 g (55%) of pure diethylpropylphosphonate or 26.5 g (53%) of pure diethylpentylphosphonate.

Diethylpropylphosphonate (22.5 g, 0.125 mol) or diethylpentylphosphonate (26.0 g, 0.125 mol) were then placed into a flask equipped with a reflux condenser and containing 40 mL of dry CH_2Cl_2 under an argon atmosphere. 57.4 g (0.375 mol) of Me_3SiBr were then added via syringe and the reaction mixture was stirred for 3 hours at room temperature. The solution was then concentrated under vacuum and 1.875 mol (33.75 mL) of HPLC grade water was added drop wise under an argon atmosphere. The reaction mixture is then stirred for 12 hours, concentrated in vacuum and the crude oily white solid recristallized from hot acetonitrile to obtain 13.8 g (89%) of propylphosphonic acid or 15.05 g (79%) of pentylphosphonic acid.

C_8PA, C_{12}PA, C_{18}PA, and DEPA were purchased from Sikemia and CAPA from Aldrich.

The water content of these PAs, C_{H2O}, has been measured by TGA, 12 hours isotherms at 120°C under nitrogen, and used to calculate the grafting density. PAs were also characterized by ^{31}P-NMR (liquid and MAS measurements). For each PA, the HLB value was calculated (Davies calculation method, see Chapter I). All these characteristics are given in table 2.3 below.

Table 2.3: Phosphonic acid molecules used for grafting alumina-silica and titania NPs, classed by their hydrophobicity.

Phosphonic acid	Notation	HLB	^{31}P-liquid state NMR Shifts (ppm)	MAS-NMR shifts ^{31}P (ppm)	Water content C_{H2O} (wt%)
$H_3C(CH_2)_{17}PO(OH)_2$	$C_{18}PA$	11.75	26.6 (DMSO)	30.4	- 1.9
$H_3C(CH_2)_{11}PO(OH)_2$	$C_{12}PA$	14.6	26.9 (DMSO)	30.7	- 3.1
$H_3C(CH_2)_7PO(OH)_2$	C_8PA	16.5	30.4 (MeOD)	37.9	- 2.2
$H_3C(CH_2)_4PO(OH)_2$	C_5PA	17.9	31.2 (D_2O)	35.1	- 0.6
$H_3C(CH_2)_2PO(OH)_2$	C_3PA	18.9	30.9 (D_2O)	34.2	- 4.7
$HOOC(CH_2)_5PO(OH)_2$	CAPA	20.0	30.7 (D_2O)	33.1; 35.5	- 2.6
$H(OCH_2CH_2)_3PO(OH)_2$	DEPA	21.9	27.2 (D_2O)	33.3*	- 12.2

*Note that DEPA is a viscous liquid, the MAS-NMR measurement was done at 330 Hz.

In chapter VI, other PAs were used to test the limits of the phase transfer. Tert-butyl (tBuPA) and phenyl-phosphonic acids (PPA) were purchased from Acros Organics and Aldrich, respectively.

VI - Characterization of TiO_2 nanoparticles

The main characteristics of the two stable aqueous sols of TiO_2 in water and the dry TiO_2 nanoparticles used in chapter VI are given below.

1 - Lotus Synthesis

The first NPs used are commercial, named Lotus Synthesis 101 (LS101) and were a gift from Lotus Synthesis. This product is a stable aqueous suspension of TiO_2 NPs (95% anatase, 5% brookite, according to the manufacturer), at pH<1, with 23 wt% solid content. The X-Rays Diffraction (XRD) spectra are given in figure 2.7. The diffraction peaks can be assigned in both cases to a mixture of predominantly TiO_2 anatase (JCPDS card #84-1286) and brookite (JCPDS card #72-0100), as shown by the minor peak at ca 31 degrees.

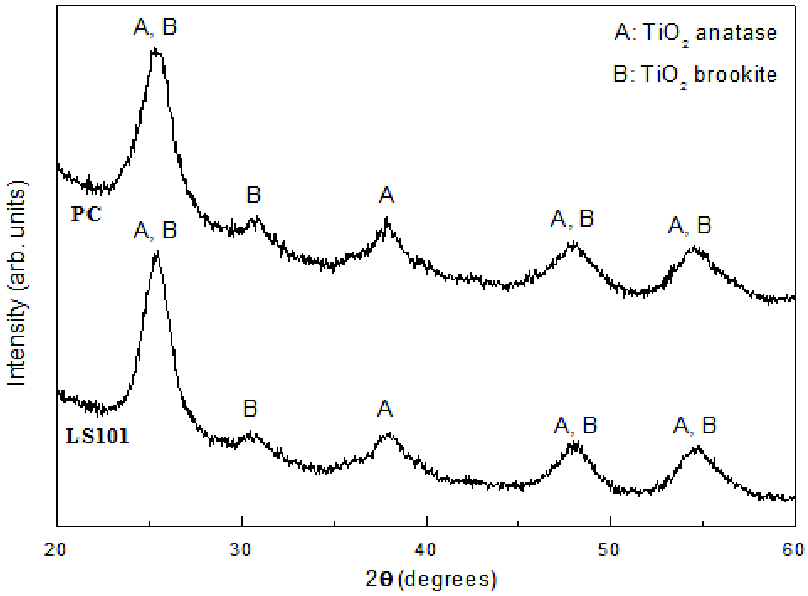

Figure 2.7: XRD spectra of LS101 and PC TiO_2 nanoparticles.

According to the manufacturer, the average of the primary nanoparticles size is 5-7 nm. We measured an average (out of 130 NPs) primary nanoparticles diameter of 5.2 nm by TEM, see figure 2.8 for TEM image.

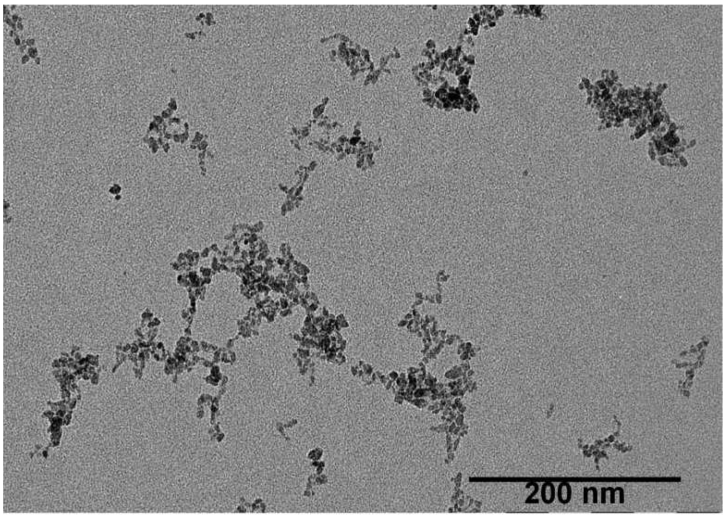

Figure 2.8: TEM image of LS101 nanoparticles.

Further characterization by SAXS and DLS indicate that in the sols these primary nanoparticles aggregate to build larger TiO_2 clusters. For comparison with contrast variation experiments (see chapter VI), LS101 NPs have been characterized in dilute (0.13 %vol) aqueous suspension by SAXS. The scattered intensity is shown in figure 2.9. Two levels of structural organization are found. At intermediate to large q-values (cf. fit with scattering of polydisperse spheres, red solid line), the primary NPs are seen. From its low-q limit, the concentration and the contrast, one can estimate the average volume of these primary NPs, which could be described with a log-normal size distribution (R_0 = 2.4 nm, σ = 0.30) of small spheres, in good agreement with XDR and TEM results (see figure 2.8 for TEM image). On a larger scale (cf. low-angle Guinier fit, blue dotted line), aggregation of the primary particles to build the TiO_2 clusters is observed. The cluster radius corresponding to an equivalent homogeneous sphere is 32 nm, and a short fractal domain with dimension 1.8 describing the internal structure is also seen. DLS also shows that primary NPs form small clusters in solution, of average hydrodynamic radius $R^{DLS} = 24 \pm 3$ nm at pH 2.

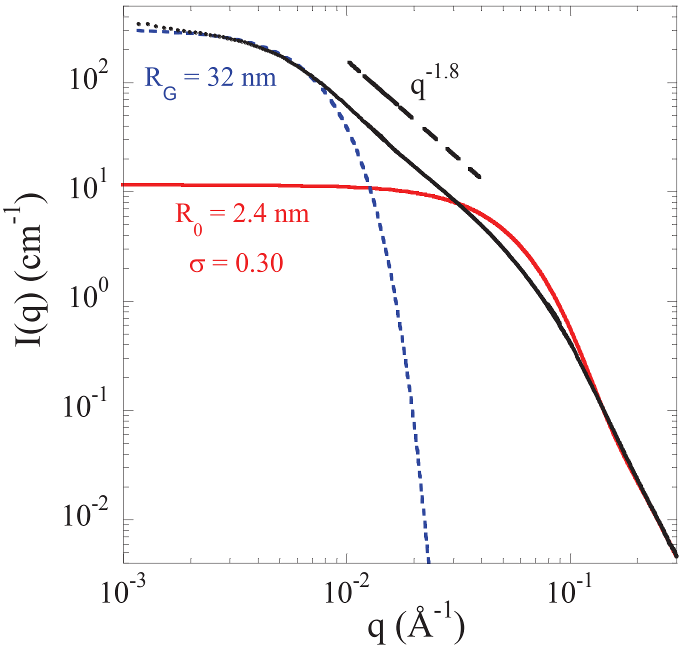

Figure 2.9: Structure of LS101 TiO_2 NPs in aqueous solution studied by SAXS. The two levels of organization are described by the relevant scattering laws (see text). The intermediate scattering is compatible with a power law corresponding to a fractal dimension of 1.8.

The specific surface area was measured by nitrogen adsorption - desorption at 77K on dried and degassed (120°C under vacuum overnight) powder. Zeta-potential measurements gave 41 ± 3 mV at pH 1.4 and 49 ± 11 mV at pH 2.0. The main measured parameters are given in the table 2.4 below.

Table 2.4: Main characteristics of Lotus Synthesis 101 nanoparticles.

R^{DLS}	24 nm
R^{TEM}	2.6 nm
R (SAXS)	Primary NPs: 2.4 nm Aggregates: 32 nm
S_{BET}	200 m^2/g
Density	3.43 g/cm^3

2 - Plasmachem

The second titania NPs used are also commercial, named Plasma Chem (PC) and were purchased from Plasmachem (ref. PL-TiO-10p). This product is a stable aqueous suspension of TiO_2 NPs, at pH<1, with 10 wt% solid content. The XRD is given in figure 2.7. The NPs consists in a mix of anatase (major part) and brookite (minor part), as in the case of TiO_2 LS101 NPs.

According to the manufacturer, the average particle size in the sol is in the 4-8 nm range, which is consistent with the diameter of 3.2 nm found by us with TEM (out of 100 NPs) given the high polydispersity. From DLS measurements, a hydrodynamic radius of 10 ± 1 nm is obtained. As can be seen in figure 2.10, the PC NPs have a structure similar to that of LS101 NPs, with clusters of typical radius 49 nm and a fractal dimension of 1.7, built of primary NPs of typical radius 1.8 nm, with a high polydispersity, σ = 0.30.

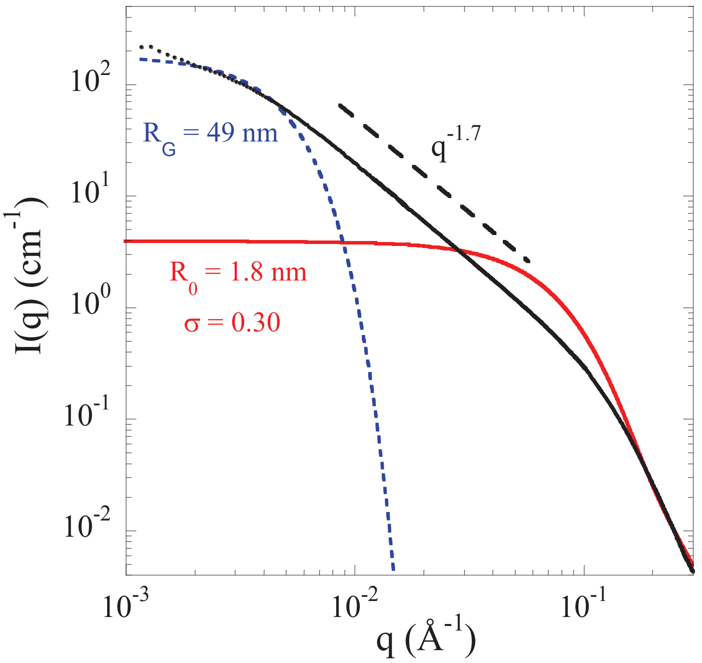

Figure 2.10: Structure of PC TiO_2 NPs in aqueous solution studied by SAXS. The two levels of organization are described by Guinier laws, and the intermediate scattering is compatible with a power law corresponding to a fractal dimension of 1.7.

The zeta-potential of the NPs was 12 ± 3 mV at pH 1.1 and 8 ± 4 mV at pH 2.2. The main characteristics are summed up in table 2.5.

Table 2.5: Main characteristics of PlasmaChem nanoparticles.

R^{DLS}	9 nm
R^{TEM}	1.6 nm
R (SAXS)	Primary NPs: 1.8 nm Aggregates: 49 nm
Density	3.48 g/cm^3

3 - P25 Degussa

Fumed TiO_2 Aeroxide dry powder from Evonik (noted TiO_2 P25) was also used in order to perform transfers with pre-aggregated NPs. TiO_2 P25 (Degussa) consists of aggregated TiO_2 NPs of about 30 nm in diameter, specific surface area S_{BET} = 55 ± 15 m^2/g, and 80/20 anatase/rutile ratio.

Note that Al_2O_3 Aeroxide powder from Evonik (named Al_2O_3 C) was used to show the generality of the phase transfer with other oxides. Al_2O_3 C consists of aggregated γ- and δ-alumina NPs of about 13 nm in size; its specific surface area is about 90 m²/g.

Both powders were dried under vacuum before use.

VII - Latex

1 - Synthesis

PEA latexes were synthesized in a thermostated reactor (at 80°C) under argon flow, with a free radical emulsion using semi continuous batch method. It was adapted from similar protocols.[127, 156] Ethylacrylate (EA, Aldrich, 99% purity), 2,2'-Azobis (2-methylpropionamidine) dihydrochloride (AIBA), Cetyltrimethylammonium bromide (CTAB) and Sodium phosphate monobasic monohydrate (NaH_2PO_4, H_2O) were used as monomer, initiator, surfactant, and buffer respectively.

First, oxygen was removed from the reactor by bubbling argon in a mix of ultra-pure water (184 mL), surfactant (1.35 g), and buffer (0.97 g) during 10 min under stirring (250 rpm). Then, the solution was heated in the glass reactor under argon flow at 80°C. Once the temperature was stabilized, in the mean time, 1 mL of aqueous solution of initiator (0.38 g in 2 mL) was added into the reactor, and the two feed streams were started. The monomer was added at 0.38 g/min and a mix of water (87 mL), surfactant (3.94 g), initiator (0.128 g), and buffer (0.27 g) was introduced in parallel at 0.72 g/min. After one-hour addition, the final solution was kept 30 min at 80°C under gas flow and stirring.

After synthesis, the latex was first dialyzed against resin (Serva Serdolit MB) and water during 1h then one week in water alone to remove salts, residual monomer, … After dialysis, the latex was centrifuged at 20000 rpm during 30 min and filtered (0.20 µm). To remove the maximum of surfactant, 2.5 wt% of resin (in regard of aqueous suspension) was added in the latex. The dispersion is then stirred during 1h and filtered. The polymer contain of the obtained nanolatexes is approximately 8 wt%. A photograph of the obtained nanolatex is shown in figure 2.11.

Figure 2.11: Photograph of an obtained PEA nanolatex after filtration and centrifugation. One can see that the dispersion is transparent.

2 - Characterization

The aqueous latexes were characterized by DLS to get the size and polydispersity in sizes (σ) of the polymer beads in solution. The dispersions were also dried at 80°C overnight to obtain the solid content.

After drying, the PEA was analyzed by:

- DSC to measure the glass transition temperature, Tg.
- SEC to evaluate the length and polydispersity of the polymer chains. Mw corresponds to the average in weight of the chain lengths. The polydispersity, PD, is defined by: PD = Mw/Mn with Mn the average in number of the chain lengths. Note that the results were obtained with PMMA calibrations.

The results are summed up in the table 2.6.

Table 2.6: Characteristics of synthesized PEA latexes.

Reference	**Solid content (wt%)**	**DLS**		**DSC**	**SEC**
		Rapp (nm)	**σ**		
CS197	8.3	14	0.67	Tg = - 9°C	Mn = 74 k Mw = 181 k PD = 2.5
CS221	8.7	13	0.51		
CS222	8.1	12	0.39		

VIII - Water-borne nanocomposites

Nanolatex and modified nanoparticles aqueous dispersions were adjusted at pH 5 (if necessary) then mixed in the good proportions to obtained different volume fractions. The obtained dispersion was dried at 70°C during 24h at atmospheric pressure in a Teflon pan, annealed at 120°C during 5.5 days under vacuum, pressed at 120°C during 2 min and finally annealed at 120°C under vacuum during 40h.

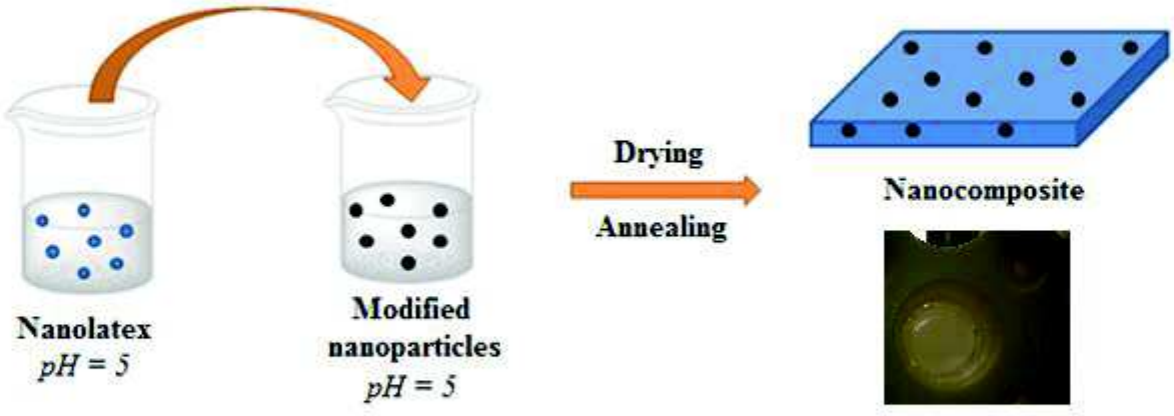

Figure 2.12: Elaboration of nanocomposites in water.

The nanocomposites were placed at -10°C during a few minutes before removing from pan. The obtained films were measured at SAS without another treatment.

Chapter III – Impact of grafting of phosphonic acids on nanoparticles interactions and stability in aqueous solutions

The main part of the results presented in this chapter were published in reference [1].

The control of interactions, and thus of aggregation of NPs in aqueous suspensions, can be varied by modifying the NPs surface with organic molecules. However, the commonly used silanization is hardly applicable in water. In this chapter, the surface of alumina-coated silica nanoparticles in aqueous suspension (L200S) has been modified with phosphonic acids bearing low molecular-weight organic groups of various hydrophobicity and charge. As mentioned in the bibliographic part (chapter I), surface modification of silica NPs with PAs is not possible in aqueous medium, due to the low hydrolytic stability of Si-O-P bonds. Hence, we used alumina-covered silica NPs, because of the stability against hydrolysis of the Al-O-P bonds.

The purpose was to explore the modification of aqueous sols of alumina-coated silica stabilized by electrostatic repulsions with different phosphonic acids, and to asses the impact of the surface modification on the interactions (electrostatic, steric, hydrophobic, etc) between NPs in solution, with special attention to the colloidal stability. Five different PAs with increasing hydrophilic-lipophilic balance (HLB) values have been used: three PAs with electrically neutral alkyl groups of increasing number of carbon atoms (propyl, pentyl, and octyl PAs, denoted respectively C_3PA, C_5PA and C_8PA), conferring increasing hydrophobicity to these groups, and two PAs bearing hydrophilic groups, either a neutral diethylene glycol (DEPA) or a potentially charged carboxylic group (CAPA). They have been grafted up to densities of $\rho = 4$ P/nm^2. This study opens the way to control first the aggregation of NPs in solution, and ultimately the structure of water-borne NP-polymer mixtures, like e.g. silica-latex nanocomposites (cf. chapter I, paragraph IV-1-b).

The outline of this chapter is the following. After a description of the grafting parameters, the characterization of the grafted NPs is detailed, then the evolution of colloidal stability is investigated using DLS, and the aggregation in solution is quantified using DLS, TEM, and SAS methods.

I - Surface modification of nanoparticles in colloidal solution in water

The grafting of the NP sols was performed as followed. 5 g of commercial colloidal solution was diluted by adding 10 mL of ultra-pure water and then the pH was increased up to 5 by drop wise addition of 0.1 M NaOH. The phosphonic acid grafts (see chapter II for nomenclature) were separately dissolved in 15 mL of water and the pH of the resulting solution also adjusted to 5. Both solutions were then mixed yielding a final concentration of NPs in the solution of 5 wt%, and stirred at 200 rpm at room temperature for 24 h.

For characterization by elemental analysis, TGA, NMR, and FTIR spectroscopies, the grafted NPs in the colloidal suspension were isolated by centrifugation during 20 min at 20 000 rpm, then washed twice with ultrapure water to remove phosphonic acid in excess by centrifugation, removing the supernatant, and redispersion in water. The final wet cake was dried at room temperature under vacuum overnight. The dried NPs were grinded with mortar and pestle prior to analysis. For structural analysis in water, the pH was always fixed to 5.

The different parameters varied during this study are:

- the nominal grafting density
- the nature of the grafted phosphonic acid

The nominal grafting density ρ_{nom} expressed as the number of phosphonic acid functions per unit nanoparticle surface (P/nm²) reads:

$$\rho_{nom} = \frac{m_{PA}\ N_A\,(1-C_{H2O})}{M_{PA}\ S_{BET}\ m_{NPs}} \qquad \text{(eq.3.1)}$$

Where N_A is the Avogadro number, M_{PA} the molar mass of the PA, S_{BET} the specific surface area of the dried NPs, m_{PA} the mass of phosphonic acid, and m_{NPs} the one of NPs in solution. Note that ρ_{nom} is corrected for the PA water content C_{H2O}. The range of nominal grafting densities studied here extends up to typically ρ_{nom} = 5 P/nm^2. The resulting real grafting density ρ measured by ICP will be given below.

The surface of NPs was modified by reaction with the phosphonic acids termed C_3PA, C_5PA, C_8PA, CAPA and DEPA, given in table 2.3 in the previous chapter. These PAs have been classed by their hydrophobicity. As said in part I, it can be evaluated via the HLB calculation: in this study, we have used Davis method. All the HLB values are given in table 2.3. All these molecules are water-soluble at the concentrations used, which for instance is not the case for dodecyl- or octadecylphosphonic acids, discarded for this study. The pH of reaction was fixed to 5 to minimize the dissolution of surface aluminium species and precipitation of aluminium phosphonate phases.[62, 76] The surface modification was monitored by FTIR and ^{31}P solid-state NMR spectroscopies, TGA, and ICP-OES of the washed and dried NPs.

II - Characterization of surface-modified NPs

FTIR, TGA, and NMR measurements were used to prove the presence of phosphonic species at the NPs surface. The grafting density was then quantified by ICP-OES.

1 - FTIR

The FTIR spectra of a series of NPs reacted with increasing amounts of phosphonic acid C_8PA are compared in figure 3.1 with the spectrum of the bare NPs. The spectrum of the bare NPs shows a broad vibration in the 3700-3100 cm^{-1} range arising from O-H stretching in hydroxyl groups (Si-OH and Al-OH) and adsorbed water. The weak bands at 2010 and 1880 cm^{-1} arise from Si-O overtone and combination modes. The presence of adsorbed water is confirmed by the deformation vibration at 1630 cm^{-1}. The spectra of the modified NPs show the presence of additional vibrations between 2800 and 3000 cm^{-1}, the intensity of which increases with the nominal grafting density. These bands correspond to the stretching of C-H bonds in the grafted phosphonate groups with the methylene symmetric and asymmetric stretching modes at 2857 and 2927 cm^{-1}, respectively, and one asymmetric stretching mode for the methyl group at 2960 cm^{-1}. The high wavenumber values observed for the C-H vibrations show that even at high grafting density the octyl chains in the monolayer are rather disordered. Below 1400 cm^{-1}, the bands arising from P-O vibrations in the 1200-900 cm^{-1} range overlap with the intense bands due to Si-O vibrations of the bare NPs. The vibrations in the 1000-1300 cm^{-1} range can be ascribed to the antisymmetric Si-OM (M = Si or Al) stretching, the shoulder at ca 950 cm^{-1} to Si-OH (possibly Al-OH) antisymmetric stretching. The sharp vibration at 810 cm^{-1} is ascribed to the symmetric Si-OM (M = Si or possibly Al) stretching (used for the normalization of the spectra).

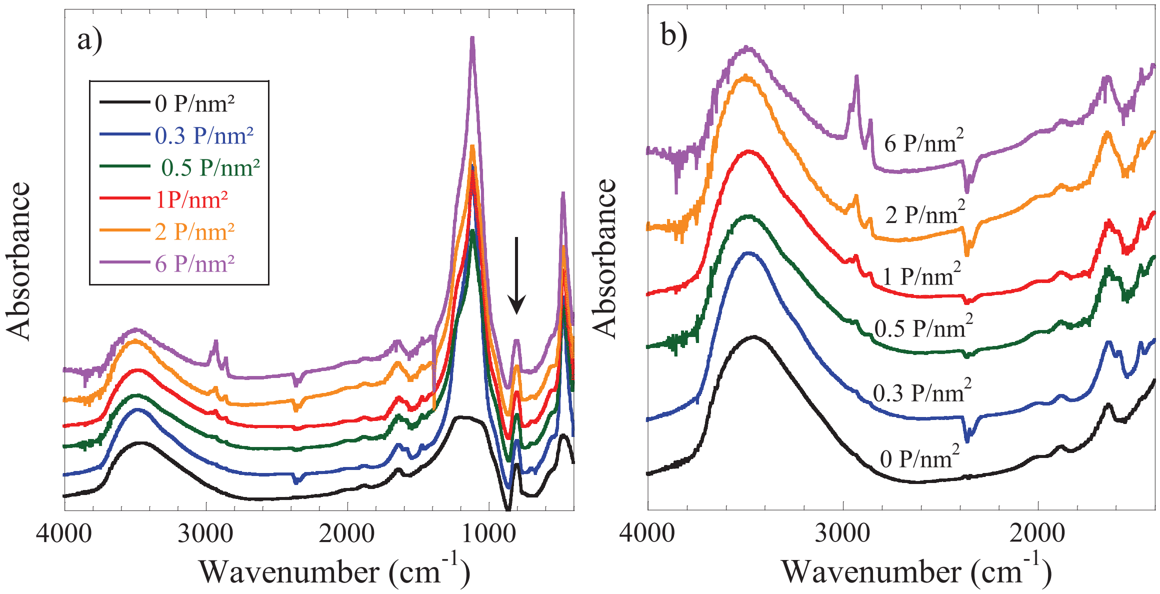

Figure 3.1: FTIR spectra of NPs grafted with C_8PA at nominal grafting densities between ρ_{nom} = 0 (bare NPs) and 6 P/nm^2. **a)** FTIR spectra in the 4000-400 cm^{-1} range. The arrow indicates the band used for normalization. **b)** FTIR spectra in the 4000-1600 cm^{-1} range. Spectra are normalized and shifted vertically for clarity.

Spectra of NPs modified by the other PAs (C_3PA, C_5PA, CAPA, and DEPA) showing the same characteristic vibrations are given in figure 3.2. It shows the vibrations associated to the C-H stretching of the methyl and methylene groups. The asymmetric CH_2 stretching at 2937 cm^{-1} in C_3Pa is shifted to lower wavenumber values when increasing the length of the alkyl group (2926 cm^{-1} in C_8Pa). These values suggest that the monolayers are rather disordered, with order increasing with the alkyl chain length. The same trend is observed in self-assembled monolayers of long-chains alkylphosphonic acids.[157] Note that such an effect is also observed on the symmetric CH_2 stretching vibrations around 2860 cm^{-1} (see arrows in figure 3.2).

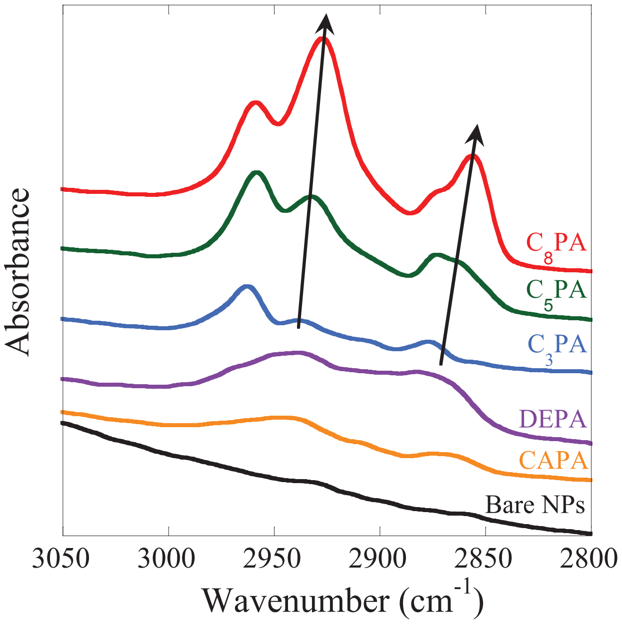

Figure 3.2: FTIR spectra of the C-H stretching region of the bare NPs and NPs grafted with the different PAs (ρ_{nom} = 4 P/nm^2). Spectra are shifted vertically for clarity.

In figure 3.3, we have compared the spectra of CAPA and of NPs grafted with CAPA. Carboxylic acids can be used to modify alumina surfaces, although they are easily exchanged.[36, 158] In self-assembled monolayers formed by reaction of carboxydodecylphosphonic acid with a metal oxide surface, the phosphonic acid groups were found to bind preferentially to the surface, leading to monolayers terminated by carboxylic acid groups.[74]

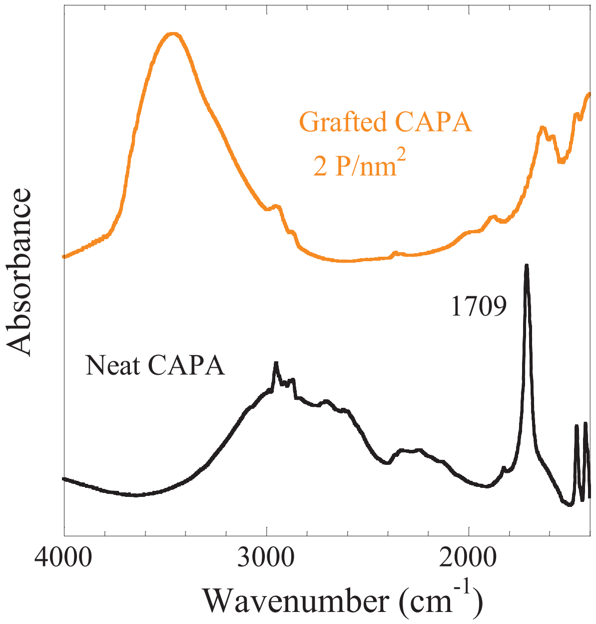

Figure 3.3: FTIR spectra of pure and NPs grafted by CAPA (2 P/nm^2). Spectra are shifted vertically for clarity.

In the spectrum of grafted CAPA, the absence of the C=0 stretching band at ≈ 1710 cm^{-1} (characteristic of the COOH group) indicates however that the carboxylate group is bonded to the NP surface as shown in figure 3.4; this situation is likely favored by the low grafting density of our monolayers.

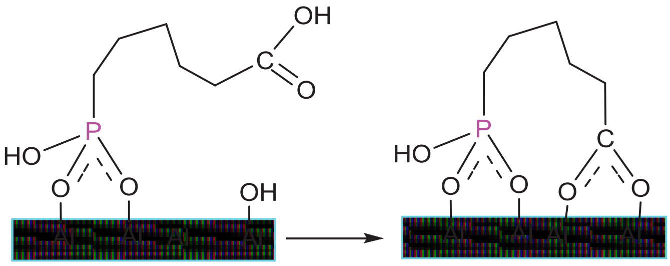

Figure 3.4: Grafting of CAPA to an alumina surface by both phosphonate and carboxylate groups.

Infrared characterizations show the presence of phosphonate species. As the modified NPs were washed thoroughly prior to analysis, it can be assumed that these phosphonate species are grafted to the NPs and not simply physisorbed.

2 - TGA

The TGA curves in air of bare and modified NPs confirm the grafting (cf. figure 3.5).

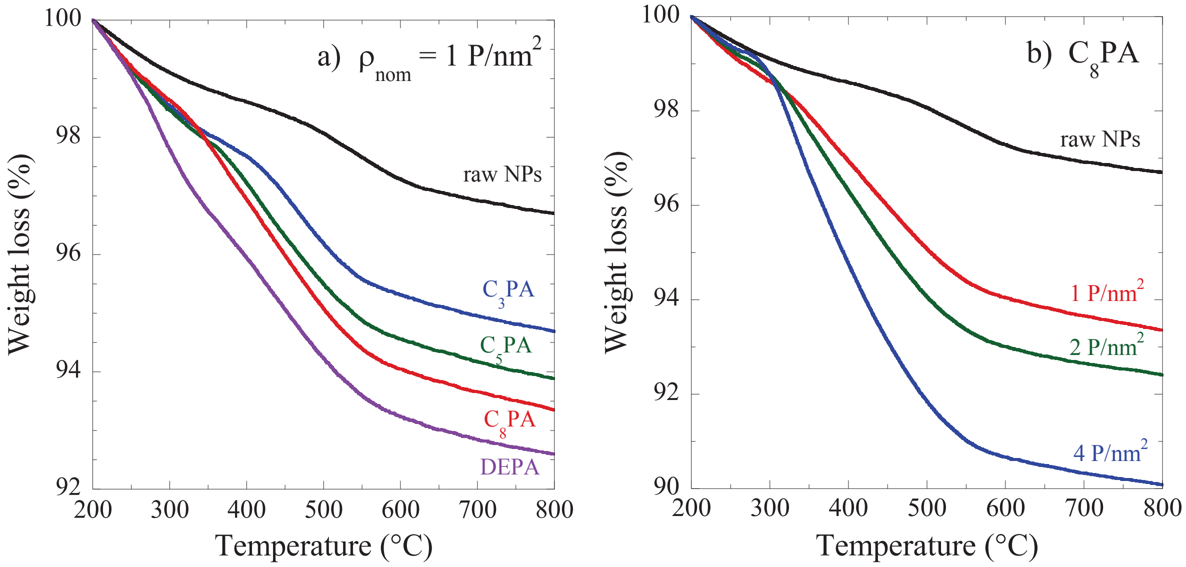

Figure 3.5: TGA curves for the modified and bare NPs. **a)** Grafting with various phosphonic acids with nominal grafting density ρ_{nom} = 1 P/nm^2. **b)** Grafting with C_8PA, ρ_{nom} = 0 – 4 P/nm^2.

The weight loss between 200 and 800°C increases with the molecular weight of the PA and with the grafting density. This weight loss corresponds not only to the degradation/combustion of the organic groups and formation of a phosphate residue, but also to the condensation of the residual hydroxyl groups. This makes a precise determination of the actual grafting density difficult, particularly for low grafting densities and low molecular weight organic groups. For this reason, we did not evaluate the grafting densities from TGA as for instance in refs [159, 160]. The associated weight losses are given in table 3.1.

Table 3.1: Weight loss between 200 and 800°C in air for the different NPs investigated.

PA	Nominal ρ (P/nm^2)	ΔM/M
Bare NPs	0	3.3 %
C_3PA	1.0	5.3 %
C_5PA	1.0	6.1 %
C_8PA	1.0	6.6 %
C_8PA	2.0	7.6 %
C_8PA	3.9	9.9 %
DEPA	1.1	7.4 %
DEPA	1.9	9.0 %
DEPA	5.3	14.8 %

Due to washing, they are most probably grafted, but the formation of an independent aluminium phosphonate phase by a dissolution-precipitation mechanism cannot be ruled out.[62, 76] ^{31}P-NMR measurements were therefore used to complete this characterization.

3 - ^{31}P MAS-NMR

^{31}P MAS-NMR spectroscopy is a tool of choice to evidence the formation of grafted phosphonate species. With this method, the presence of physisorbed PAs molecules or crystalline metal phosphonate phases can easily be detected.[161] However, ^{31}P MAS-NMR gives no direct information on the exact binding modes of phosphonate species to the surface, contrary to ^{17}O MAS-NMR.[64] The ^{31}P MAS-NMR spectra of grafted NPs in figure 3.6 a and b show in all cases broad resonances in the 0-35 ppm range. These broad signals confirm the presence of phosphonate units grafted onto the silica-alumina surface via P-O-Al bonds and also P-O-Si bonds. These P-O-Si bonds result from the condensation of P-OH groups with Si-OH groups during the drying treatment, as previously reported in the surface modification of aggregated silica-alumina nanoparticles by octylphosphonic acid.[76] Note that in aqueous solution, due to the sensitivity of P-O-Si bonds to hydrolysis[75] the phosphonate species should be grafted via P-O-Al bonds only.

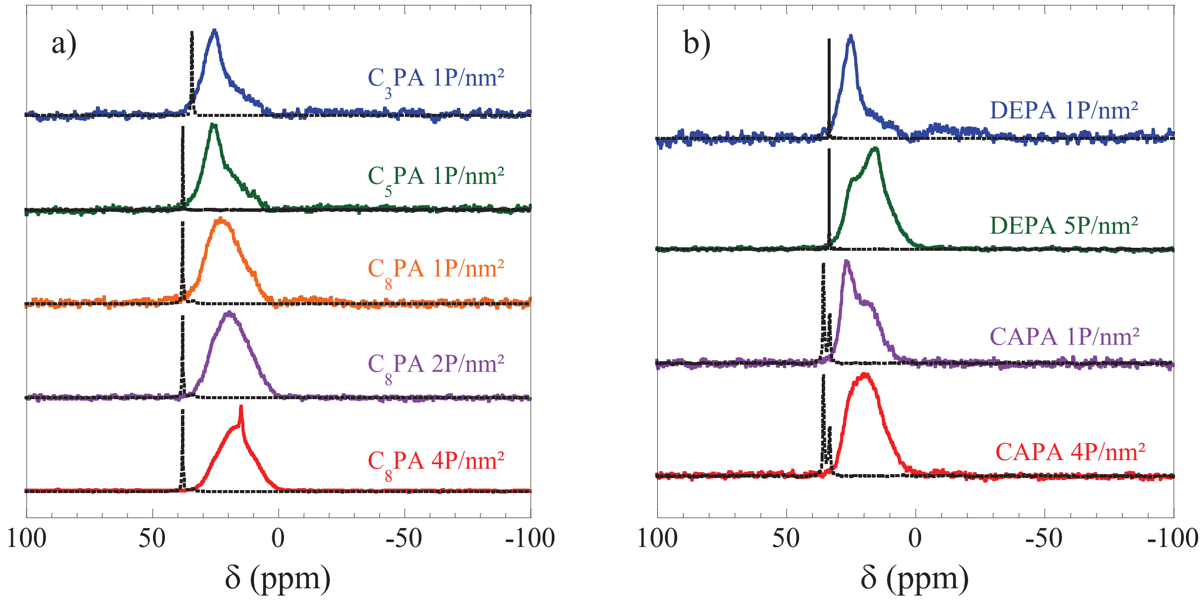

Figure 3.6: ^{31}P MAS NMR of neat PAs (dotted lines) and NPs modified (solid lines) **a)** with alkylphosphonic acids C_3PA and C_5PA at nominal grafting density of 1 P/nm^2, and C_8PA at 1, 2 and 4 P/nm^2 as indicated above each spectrum, and **b)** with CAPA and DEPA at low and high nominal grafting densities (idem).

The absence of a sharp resonance around 30 ppm arising from free phosphonic acid (see dotted lines for the neat PAs in figure 3.6) indicates that physisorbed phosphonic acid molecules were effectively removed by the washing steps. A small, sharp resonance at ca 15 ppm was detected in the spectrum of the NPs modified with 4 C_8PA/nm^2, indicating the minor formation of an aluminium phosphonate phase (less than 3% by integration of the spectrum) by dissolution and precipitation. In all other modified NPs, the absence of such sharp signals allows to rule out the presence of aluminium phosphonate phases.

4 - ICP-OES

As said previously, TGA in air is commonly used to determine grafting densities in self-assembled monolayers. However, formation of P_2O_5 and condensation of the residual hydroxyl groups take place in the same temperature range than phosphonic acids degradation. This makes a precise determination of the actual grafting density difficult, particularly for our low grafting densities and low molecular weight organic groups. Accordingly, the real grafting density was derived from the P content of the modified NPs, measured using ICP-OES and from the specific surface area of the bare NPs given in the experimental section. The nominal grafting densities of the modified NPs are given in table 3.2, where they are compared to the values measured using ICP-OES.

Table 3.2: Nominal and measured grafting density for the modified NPs. The nominal values are corrected for the PA water content.

PA	Nominal ρ (P/nm^2)	Measured ρ (P/nm^2)
C_3PA	0.47	0.40
C_3PA	0.96	0.93
C_3PA	4.19	3.62
C_5PA	0.51	0.40
C_5PA	1.00	1.09
C_5PA	4.37	3.88
C_8PA	0.29	0.18
C_8PA	0.48	0.41
C_8PA	0.98	1.05
C_8PA	1.08	1.09
C_8PA	1.90	1.84
C_8PA	2.15	1.97
C_8PA	3.85	3.52
C_8PA	4.30	3.99
C_8PA	5.76	6.07
DEPA	0.55	0.44
DEPA	0.94	0.71
DEPA	1.64	1.13
DEPA	4.68	3.02
DEPA	5.27	3.86
DEPA	5.54	4.16
CAPA	0.49	0.53
CAPA	0.98	0.99
CAPA	1.95	2.03
CAPA	3.89	2.59
CAPA	4.84	2.75

The general tendency of the data can be approximated with the following linear law, which can be seen as the low coverage part of a Langmuir isotherm:

$$\rho = 0.82\ \rho_{\mathrm{nom}} \qquad \text{(eq.3.2)}$$

where ρ_{nom} is the nominal grafting density. Throughout the rest of the chapter, the real grafting density thus determined is given. The upper limit of its error bar is estimated to ± 0.5 P/nm^2 in order to account for dispersion introduced by sample preparation and ICP measurements.

To summarize, the combination of FTIR, ^{31}P-solid state NMR, TGA and ICP-OES results demonstrates the successful modification of the NPs by various phosphonic acids linked to the surface by P-O-M (M = Al, Si) bonds. There are no physisorbed phosphonic acid molecules, and the amount of aluminium phosphonate phases is negligible. Accordingly, the P content gives a reliable estimation of the effective grafting density.

III - Stability of the obtained colloidal solutions

The results of different experimental techniques of increasing spatial resolution (DLS, TEM, SAXS, and SANS) are given in next part. These experiments have been performed at different intervals of time after grafting, from a few hours after grafting for DLS and zetametry to a few days later for small-angle scattering, and it is therefore essential to characterize the evolution of the solution structure with time. This has been achieved with DLS measurements as a function of time over 6 days, for two NP concentrations, 1 wt% (as in zetametry) and 0.1 wt% (as with scattering), for various grafting densities of C_3PA and C_8PA. The results are shown in figure 3.7. Grafting of C_8PA (and to a minor extent, of C_3PA) leads to the aggregation of the modified NPs, and will be discussed in next part.

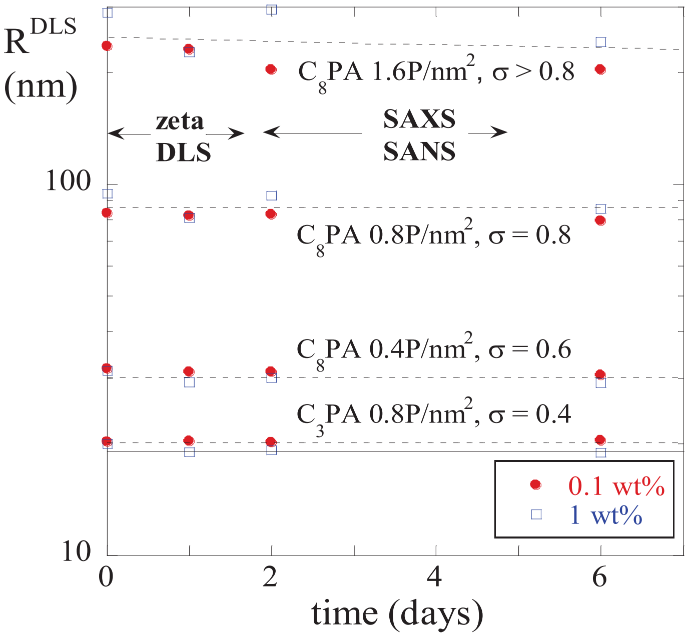

Figure 3.7: Stability of dilute suspensions of NPs (1 wt% and 0.1 wt%) observed by DLS. The apparent hydrodynamic radius deduced from a cumulant analysis is plotted as a function of time. The solid line stands for R^{DLS} of the bare NPs. The legend indicates the different grafts with their real grafting density ρ, and polydispersity σ. The arrows refer to the time windows of various characterization methods.

This stability study shows that there is a first stage of aggregation during grafting or immediately after, which leads to an increase of DLS radii compared to the bare NPs. The apparent polydispersity (σ) also increases to rather high values, indicating the polydisperse character of these aggregates. The key result is that between 1 h and 6 days there is no further significant evolution with time considering the dispersion of the data. This allows direct comparison of the results of experiments on different length scales, which have necessarily been conducted after different lapses of time.

We have also checked the influence of shaking the sample as usually done just before the experiments. It was found that this led to minor modifications of the order of 10% in R^{DLS} only for the highest grafting densities of C_8PA, which also showed some sedimentation by visual inspection. The more concentrated solutions – 5 wt% and 1 wt% as compared to 0.1 wt% – were found to be as stable in time as the dilute ones, with similar R^{DLS}.

To conclude, the state of aggregation of NPs in solution does not significantly evolve during the lapse of time of our state dispersion measurements, which allows comparing the results given by the different measurements techniques.

IV - State of dispersion in water

In aqueous suspension, grafting PAs on the surface of the NPs should modify the interactions between NPs in two ways. The first one is the decrease of the electrostatic repulsions due to the decrease of the surface charge of the NPs, resulting from the consumption of one or two surface OH groups, the possible presence of residual P-OH groups, and, in the case of CAPA, of the presence of COOH groups. This possibility is checked by zeta potential measurements below. Secondly, grafting will result in a modification of the surface hydrophilicity, see table 2.3 in chapter II for HLB-values. The PA hydrophilic character is decreasing in the following way: DEPA > CAPA > C_3PA > C_5PA > C_8PA. The goal of this study is to see how changing the balance between electrostatic repulsions and hydrophobic attraction may induce aggregation of NPs in solution.

1 - Impact of grafting on zeta potential

In order to check the effect of grafting on the surface charges, the electrostatic potential of grafted NPs was evaluated at the end of the grafting reaction using zetametry, and the results are presented in figure 3.8.

The zeta-potential is seen to decrease progressively with the grafting density. Up to moderate grafting densities ρ of ca. 1 P/nm^2, the relative impact on the surface charge is weak, within experimental error, but at high grafting density, the charge of the particles tends toward zero. Note that zeta potentials could not be measured over the whole range of grafting densities due to aggregation. The data can be divided into two families of curves: in the case of CAPA-grafted particles, the zeta-potential decreases more quickly than with the C_nPA-family or with DEPA. Qualitatively, the decrease of the zeta-potential can be explained by the condensation of P-OH groups with surface Al-OH groups, which are at the origin of the positive charge of the particles. In the case of CAPA, the faster decrease of the zeta-potential can be explained either by the partial dissociation of the free carboxylic acid end-groups (60% dissociation at pH 5 assuming a pKa of 4.85 as for hexanoic acid), or by complexation to the surface, consuming additional Al-OH groups (cf. figure 3.4).

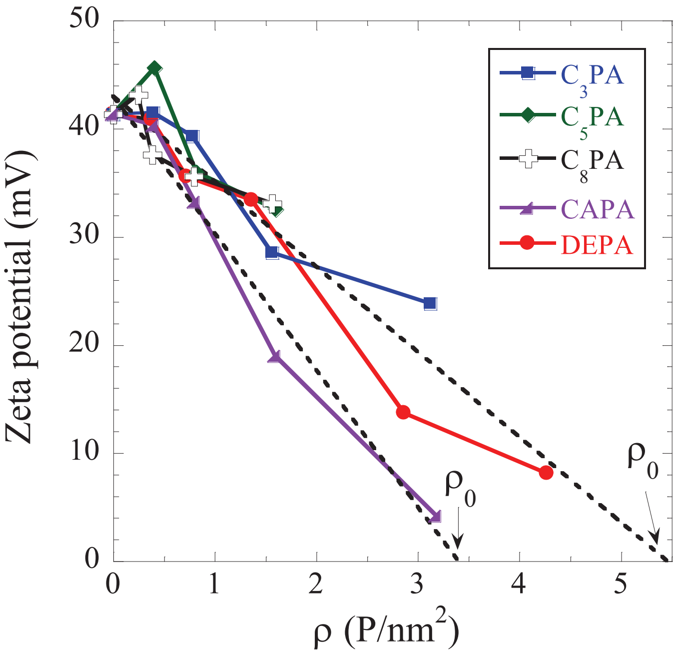

Figure 3.8: Zeta-potential of dilute suspensions (1 wt%) of modified NPs in water as a function of the grafting density ρ at pH 5. The grafted PA-molecules are indicated in the legend. Zeta potentials of CAPA, and of the C_nPA-family and DEPA, are compared to linear functions (dotted lines).

In figure 3.8, we have described the zeta potentials of the C_nPA-family and DEPA, and independently those of CAPA, with linear fits (dotted lines). As the number of charged surface sites participating in the grafting of one PA molecule can be expected to be constant whatever the grafting density, this linearity suggests that the zeta potential goes down linearly with the charge of the particle in this specific electrostatic regime, similarly to what one may expect, e.g., in the Debye Hückel approximation.[162] In particular, when the charge vanishes the zeta potential reaches zero. This is the case at a real grafting density extrapolated to $\rho_0 = 5.5 \pm 0.3$ P/nm^2 for the C_nPAs and DEPA, and 3.4 ± 0.3 P/nm^2 for CAPA. The ratio of these ρ_0 (or, equivalently, of the slopes) indicates that about 1.6 time more positive charges are annihilated per grafted CAPA than with the other PAs. Thus, for NPs modified by a dense alkylphosphonate monolayer (approx. 5 P/nm^2) the zeta-potential is practically zero, which suggests that all the Al-OH groups at the origin of the positive charge have been consumed by the grafting. In this case, the only possible mechanism for sol stabilization would be steric repulsion.

Unfortunately, a reliable estimation of the net charge annihilated by any phosphonic acid and/or carboxylic acid grafting is not available due to the inherent complexity of these reactions. If the alumina surface is globally positive suggesting the existence of Al-OH_2^+ groups, many other hydroxyl groups coexist and may participate in the grafting. However, if we make the hypothesis that the zeta-potential is proportional to the number of Al-OH groups, and that all of the carboxylic acid groups of the CAPA molecules react with the surface (as suggested by the FTIR spectra in figure 3.3), the ratio of the slopes gives an estimation of the average number (between 1 and 2) of P-OH/Al-OH condensations involved in the grafting of a $P(O)(OH)_2$ group to the surface, and of the density of Al-OH groups of the aluminium oxohydroxide layer at the surface of the raw NPs. Indeed, each carboxylic acid group condenses with one Al-OH group, and the grafting of CAPA (1 PO_3H_2 and 1 COOH group) consumes 5.5/3.4 ≅ 1.6 times more Al-OH groups than the grafting of C_nPA or DEPA (1

PO_3H_2 group). Thus, the average number of Al-OH groups consumed by the grafting of a PO_3H_2 group is given by $1/(5.5/3.4-1) \cong 1.7$. This is a reasonable value, suggesting that about 85% of the P-OH groups are condensed with Al-OH groups. From this value we can deduce the starting number of Al-OH groups, which should be equal to 1.7 multiplied by ρ_0, the extrapolated density of grafted PO_3H_2 groups ($\rho_0 = 5.5 \pm 0.3$ P/nm^2). This gives a density of $1.7 \times 5.5 \approx 9.3$ Al-OH/nm^2. Again this value is reasonable: for comparison, the Al-OH density at the surface of the (0 1 0) face (the most exposed face) of γ-AlOOH is also 9.3 Al-OH/nm^2.[155]

To summarize, electrostatic repulsions decrease with ρ, leading to increased probability of collisions in suspension, and thus aggregation of NPs may be induced. Due to aggregate formation, the zeta potential of the NPs with highest grafting densities could not be measured, but the grafting density corresponding to zero charge can be estimated by extrapolation. If the charge density alone were responsible for the NP interactions, then no significant aggregation would be expected for zeta potential higher than ≈ 20 mV, that is below ≈ 3 P/nm^2 for the C_nPA-family and DEPA, or below ≈ 2 P/nm^2 for CAPA. The structural characterization of aggregate formation reported in the next sections will show that the aggregation behavior is more subtle.

2 - Evolution of aggregate size followed by DLS

The structural evolution induced by the changes in interparticle interactions due to surface modification with PAs has been followed by DLS. The results for the different PAs are shown in figure 3.9. The apparent hydrodynamic aggregate radius R^{DLS} has been measured during the first day after grafting, and deduced from a cumulant analysis. Note that the largest aggregates ($R^{DLS} > 50$ nm) are highly polydisperse, with σ typically above 0.5.

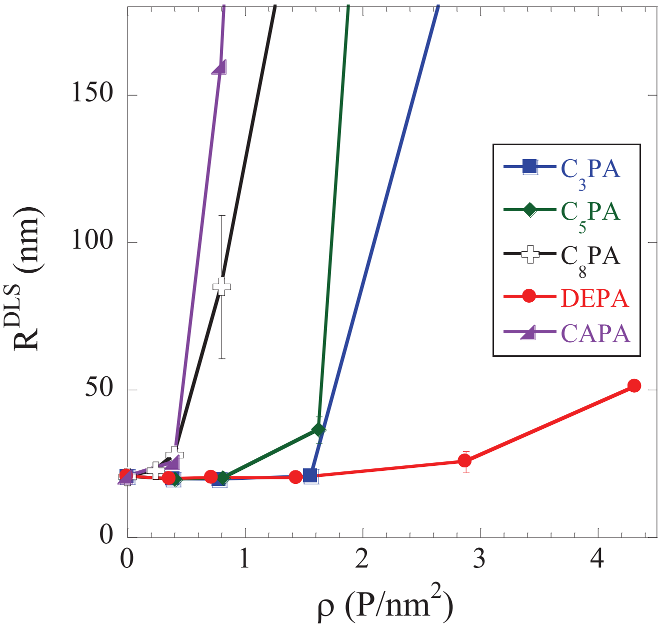

Figure 3.9: Apparent hydrodynamic radius R^{DLS} of NPs and NP-aggregates as a function of grafting density ρ, for different PAs as indicated in the legend.

According to figure 3.9, the apparent hydrodynamic aggregate radius increases first weakly with increasing grafting density, and then strongly above a critical value depending on the nature of the graft. DEPA grafting induces aggregation only at the largest ρ, and the critical grafting density decreases as follows: DEPA > C_3PA > C_5PA > C_8PA > CAPA. Confronting these results with the zetametry (figure 3.8), it may be noted that the onset of aggregation for the C_nPA family is shifted to smaller grafting densities as the hydrophobicity of the graft increases, while the NP charge remains invariant. The strongest difference in aggregation behavior is observed between DEPA and CAPA grafting. In the case of the CAPA-modified NPs, aggregation starts at a surprisingly low grafting density $\rho < 1$ P/nm^2, considering that the carboxylic acid end group is highly hydrophilic and that the decrease of zeta potential at $\rho < 1$ P/nm^2 remains moderate. The fast aggregation observed for CAPA suggests that, due to the low grafting densities and relatively short alkyl chain (C_5), the carboxylate groups effectively bind to the positively charged alumina surface as discussed above for the dried particles, so that the hydrophobic methylene groups are exposed at the surface of the NPs. On the contrary, the more hydrophilic DEPA does not lead to aggregation of the NPs even up to high grafting densities. To summarize, DLS now gives a first quantitative measurement of differences in aggregation behavior induced by the different hydrophobicities and functions of the PA molecules.

3 - Aggregation followed with TEM

In order to visualize aggregate formation, TEM of dried colloidal solutions has been used as a method of higher spatial resolution. If this technique provides qualitative evidence for aggregation, further aggregation of NPs during drying of the solutions on the TEM grids might occur. To minimize aggregation during drying, the solutions were highly diluted in ethanol down to less than 0.01 wt% of NPs, which allows drying under ambient conditions within one hour. The resulting TEM images for C_8PA-grafting are shown in figure 3.10. Note that unmodified NPs that are well dispersed in solution stay well dispersed (figure 3.10 a), while grafted NPs form aggregates progressively as seen in figures 3.10 b and c. Thus, even if the observed state (after drying) is more concentrated than the suspension, TEM images confirm the increase in aggregation with the C_8PA-grafting density.

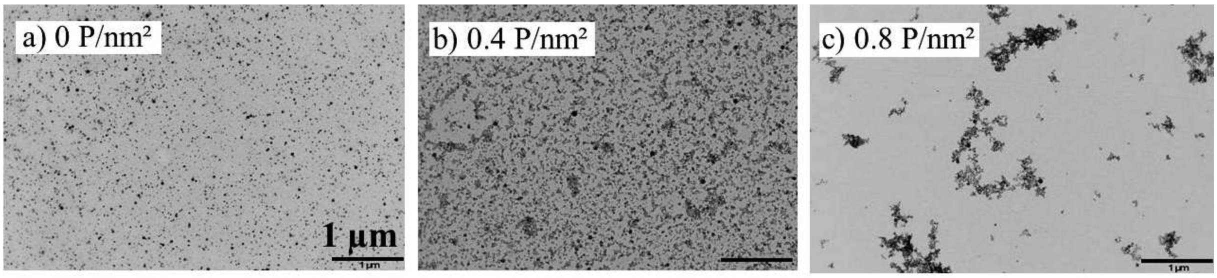

Figure 3.10: TEM images showing the increase of NP-aggregation with the grafting density of C_8PA. From left to right: **(a)** bare NPs, **(b)** 0.4, and **(c)** 0.8 P/nm^2.

4 - Changes in interactions evidenced by SAS

The problem of aggregation during drying for electron microscopy can be avoided with small-angle scattering studies directly in suspension, which gives a non destructive measurement of high spatial resolution.[163, 164] Experiments have been carried out typically a few days after synthesis. With scattering, the difficulty shifts to data interpretation, which is less straightforward than with TEM. Note that due to variations in capillary diameter and NP concentration induced by sedimentation, the scattered intensities have been normalized to the high-q intensity of the bare NPs representing the form factor P(q). In figure 3.11, the SAXS intensities for a series of grafted C_8PA-molecules with different grafting densities are compared, including the bare NPs ($\rho = 0$).

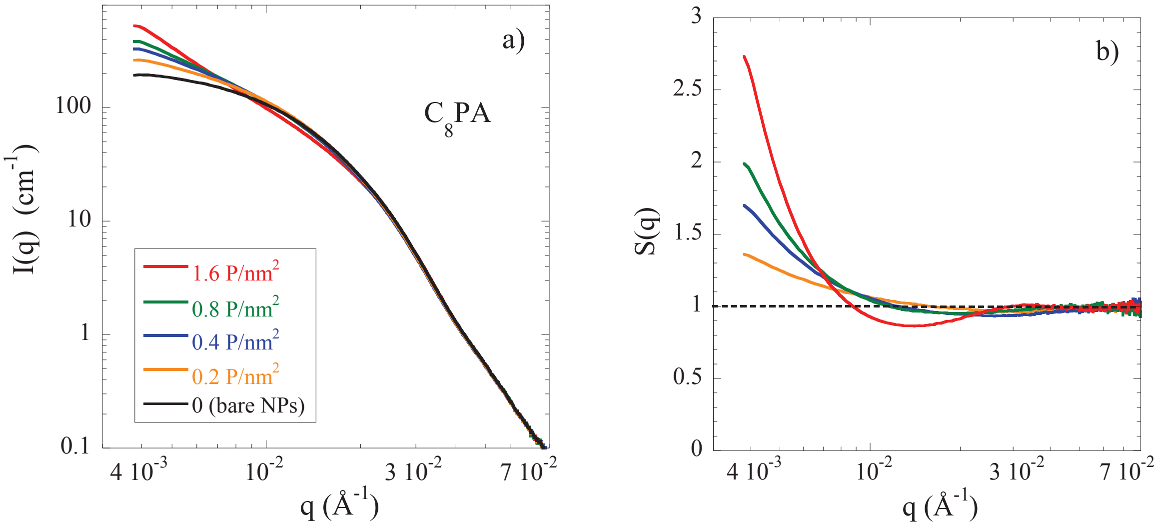

Figure 3.11: **a)** SAXS scattered intensity and **b)** structure factor for NPs grafted with C_8PA at 0.2 %vol in water. The grafting densities vary from 0 (bare) to 1.6 P/nm^2. The dotted line in b) represents the interaction-free case (S = 1).

The intensities superimpose over a large q-range, and significant deviations are found only at the lowest q values, below 10^{-2} Å^{-1}. The low-q upturns observed follows nicely the grafting densities, the highest ρ leading to the strongest upturn. At intermediate q, between 1 and 3x10^{-2} Å^{-1}, an inversion of the order of the curves is observed, the highest ρ now giving the weakest intensity. Finally, at the highest q, all intensities superimpose necessarily, which is due to the identical local structure, i.e. identical NPs in this case. The observed behavior over the entire q-range is the signature of an aggregation process of NPs. To see this, one can determine the apparent interparticle structure factor S(q), by dividing the experimental intensity I(q) by the average NP form factor P(q) – measured on bare NPs in figure 3.11 a –, as I(q) is given by (cf. chapter II):

$$I(q) = \Delta\rho^2 \, \phi \, V \, P(q) \, S(q) \qquad \text{(eq.3.3)}$$

where Δρ is the scattering contrast, ϕ the particle volume fraction, and V the individual NP volume. The resulting structure factors are shown in figure 3.11 b. They highlight the signature of aggregation described above, with a strong increase at low q, a moderate decrease at intermediate q – the correlation hole –, and structure factors tending to one within error bars for higher q-values. In the rest of this article, we will focus on the low-q increase as quantitative characteristics of aggregation. Note that in principle a low-q upturn may also be caused by weak reversible attractive interactions leading to large-scale density fluctuations of stable suspensions. For simplicity, only the term “aggregation” will be used.

For 3D-visualization of particle configurations compatible with our experimentally observed scattered intensities, a reverse Monte Carlo (RMC) algorithm was applied to I(q). The scattered intensities in figure 3.11 and the corresponding structure factor can be analyzed using a reverse Monte Carlo simulation as outlined in chapter II, paragraph II-4. The result is a fit of the apparent structure factor based on the experimental size distribution given chapter II, paragraph IV-1. Such a fit is shown in figure 3.12 for the C_8PA at 1.6 P/nm^2. For better visibility, a slice of thickness 100 nm is shown in the inset. It corresponds to a typical configuration of NPs which is compatible with the experimental structure factor. Clearly, some small aggregates, but also individual NPs, are visible in the picture. Note that contrarily to the dried TEM pictures, the NP configuration shown in the slice corresponds to the equilibrium configuration in suspension.

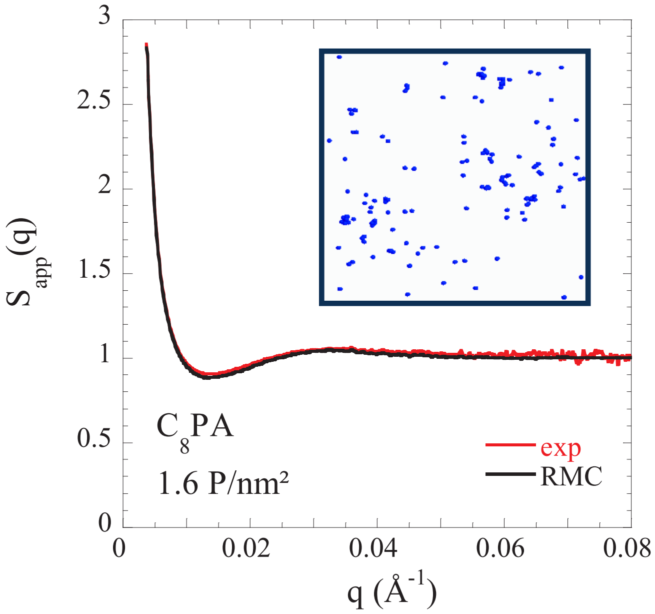

Figure 3.12: RMC fit of the apparent structure factor of C_8PA-grafted NPs at 1.6 P/nm^2. In the inset, a 100 nm-slice of the configuration of NPs in space corresponding to the fit is shown.

Having shown that attractive interactions induced by C_8PA-grafting in solution are visible also by SAS, the modifications of electrostatic and hydrophobic interactions brought by the grafting can be investigated on these length scales. The influence of grafted PAs with increasing hydrophilicity has been checked in figure 3.13, for a grafting density of ρ = 0.8 ± 0.5 P/nm^2.

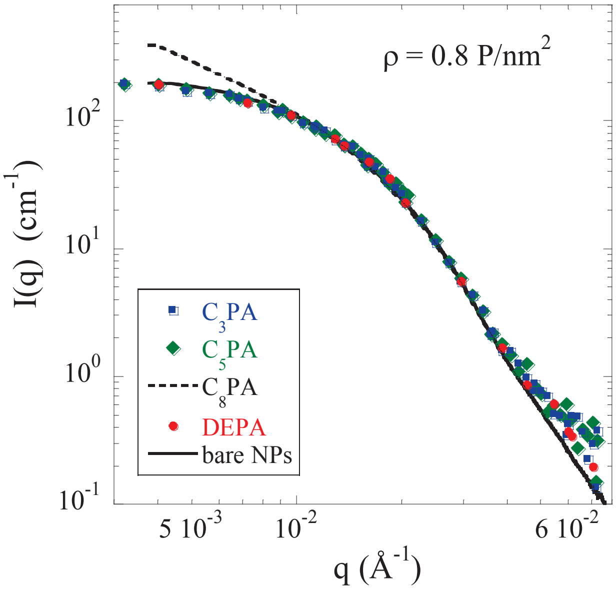

Figure 3.13: Effect of grafting increasingly hydrophilic phosphonic acids C_3PA, C_5PA, C_8PA, and DEPA on NP interactions for a grafting density ρ = 0.8 P/nm^{-2}, at 0.2 %vol in water. The scattered intensities from SANS (symbols) were rescaled to the same contrast as the SAXS form factor (lines).

The scattered intensities of NPs grafted with C_5PA, C_3PA, and DEPA are seen to superimpose nicely on figure 3.13. They all coincide with the average NP form factor, which immediately gives S(q) = 1 for these samples according to (eq.3.3), i.e., there are no interactions between these NPs. In particular, there is no attraction, and hard-sphere repulsion is negligible at this dilution. Grafting only ≈ 1 P/nm^2 of C_5PA, C_3PA, and DEPA thus has no impact on interactions, i.e., does not lead to aggregation, in agreement with the DLS observations reported in figure 3.9. On the contrary, the results for C_8PA and CAPA at the same ρ indicate that aggregation induced by these grafts, as observed in DLS at this grafting density, is thus reflected by a corresponding low-q increase in SAS.

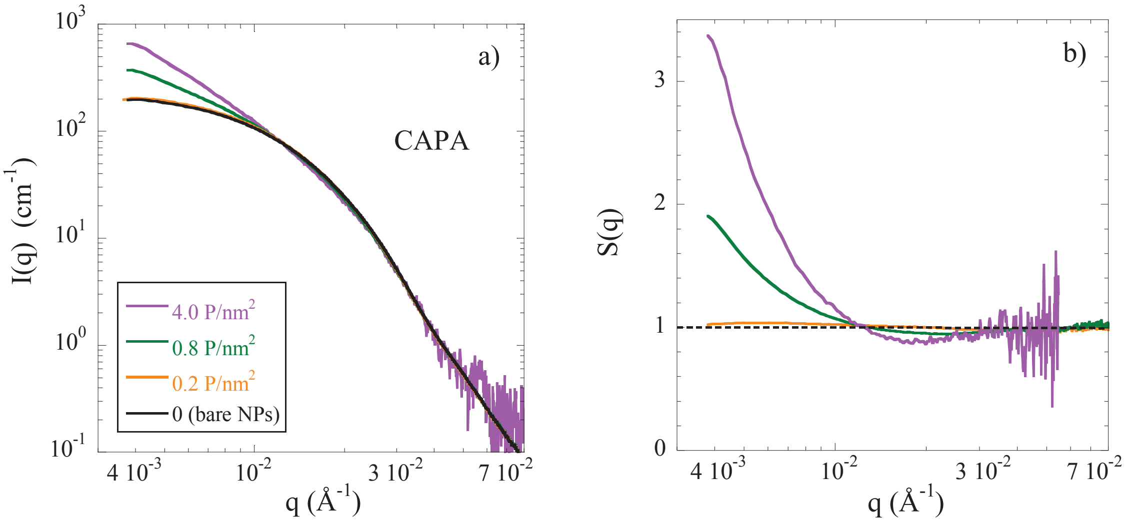

Figure 3.14: **a)** Scattered intensity from SAXS and **b)** structure factor for NPs grafted with CAPA at 0.2 %vol in water. The grafting densities are 0 (bare), 0.2 and 0.8 P/nm^2. For comparison, the strongly aggregated case of the much higher grafting density of 4 P/nm^2 is also shown, see text for details.

The data obtained for the particles modified with CAPA, carrying a carboxylic acid end-group, bring further insight for the interpretation of the results with respect to the influence of hydrophobicity and electrostatic charges. In DLS, CAPA-grafting was found to make the system more prone to aggregation. Reflecting structure on a more local scale, the scattered intensities are compared in figure 3.14 a, for increasing CAPA-grafting densities. The series of intensities follows the grafting density. At the lowest grafting density, ρ = 0.2 P/nm^2, the result is superimposed to the form factor scattering, indicating absence of interactions. For ρ = 0.8 P/nm^2, the low-q upturn below 0.01 Å^{-1} leads to S(q) approaching two in our q-window, and the local structure at high q stays identical. The highest grafting density of 4.0 P/nm^2, which according to figure 3.9 corresponds to strongly aggregated samples, is shown for comparison. The scattering stems from the (even more dilute) supernatant, which explains the important noise. Nonetheless, the strong upturn characteristic for the interactions between the remaining NPs is in line with the previous observations. Again, the structure factors shown in figure 3.14 b highlight the same generic behavior characteristic for aggregation, and provide a measurement on a more local scale of the aggregation phenomenon already observed with DLS.

The next step is to increase the grafting densities of the most hydrophilic PA, DEPA, to check if higher grafting densities and the corresponding decrease of electrostatic repulsion can also trigger aggregation. In figure 3.15, the impact of three amounts of DEPA (ρ = 0.7, 1.4, and 2.9 P/nm^2) on the scattered intensity is displayed.

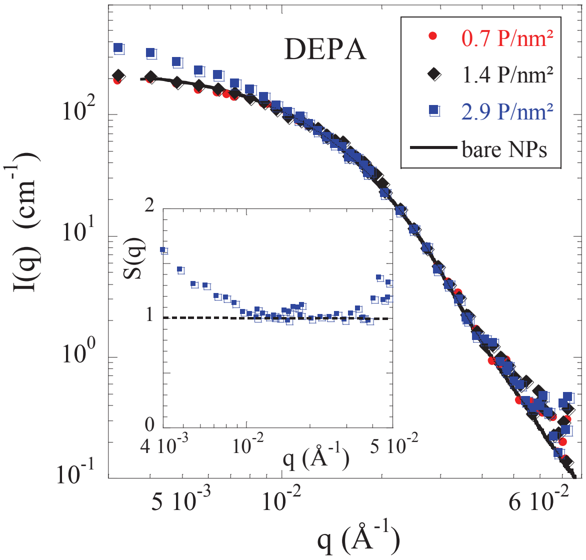

Figure 3.15: Scattered intensity from SAXS (line) and rescaled to same contrast from SANS (symbols) for the NPs grafted with DEPA at 0.2 %vol in water. The grafting densities vary from 0 (bare) to 2.9 P/nm^2. Inset: structure factor for NPs with 2.9 P/nm^2.

The data in figure 3.15 show that up to ρ = 1.4 P/nm^2, there are virtually no changes in the scattered intensity which superimposes again well to the form factor. At the highest grafting density, ρ = 2.9 P/nm^2, the low-q intensity increases (as one sees with S(q) in the inset), which is the signature of aggregation. In the framework of the balance between interactions discussed above, this is thus interpreted as the result of the decrease of the electrostatic charges on the NPs, as there is little hydrophobicity introduced by DEPA grafting. The apparent structure factor S(q) is shown in the inset of figure 3.15. Its low-q increase starts around q = 0.01 Å^{-1}, up to a value of about 1.5 in our experimental q-range. This moderate increase is in line with the weak increase observed by DLS in figure 3.9. In the framework of the balance between interactions discussed above, this is interpreted as the result of the decrease of the electrostatic charges on the NP, as DEPA grafting should not increase the hydrophobicity of the NPs. We will see later how these values compare among the different PAs employed.

We will now compare the influence of the different PA-grafts, as a function of the real grafting density, based on the experimentally determined structure factors. The aggregates being too big to enter the available q-range, there is no low-q plateau indicative of average aggregate mass and size (e.g., via a Guinier regime) in figures 3.11, 3.13, 3.14 and, 3.15. We therefore propose a measure of extent of aggregation via the strength of the upturn through the value of S(q*) taken at a common wave vector q*, and will use q* = 4x10^{-3} Å^{-1}. Note that due to the absence of a low-q plateau, it is not possible to link the experimental low-q value of S(q) to the average aggregation number N_{agg}. Comparisons between different structure factors remain nevertheless possible. In figure 3.16, the values of S(q*) are reported as a function of the grafting density for all PAs studied in this article.

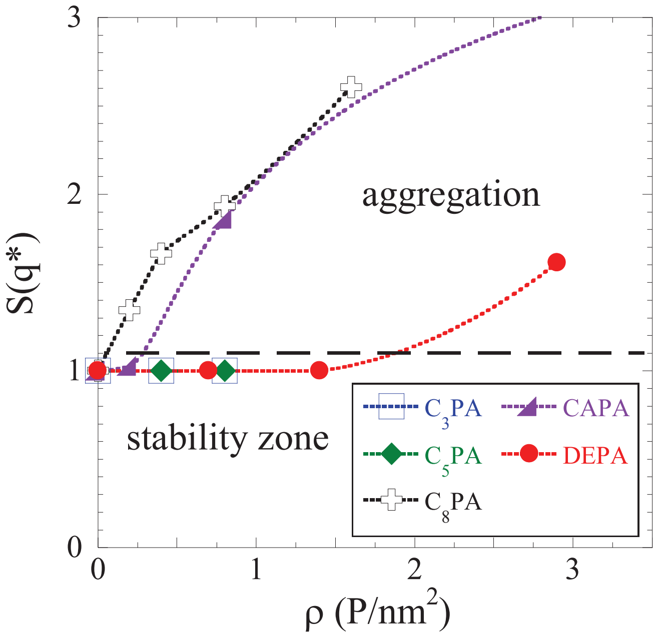

Figure 3.16: Summary plot of aggregation behavior of NPs grafted with various PAs as indicated in the legend. S(q* = 4x10^{-3} Å^{-1}) represents the strength of the low-q upturn measured by small-angle scattering, as a function of the grafting density. An arbitrary limit at S(q*) = 1.1 is drawn to separate the stable suspensions from those with aggregation. For CAPA, the line is continued towards the highest grafting density of 4 P/nm^2 as a guide to the eye.

In figure 3.16, the values of S(q*) are reported as a function of the grafting density for all PAs studied in this chapter. The data in figure 3.16 characterize the degree of attractive interaction between NPs. The figure is thus a convenient tool to summarize all findings on changes in NP-interactions. C$_3$PA and C$_5$PA have been measured only at the lowest ρ, and together with DEPA they stay in the stable zone, below the limit arbitrarily positioned at S(q) = 1.1. From DLS in figure 3.9, they were found to aggregate at intermediate ρ, the more hydrophobic C$_5$PA making the suspension unstable before C$_3$PA and finally DEPA, which is indeed seen to have its low-q structure factor cross the zone boundary around 2 P/nm^2. The most hydrophobic C$_8$PA has the most pronounced low-q increase. Indeed, aggregates of intermediate radius were found by DLS already at about 1 P/nm^2, which is reflected here by S(q*) around 2. More surprisingly, the increase of attractive interactions between NPs grafted with CAPA is less steep than with C$_8$PA, contrary to the DLS result. It is probable that this reflects the dispersion in the data, and could also be due to the formation during grafting of very large aggregates which are outside the small-angle q-window. Altogether, the message of figure 3.16 is clear: aggregation of the NPs in suspension can be controlled by grafting well-defined amounts of PAs, C$_8$PA and CAPA being most effective in inducing aggregation, and DEPA on the contrary preserving stability most.

V - Conclusion

We have proposed an original method to modify the surface of alumina-coated silica NPs by organic groups in aqueous sols. Using phosphonic acids instead of organosilanes, sols of NPs modified by a wide range of organic groups can be prepared, with grafting densities up to 4 groups/nm^2 (contrary to the organosilane modification of aqueous silica sols). The grafting reaction has been characterized in detail by FTIR, NMR, and elemental analysis. This grafting procedure performed in water is of considerable interest for two main reasons: first, it avoids the use of organic solvents, and secondly, for aqueous colloidal sols, it allows performing the grafting directly in the synthesis medium, thus avoiding transfer and drying steps prior to surface modification. In addition, this procedure does not involve the manipulation of dried NPs, thus decreasing the risk of inhalation.

The impact of grafting small PA molecules of various nature (charge, amphiphilicity) on NPs aggregation and stability in water has been studied by zetametry, DLS, TEM, SAXS and SANS, and visualized using a RMC simulation. The analysis of apparent hydrodynamic radii and the low-q structure factor provides a systematic classification of the impact of the different grafts on interactions, as a function of grafting density, ρ.

To conclude on NP interactions, one may note that electrostatic stabilization and hydrophobic destabilization both evolve with the density of grafting, but differently according to the nature of the graft. The electrostatic charge of the NPs remains positive for all grafts. It was found to decrease faster with the grafting density for CAPA than for all other grafts (C_nPA-family and DEPA). For all grafts but CAPA, the electrostatic repulsions remain significant (zeta potential > 20 mV) up to grafting densities $\rho \approx 3$ P/nm^2, and aggregation depends on the hydrophobicity of the organic group of the PA: the higher the hydrophobicity, the lower the onset of aggregation. For grafting densities up to ca 2 P/nm^2, the charges remaining on the grafted NPs stabilize the suspensions for short alkyl groups only (e.g., C_3PA) and in the case of the hydrophilic DEPA. Conversely, NPs grafted by C_8PA are aggregated even at very low grafting density and low charge reduction.

Quite unexpectedly, CAPA destabilized the suspensions strongly even at low grafting density and low charge reduction. This is ascribed to the grafting of the carboxylic acid group to the alumina-surface, leaving only the hydrophobic methylene groups exposed.

Both high ρ and high degrees of hydrophobicity of the groups on the PA induce aggregation, whereas suspensions of NPs grafted by DEPA remain stable up to the highest ρ. Unexpectedly, CAPA-modified NPs show aggregation even at low grafting density, suggesting that the carboxylic end group is also grafted to the surface. PA surface modification in water allows thus for the grafting of a higher density and a wider variety of organic groups than organosilanes.

This surface modification method offers the possibility to tune the interactions (electrostatic, steric, hydrophobic...) between NPs in aqueous sols by playing with the nature of the organic group on the PA and on the grafting density. Consequently, it opens the way to the elaboration of waterborne nanocomposites like, e.g., silica-latex nanocomposites, with a structural control obtained by playing on the nature and density of the organic groups. This should allow tuning of attractive interactions, and thus a control of aggregate formation, and thereby of rheological properties in water-borne polymer nanocomposites.

Chapter IV – Spatial arrangement and interfacial dynamics of the dried nanoparticles

In the bibliographic part (chapter I), we have seen that grafting organic molecules on nanoparticles allows modifying the interactions between NPs in solution and between NPs and polymer chains in the nanocomposites.[111] In the case of silica NPs, this is usually done in organic medium using organosilane molecules.[36] As reported in chapter III, we are able to graft small molecules of phosphonic acids on the surface of alumina-coated silica NPs (L200S) in aqueous medium and to vary the state of dispersion of these NPs in aqueous sols by playing on the surface modification parameters, e.g. the grafting density and the nature of the grafts.

In this chapter, raw L200S NPs and phosphonic acid-surface modified NPs, with the protocol described in chapter III, are studied. The obtained colloidal dispersions are washed, dried, and the resulting powders are stored under different relative humidities. The objective is first to study the dynamics of the raw L200S NPs, then to follow the impact of the surface modification (nature of the PA and grafting density) on the dynamics of the NPs, by means of SAXS and Broadband Dielectric Spectroscopy (BDS). In a first step, the structure of powders of the raw L200S NPs will be characterized, and then their dynamical response will be studied. In particular, we will follow the impact of the surface modification (nature of the PA and grafting density) on the structure and dynamics of these NPs. BDS experiments performed on precipitated silica NPs in the dried state have evidenced several processes related to the dynamics of hydration water and hydrated silanol groups.[165] To our best knowledge, such an investigation on Al/SiO_2 NPs with Al-OH groups on the surface is a novelty in the field. In addition, we expect to detect a dielectric signal for the local relaxation of the grafted molecules. Note that the dipolar moment of hexylphosphonic acid, $C_6H_{13}PO(OH)_2$, grafted on metal oxide is 1.77 D [166] (see appendix 5 for illustration), i.e. comparable to the one of water.

For the nanocomposite application, organization and dynamical properties of the grafted layer are important physical features to consider in order to optimize the NPs surface and its interactions with the polymer. The final purpose of this will be the final aggregation state in the nanocomposites linked to reinforcement effects.

The outline of this chapter is the following. First, the spatial arrangement of the dried NPs powders is characterized by SAXS as a function of the grafting density of C_8PA. Then, a brief state-of-the-art on the interfacial dynamics of (unmodified) silica nanoparticles is given. Finally the interfacial dynamics of raw and surface-modified nanoparticles is studied by BDS, with a particular focus on the effects of both the hydration level and the nature of the grafted phosphonic acid on the dynamics.

I - Sample description

The dried NPs were obtained as follows. The modified colloidal suspensions (see details in chapter III) were dried at 85°C during 6 days. The resulting powders were washed 3 times with ultra-pure water (see chapter II for washing conditions), dried again 24 hours at 90°C under atmospheric pressure, milled, and dried 48 hours at 120°C under vacuum.

In order to study the dynamics of water molecules, the hydration level of the powders were varied by keeping them in hermetic boxes of fixed relative humidity (RH). By using saturated salt solutions of LiCl, $MgCl_2$, K_2CO_3, and NaCl, the RH was set to 11%, 33%, 43%, and 75%, respectively.[154] The hydrated powders were incorporated at low temperature (T = 100 K) in the BDS apparatus to avoid dehydration, and the measurements were done at maximum T = 250 K to avoid changes in the water content of the samples.

To determine the dynamical response in the dried state (without adsorbed water), "dried" powder samples have been studied as a reference case. These samples were conserved in a nitrogen oven under vacuum, and transferred between two metallic electrodes in a glove-box just before starting the BDS experiment. Subsequently, they were incorporated and kept 4 hours at 120°C under nitrogen flow within the BDS apparatus. For the SAXS measurements, the powders were measured in sealed capillaries for low-q values and on kapton supports for high-q values.

Table 4.1: Summary of the samples, with corresponding water contents and presence or not of crystallized water.

Sample	RH of the storage box	Water content by TGA (wt%)	Crystallization ? (DSC)
Raw L200S	11%	4.0	No
	33%	4.7	No
	43%	5.6	No
	75%	7.6	Yes
C_8PA-L200S 4 P/nm²	11%	3.3	No
	33%	4.3	No
	43%	4.8	No
	75%	6.8	Yes
C_8PA-L200S 2 P/nm²	33%	4.3	No
C_8PA-L200S 1 P/nm²	33%	4.9	No
C_5PA-L200S 4 P/nm²	33%	4.7	No
C_3PA-L200S 4 P/nm²	33%	4.8	No
DEPA-L200S 4 P/nm²	11%	3.5	No
	33%	4.6	No
	43%	5.5	No
	75%	8.7	No

The water content in the powders was obtained from TGA measurements using the following sequence: from 20 to 120°C with a heating rate of 5°C/min, followed by an 120°C isotherm of 2 hours under nitrogen flow, which allowed reaching a plateau in the evolution of the mass (no further loss of water, as shown in appendix 5). The water contents stand in the range from 3.3 to 8.7 wt%, with in all cases an increase of the hydration level with the RH value, as can be seen in table 4.1. Surprisingly, the water content of the powders does not seem to be impacted by the chemical nature of the graft and the grafting density. We assume that long equilibration time (about 10 days) leads to a saturated amount of adsorbed water molecules.

As described in the bibliographic part, crystallized water has a different behavior than “free” water molecules adsorbed at the surface. DSC measurements allow evidencing the presence of such a crystallized phase. They were done using a 20°C/min cooling and heating rate in the range from -120 to +25°C. Note that only two samples in table 4.1 display a crystallization peak at T = -45°C = 228 K upon cooling, and a large and badly-defined melting peak around -20°C upon heating. Examples of non-crystallized and crystallized samples DSC results are given in appendix 5.

II - Spatial arrangement of nanoparticles in powders by SAXS

In this chapter, the aim is to characterize the surface and interfacial properties of the NPs. The SAXS study will allow getting information about the spatial arrangement of the NPs in the powders. The powder can be seen as a two-component system made of empty spaces and dense NPs zones, the local volume fraction of which can be estimated from the scattering data. We will focus on C_8PA-grafted NPs at different grafting densities. As the spatial arrangement is directly linked to the surface properties, e.g. to the interfacial interactions between NPs, it should evolve with the grafting density of C_8PA.

Figure 4.1 presents the scattered intensities of the raw and C_8PA-grafted NPs, at fixed humidity level (RH = 11%). Note that within experimental errors, the water content in the powders was found to have no impact on the scattering curves. Due to some difficulties in evaluating the exact quantities of powder in the beam, intensities in figure 4.1 are given in arbitrary units. The curves are shifted vertically to overlap at large-angles (starting from ca. q = 3 10^{-2} $Å^{-1}$).

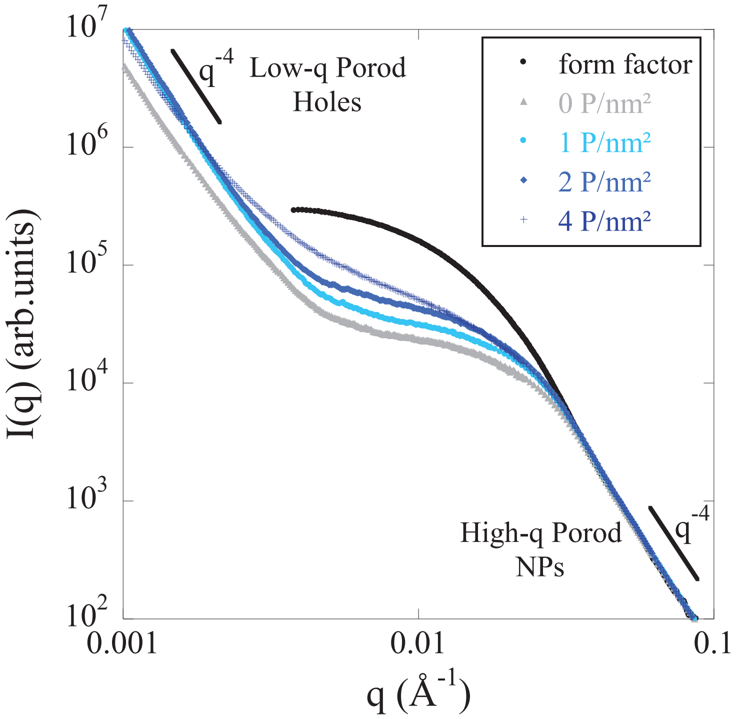

Figure 4.1: Scattered intensities for C_8PA-modified NPs powders with different grafting densities. The form factor of the raw NPs in solution is represented in black.

The intensities at large angles are identical and superimposed with the NPs form factor, because they are the signature of the raw NPs. At very high q, we get a scaling of q^{-4}, which is characteristic of the

Porod scattering associated with the NPs surface. The differences observed in the intermediate q-range are representative of different organizations of the NPs in the powder. The lower the grafting density of C_8PA, the lower the intermediate-q intensity. Finally, at low angles, the spectra display a strong upturn, which follow a q^{-B} power law. The prefactors and exponent of the corresponding (low q) power laws are given in table 4.2. One can see that the exponents are close to 4, i.e. there is a second Porod regime. This suggests the existence of holes in the powder.

Table 4.2: Low-q power law values for the C_8PA-modified powders with different grafting densities (RH = 11%).

	Power law: $A\ q^{-B}$	
C_8PA	A	B
0 P/nm²	$1.95\ 10^{-5}$	3.81
1 P/nm²	$2.09\ 10^{-5}$	3.90
2 P/nm²	$2.85\ 10^{-5}$	3.87
4 P/nm²	$9.34\ 10^{-5}$	3.65

A powder can be considered as a biphasic material with empty spaces and nanoparticles. With this idea in mind, we propose a schematic representation of our samples in figure 4.2, with two distinct phases. One phase is made by the "holes", i.e. only air, and represents a volume fraction Φ_{holes}^{phase} of the total sample. The second phase is the matrix, i.e. dense NPs zones, with a volume fraction $\Phi_{dense\ NPs}^{phase}$ ($\Phi_{holes}^{phase} + \Phi_{dense\ NPs}^{phase} = 1$). The later phase also contains a fraction of air between NPs, Φ_{air}. The volume fraction of NPs in the dense zones is noted Φ_{NPs} ($\Phi_{NPs} + \Phi_{air} = 1$).

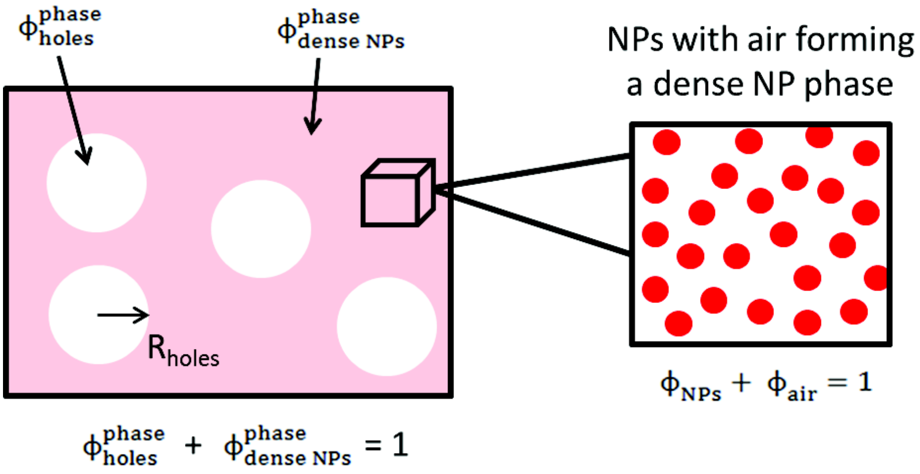

Figure 4.2: Schematic representation of the powder.

NPs in the dense zones contribute to the scattering at high angles with their surface scattering (high-q Porod). On the other hand, in the picture proposed in figure 4.2, the empty spaces ("holes") display a well-defined interface with the NPs matrix, which also lead to surface scattering but in the low-q range (low-q Porod). Such a picture is supported by the power law exponents reported in table 4.2 (B $\approx$ 4).

In this case, the prefactor A_{LQ} of the low-q Porod regime can be expressed as:

$$A_{LQ} = \frac{2\pi S(\Delta\rho)^2}{V} = \frac{2\pi\left(3\,\Phi_{holes}^{phase}\right)(\rho_{NPs}\,\Phi_{NPs})^2}{R_{holes}} \qquad \text{(eq.4.1)}$$

where S and R_{holes} are the surface area and average radius of the holes, respectively. V is the sample volume. ρ_{NPs} is the scattering length density of the NPs, and $\Delta\rho$ the scattering contrast between the holes and the dense NPs phase.

On the other hand, the prefactor A_{HQ} of the high-q Porod regime can be expressed as

$$A_{HQ} = \frac{2\pi\,(3\,\Phi_{L200S})(\rho_{NPs})^2}{R_{NPs}} \qquad \text{(eq.4.2)}$$

where Φ_{L200S} is the total fraction of NPs in the sample ($\Phi_{L200S} = \Phi_{NPs} * \Phi_{dense\ NPs}^{phase}$). The NPs radius is R_{NPs} = 7.4 nm (chapter II). As mentioned above, we do not have in hands the absolute values of the intensities (the sample mass is unknown). However, the ratio of the prefactors of both Porod laws (eq.4.1) and (eq.4.2) allows deducing the hole's size defined by R_{holes}:

$$R_{holes} = \frac{A_{HQ}}{A_{LQ}}\, R_{NPs}\, \Phi_{NPs}\, \frac{\Phi_{holes}^{phase}}{1-\Phi_{holes}^{phase}} \qquad \text{(eq.4.3)}$$

It assumes that we know the NPs volume fraction in the dense phase Φ_{NPs}, and the total amount of air in the sample:

$$\Phi_{tot\ air} = (1 - \Phi_{NPs}) * \Phi_{dense\ NPs}^{phase} + \Phi_{holes}^{phase} \qquad \text{(eq.4.4)}$$

It is possible to extract Φ_{NPs} from the scattering data in the intermediate q-range. As introduced in chapter II, the scattered intensity for monodisperse spheres is given by:

$$I(q) = I_0\, P(q)\, S(q) \qquad \text{(eq.4.5)}$$

with I_0 a prefactor, P(q) the form factor of the L200S NPs, and S(q) the structure factor, which reflects the spatial correlation between NPs in the dense zones of the powder. In the polydisperse case, one has to consider an apparent structure factor, $S_{app}(q)$, in (eq.4.5), see reference [145] for details. To obtain $S_{app}(q)$, the contribution of the low-q power law is subtracted and the intensity is divided by the form factor. An example of such decomposition is shown in figure 4.3.

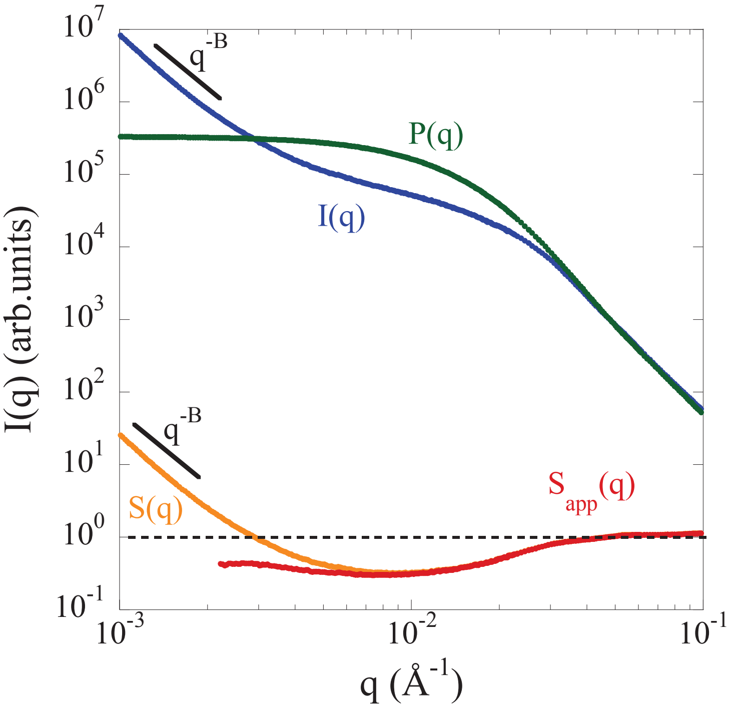

Figure 4.3: Decomposition of the scattered intensity for the C_8PA-modified NPs powder (4 P/nm²) according to (eq.4.5).

The structure factor resulting from the decomposition shown in figure 4.3, is plotted in figure 4.4a for the different grafting densities. The low-q limit of these curves allows determining Φ_{NPs} using a Percus-Yevick structure factor to describe the interactions between NPs:[167]

$$S(q \to 0) = \frac{(1-\alpha\Phi_{NPs})^4}{(1+2\alpha\Phi_{NPs})^2} \qquad \text{(eq.4.6)}$$

where α is a prefactor for the NPs volume fraction, which takes into account the NPs polydispersity.[145] In the standard formula of Percus-Yevick, α = 1 for monodisperse objects. In our case, the polydispersity in size of the L200S NPs is σ = 38% (cf. chapter II), which leads to α = 0.54 according to reference [145]. For the determination of the limiting value of $S_{app}(q \to 0)$, we focus on the region around q* = 0.005 Å^{-1}. The values obtained for Φ_{NPs} according to (eq.4.6) are reported in figure 4.4b.

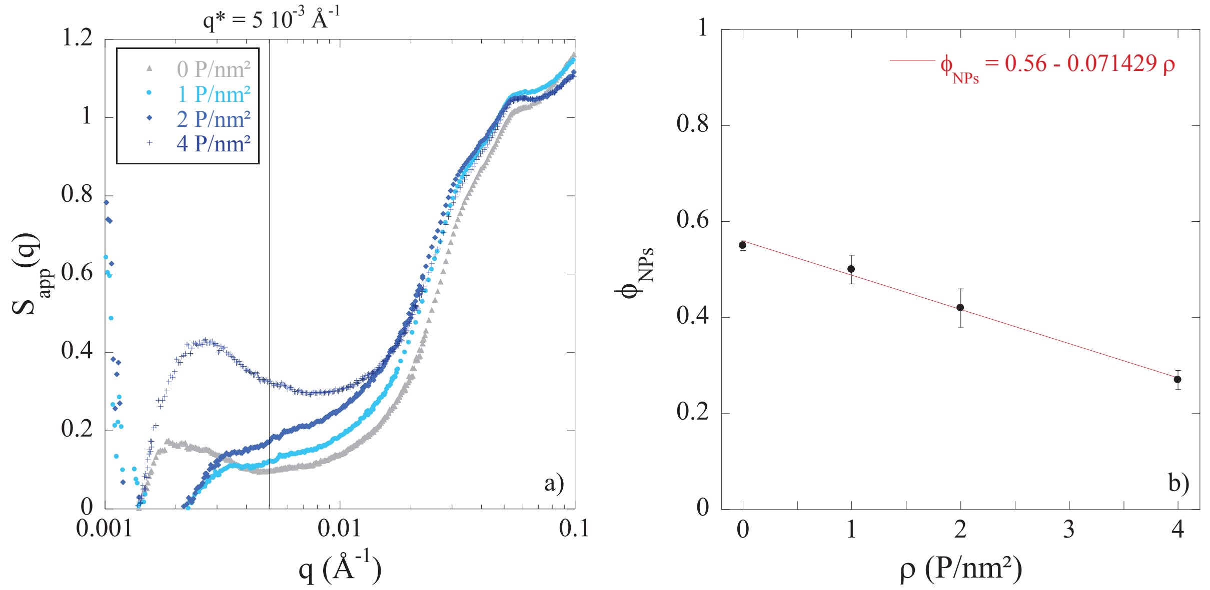

Figure 4.4: **a)** Evolution of the apparent structure factor (see text for details). The value at q* = 5 10^{-3} $Å^{-1}$ is used for the estimation of Φ_{NPs}. **b)** Evolution of Φ_{NPs} with the grafting density of C_8PA.

As shown in figure 4.4b, the volume fraction of NPs in the dense zones decreases with the grafting density of C_8PA. In other words, the surface modification of the NPs leads to dense zones of lower compacity. This tendency can be attributed to the steric hindrances between grafts.

We are now left with only one parameter missing for the determination of R_{holes} (eq.4.3) and (eq.4.4), i.e. the total fraction of air in the powder. Such a quantity is extremely difficult to evaluate. Indeed, one can think of weighting the amount of powder needed to fill a given volume. However, such a measurement strongly depends on the way of compressing the powder within the volume. As a consequence, $\Phi_{tot\ air}$ has been fixed arbitrarily to 0.75, a value which agrees in order of magnitude with estimations based on the amount of air estimated from the BDS normalization discussed in the next section.

The resulting values of R_{holes} are reported in table 4.3.

Table 4.3: Characteristics of the powder represented as a two-phase system with holes (air) and dense NPs zones containing a local NPs fraction, Φ_{NPs}. The total amount of air is fixed to 0.75.

C_8PA	Φ_{NPs}	Φ_{holes}^{phase}	R_{holes} (nm)
0 P/nm²	0.55	0.55	4886
1 P/nm²	0.50	0.50	1839
2 P/nm²	0.41	0.39	904
4 P/nm²	0.26	0.04	47

One can see that, in parallel to a decrease of the local NPs concentration in the dense zones, the average size of the holes decreases when the grafting density is increased. Such an effect results both from the increase of the low-q Porod contribution (figure 4.1), and the lower density (implying more air) in the particle phase. The raw NPs powder contains some very large holes (µm), whereas the surface-modified NPs contains a large number of very small holes (nm) leading to a more homogeneous system. To finish, one may note that this evolution towards smaller holes is accompanied by a decrease of their total fraction as reported in table 4.3. The overall situation, however, is that even if the total fraction of holes diminishes by a factor of ten, the volume of each hole decreases simultaneously by a factor of 100^3. The total number of holes thus increases by about 100 000, and all these small holes are distributed across the powders, presumably more homogeneously in presence of grafting than the few big ones for bare NPs.

III - State-of-the-art on interfacial dynamics of silica nanoparticles

To understand the interfacial dynamics of our surface-modified nanoparticles, we used dielectric spectroscopy as a probe to follow the dynamics of both, the adsorbed water molecules and the groups present at the surface of the nanoparticles.

In the case of hydrated silica NPs, two main dipoles are involved: water and silanol (Si-OH) present at the silica surface. The dipolar moment of water is μ(eau) = 1.85 D, and the one of silanols in SiH_3OH is μ(Si-OH/SiH_3OH) = 1.29 D.[168] In our system, the raw NPs are alumina-coated silica NPs. The dipolar moment of AlOH is 0.98 D, i.e. lower than for SiOH, but still with a fair degree of charge transfer. According to the elemental analysis results (chapter II), the surface density of AlOH groups is 7.9 Al/nm², indicating that the NPs surface is most probably fully covered by AlOH groups. However, one cannot exclude the presence of residual SiOH groups.

Concerning the water molecules, they are present in many materials, and may have a strong impact on the physical properties. Consequently, it is relevant to study their localization and dynamics. The first step is to identify where the water molecules can be located. There are two different possibilities:

- the water molecules can be trapped in the material.
- the water molecules can be adsorbed at the surface of the material.

Both possibilities are developed in the next sections.

1 - Confined water

When the water molecules are trapped in the material, it is called “confined water”. These water molecules display a different behavior than bulk water molecules. For instance, water molecules in our body can be considered as confined, because these molecules are very close from other biomolecules such as proteins or lipids.[169] Other examples of molecules, which can trapped water are polymers[170] or reverse micelles[171]. Water molecules can also be trapped in pores. As many materials are porous, several examples of dynamics of confined water were studied in the literature: for instance, clays, cements like materials, or hydrogels.[172-174]

In the case of confined water, it has been shown that the dynamics of confined water molecules in porous materials depends on the size and organization of the pores, on the confinement geometry, and on the water-pores interactions.[175] It is agreed that the relaxation time of such trapped water molecules presents a crossover from Arrhenius to non-Arrhenius behavior with the increase of temperature (see chapter II for definition of such behaviors).[176, 177]

In our system, according to nitrogen adsorption-desorption measurements at 77 K (see chapter II), the L200S nanoparticles are not porous. As a consequence, confined water should not be observed. We expect only the presence of adsorbed water molecules.

2 - Adsorbed water

The second localization of water is at the surface or interface of the material. In the case of oxide NPs, the water molecules can be in strong interaction with the NP surface, for instance by hydrogen-bonding with the silanol groups as it is illustrated in figure 4.5 in the case of silica NPs.

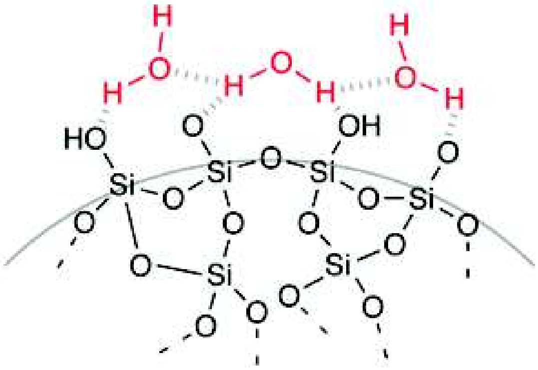

Figure 4.5: Adsorbed water molecules at the surface of silica nanoparticles by hydrogen-bonding.[178]

Water molecules can be adsorbed in different layers on the NP surface. If it is adsorbed directly on the surface to hydrate surface groups, for instance the silanol groups, it forms a shell called the “inner layer”. Other adsorbed water layers can also be formed, the “outer layers”. Note that the surface of oxide nanoparticles presents heterogeneities. For instance, in the case of silica, the siloxane groups at the surface are forming hydrophobic patches, on which the water will not adsorb.[179] For this reason, the inner layer is not uniform, whatever the surface state of the NPs.

On the other hand, water molecules may group to form clusters. The presence of these clusters can be detected using DSC measurements with the appearance of a melting peak during heating. Samples where crystallization has been observed are identified in table 4.1.

The dynamics of adsorbed water was recently investigated by Cerveny et al. in reference [165] in raw silica nanoparticles powders (precipitated silica, Zeosil from Rhodia) with different hydration levels. The aim of the following paragraphs is to resume, to our best comprehension, the different relaxation processes described in this reference and their attributions.

Three relaxation processes have been observed by BDS in the range of temperature from 110 to 200 K and frequency (f = 10^{-1} - 10^{6} Hz): they are labeled 1, 2, and 3 from the fastest one (process 1) to the slowest one (process 3). The measurements were performed on different samples, with different hydration levels and surface states. The temperature dependence of the three processes was found to follow an Arrhenius behavior. Note that other papers report on the dynamics of water molecules adsorbed on different oxide surfaces, e.g. TiO_2 or CeO_2, studied by Quasi-Elastic Neutron Scattering (QENS) experiments.[180-183] These studies highlight the existence of a crossover between high-temperature non-Arrhenius behavior and low-temperature Arrhenius behavior of the adsorbed water dynamics. The attribution of this crossover was largely debated, but Cerveny et al. did not observe such a crossover in the case of silica NPs.

At low temperature - high frequency, process 1 is difficult to observe due to its low intensity. It is assumed to be linked to the relaxation of silanols on the surface of silica NPs. The activation energy is $E_a = 0.11$ eV and $\log(\tau_0) = -10.70$.

Process 2 is attributed to the relaxation of water molecules in the outer layers. For this process, the dielectric strength, which depends on the number of dipoles involved, was found to increase with the amount of hydration water. E_a and $\log(\tau_0)$ depend also on the amount of water.

Process 3 is due to the reorientation of hydrated silanol groups and to water molecules in interaction with the silanol groups. It only varies little with the amount of water, as in this case the number of dipoles involved is fixed by the amount of silanol groups, which can be hydrated or in interaction with water. The activation energy of this process has an average value of approximately 0.60 eV.

Figure 4.5 summarizes the different localization of water molecules in a silica powder and the associated dielectric processes with increasing amounts of water from sample (a) to sample (d).

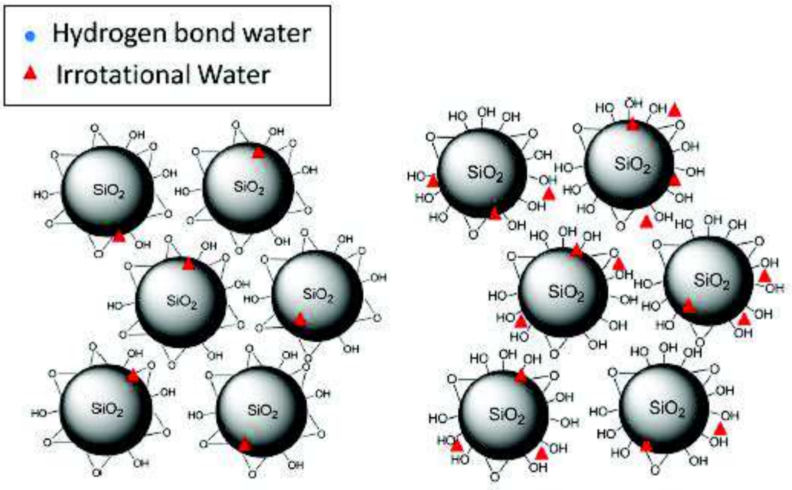

(a) No dielectric response

(b) Process 3 (▲)

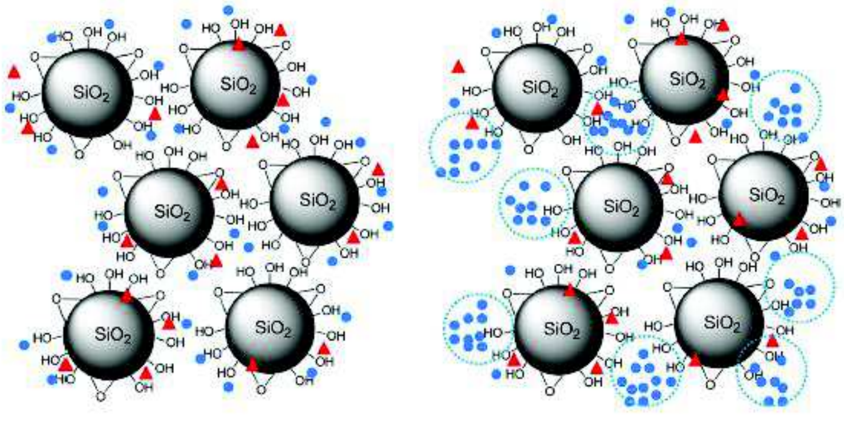

(c) Processes 2 (●) and 3 (▲)

(d) Processes 2 (●) and 3 (▲)

Figure 4.6: Localization of adsorbed water at the surface of silica nanoparticles and the corresponding dielectric processes. Figure from reference [165].

In figure 4.6, the first sample (a) consists in calcinated silica NPs. Few silanol groups are present on the surface. The hydration water is supposed to be completely removed, and no dielectric response is observed. The second sample (b) contains water molecules that are hydrating some silanol groups. One dielectric relaxation is observed: the process 3 attributed to hydrated silanols and water molecules in interaction with silanols. Sample (c) is more hydrated: in addition to the water molecules, which are hydrating the silanol groups in the inner shell, some additional water molecules are forming an outer hydration layer. These last ones are involved in process 2. At last, in sample (d), additional water is not contributing to form a more homogeneous inner layer, because of the heterogeneity of the silica surface. Despite of being adsorbed close to the siloxane groups, it will fill the outer shell and form clusters.

IV - Interfacial dynamics of nanoparticles with different hydration level by BDS

Different questions will be tackled in this section. First, the dynamics of raw L200S NPs will be studied by BDS, in the dry state and with different hydration levels. As our samples are not porous, no process linked to confined water should be detected. The three dielectric processes observed in silica NPs[165] and discussed in the previous section are expected to be observed. The effect of hydration on these relaxation processes will be explored. In addition, as the NPs are alumina-coated, relaxation dynamics of the AlOH surface groups can be detected.

The second part of our study is focused on PA-grafted L200S NPs. BDS experiments on the modified powders should provide information regarding the physical (grafting densities via dielectric strengths) and chemical properties (hydrophobicity via different grafts) of the NPs surface. We focus on two types of grafted molecules: DEPA and C_8PA. These molecules have approximately the same length, but not the same dipolar moments. The dipolar moment of C_8PA is relatively low in comparison with DEPA as it bears an alkyl chain, whereas the DEPA-chain is PEO-like. In addition to water dynamics, we thus expect to detect the local relaxation of the grafted molecules, e.g. reorientational dynamics or local relaxation of the alkyl groups with rotation of the central bond in four-atom sequences.

1 - Raw L200S

We begin with the dielectric response of the raw L200S nanoparticles. The expected processes are those related to the surface hydroxyl groups (labeled process 1 in the state-of-the-art paragraph), and water adsorbed on the surface (named processes 2 and 3).

In order to detect process 1, a measurement is performed at the lowest accessible temperature, T = 77 K. Three consecutive measurements were done on raw NPs in the dry state, in order to check reproducibility. Results are shown in figure 4.7, representing $\tan \delta = \varepsilon''(\omega)/ \varepsilon'(\omega)$ as a function of the frequency.

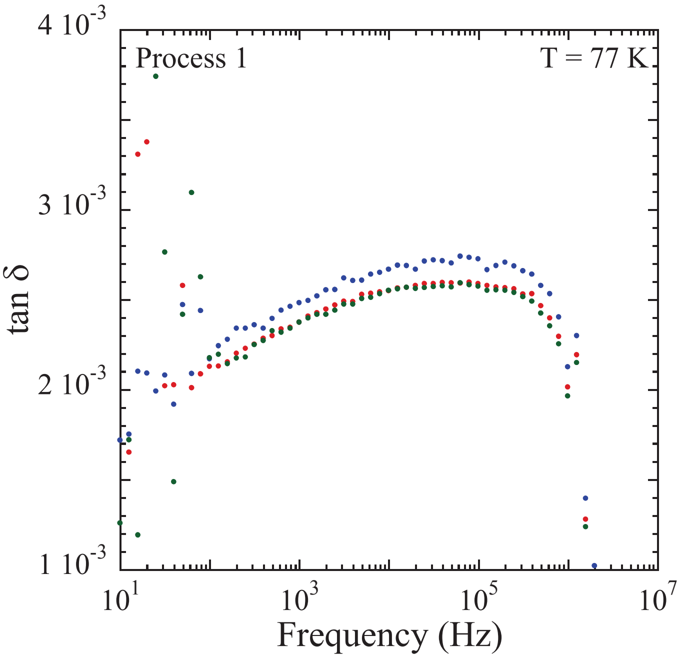

Figure 4.7: Three consecutive dielectric measurements of tan δ at T = 77 K for raw L200S NPs in the dry state.

The dielectric spectra in figure 4.7 reveal a relaxation process, the maximum of which is located at about 10^5 Hz. According to our drying protocol (inside the BDS chamber), the only dipoles contributing to the signal are expected to be the surface hydroxyl groups, without any residual water molecules. Consequently, we attribute this relaxation process, to the reorientation of the surface AlOH groups. This process appears slightly shifted towards higher frequency as compared to the process 1 observed in precipitated silica NPs.[165] It suggests that the reorientation of the AlOH groups is faster than the one of the SiOH groups. Additional measurements on the dried NPs were performed at 10^3 Hz increasing the temperature up to 250 K (see figure 4.8a), but no other relaxation process could be detected. The absence of process 3 in this sample confirms the absence of any residual water molecules.

We now switch to the measurements of hydrated L200S powders. Apart from the isotherms performed at fixed temperature by varying the frequency (for instance, figure 4.7), it is also possible to fix the frequency and to vary the temperature to obtain isochrones. The same information can be obtained by these two methods: there is an equivalence between temperature and frequency, i.e. a process will be shifted to higher temperature by increasing the frequency and vice versa. Figure 4.8 presents the results obtained for different hydration levels and illustrates this temperature-frequency equivalence.

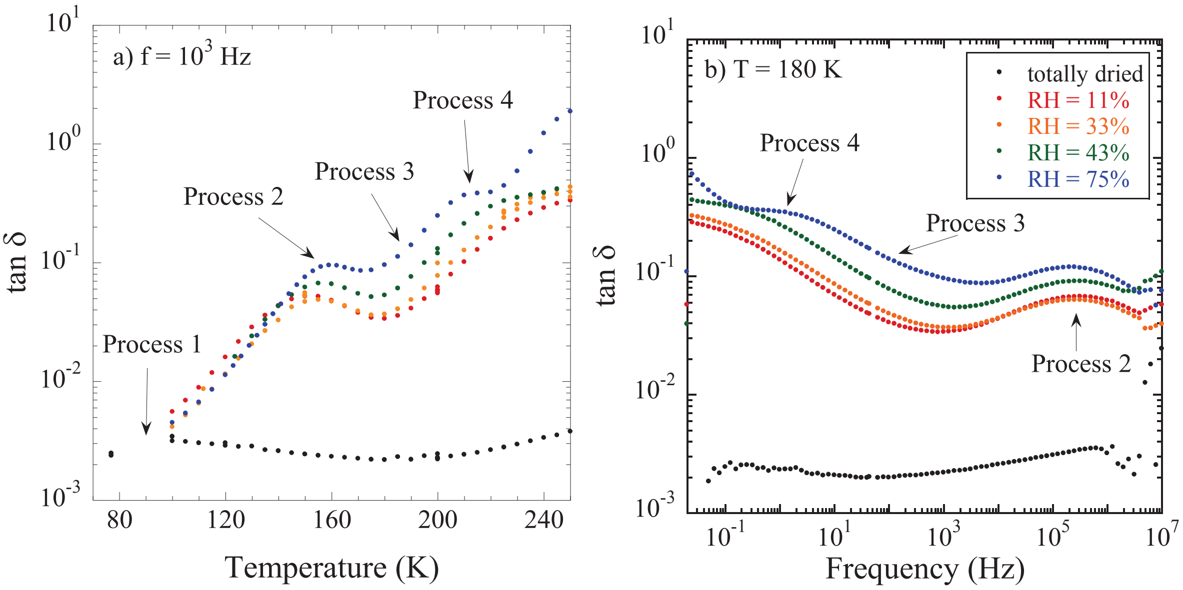

Figure 4.8: Evolution of tan δ of the raw L200S NPs for different relative humidities of the storage medium **a)** with the temperature (at fixed frequency, f = 10^3 Hz) and **b)** with the frequency (at fixed temperature, T = 180 K).

On figure 4.8b, one can clearly see a maximum of tan δ at about f = 3 10^5 Hz (at T = 180 K) for the hydrated powders. The same relaxation process presents a maximum in figure 4.8a in the range of temperature T = 150 - 160 K (at fixed frequency, f = 10^3 Hz). On both figures 4.8a and b, one can see that this maximum is increasing with the amount of water. Regarding the literature, as the dielectric strength of this process increases with the amount of water, this process can be attributed to adsorbed water, and corresponds to “process 2”.

Moreover, in figure 4.8b, tan δ presents a second visible peak, large and badly defined, whose position is around f = 2 Hz at 180 K, for the most hydrated sample (RH = 75%). It appears slightly shifted towards lower frequencies (higher temperature) for lower hydration levels. As we will see below, such a process only partially corresponds to the third process observed by Cerveny et al.

We now try to obtain information about the dielectric strength and the activation energy associated to these processes by fitting the BDS isotherms. Each relaxation process was fitted using a Cole-Cole function (see chapter II for details). At 180 K, it is not possible to describe the obtained isotherms with only 2 processes, see black line in figure 4.9 as compared with a fit using 3 processes. A third process needs thus to be added. In the following, these three processes are labeled process 2, 3, and 4, going from the fastest one to the slowest one (see in figure 4.8).

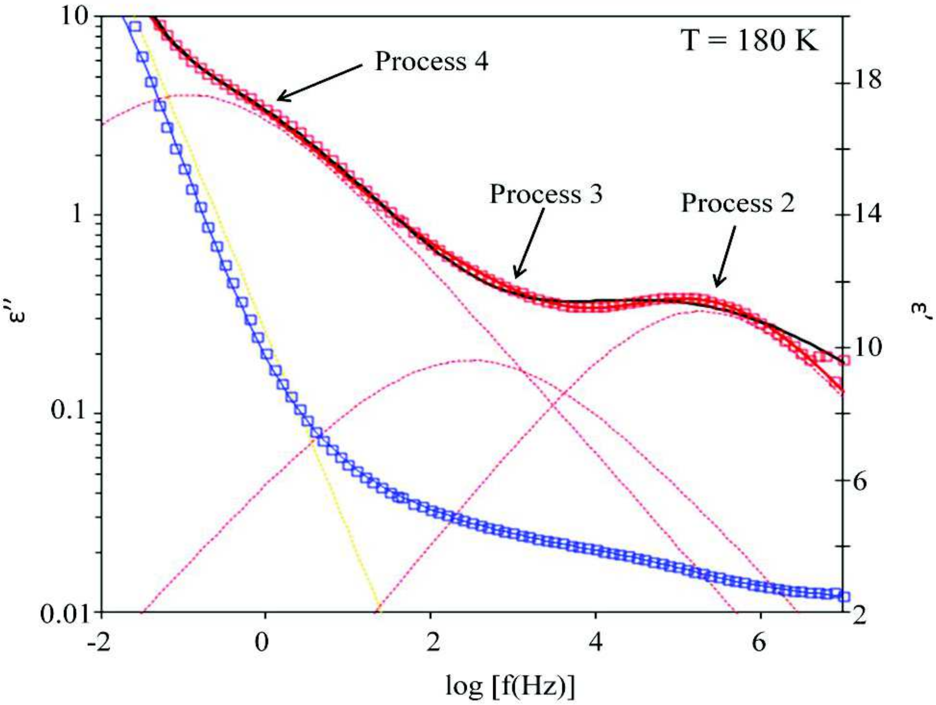

Figure 4.9: BDS spectrum at T = 180 K for the most hydrated L200S powder (RH = 75%). Evolution of the real (blue squares) and imaginary (red squares) parts of the permittivity with the frequency. Solid lines represent the fits to the experimental data with either 2 (black) or 3 processes (red). The individual contribution of processes 2, 3, and 4 to the dielectric loss are visible in red dotted lines. A purely dissipative conductive contribution (which only impacts ε'') was added at low frequency (orange dotted line).

To characterize the different relaxation processes, one method consists in drawing the relaxation map of the sample. For a given temperature, the frequency corresponding to the maximum value of ε'' is extracted from the fit. The associated relaxation time, τ, is given by the relation:

$$\tau = \frac{1}{2\pi f_{\max}} \qquad \text{(eq.4.7)}$$

The relaxation map is given by the evolution of log τ as a function of 1000/T. For the most hydrated sample (RH = 75%), the relaxation map is shown in figure 4.10.

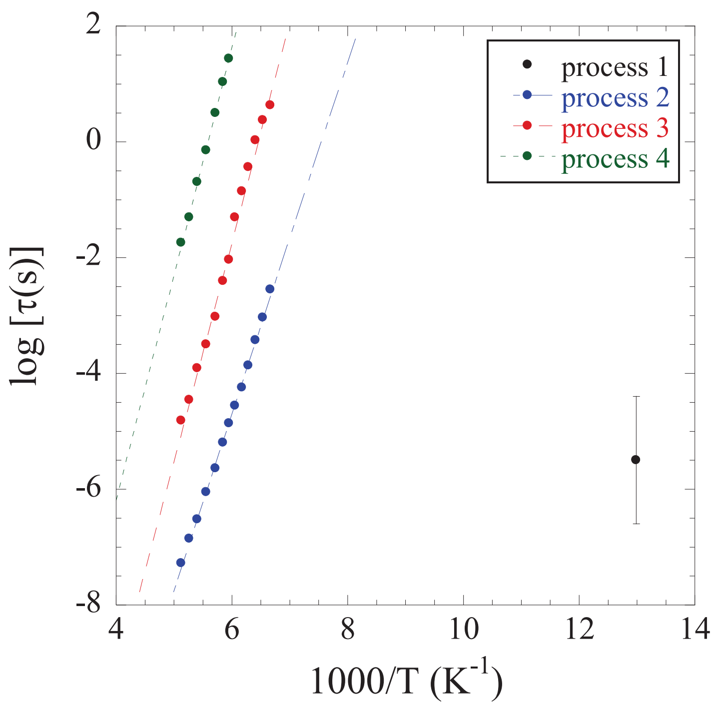

Figure 4.10: Relaxation map of raw L200S NPs with the highest hydration level (RH = 75%) and Arrhenius fit (dotted lines) of the temperature dependence of processes 2, 3, and 4. Process 1 was only measured in the dry state.

As can be seen in figure 4.10, the temperature dependence of the relaxation processes 2, 3, and 4 follows an Arrhenius-type behavior (see chapter II for more details), and no crossover is detected in the low-temperature range. Consequently, the activation energy, E_a, and the pre-exponential factor, log (τ_0), can be calculated with:

$$\tau = \tau_0 \exp\left(\frac{E_a}{kT}\right) \qquad \text{(eq.4.8)}$$

The corresponding values are given in table 4.4.

Table 4.4: E_a and log τ_0 values for the dielectric processes 2, 3, and 4 in L200S NPs with RH = 75%.

	Process 2	Process 3	Process 4
E_a (eV)	0.60	0.75	0.77
log [τ_0(s)]	-22.9	-24.4	-21.8

One can remark that the values of log τ_0 are all below -14, which is associated with typical vibrational times, and have thus no physical meaning. This point has been emphasized by Cerveny et al.[165], and would relate to the fact that the repartition of water around the NPs is not uniform. On the other hand, the activation energy values evolve slightly. The slower the relaxation process, the higher the activation energy.

Comparing with the results given in reference [165] for silica NPs at the same hydration level, process 3 values (log τ_0 = -24.88 and E_a = 0.74 eV) are comparable, whereas the values for process 2 (log τ_0 = -20.02 and E_a = 0.49 eV) are different. The fact that both, the time scales and the activation energy of process 3 do not depend on the surface chemistry (AlOH or SiOH coverage), indicates that this process relates to the hydrated hydroxyl groups, and water in the inner shell. The attribution of process 4 is uncertain at this step of the study, but one can guess that it would also relate to the hydration water. Indeed, one can clearly see in figure 4.8a that this process becomes more intense when increasing the hydration level.

We are now focusing on the evolution of process 2. As this process exhibits a well-defined maximum, it could be followed for all the hydration levels under investigation. The position of the maximum of the dielectric loss was picked-up manually (it was only fitted for the most hydrated powder). As shown in figure 4.11, the temperature dependence clearly depends on the amount of hydration water, with the activation energy which increases with the water content.

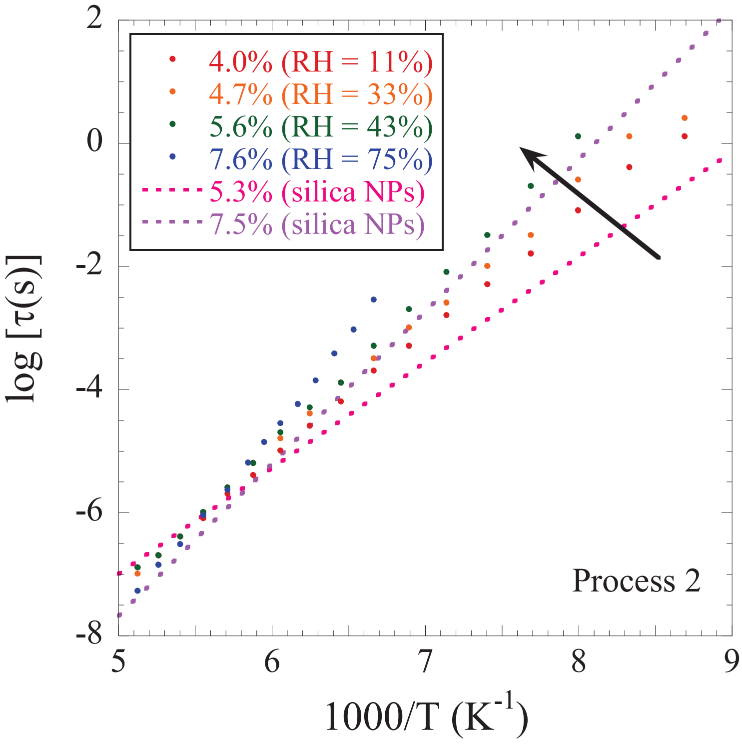

Figure 4.11: Relaxation map showing the evolution of process 2 for different amount of hydration water for alumina-coated silica NPs (L200S) and silica NPs (Zeosil, dotted lines). Data for silica NPs are taken from reference [165].

As shown in figure 4.11, the L200S and Zeosil NPs display the same evolution when increasing the hydration level. Such a result confirms that process 2 has a common origin in the two systems, i.e. it is due to the relaxation of water molecules in the outer hydration shell. However, the activation energy for a given water content in L200S is slightly higher in comparison with the silica NPs (see table 4.3 and figure 4.11 for the two common hydration levels). For the L200S, it reaches a value slightly superior to the activation energy associated with the reorientation of water involving many hydrogen bonds (E_a = 0.54 ± 0.4 eV).[184] As it is attributed to the relaxation of water molecules in the outer shell, the differences may relate to the geometry of our NPs in regard with Zeosil NPs, which may lead to the building of different external water layers.

To summarize the study of raw L200S nanoparticles, process 1 can be attributed to the reorientation of AlOH surface groups. Process 2 can be attributed to the relaxation of water molecules in the outer shell of hydration. This process is impacted by the amount of water, which is in agreement with its attribution. As said above, process 3 is attributed to the relaxation of water molecules in the inner hydration shell. The attribution of process 4 remains uncertain, though it also related to the hydration water. All these processes display an Arrhenius behavior and their activation energies have been quantified.

2 - Grafted NPs

We now switch to the study of surface modified nanoparticles with different phosphonic acids. In the first part, we propose a relative quantification of the grafting density using the dielectric strength of process1. In the second part, we study the relaxations of C_8PA-grafted NPs. In the last part, we focus on DEPA-grafted NPs.

a - Quantification of the grafting density by BDS

As detailed in the preceding section, the relaxation process 1 observed at low temperature and high frequency is attributed to the reorientation of AlOH groups on the NPs surface. When phosphonic acids are grafted on the NPs surface, hydroxyl groups are consumed (see chapter I). Consequently, as the dielectric strength depends on the number of dipoles involved, we expect the strength of process 1 to be lower for the surface modified nanoparticles. Therefore, following the decrease of $\tan \delta = \varepsilon''(\omega)/\varepsilon'(\omega)$ at fixed frequency and temperature should allow following the consumption of AlOH groups present at the surface of the NPs, and thus the increase of the grafting density.

Values for the loss tangent at 77 K are taken at $10^{4.8}$ Hz, i.e. close to the maximum of the relaxation peak (see figure 4.7). They are plotted in figure 4.12 as a function of the grafting density for the raw and surface modified NPs. Grafting densities were quantified using elemental analysis (ICP-OES) as in chapter III.

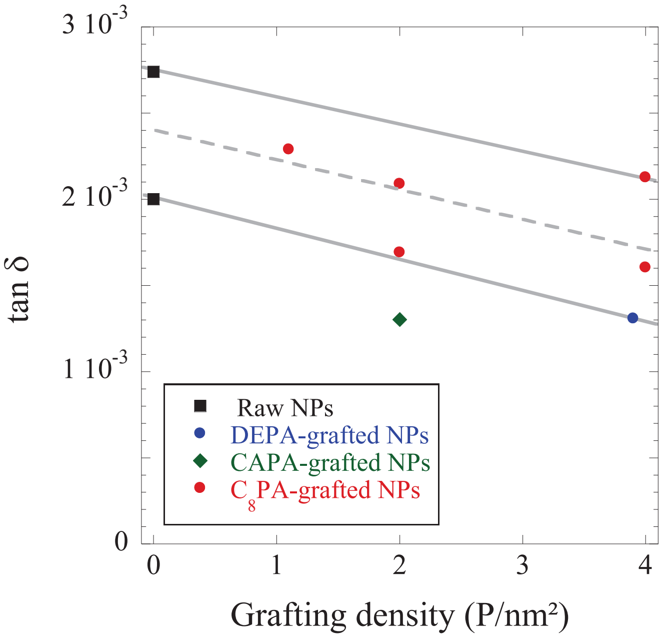

Figure 4.12: Evolution of tan δ with the grafting density at T = 77 K and f = $10^{4.8}$ Hz for different grafted PAs. Lines are guides for the eyes.

To evaluate the precision of our method, the raw L200S NPs and the C_8PA-grafted NPs with the highest grafting density (4 P/nm²) were measured twice starting from two different samples. In figure 4.12, the solid lines are constructed using these results and gives the confidence interval of the evaluation. One can see that the deviation is quite high, in which the main uncertainty relates to the effective amount of powder in between the two BDS electrodes. Indeed, the sample mass is used in the normalization to calculate $\varepsilon'(\omega)$ and $\varepsilon''(\omega)$ starting from the measurement of the complex sample capacity. For this purpose, our system was modeled as two capacitors in parallel, one for the NPs (and water) and one for the empty spaces in between NPs (air). It leads to a normalization of the form $A\varepsilon''(\omega)/[A\varepsilon'(\omega)+B]$, see appendix 4 for details about the coefficients A and B. Note that, in this case, the use of the tangent loss does not allow to suppress the geometrical aspects. Therefore, it is difficult to cancel errors, when comparing different samples due to the uncertainties on both the mass and the thickness.

Nonetheless, a clear trend is visible in figure 4.12: tan δ decreases when increasing the grafting density for both the C_8PA and DEPA grafts. Such a decrease is highlighted by a dotted line which represents the average decrease of tan δ. It gives a direct proof of the efficiency of PA grafting on the L200S NPs, in parallel to other methods (NMR, FTIR, and elemental analysis) as developed in chapter III.

To complete this part, one may consider the particular case of CAPA-grafted NPs. In chapter III, we assumed that the CAPA molecule could graft with both phosphonic acid and carboxylic acid groups at the NP surface, which involved a higher hydroxyl group's consumption than for the other PAs. In figure 4.12, one can see a higher decrease of tan δ for the CAPA-grafted NPs (unfortunately only one sample with CAPA could be investigated), i.e. the CAPA-grafts consume more hydroxyl surface groups by grafting than C_8PA and DEPA, which confirms our hypothesis.

To conclude, BDS allows following the impact of the PA grafting density on the dielectric loss tangent, despite a significant standard deviation. Such an effect relates to the consumption of hydroxyl groups. Therefore, our results confirm the attribution of process 1 to the reorientation of AlOH groups at the surface of the PA-grafted L200S NPs.

b - C_8PA-grafted nanoparticles

In addition to the relaxation processes observed for the raw L200S NPs, we expect to detect the dielectric relaxation of the alkyl chain of the graft. Figure 4.13 represents the evolution of tan δ with the temperature at fixed frequency (figure 4.13a, f = 10^3 Hz), and with the frequency at fixed temperature (figure 4.13b, T = 180 K).

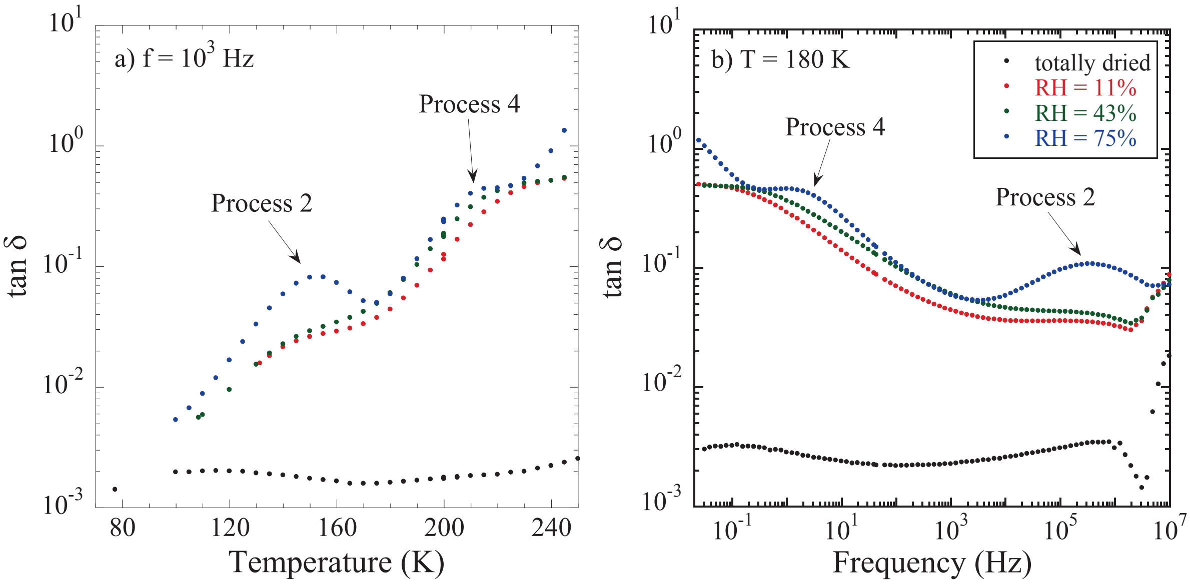

Figure 4.13: Evolution of tan δ with the hydration rate for C_8PA-grafted NPs at **a)** fixed frequency (f = 10^3 Hz), and **b)** fixed temperature (T = 180 K).

For the most hydrated sample (RH = 75%), the real and imaginary parts of the permittivity are fitted using (eq.2.18) with three relaxation processes, as shown in figure 4.14 at T = 180 K.

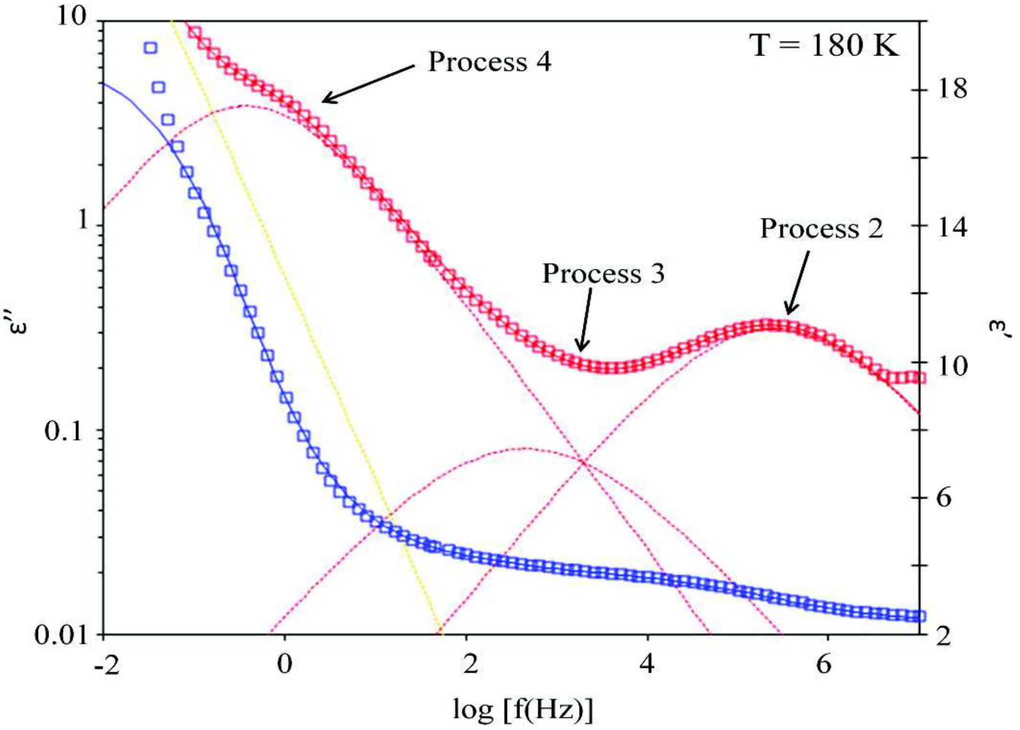

Figure 4.14: BDS spectrum at T = 180 K for the most hydrated C_8PA-grafted NPs (RH = 75%). Evolution of the real (blue squares) and imaginary (red squares) parts of the permittivity with the frequency. Solid lines represent the fits to the experimental data. The individual contribution of processes 2, 3, and 4 to the dielectric loss are visible in red dotted lines. A purely dissipative conductive contribution (which only impacts ε'') was added at low frequency (orange dotted line).

As observed for the raw NPs with different hydration levels (see figure 4.8), the 3 processes associated to water dynamics in the high-temperature range are detected for the C_8PA-grafted NPs. However, in the studied temperature- and frequency-ranges, the relaxation process of the alkyl chains is not observed. This is most probably due to the low dipolar contribution of the alkyl groups.

In the case of process 3, one can see that it is less intense than for the raw NPs in figure 4.9 (same water content in both cases, see table 4.1). The dielectric strength is about 50% less, in absolute value and also when it is normalized to the dielectric strength of process 4. As the NPs are surface modified, the surface hydroxyl groups are consumed. As process 3 relates to the dynamics in the inner shell (water in interaction with the hydroxyl groups), its strength decreases when the NPs are grafted due to the consumption of the Al-OH groups.

In the case of process 2, figure 4.15 shows the evolution of tan δ at fixed temperature (T = 160 K) and frequency (f = 10^4 Hz) with the water content of the sample (figure 4.15a) and the grafting density of C_8PA (figure 4.15b).

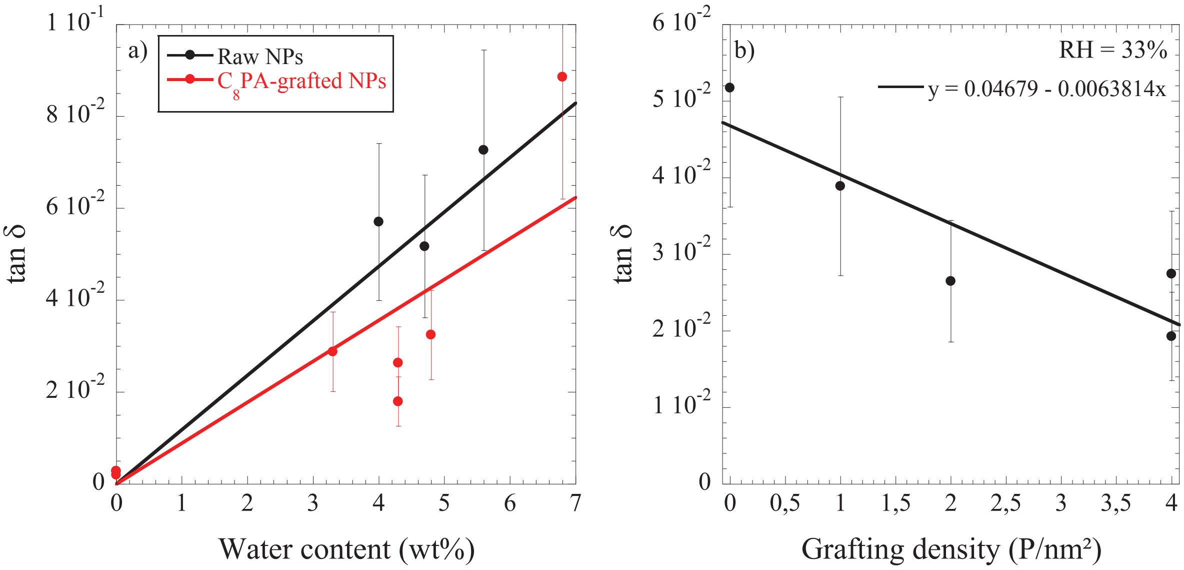

Figure 4.15: Evolution of tan δ **a)** with the water content of the raw NPs and C_8PA-grafted NPs (4 P/nm²) and **b)** the grafting density of C_8PA (RH = 33%, water content = 4.4 ± 0.5 wt%). Both evolutions are given at fixed temperature (T = 160 K) and frequency (f = 10^4 Hz), which corresponds approximately to the maximum of the relaxation peak associated with process 2. Errors bars are arbitrary fixed to 30% of the value.

One can clearly see that process 2 is impacted by the amount of water in the powder. Indeed, the dielectric strength of process 2 increases with the total amount of hydrating water. The same observation is made for the raw L200S NPs. It is in agreement with the attribution of this process to the relaxation of water molecules in the outer hydration shell, with a smaller contribution for C_8PA-grafted NPs. Regarding the impact of the grafting density of C_8PA, increasing the amount of grafted molecules leads to a decrease of the strength of process 2 (figure 4.15b). As the water content in these samples is similar (4.6 ± 0.4 wt%, cf. table 4.1), it suggests that less water molecules are involved in process 2 when the grafting density is increased.

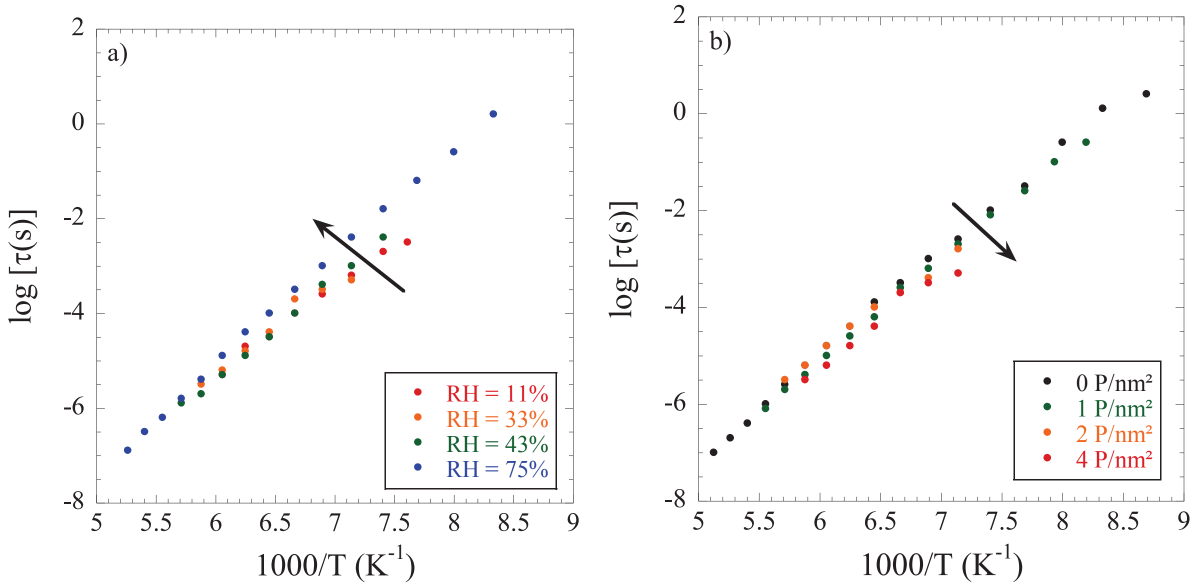

Figure 4.16: Temperature dependence of the relaxation times associated to process 2 for C_8-PA grafted NPs for different **a)** relative humidities (4 P/nm^2), and **b)** grafting densities of C_8PA (RH = 33%).

Figure 4.16 shows that the impact of different parameters on the characteristic times of process 2 is rather weak. As it was observed for the raw L200S NPs, the activation energy increases with the water content. Moreover, an increase of the grafting density leads to a slight decrease of the activation energy. Seemingly, at constant hydration level, the presence of the grafts impacts the relaxation of the water molecules in the outer shell, as compared to the relaxation of “free” water molecules. Note that there was no significant variation of the water content with the grafting density (see table 4.1).

To summarize our results on process 2, the increase of the hydration level leads to an increase of both tan δ, i.e. the number of dipoles involved, and the corresponding activation energy. One may assume that when the water molecules are more abundant, they can easily form hydrogen bonds. Their relaxation requires more energy, and we approach the value obtained for the reorientation of pure water.[184] On the contrary, increasing the grafting density leads to a decrease of both tan δ and E_a. In other words, when the NP coverage (with C_8PA) is denser, less water molecules are localized in the outer shell, due to the hindrance generated by the grafted PAs. Moreover, it could be that the grafts are somehow disturbing the formation of hydrogen bonds between the water molecules in the outer shell. Consequently, the required energy needed for the water molecules is lower.

To conclude on C_8PA-grafted NPs, the relaxation of the grafted molecules is not observed, but water-related processes 2, 3, and 4 are detected, and found to be affected by grafting. We are now switching to the DEPA-grafted NPs. As the dipolar moment of DEPA is higher than those of C_8PA, one can expect to detect the relaxation of the grafts.

c - DEPA-grafted nanoparticles

We now switch to the DEPA-grafted NPs. In addition to the processes related to water dynamics, two relaxations associated with the dynamics of the DEPA graft are expected as the dipolar moment of this molecule is significantly higher than for C_8PA: the α-relaxation linked to the glass transition, and a secondary (β) relaxation due to localized conformational changes.

As the α-process is associated with cooperative motions involving different segments, the characteristic time of such a process may be strongly impacted by grafting on the NPs surface. To answer this question, we performed DSC measurements on neat (pure) DEPA and on the DEPA surface modified NPs, both in the dried state. Results are shown in figure 4.17.

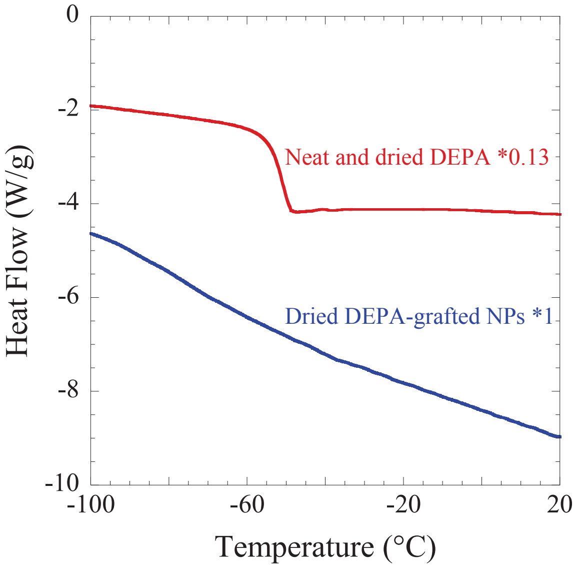

Figure 4.17: Heat flow measured by DSC of pure DEPA and dried DEPA-grafted L200S NPs (grafting density 4 P/nm²), during heating (scan rate = 20 K/min).

The heating scan of pure DEPA in figure 4.17 shows a glass-transition temperature at - 51°C (222 K). On the contrary, no hint of a glass-transition phenomenon is detected for the grafted DEPA, though the DEPA molecules represent about 13% of the total sample mass. Note that in figure 4.17, the heat flow of pure DEPA has been normalized to this latter value to allow for a proper comparison. Such a result suggests that the dynamics associated with the α-process of the DEPA molecules is strongly suppressed for molecules attached to NPs. Accordingly, it should not be observed by BDS. Interestingly, a recent study from Barroso et al. on the dynamics of PEO chains confined in between graphite oxide layers evidenced the same result for short PEO segments containing 3 repeat units (i.e. similar to DEPA).[185] In this system, the suppression of the glass transition was attributed to geometrical restrictions.

Figure 4.18 presents the evolution of the dielectric loss tangent for neat DEPA and DEPA-grafted nanoparticles in the dried state.

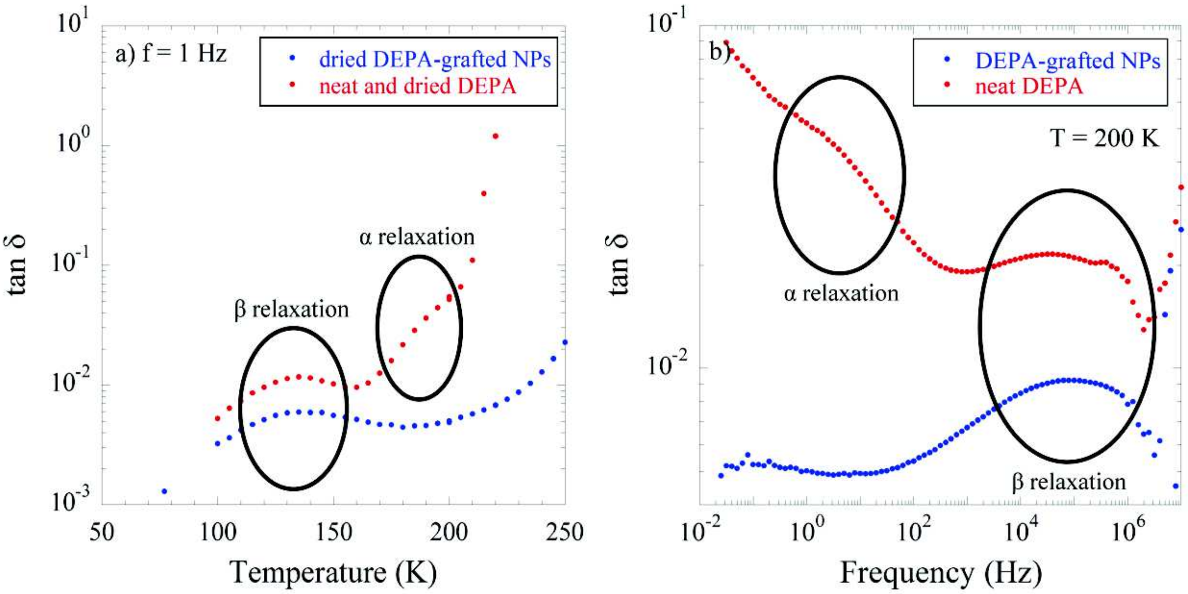

Figure 4.18: Evolution of tan δ **a)** with the temperature at fixed frequency (f = 1 Hz), and **b)** with the frequency at fixed temperature (T = 200 K) for dried neat DEPA and DEPA-grafted NPs (4 P/nm²).

The first relaxation peak is observed at about 140 K for the pure and grafted DEPA molecules. It corresponds to the β-relaxation of DEPA. For the neat DEPA, the second relaxation peak located at about 190 K is attributed to the α-process. In agreement with the DSC measurements (figure 4.17), it is not detected in the grafted NPs.

Figure 4.19 shows the temperature dependence of the β-relaxation for both, the neat and grafted DEPA. Both curves are nicely superimposed: grafting does not impact the relaxation time of the molecular motions associated with the β-mechanism, as it is expected for a local process. The energy parameters associated with this process are: E_a = 0.36 eV and log [τ_0(s)] = -14.72.

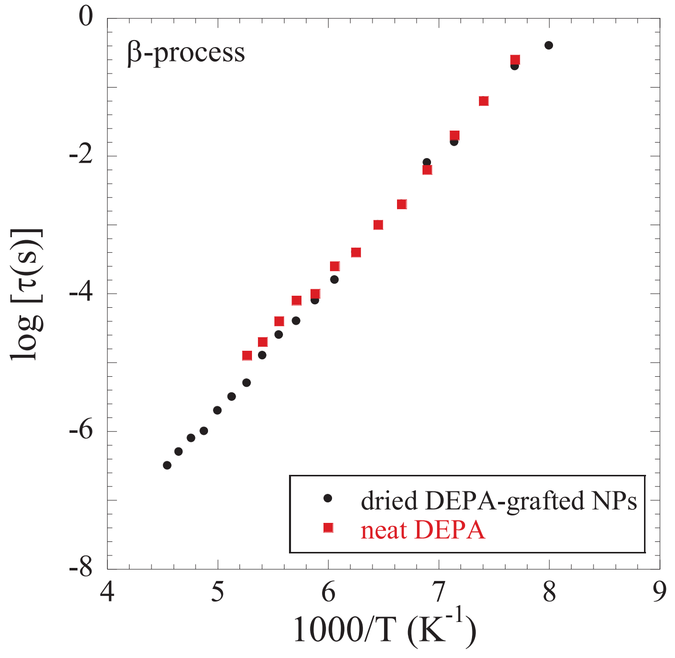

Figure 4.19: Evolution of log τ with 1000/T for dried neat DEPA and DEPA-grafted NPs (4 P/nm²).

d - DEPA-grafted nanoparticles: impact of relative humidity

The impact of the water content has also been studied for the DEPA surface modified NPs at fixed grafting density (4 P/nm^2). Unfortunately, the strong β-relaxation of the DEPA grafts takes place in a similar temperature and frequency range than the process 2 linked to the hydration water in the outer shell. Therefore, a careful data treatment implying a simultaneous description of these two processes is required (currently under progress). At this stage, the maximum (picked up by eye) of the relaxation peak associated to both processes is given in figure 4.20.

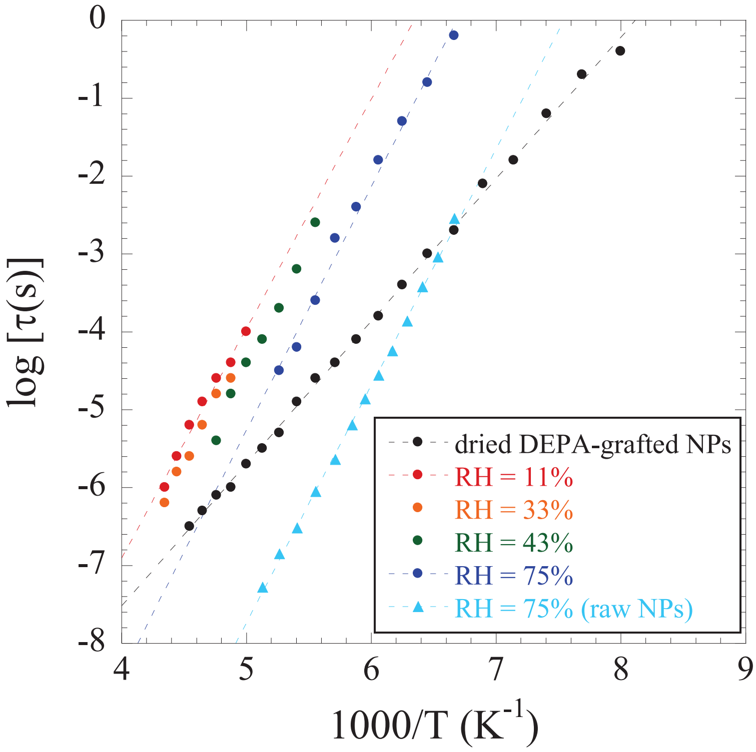

Figure 4.20: Relaxation map of DEPA-grafted NPs (4 P/nm^2) with different hydration levels. The relaxation times of the raw NPs with RH = 75% are added for comparison.

In figure 4.20, the temperature dependence of the relaxation time evolves slightly with the hydration level (from 0.58 to 0.62 eV, for RH values from 11 to 75%, respectively), and one can see that it is very similar to the one of the raw NPs with the highest hydration (RH = 75%, E_a = 0.60 eV), i.e. similar to bulk water[184]. The activation energies with DEPA-grafted NPs are clearly different from the one of the β-process (E_a = 0.36 eV, black curves). Therefore, the maximum of the signal observed by BDS in the DEPA-grafted NPs reflects mainly the dynamics of process 2. Moreover, even at low hydration level, the activation energy with DEPA is already close to the one of the bulk water. DEPA thus plays the role of water molecules in the dynamics of process 2. It is presumably due to the formation of hydrogen bonds between the DEPA molecules (chain with -CH_2-CH_2-O-) and water molecules in the outer shell.

V - Conclusion

In the first part, the structure of C_8PA-grafted nanoparticles was investigated by SAXS. The grafting density of C_8PA clearly impacts the structure of nanoparticles in the powder, e.g. their internal volume fraction, which was found to decrease linearly with the increase of grafting density. A tentative description of air-containing holes in the powders based on a low-q Porod law was also proposed. This analysis suggests that grafting leads to the formation of many more smaller and more homogeneously distributed holes.

The second part of this chapter was a BDS-study on powders. First, the raw L200S NPs dynamics was investigated: four relaxation processes were observed. Process 1 was attributed to the reorientation of Al-OH surface groups. Note that this process was also visible in the dried state, consequently it does not relate to water dynamics. Process 2 was attributed to water molecules localized in the outer hydration shell and its activation energy was found to depend on the water content in the powders. Process 3 is attributed to the hydrated OH-surface groups and to the water molecules in interaction with these groups (inner shell). This process was found to display the same energy parameters than obtained by Cerveny et al. in the case of precipitated silica powders, indicating that its dynamics is independent of the NPs surface (SiOH or AlOH). It was not the case for process 2. An additional relaxation process as compared to silica powders was observed (process 4), but its attribution remains uncertain at this point.

In the case of surface-modified NPs, the evolution of the dielectric loss tangent with the grafting density confirmed the attribution of process 1, as it decreased with the consumption of OH groups with the increase of grafting density. Then, the study of C_8PA-grafted NPs was a partial success. Neither α-, nor β-relaxation was detected for the grafted chains. One explanation is that the dipolar moment of the alkyl chain is too low to be detected. However, the powders exhibit the relaxation processes 2, 3, and 4 associated with the hydration water. As expected, process 1 (attributed to surface OH groups) was not detected in the case of NPs modified by a dense monolayer of C_8PA. Process 2 was shown to be impacted by the hydration level, and the C_8PA grafting density. The later parameter also strongly impacts the process 3.

At this stage, it was not possible to link the structural to the dynamical features of the powders. The dynamics focused on water-based processes, which does not seem to be influenced by NP structure with holes. An interesting perspective of this approach would be to follow interfacial polarization processes (the so-called MWS processes) at high temperature, which should be sensitive to structural evolution. This was excluded in the present study to avoid evaporation during measurements.

Finally, the study of DEPA-modified NPs highlighted the existence of a local relaxation process of the grafts, β-process. The α-relaxation process, linked to a cooperative motion of the grafted chains, could not be detected. The suppression of this process is most probably due to the attachment of the grafts onto the NPs surface.

Chapter V – Surface-modified NPs/PEA nanocomposites

As developed in the bibliographic part (chapter I), a nanocomposite is a multicomponent system, in which at least one phase has a typical dimension in the nanometer range. In this thesis, we focus on polymer nanocomposites (NCs). The macroscopic properties of such a material, especially rheological and mechanical ones, are correlated to the filler structure, i.e. the state of dispersion of NPs within the nanocomposite.[116, 186, 187] It is thus important to be able to control and to tune the state of dispersion (referred to as "structure") of the NPs in the polymer matrix.

Grafting small organic molecules on inorganic NPs is a convenient way to modify their interactions and then their state of aggregation in solution and ultimately in a polymer matrix.[111] As reported in chapter III, we are able to graft small phosphonic acids on the surface of alumina-coated silica NPs (L200S) in water and to vary the state of dispersion of these NPs in colloidal aqueous sols by playing with the surface modification parameters. In dispersion in solution, the aggregate size increases with the hydrophobicity of the grafted molecules (C_8PA>C_5PA>C_3PA>DEPA), and with the augmentation of the grafting density, due to the decrease of electrostatic repulsions between NPs.

The modified NPs are incorporated in a polymer matrix following an aqueous route (see chapter II). The scientific goal of this chapter is to find out if the same aggregation state as in sols is conserved, or if the graft of hydrophobic PAs can lead to a better compatibilization with the polymer matrix. To this end, the filler microstructure state in the nanocomposites is studied using small-angle neutron scattering. In particular, we investigate the impact of different parameters linked to the surface chemistry of the NPs: the nature of the grafted PA (hydrophilic or hydrophobic, chain length of the graft), and the grafting density.

I - Sample description

Water-borne nanocomposites were elaborated by mixing the aqueous colloidal suspension of raw or grafted NPs with a lab-made PEA nanolatex. The nanolatex preparation method and characterization are given in chapter II.

Different parameters were varied to study their impact on the filler microstructure in the polymer matrix:

- the NP volume fraction (ϕ) in the nanocomposite: approximately from 1 to 10 %vol.
- the nature of the PA grafted on the NPs surface: C_3PA, C_5PA, C_8PA, and DEPA.
- the grafting density (ρ) of PA: from 0 to 1.5 P/nm² for alkylphosphonic acids (up to 4.0 P/nm² for DEPA).

The sample characteristics are given in table 5.1. The "introduced volume fraction" corresponds to the volume fraction of NPs as deduced from weighting and solid content of the solutions. The volume fraction in the final NCs was also measured by TGA. Both values are compared in table 5.1 and in figure 5.1.

Table 5.1: Samples characteristics.

Reference	Phosphonic acid	Grafting density (P/nm^2)	Volume fraction ϕ (%vol)	
			Introduced	TGA
CS244	None: polymer matrix		0.0	0.2
CS245	None		1.0	0.9
CS246			4.9	6.5
CS247			9.7	10.8
CS248	C_8PA	0.5	1.0	1.7
CS249			4.6	5.8
CS250			9.3	11.9
CS251		1.0	0.9	1.4
CS252			4.6	4.1
CS253			9.3	11.3
CS254		1.5	0.9	0.8
CS255			4.6	4.4
CS256			9.3	8.8
CS258	C_5PA	0.5	4.6	6.4
CS259			9.3	11.9
CS261		1.0	4.5	5.4
CS262			9.3	10.2
CS266	C_3PA	1.0	1.0	1.1
CS267			4.9	5.0
CS268			9.9	11.4
CS272	DEPA	1.0	1.0	1.6
CS273			4.9	4.4
CS274			9.9	12.8
CS275		1.5	1.0	1.2
CS276			5.0	5.1
CS277			9.9	11.4
CS281		4.0	1.0	1.4
CS282			9.9	10.8

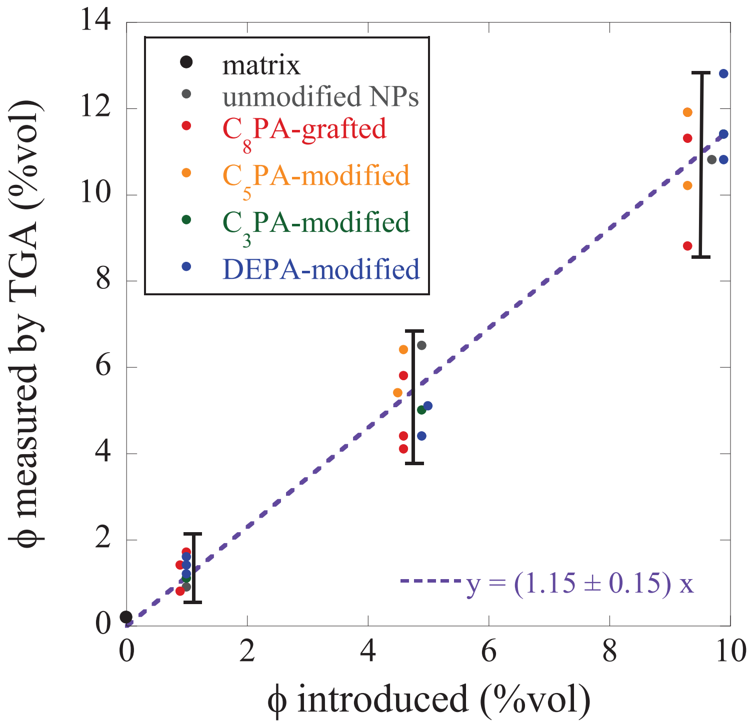

Figure 5.1: Correlation between the NP volume fractions introduced and measured by TGA in the nanocomposites.

Figure 5.1 presents the correlation between the introduced NP volume fraction (calculated with the mass of latex and NPs sols) and the measured NP volume fraction (TGA). One can see that both values are in the same range. The data in figure 5.1 can be fitted with a linear law: $\phi_{TGA} = \alpha\ \phi_{introduced}$, with $\alpha = 1.15 \pm 0.15$. It follows that Φ_{TGA} is higher than $\Phi_{introduced}$, but both values are compatible within error bars. A possible explanation for the deviation is the degradation of the grafted organic chains, which is not taken into account in the calculation of $\Phi_{introduced}$. In the following, we use the introduced volume fractions, noted ϕ.

II - Study of the structure of nanocomposites by SANS

The dispersion state of nanoparticles in the PEA matrix was studied by SANS. The form factor of the bare nanoparticles (L200S without grafting) was determined by a SAXS measurement and rescaled to neutron contrast (see chapter II). All curves were then shifted to match this form factor at large angles (starting from ca. $q = 3\ 10^{-2}$ Å^{-1}).

The scattered intensity can be expressed (strictly speaking only for monodisperse spherically symmetric objects) as follows:

$$I(q) = I_0\, P(q)\, S(q) \qquad \text{(eq.5.1)}$$

with I_0 a prefactor, P(q) the normalized form factor of the L200S nanoparticles, and S(q) the structure factor, which reflects the center-of-mass spatial correlation between NPs in the polymer matrix. According to (eq.5.1), the structure factor can be obtained by dividing the scattered intensity by the form factor. As an example, figure 5.2 presents the different intensities for a sample with DEPA-grafted NPs in PEA ($\rho = 4$ P/nm², and $\Phi = 10\%$).

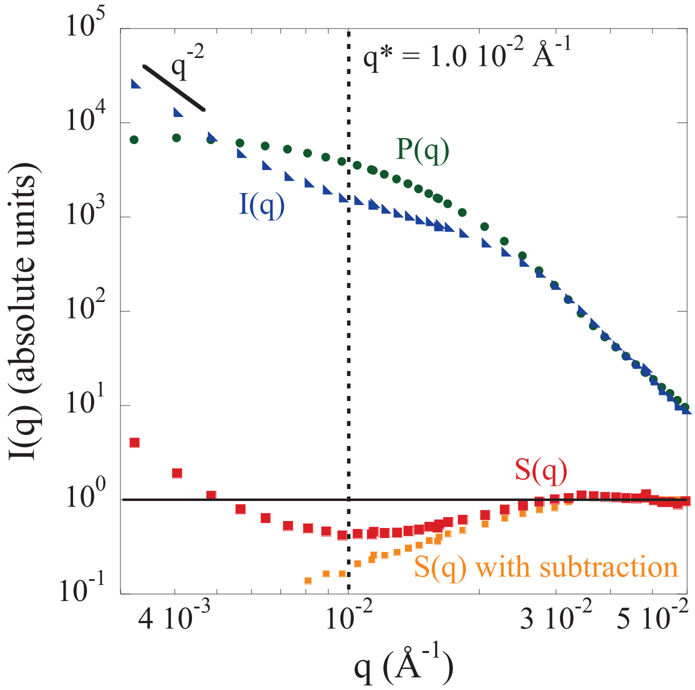

Figure 5.2: Decomposition of the scattered intensity to obtain S(q).

The structure factor provides structural information. On one hand, in absence of interactions between aggregates, if S(q) increases and reaches a plateau at low q, its level is equal to the average aggregation number, N_{agg}, i.e. the number of NPs forming an aggregate (see details in chapter I). On the other hand, as can be seen in figure 5.2, the structure factor in our samples does not reach a plateau at large length scales. The low-q intensity increases following a power law: this power law gives the fractal dimension of the aggregates, which fluctuates around 2 for our samples (see appendix 6). S(q) also contains information on the aggregate compacity, κ. When NPs are aggregated, the structure factor decreases in the intermediate q-range, which reflects the repulsive interactions between NPs: this is the so-called "correlation hole". The deeper the correlation hole, the more coordinated the NPs, i.e. the denser the aggregates. The minimum value of this correlation hole is approximately obtained for $q^* = 10^{-2}$ Å^{-1}. Consequently, the value of S(q*) where q* is smaller than $\pi/\langle R_{NP}\rangle$ (= π/(79.5 Å) ≈ 4 10^{-2} Å^{-1}) should be related to the compacity of the aggregates, κ, i.e. the volume fraction of NPs in an aggregate, as illustrated in figure 5.3.

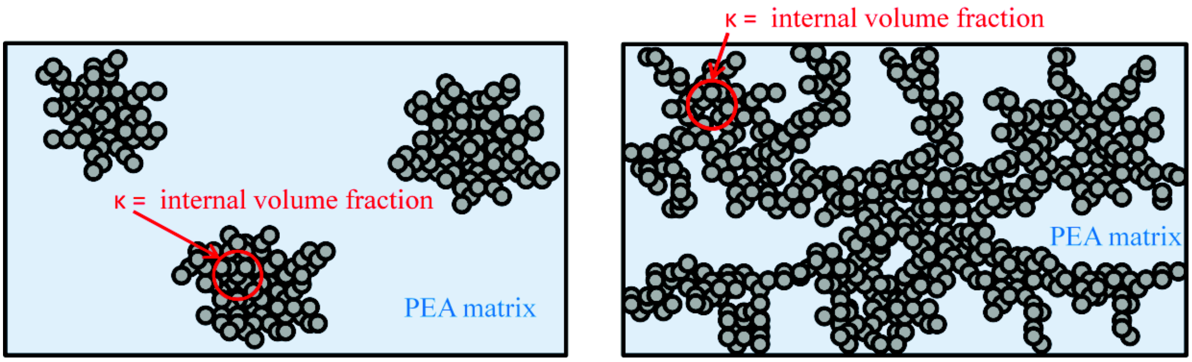

Figure 5.3: Two different schematic representations of the nanocomposites: NPs aggregates or NPs network of aggregates (branches) within the polymer matrix.

Unfortunately, our scattering data cover a restricted q range, and it is thus difficult to conclude on the true nature of the aggregates or dense networks. To obtain the "real" fractal dimension of our objects, measurements at lower q values would be necessary. In this context, we chose to use the "raw" structure factor (without subtraction of any power law) for the data interpretations, e.g. for the calculation of aggregate compacity within the network branches or in aggregates, which will be discussed in this chapter. Note that we also tried to subtract the low-q power law from the structure factor in order to obtain a "local" structure factor and estimate an upper bound of the compacity.

As an example taken from the literature, Banc et al. observed the same type of scattered intensity for silica-PEMA nanocomposites at low NP volume fraction ($\Phi = 1\%$), as shown in figure 5.4.[127]

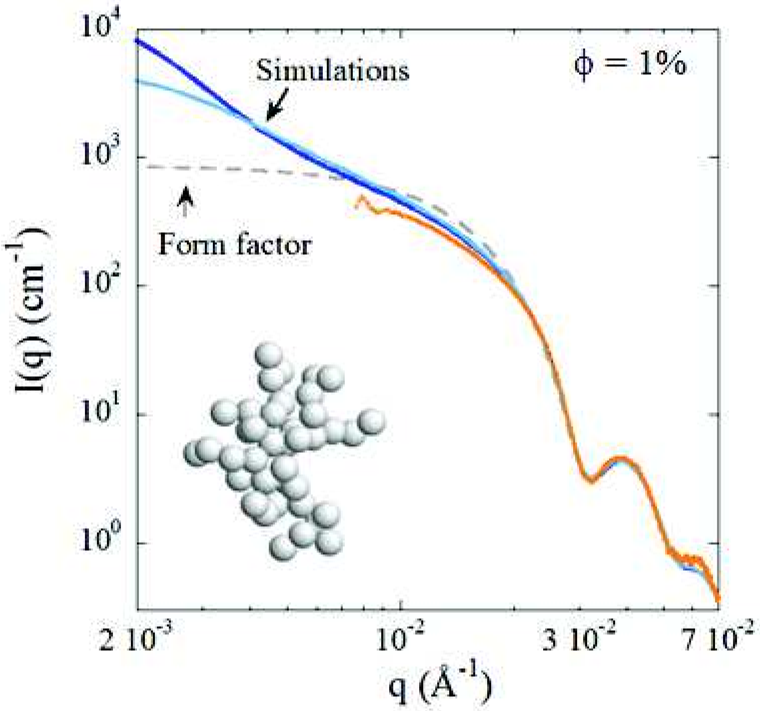

Figure 5.4: Scattered intensity of silica-PEMA nanocomposites for $\Phi = 1\%$. Figure taken from reference [127].

Aggregation generally induces an increase of the low-q scattered intensity, which is accompanied by a decrease with respect to the form factor of the intermediate-q intensity (correlation hole). Both features can be observed in figure 5.4. The correlation hole is a consequence of the close vicinity and aggregation of the NPs. At the highest q, the intensity follows the NP form factor. At intermediate q values, a power law is observed and gives a fractal dimension $D_f = 2.5$, which speaks in favor of aggregation. Note that for our samples, we found fractal dimensions around 2 for the same NP volume fraction. At the lowest q values, the increase in intensity is linked to the weighted average of the mass of aggregates. Indeed, according to Banc and co-workers, the low-q scattered intensity can be interpreted as the form factor scattering of independent aggregates, with a broad distribution in size at high dilution ($\Phi = 1\%$). By keeping this idea in mind, for low NP volume fraction samples ($\approx$ 1%), we will interpret the low-q intensity increase as an increase of aggregates' mass. By increasing the NP volume fraction, the interactions between aggregates are no longer negligible, and the low-q intensity is affected by this inter-aggregate structuration. In this chapter, the evolution of the low-q scattered intensity will thus be considered only in the diluted case, i.e. for $\Phi = 1\%$. On the other hand, it is possible to interpret quantitatively the intensities in the intermediate q-range for all filler fractions.

The quantitative relationship between the structure factor in the correlation hole (at q*) and the compacity κ can be achieved using a Percus-Yevick structure factor.[167] The same method was used in reference [145]. The limiting value of S(q→0) can be described by:

$$S(q \rightarrow 0) = \frac{(1-\alpha\kappa)^4}{(1+2\alpha\kappa)^2} \qquad \text{(eq.5.2)}$$

The introduction of a prefactor α allows taking into account the polydispersity of the NPs in the Percus-Yevick equation (α = 1 in the monodisperse case).[145] The NPs polydispersity is 38% (cf. chapter II), so we use α = 0.54 in (eq.5.2), according to reference [145]. The value of S(q*), which can be taken as an estimate of S(q → 0), allows determining the aggregates' compacity, κ, using (eq.5.2). For comparison, applying (eq.5.2) to the data by Banc and co-workers on silica-PEMA nanocomposites, a compacity of 6.5% is found, which is in good agreement with the compacity deduced from numerical simulations (between 6 and 10%) and from TEM images (11% in average) in the same article.[127]

Concerning the influence of the different experimental parameters on aggregation, different tendencies can be expected. By increasing the NP volume fraction, the distances between NPs will be reduced. As a consequence, the NPs are more likely to collide, and thus, to aggregate. Besides, the grafting density and the nature of the grafted PA will change the hydrophilicity of the NPs. Initially, alumina-coated silica NPs are hydrophilic due to the presence of surface OH-groups. When their surface is modified with C_8PA, NPs form aggregates in solution, because of the hydrophobicity of the graft (cf. chapter III). In addition, NP aggregation in solution increases with the grafting density for all types of grafts studied here, from the most to the least hydrophobic graft: C_8PA > C_5PA > C_3PA > DEPA. We also found that at high grafting density, the lack of electrostatic repulsions favors aggregation. However, another parameter must be taken into account: the PEA polymer matrix is hydrophobic. Consequently, the most hydrophobic NPs, which are also the most aggregated in solution, are the ones which are most compatible with the matrix. As NPs can migrate during the annealing of the NC, one can assume that the hydrophobic NPs may redisperse in the NC, giving two different possible scenarios: the NP aggregation in sols can be conserved or the NPs can redisperse during annealing due to a better compatibilization between NPs and the matrix. Moreover, the most hydrophilic NPs can aggregate during their incorporation in the polymer.

1 - Influence of volume fraction

In this part, the filler fraction in the nanocomposite is varied for different types of nanoparticles: unmodified NPs, NPs modified with the most hydrophobic graft (C_8PA), and NPs modified with the most hydrophilic graft (DEPA). The scattered intensities are plotted in figure 5.5 for a given surface modification, at fixed grafting density. As the intensity is proportional to the NP volume fraction, we represent the reduced intensity, I(q)/Φ, to highlight the impact of the volume fraction on the filler microstructure.

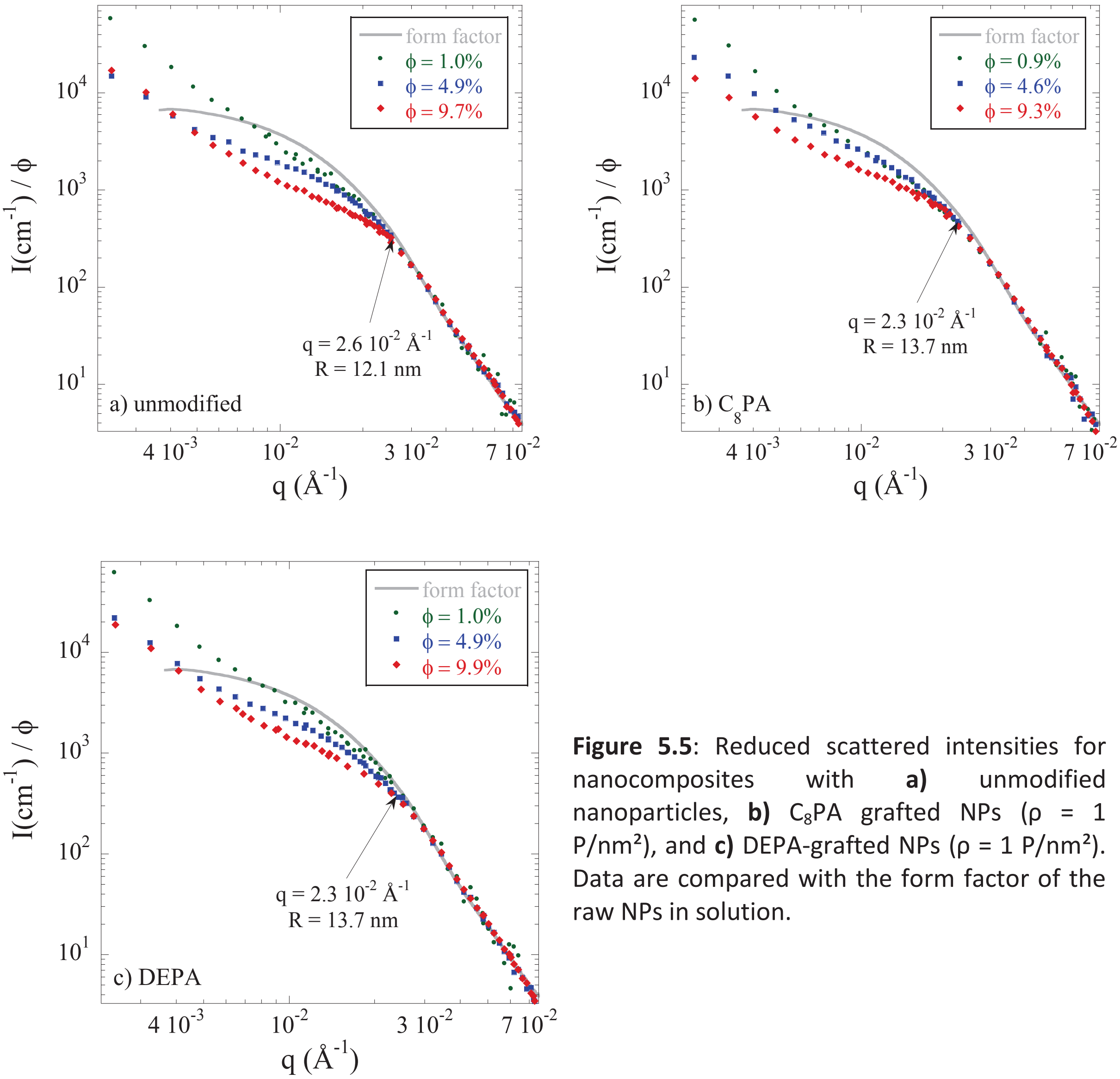

Figure 5.5: Reduced scattered intensities for nanocomposites with **a)** unmodified nanoparticles, **b)** C_8PA grafted NPs (ρ = 1 P/nm²), and **c)** DEPA-grafted NPs (ρ = 1 P/nm²). Data are compared with the form factor of the raw NPs in solution.

At large angles, in figure 5.5, one can see that the local organization is identical for the different surface-modified NPs, because it is representative of the NP (L200S). Some differences are observed in the intermediate and low-q range. Indeed, there is more and more aggregation (low-q upturn), from the lowest concentration on. It is accompanied by the formation of the correlation hole at intermediate q (around 0.01 $Å^{-1}$), which proves that nanoparticles are interacting repulsively, and presumably in close contact. The q-value, which corresponds to the beginning of this correlation hole (see arrows in figure 5.5), gives the distance D between two centers of mass of the NPs: $q = 2\pi/D$. One can deduce the radius of the NPs (R=D/2). It is found to increase with the surface modification from approximately 12 to 14 nm. Note that the radius obtained in this way for the unmodified NP is higher than the one obtained from the form factor in solution (average radius: $R_0 \exp(\sigma^2/2) = 7.4 \exp(0.38^2/2) \approx 8$ nm, see chapter II). As this size is too small to correspond to aggregates, one can imagine that the radius deduced from the average distance is higher than the individual NP radius due to the disordered arrangement of NPs, see figure 5.6. Nonetheless, the increase of radius of ca. 2 nm from the raw to the surface-modified NPs corresponds to what can be expected taking into account the length of the grafted molecules (between 1.1 and 1.3 nm for both PAs).

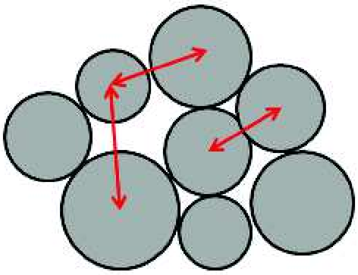

Figure 5.6: Schematic representation of the disordered arrangement of polydisperse NPs, which leads to an increase of the average distance between NPs centers-of-mass.

Turning to the correlation hole, one can see in figure 5.5 that the scattered intensity in the intermediate q-range decreases nicely for increasing NP fractions. According to (eq.5.2), S(q*) values allow deducing the aggregate compacity, κ, for the different samples. Figure 5.7 presents the evolution of the κ values with the NP volume fraction in the nanocomposites.

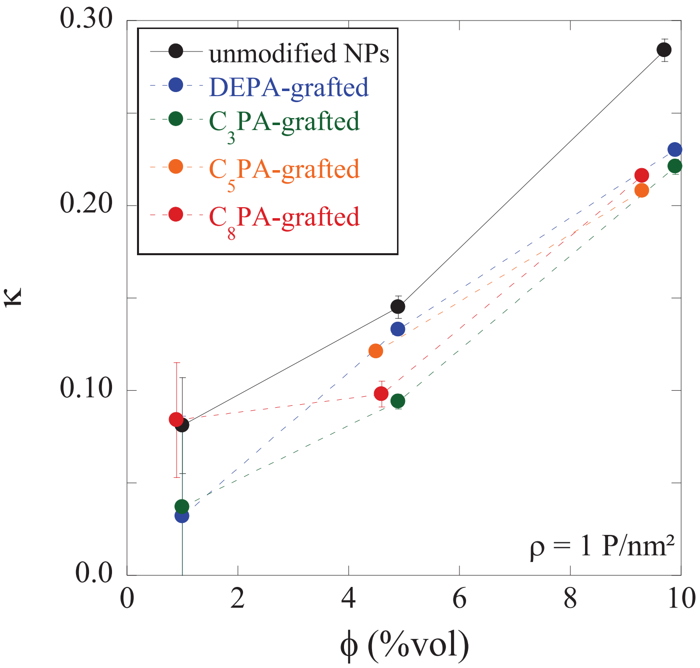

Figure 5.7: Evolution of κ with the NP volume fraction for the different types of surface modification at fixed grafting density, ρ = 1 P/nm².

One can see in figure 5.7 that increasing the NP volume fraction in the polymer matrix leads to an increase of κ, i.e. to denser aggregates. This can be explained by the fact that as the volume fraction increases, the NPs are, again, more likely to encounter in the polymer matrix, thus to aggregate more strongly, and form denser aggregates. A similar evolution was observed with the subtracted structure factor (see discussion of figure 5.2), but the aggregates compacity was found to be higher (κ varies from 0.2 for Φ = 1% to 0.6 for Φ = 10%). Besides, surface-modified nanoparticles seem to form sparser aggregates than unmodified nanoparticles, suggesting a better compatibilization of the modified NPs. In the next part, we will thus focus on the impact of the grafting density on the aggregates compacity.

2 - Grafting density and nature of the grafted PA

The aim is now to study the impact of the grafting density and of the nature (hydrophilic or hydrophobic) of the grafted PA. To this purpose, the evolution of the scattered intensity (normalized by the NP volume fraction, as in the previous paragraph) is plotted at fixed NP volume fraction for one type of graft. This procedure is done first for C_8PA-modified NPs, then for DEPA-modified NPs.

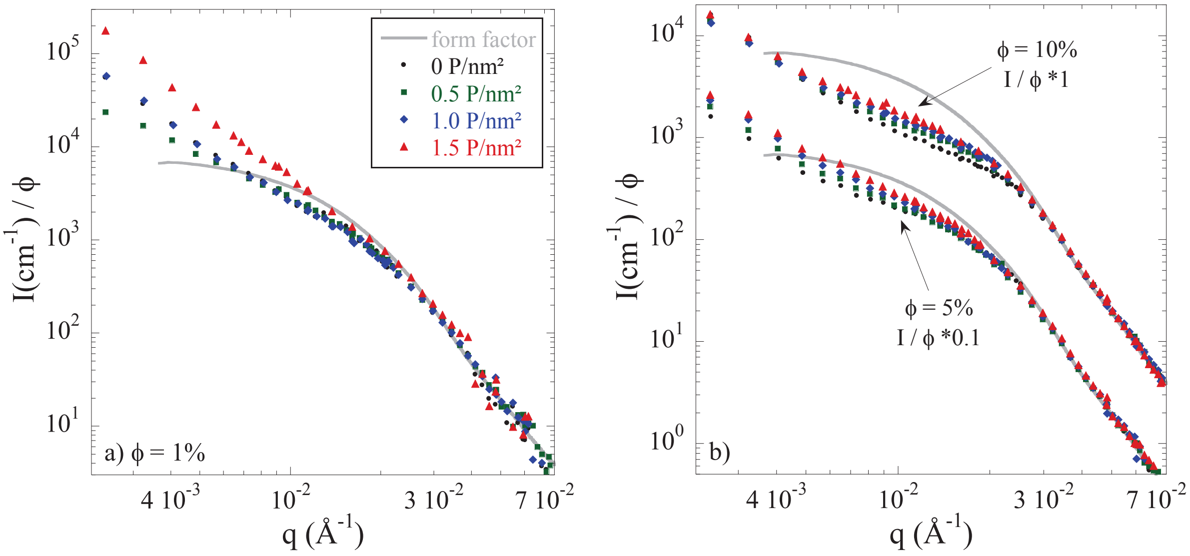

Figure 5.8: Scattered intensities of C_8PA-grafted L200S in PEA for volume fractions of NPs **a)** ϕ = 1%, **b)** ϕ = 5% (shifted vertically for clarity) and 10%.

Figure 5.8 shows the impact of the grafting density (ρ) of C_8PA on the organization of nanoparticles in the matrix at different volume fractions. As in the previous chapters, the grafting density is given by molecule of graft per nm² of nanoparticle surface (which corresponds also to the number of phosphorus atom per nm² of NP). Note that a grafted monolayer of phosphonic acid corresponds nominally to 4 P/nm². One can see in figure 5.8 that the structure of the C_8PA-grafted nanoparticles evolves with the grafting density: the correlation hole in the intermediate q-range is less prominent with an augmentation of the C_8PA-grafting density for all filler fractions. As commented above, in the diluted case (Φ = 1%), the increase of the low-q intensity in figure 5.8a can be interpreted as an increase of the aggregates' mass. For surface-modified NPs, increasing the C_8PA-grafting density leads to bigger aggregates, or to more compact aggregates.

Figure 5.9 presents the evolution of the scattered intensities of DEPA-grafted NPs in the polymer matrix, for different grafting densities and NP volume fractions.

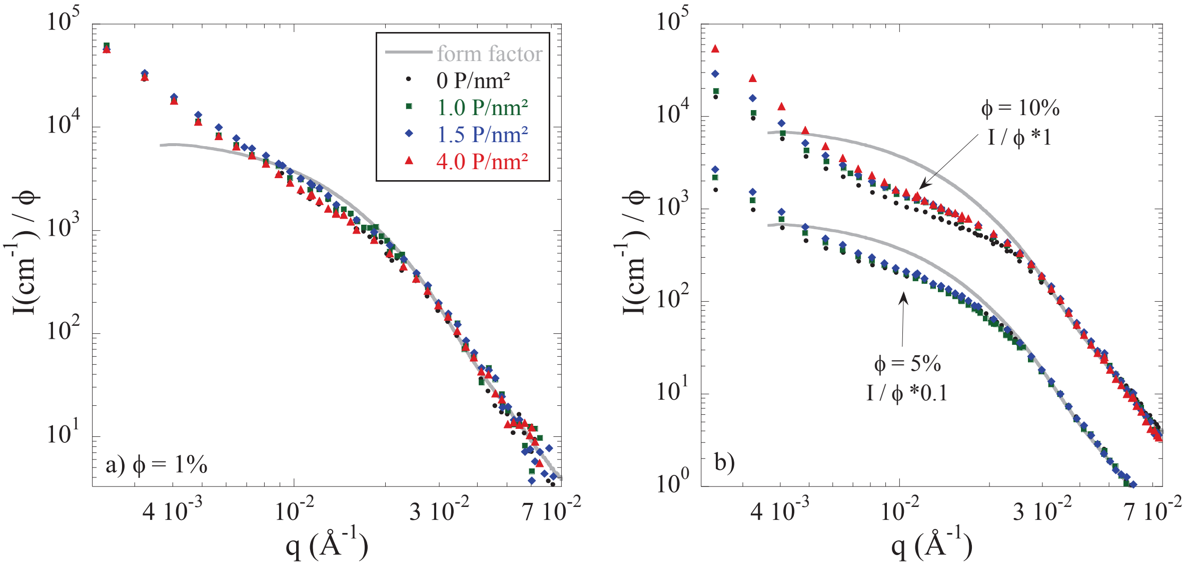

Figure 5.9: Scattered intensities of DEPA-grafted NPs in PEA for volume fractions of NPs **a)** ϕ = 1% and **b)** ϕ = 5% (shifted vertically for clarity) and 10%.

The first observation is that, in figure 5.9a at Φ = 1%, the low-q intensities are superimposed, whereas at higher NP volume fractions (5 and 10%) the scattered intensities are increasing with the grafting densities. For the diluted samples, one can conclude that the aggregates' mass is the same for all DEPA-grafting densities.

In the intermediate-q range, the correlation hole seems less pronounced for ϕ = 1 and 5% as compared to C_8PA-grafted NPs. At ϕ = 1%, the correlation hole slightly deepens with the grafting density, whereas it is the opposite for samples with ϕ = 10%. The change in NP structure with the grafting density is quite surprising, because it means that grafting a short hydrophilic graft on a hydrophilic NP allows modulating its aggregation state in a hydrophobic polymer matrix. Moreover, as studied in chapter III, the structure of DEPA modified NPs dispersed in water was exactly the same for grafting densities from 0 to 2 P/nm². As we are elaborating the NCs via an aqueous route, it means that these differences of structure may occur during the drying steps.

Using (eq.5.2) and the value of the structure factor, one can calculate the aggregates compacity κ. Figure 5.10 shows the evolution of κ with the grafting density for the different PAs at fixed filler fraction in the nanocomposites.

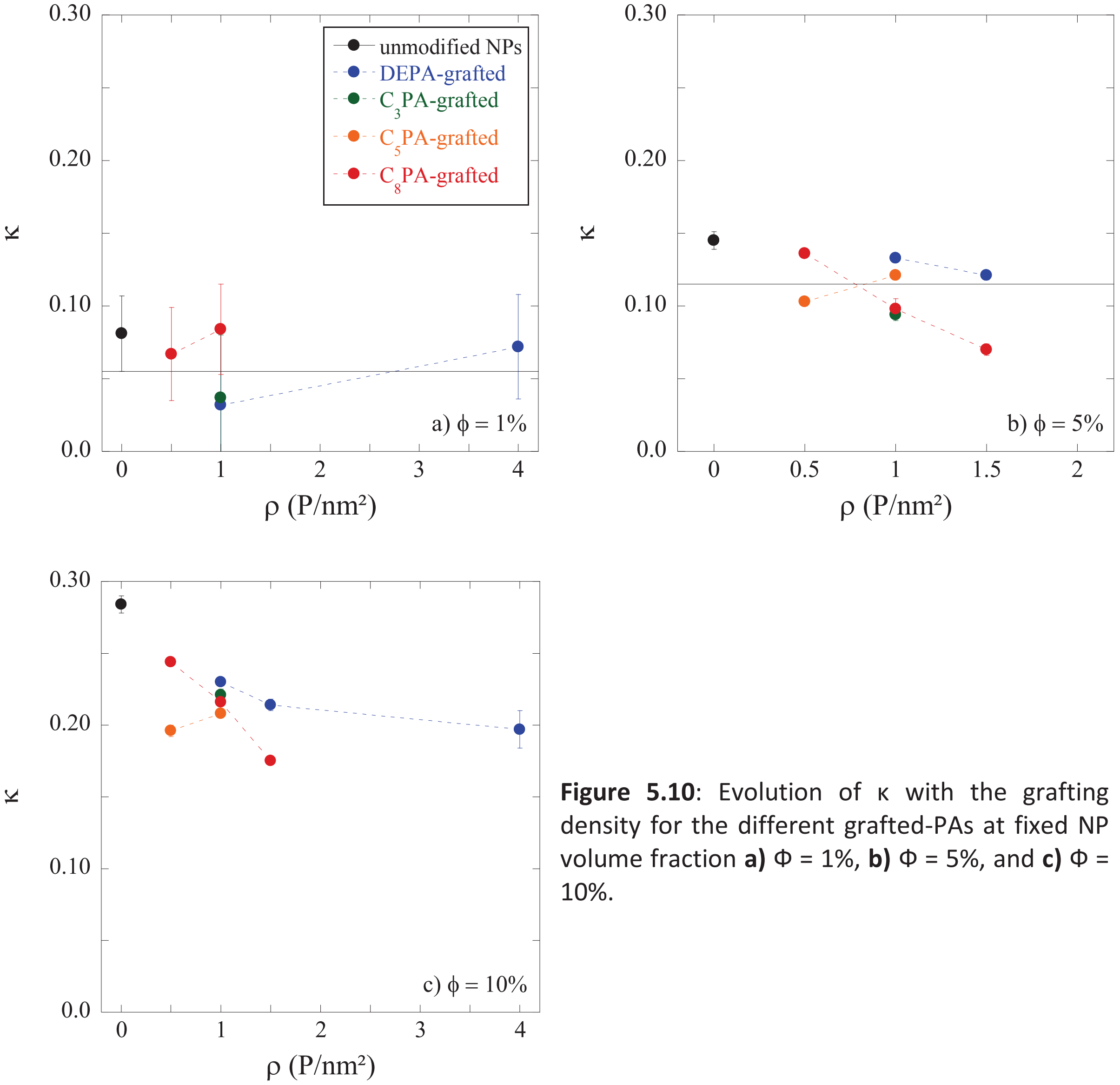

Figure 5.10: Evolution of κ with the grafting density for the different grafted-PAs at fixed NP volume fraction **a)** Φ = 1%, **b)** Φ = 5%, and **c)** Φ = 10%.

Figure 5.10 allows the comparison between C_8PA- and DEPA-grafted NPs (represented by red and blue dots, respectively). These two grafted molecules have the same length, only the nature of the chain is changing. The aggregates' compacity for the different samples varies between 0.05 and 0.3, i.e. the aggregates contains between 5 and 30% of NPs. In figure 5.10a, for Φ = 1%, one can see that κ varies randomly around 5 - 6%. For Φ = 5% (figure 5.10b), the same random variation is observed for all types of grafted PA, with κ ≈ 0.11 - 0.12.

At high filler fraction (figure 5.10c), the aggregates' compacity decreases with the increase of the grafting density for both grafts. This means that, in this case, increasing the number of grafts at the NP surface leads to sparser aggregates for C_8PA- and DEPA-grafted NPs, and grafted NPs are forming sparser aggregates in comparison with raw NPs. One can assume that this decrease of κ is due to the steric hindrances between NPs during drying and annealing of the nanocomposite. Moreover, at fixed grafting density, the κ values for the different grafts are close, i.e. the aggregate density does not depend on the nature of the PA at high NP volume fraction. Note that the same tendencies were observed using the structure factor obtained after subtraction of the low-q power law. The decrease of aggregates' compacity with the grafting density can be interpreted as a compatibilization of the

NPs with the polymer matrix at small length scales. The contact between polymer chains and nanoparticles is favoured, and nanoparticles are thus better dispersed to maximize contacts.

To conclude, at low filler fractions, the aggregates' density seems to vary in a random manner around 10% with the nature of the graft and grafting density, which probably means that it remains unchanged, within experimental error. However, at high NP volume fraction, the aggregates' compacity decreases with the grafting density in the same way for both type of grafted PAs. In both cases, increasing the grafting density leads to a small length scale compatibilization.

For diluted samples, we also concluded on an increase of the aggregates' mass in the case of C_8PA-grafted NPs, whereas DEPA-grafting has no impact on the aggregates' mass. As the compacity of aggregates is constant with the increase of grafting density, one can deduce that the aggregates' size increases with the increase of C_8PA-grafting density. One can note that the aggregates' mass follows the same evolution than in solution (cf. chapter III), i.e. it increases with the grafting density of C_8PA, and remains constant for small grafting densities ($\rho < 1.5$ P/nm²) of DEPA.

3 - Chain length of the grafted PA

The last objective is now to study the impact of the chain length of the grafted molecule on the NP structure in the NC. Accordingly, the evolution of the scattered intensity is given at fixed values of both NP volume fraction and grafting density for different chain lengths of grafted alkylphosphonic acids: C_3PA, C_5PA, and C_8PA.

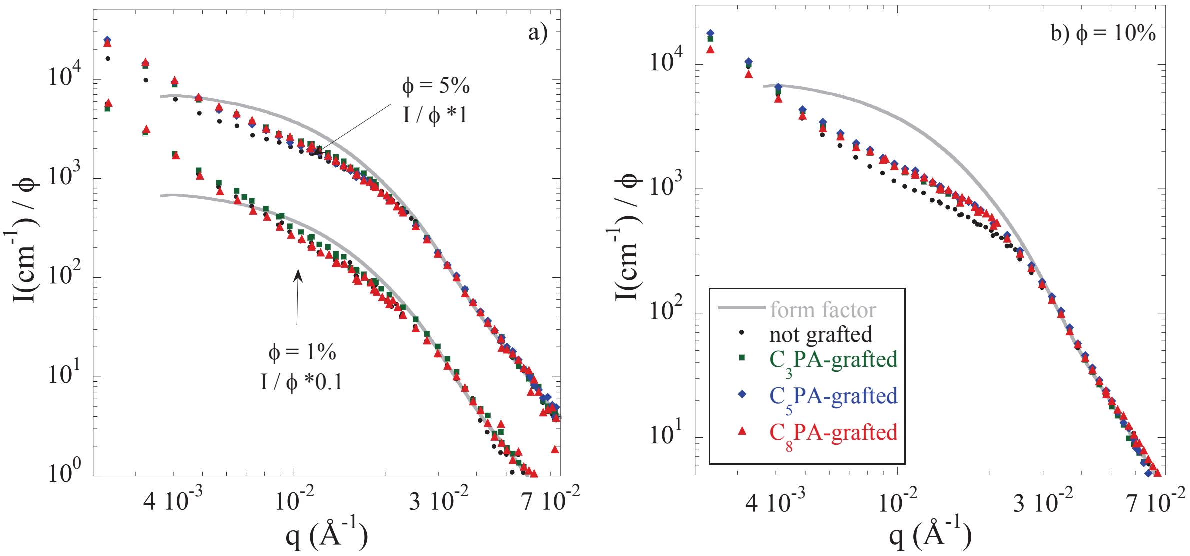

Figure 5.11: Evolution of the reduced scattered intensity with the chain length of grafted alkylphosphonic acid for NP volume fraction **a)** $\phi = 1\%$ (shifted vertically for clarity) and 5%, and **b)** $\phi = 10\%$. The grafting density is fixed, $\rho = 1.0$ P/nm².

Figure 5.11 demonstrates that the chain length of the phosphonic acid (at fixed grafting density) has only little impact on the aggregates' structure in the nanocomposite, however there is a difference between the structure of bare nanoparticles and NPs grafted with alkylphosphonic acids: aggregates seems denser for unmodified NPs, as it was observed in the case of DEPA-grafted NPs. This evolution supports again the hypothesis that grafting induces a compatibilization at small length scales between the nanoparticles and the polymer matrix. For diluted samples, the low-q scattered intensities are superimposed, i.e. the aggregates' mass is similar for C_3PA and C_8PA-grafted NPs.

We have seen in the previous section (figure 5.10) that the increase of grafting density leads at 10% filler fraction to a decrease of the κ values, i.e. to sparser aggregates. However, in the case of C_5PA-grafted NPs this decrease is not observed. The compacity values hardly vary for $\Phi = 5\%$ (from 10 to 12%) and $\Phi = 10\%$ (from 20 to 21%). One can consider such evolutions as negligible. Moreover, there is no impact of the chain length on the aggregates' compacity, as can be seen in figure 5.10 by comparing C_8PA, C_5PA, and C_3PA.

III - Conclusion

In this chapter, nanocomposites were successfully elaborated with the surface-modified nanoparticles studied in chapter III. The originality is the use of an aqueous route for the formulation of nanocomposites. This method of NP incorporation in a polymer matrix presents various advantages. First, it avoids the use of nanoparticles in the dried state, which is quite controversial, especially in terms of safety. Secondly, the colloidal dispersions are used directly after the grafting procedure: there is no need of additional drying or washing steps in the synthesis protocol. Moreover, the use of organic solvent is avoided. The final nanocomposite films seem to be homogeneous: no demixing is observed. However, the nanoparticles form big aggregates or networks of aggregates (size > 200 nm) as the scattered intensities measured by SANS do not reach a plateau at low-q values, for any sample, in the q-range measured here.

For diluted samples, the evolution of the scattered intensity in the low-q range with the grafting density allows to conclude on the mass of aggregate: the aggregates' mass increases with the C_8PA grafting density, whereas DEPA grafting density does not impact the aggregates' mass. The same evolution was observed in sols (see chapter III). One can conclude that aggregation occurred in the sols before filmification and not during the drying steps.

Besides, we followed the evolution of the compacity κ of the formed aggregates. To this purpose, we studied the structure factor evolution for a given q-values (q*), which we found representative of the intensity of the correlation hole, and deduced κ from a modified Percus-Yevick equation, in which we take into account the NP polydispersity. We concluded that the structure of the NPs is strongly impacted by the volume fraction of nanoparticles in the matrix. An increase of NP volume fraction in the polymer matrix leads to denser aggregates (up to 30%) for unmodified as well as for surface-modified NPs, no matter the type of grafted PA.

The study of nanocomposites containing low filler fractions, $\Phi = 1$ and 5%, shows that the aggregates' compacity seems to vary randomly around about 10% within the error bar. In the higher NP volume fraction case, $\Phi = 10\%$, we found that the aggregates' compacity decreases with the increase of the grafting density for C_8PA and DEPA. In other words, for the different grafts investigated, hydrophobic and hydrophilic, the surface modification of the NPs leads to sparser aggregates, with respect to unmodified NPs. One can explain this fact with the steric hindrance of grafted NPs compared with unmodified NPs. However, this result is quite surprising as the grafted PAs used in this study are small molecules (length of about 1 - 2 nm) and the grafting densities are low (in most cases, less than a half surface coverage = 2 P/nm²). A more probable explanation is the compatibilization at small length scale of the NPs with the matrix, even in the case of the more hydrophilic graft (DEPA).

To complete this study, higher grafting densities of alkylphosphonic acids (up to 4 P/nm²) should be elaborated. Moreover, as said previously, aggregation may occur during the drying and annealing steps, thus a research of optimal duration times and about their impact on the structure of NPs would be helpful. Additionally, we tried to make TEM images of the nanocomposites, however the low glass-transition temperature of the polymer matrix prevents obtaining slices of well-defined shape. It is thus not possible to conclude yet on the real shape of the aggregates in the matrix: formation of big aggregates, or aggregates building a network.

Chapter VI – Simultaneous phase transfer and surface modification of TiO_2 nanoparticles using alkylphosphonic acids

The main part of the results presented in this chapter were published in reference [2].

As said in the bibliographic part, the incorporation of oxide NPs in a polymer matrix can be difficult, because NPs are hydrophilic while the polymer matrix is, in the most cases, hydrophobic. One possibility to avoid demixing of NPs in the polymer is the use of organosoluble NPs, and the direct obtention of nanocomposite by mixing the polymer solubilized in organic solvent with these organosoluble NPs.

However, to disperse hydrophilic oxide NPs in an apolar organic solvent, it is necessary to modify their surface with organic molecules, in order to make the NPs hydrophobic and thus organodispersible, and to provide steric stabilization. Some remaining electrostatic charge can also contribute to repulsion in organic solvents, but without surface modification the originally hydrophilic NPs cannot be transferred into these solvents.

This surface modification can be difficult to perform in aqueous medium, and for oxide NPs the transfer from aqueous to organic phase is usually done by costly and time-consuming procedures, involving several steps such as precipitation, solvent exchange, surface modification, drying, washing, and redispersion steps.[188, 189] Moreover, precipitation or drying of the NPs may cause irreversible aggregation. In addition, growing safety concerns about NPs toxicity may strongly limit the possibility to work with dry NPs, as inhalation is in most cases the main source of exposure to NPs. A direct liquid-liquid phase transfer from an aqueous to a non-miscible organic phase would avoid working with dry NPs. Such phase transfers have been extensively used for noble metal (Au, Pt, Ag) NPs using amphiphilic ligands such as alkylthiols or alkylamines.[190] The transfer is based on the adsorption of surfactants onto the NP surface making the particle lipophilic. As the solubility of long-chain alkylthiols or alkylamines in water is poor, this adsorption likely takes place at the liquid-liquid interface.[191]

In the case of metal oxide NPs, there are very few examples in the literature of direct transfer from an aqueous phase to an organic phase. Meriguet et al. reported liquid–liquid phase transfer of dispersed γ-Fe_2O_3 NPs from an aqueous colloidal dispersion to a cyclohexane organic phase, using dimethyldidodecylammonium bromide.[192] More recently, Machunsky et al. described the transfer assisted by centrifugation of magnetite NPs from an aqueous to a dichloromethane phase using fatty acids and ammonia.[193, 194] Ramakrishna et al prepared TiO_2 NPs dispersible in non-aqueous solvents by transferring TiO_2 aqueous colloids to a toluene phase using sodium dodecylbenzenesulfonate (SDBS).[46] Zhao et al. also used SDBS and sodium dodecyl sulfate (SDS) to transfer TiO_2 NPs from an aqueous phase to a petroleum ether/silicone oil organic phase.[195]

In these examples, the transfer mostly results from ionic interactions with the surface, not from the formation of strong, covalent bonds. Among the different types of molecules classically used to modify metal oxide surfaces,[36] alkylphosphonic acids appear ideally suited for phase transfer of oxide particles, but we found no study on the use of PAs for liquid-liquid phase transfer from an aqueous to a non-miscible organic phase (although we have been using it in the lab for years).

Herein we investigate the transfer of aqueous sols of TiO_2 NPs to a non miscible organic phase using alkylphosphonic acids. In the first part we explore the influence of several parameters such as the amount of PA, concentration of the initial sol, and length of the alkyl chain on the transfer of TiO_2 sols. The efficiency of the transfer was assessed visually. In the second part, the PA-grafted TiO_2 particles obtained by phase transfer are characterized in the dry state using ^{31}P solid-state NMR. In the last part, finally, we study the formation of the grafted layer by SANS, and investigate the influence of the phase transfer on the agglomeration or aggregation of TiO_2 NPs using DLS and SANS.

I - Transfer and surface modification of nanoparticles

Under typical conditions, referred to as "standard" conditions in the following, the PA (0.17 mmol) was dissolved in 10 mL of $CHCl_3$ and the resulting solution was added drop wise to 10 mL of the LS101 colloidal solution diluted to 1 wt% with ultra-pure water (resulting pH < 2) in a 96 mL glass jar. The amount of PA used per gram of TiO_2 was thus 1.7 mmol/g. The resulting mixture was magnetically stirred for 24 h at 22°C. The rotation speed (ca 1000 rpm) was adjusted so as to avoid the formation of stable emulsions or foams. For the photographs given below, small amounts (ca 1 mL) of the organic and aqueous phases were successively transferred with a pipette into 5 mL hemolysis tubes.

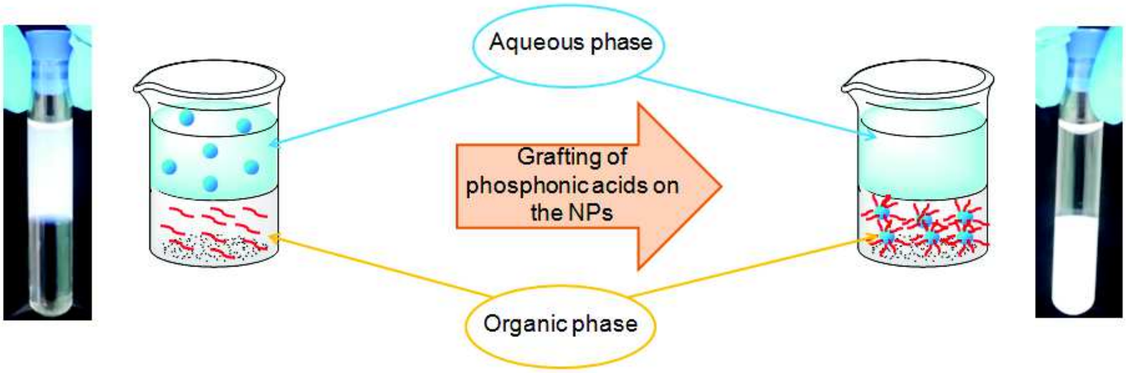

Figure 6.1: Principle of phase transfer and surface modification of nanoparticles.

Transfers in toluene (allowing to test the influence of an organic phase less dense than water) were conducted using the same procedure.

For transfers of more concentrated LS101 aqueous sols (5 and 23 wt% TiO_2), the experiments were performed using a smaller amount of concentrated aqueous sol and a higher amount of $C_{12}PA$, keeping the volume of $CHCl_3$ constant.

Note that TiO_2 NPs scatter light strongly. Therefore a virtually complete transfer can be identified by visual inspection and absence of signal in DLS measurements of the aqueous phase. Washing and drying of NPs after phase transfer was performed by separating both phases. The organic phase was first dried at 50°C under atmospheric pressure overnight. The obtained powder was then washed three times by adding absolute ethanol, centrifuging at 20 000 rpm during 10 minutes, and removing the supernatant. The wet cake was then dried at 50 °C under vacuum overnight.

The nanoparticles sols descriptions are given in “methods and materials” chapter.

II - Studied parameters

The phase transfer was initially optimized using the LS101 sol, at a concentration of 1 wt% (corresponding to a pH value of 1.8), using dodecylphosphonic acid ($C_{12}PA$) in $CHCl_3$. Several parameters were varied to test the limits of this method:

- amount of introduced phosphonic acid
- nature of phosphonic acid
- nanoparticles concentration in aqueous phase
- nature of organic solvent
- nature of the nanoparticles
- pH and salt concentration of the aqueous sol

In this part, we will only study if the NPs are fully transferred in the organic phase. The state of dispersion will be discussed in an other part.

1 - Amount of phosphonic acid

For the phase transfer to be successful, the NPs must become sufficiently hydrophobic, thus the amount of PA must be high enough to cover the surface of the NPs. The transfer was attempted with increasing amounts of $C_{12}PA$ per weight of TiO_2 NPs: 0.8, 1.7, 2.0, 2.4 and 3.4 mmol/g. As shown in figure 6.2, the transfer from the upper aqueous phase to the lower organic phase was partial for a 0.8 mmol/g amount. For a 1.7 mmol/g concentration (“standard” conditions for LS101) the transfer was complete, as evidenced by the perfectly transparent aqueous phase. In this case, if all the PA molecules were grafted, the nominal grafting density (calculated using the specific surface area calculated from the diameter derived from SAXS analysis, assuming spherical NPs) would be 3.2 P/nm^2, corresponding to a rather dense monolayer. Complete transfer was also observed for a 2.0 mmol/g concentration, but for higher concentrations the transfer efficiency decreased, as shown in figure 6.2 for the sample transferred with 2.4 mmol/g $C_{12}PA$. This lower efficiency is possibly due to the formation of a $C_{12}PA$ bilayer making part of the NPs hydrophilic.

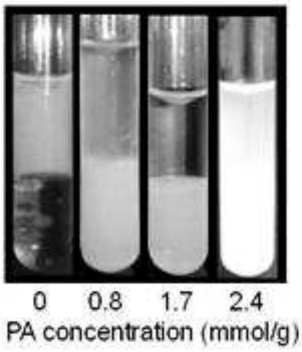

Figure 6.2: Photographs of locations of TiO_2 NPs in a water-chloroform dual-phase system as a function of the concentration of $C_{12}PA$ (LS101 sol diluted to 1 wt% in water).

According to these results, for LS101, we fixed the amount of introduced PA to 1.7 mmol/g in regard with NPs weight.

2 - Nature of the phosphonic acid

The influence of the nature of the PA was explored under "standard" conditions: LS101 sol diluted to 1 wt%, 1.7 mmol PA/g, $CHCl_3$. The PAs used were: tBuPA, PPA, C_5PA, C_8PA, and C_{18}PA (cf. figure 6.3). The transfer was complete for the alkylphosphonic acids with linear chains, C_5PA, C_8PA, and C_{18}PA (as previously found for C_{12}PA) but visual inspection of light scattered by the organic phase suggested different states of aggregation (see paragraph IV). On the other hand, the transfer with tBuPA and PPA was only partial.

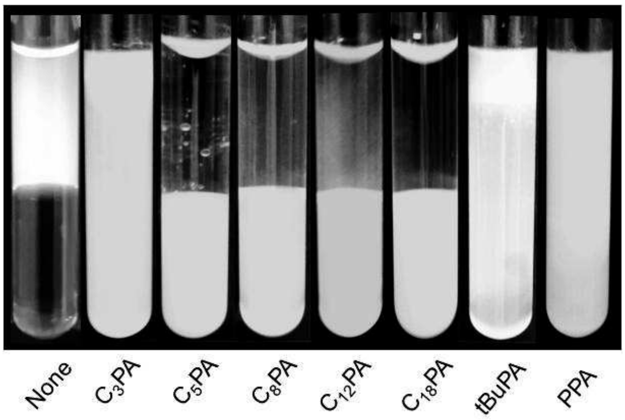

Figure 6.3: Photographs of LS101 sols transferred into $CHCl_3$ using various PAs (standard conditions).

3 - Nanoparticles concentration in the aqueous phase

Interestingly, this phase transfer protocol can be applied also to highly concentrated sols, up to 23 wt% (concentration of the commercial batch), provided that the specific concentration of C_{12}PA (in mmol C_{12}PA per g of solid TiO_2) is kept constant to 1.7 mmol/g. In all cases the phase transfer was complete, as shown in figure 6.4.

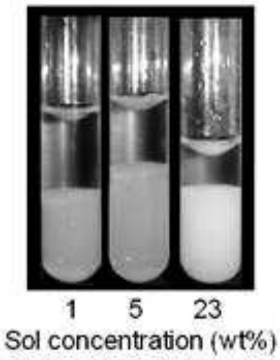

Figure 6.4: Photographs of locations of TiO_2 NPs in a water-chloroform dual-phase system as a function of the sol concentration (concentration of C_{12}PA: 1.7 mmol/g).

4 - Nature of the organic solvent

As a non-miscible organic phase we chose chloroform ($CHCl_3$), which is denser than water (chloroform density = 1.5 g/cm^3). Although the transfer also worked well using an upper organic phase, e.g. toluene (toluene density = 0.9), we found that a lower organic phase facilitated the separation of the organosol and water phase. Indeed, the dense TiO_2 NPs tend to sediment in the organic phase, especially at high concentration, and in the case of toluene they would deposit at the toluene-water interface. In addition, the low boiling point of $CHCl_3$ facilitates the drying of the NPs, and $CHCl_3$ was found to be the best solvent for the redispersion of the dry NPs (see paragraph V).

5 - Nature of the NPs

As said previously, we varied the transfer parameters for LS101 sol. In this part, we wanted to generalize the phase transfer for other NPs:

- PC: aqueous TiO_2 NPs sol
- TiO_2 P25: titania dry powder
- Al_2O_3 C: alumina dry powder

The commercial products are described in chapter II “methods and materials”.

We found that the PC TiO_2 aqueous sol could also be successfully transferred to $CHCl_3$ using for instance C_8PA, $C_{12}PA$, or $C_{18}PA$ under standard conditions, as specified in the first section. In this case, a higher PA concentration (2.3 mmol/g) was used, to take into account the increase in specific surface area of the smaller NPs and keep the nominal grafting density (calculated using the primary NP size determined by SAXS) to 3.2 P/nm^2. The photographs are given in figure 6.5 for $C_{12}PA$ and $C_{18}PA$.

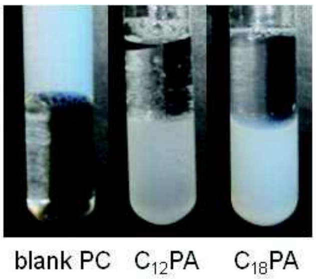

Figure 6.5: Phase transfer of PC TiO_2 sol using $C_{12}PA$ and $C_{18}PA$ under standard conditions (water-$CHCl_3$ system, PC sol diluted to 1 wt% in water, PA amount 2.3 mmol/g, stirring 24 hours at 22°C).

Phase transfer with $C_{12}PA$ was also attempted with aqueous suspensions of fumed metal oxide powders. TiO_2 P25 and Al_2O_3 C powders were redispersed as 1 wt% aqueous suspensions by sonication at pH 2 and 5, respectively. The $C_{12}PA$ concentration was decreased to 0.42 and 0.75 mmol/g, respectively, to take into account the larger diameter of the NPs in these oxide powders. In both cases, complete transfer to the $CHCl_3$ phase was observed (see figure 6.6), showing the generality of the method.

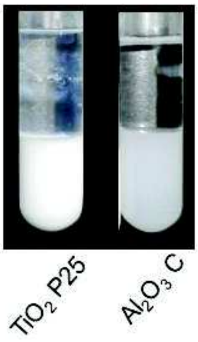

Figure 6.6: Phase transfer of TiO_2 P25 and Al_2O_3 C aqueous suspensions (1 wt%) with $C_{12}PA$. Conditions: water-$CHCl_3$ system, $C_{12}PA$ amount 0.42 mmol/g (TiO_2 P25) or 0.75 mmol/g (Al_2O_3 C), stirring 24 hours at 22°C.

To conclude, the phase transfer method can be generalized to other TiO_2 sols and to oxide dry powders, under standard conditions.

6 - Transfer of pre-aggregated nanoparticles

We have shown above that the aggregated nanoparticles in aqueous suspensions of TiO_2 P25 could be transferred to $CHCl_3$ using $C_{12}PA$. Under our conditions, the average hydrodynamic radius R_{DLS} of the particles in the aqueous sol was ≈ 155 nm, with a very high polydispersity, characteristic of aggregated NPs. After transfer, R_{DLS} of the particles in the $CHCl_3$ phase was ≈ 135 nm, showing that the transfer did not significantly modify the degree of aggregation of the NPs. This is not surprising as the TiO_2 P25 powder is manufactured by hydrolysis of $TiCl_4$ in an oxy-hydrogen flame, which leads to strongly aggregated primary NPs of about 25-30 nm.

As said previously, a common way of controlling the aggregation of NPs in aqueous solutions is to play on electrostatic repulsions between the particles. At pH 2 the zeta potential of the NPs in the LS101 aqueous sols is 50 ± 11 mV, and the stability of the sols results from the electrostatic repulsion between the positively charged TiO_2 NPs.

As said in the chapter I, there are two simple methods to provoke aggregation:

- by addition of salt, in order to screen the NPs charge, thus to reduce the electrostatic repulsions between them.
- by decreasing the positive charge of the NPs, which can be done in the present case by increasing the pH.

Accordingly we prepared two sets of LS101 aqueous sols at 1 wt%: i) sols adjusted at pH 2 but containing increasing amounts of NaCl (0, 3.7, 4.6, and 5.7 wt% relative to the total weight of the aqueous solution), and ii) sols without added salt but with pH values adjusted to 2, 4 and 5. R_{DLS} of the aggregates in these sols was measured, then the transfer in a $CHCl_3$ phase was done using $C_{12}PA$ under standard conditions, and the R_{DLS} in the resulting organic sol measured.

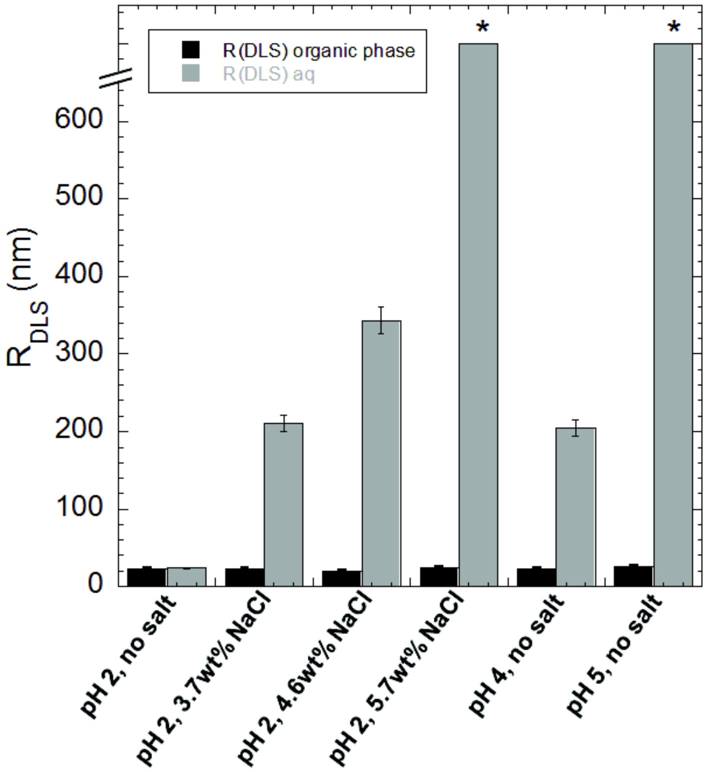

Figure 6.7: Size dependence of TiO_2 NP aggregates in aqueous suspension before transfer and in $CHCl_3$ after transfer, for different salinity and pH values. *: R_{DLS} value greater than 1000 nm.

The R_{DLS} values for the different aqueous and organic sols with LS101 are reported in figure 6.7. As expected, the size of the aggregates in the aqueous phase increases rapidly with the amount of added salt or with the pH. However, after transfer, the R_{DLS} values measured in the organic phase were similar to the value found for TiO_2 NPs transferred at pH 2 in the absence of salt (23 nm), which shows that the aggregation (or more exactly the agglomeration) induced by the reduction of electrostatic repulsions is completely reversible during the transfer.

This surprising result may be explained by the grafting by dodecylphosphonate units leading to a gradual increase of steric repulsion, apparently high enough to break the agglomerates, as proposed by Machunsky et al. who reported the de-agglomeration of magnetite NPs during their phase transfer using fatty acids and ammonia (see illustration in figure 6.8).[193, 194]

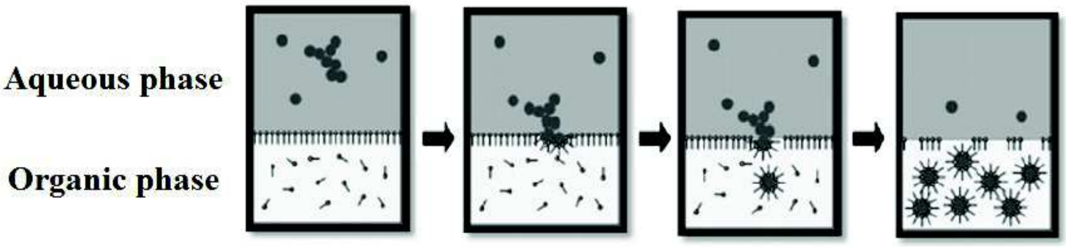

Figure 6.8: Mechanism of phase transfer according to Machunsky et al. Figure adapted from [194].

7 - Conclusion on phase transfer parameters

To sum up, the phase transfer is possible for different oxide NPs sols and powders, with a non-water miscible organic solvent in the upper or lower phase. The NPs concentration in the aqueous sol does not impact on the transfer. The transfer is successful for alkylphosphonic acids with 5 to 18 carbons, maybe more, and is only partial for the other tested PAs (C_3PA, tBuPA, and PPA). The optimal quantity of phosphonic acid is about 3.2 P/nm², and an excess of PA only leads to a partial transfer.

It is important to note that playing on the electrostatic repulsions in the aqueous phase is not enough to control the final aggregation in the organic phase.

III - Characterization of the obtained NPs

In this part, the grafted NPs (for full transfers) are characterized by FTIR, and ^{31}P solid-state MAS-NMR.

1 - FTIR

The FTIR spectra of raw and alkylphosphonic acids grafted NPs are reported in figure 6.9. The spectra of surface modified NPs are showing the vibrations associated to the C-H bonds stretching. The peak at 2956 cm^{-1} is associated to the C-H asymmetric stretching from -CH_3. The asymmetric CH_2 stretching at 2923 cm^{-1} for C_8PA grafted NPs is shifted to 2918 cm^{-1} for C_{18}PA grafted NPs. As in the case of surface modification of alumina-covered silica (in chapter III), these values suggest that the monolayers are rather disordered, with an increase of order with the chain length of the PA. The same trend, but with a smaller shift from 2852 to 2849 cm^{-1}, is observed for the symmetric CH_2 stretching vibrations. The broad vibration in the 3600-2800 cm^{-1} range is due to the O-H stretching in residual surface hydroxyl groups (Ti-OH) and to adsorbed water molecules.

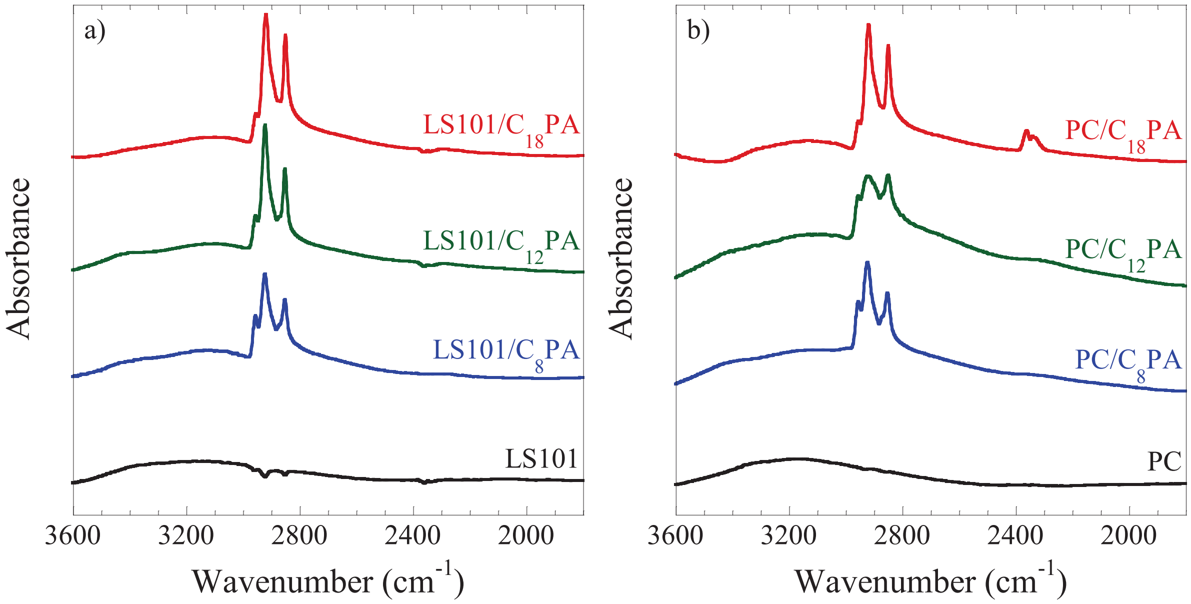

Figure 6.9: FTIR spectra in the 3600-1600 cm^{-1} range of raw NPs and NPs grafted with C_8PA, C_{12}PA, and C_{18}PA for **a)** LS101 and **b)** PC. Spectra are shifted vertically for clarity.

From these spectra, according to the C-H stretching vibrations, it may be concluded that phosphonate species are present with the NPs in the obtained powders. As the NPs were washed prior to analyses, one can supposed that the PAs are grafted onto the surface of the NPs. However, as in the case of alumina-coated silica NPs in chapter III, FTIR analysis does not allow ruling out the dissolution-precipitation of the phosphonate species with the metal oxide. Accordingly, we made ^{31}P solid-state MAS-NMR measurements.

2 - ^{31}P solid-state MAS-NMR

Two series of surface modified NPs in the organosols were characterized in the dry state using ^{31}P solid-state MAS-NMR: variation of the nature of the NPs and chain length of alkylphosphonic acid. The NPs were dried simply by evaporating the $CHCl_3$ at 50°C under atmospheric pressure overnight. As said in chapter III, ^{31}P MAS-NMR is a simple and useful method for the study of PA-grafted particles, which permits to distinguish between chemisorbed (grafted), physisorbed, and bulk titanium phosphonate species.[59, 63] However, this method gives no precise information on the binding modes of chemisorbed phosphonate species, contrary to ^{17}O MAS-NMR.[65]

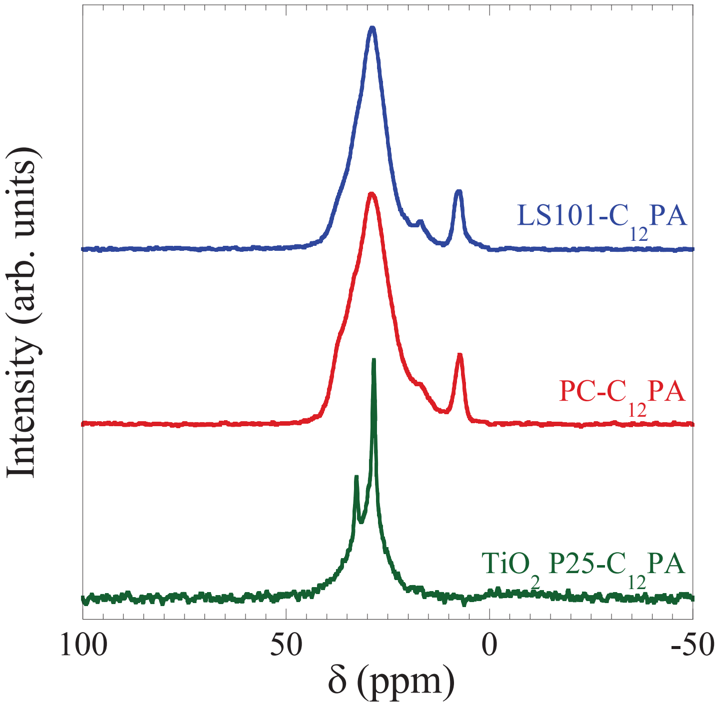

Figure 6.10: ^{31}P NMR spectra of dried LS101-C_{12}PA, PC-C_{12}PA, and TiO_2 P25-C_{12}PA organosols.

The ^{31}P MAS-NMR spectra of LS101-C_{12}PA and PC-C_{12}PA shown in figure 6.10 are quite similar. The main signals between 20 and 40 ppm are ascribed to grafted phosphonate species, linked to the surface by Ti-O-P bonds. These signals are close in terms of chemical shift and width to those found for a TiO_2-anatase high surface area support grafted by C_{12}PA in toluene.[65] The absence of a sharp resonance at ≈ 32 ppm corresponding to excess C_{12}PA suggests that all the C_{12}PA molecules introduced reacted with the NPs during the transfer. On the other hand, the resonances at about 7 ppm and 17 ppm suggest the presence of about 7-8% of a poorly crystallized titanium phosphonate phase, α-$Ti(C_{12}H_{25}PO_3)_2$.[65, 196] The formation of titanium phosphonate phases by a dissolution-precipitation mechanism has been reported previously, but under conditions of temperature and concentration harsher than the conditions used here for the phase transfer.[62] Hence, the formation of this phase suggests a higher reactivity of the NPs in the sols, likely related to their smaller size and lower degree of crystallinity.

The spectrum of the transferred TiO_2 P25 powder in figure 6.10 is similar to that reported for TiO_2 P25 grafted by C_{18}PA.[63] The signal at 29 ppm is significantly sharper than in the case of LS101 and PC sols. Usually, sharp peaks denote either a high mobility or a well-defined conformation and environment of the sites, as for instance in crystalline samples. In the present case, the P sites are linked to the TiO_2 NPs surface through Ti-O-P bonds. ^{31}P chemical shift is highly sensitive to P-O bond length and O-P-O bond angle. The sharpness of the peak suggests the presence of P sites with well-defined bond lengths and angles, likely owing to the more homogeneous and flatter surface of TiO_2 P25 particles compared to the smaller and less-crystalline LS101 and PC NPs.

The sharp signal at 33 ppm indicates the presence of a small amount of unreacted $C_{12}PA$ (approx. 5%). Finally, the absence of a signal at 7 ppm points the absence of a titanium phosphonate phase, consistent with the good chemical stability of this fumed TiO_2 sample.

The figure 6.11 represents the ^{31}P MAS-NMR spectra of raw LS101 NPs and grafted LS101 with C_5PA, $C_{12}PA$ (transfer with NPs concentration in aqueous phase at 1 and 25 wt%), and $C_{18}PA$. Note that the C_5PA-, $C_{12}PA$-(1%), and $C_{18}PA$-grafted NPs were washed with ethanol previous the measurements, contrary to the other samples. The same tendencies then for the first set of samples are observed. The broad peak between 20 and 40 ppm is representative from grafted phosphonate species. However, the peaks at 7 and 17 ppm for $C_{12}PA$ and $C_{18}PA$ highlight the presence of a crystallized titanium phosphonate phase. It is interesting to note that both spectra of LS101/$C_{12}PA$ have the same shape, only the peak at 7 ppm has increased: the NPs concentration of the aqueous phase only impacts the rate of dissolution-precipitation reaction between the PA and the metal oxide.

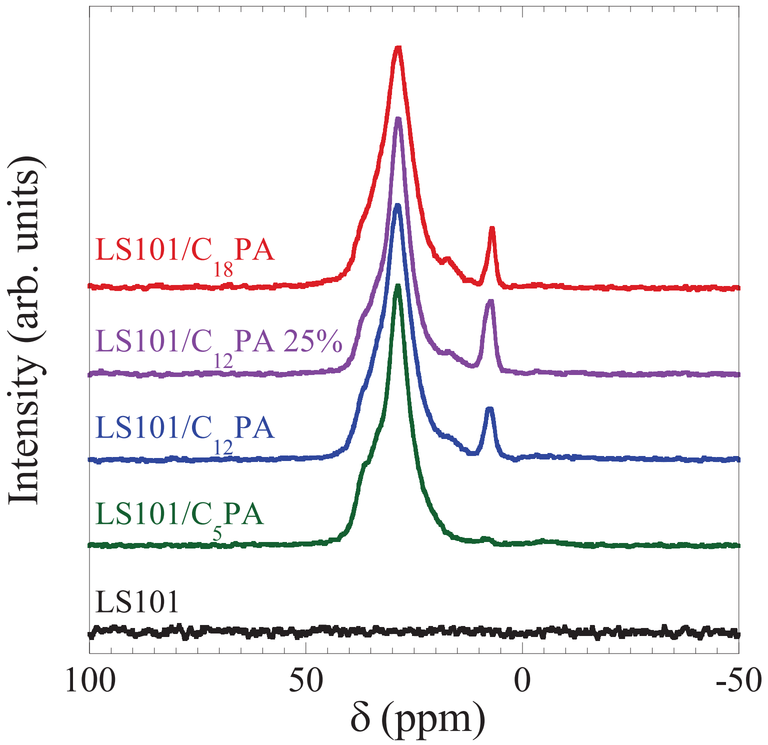

Figure 6.11: ^{31}P NMR spectra of dried LS101 unmodified, modified with C_5PA, $C_{12}PA$, $C_{12}PA$ in concentrated sol at 25 wt% in NPs, and with $C_{18}PA$.

To conclude, we have successfully modified the surface of the TiO_2 and Al_2O_3 NPs with PAs. All the PAs have been involved in the reactions, because there are no adsorbed molecules. However, we can note the presence of a minor crystallized phase for a large part of the samples.

IV - Dispersion in solution

1 - Dynamic light scattering study of nanoparticles dispersion

In paragraph II, we have investigated the conditions leading to a visually successful phase transfer. The dispersion of the grafted NPs in the different organosols obtained after complete phase transfer was quantified using DLS. The apparent hydrodynamic radii and polydispersities found for the different organosols are shown in table 6.1, and compared to the values found for the diluted aqueous sols.

Table 6.1: R_{DLS} and σ values obtained by DLS for the starting aqueous sols (samples 1 and 2) and for the PA-transferred organosols, under standard conditions (transfer from 1 wt% aqueous sols, using 1.7 mmol/g PA for LS101, resp. 2.3 mmol/g for PC sols, DLS performed at room temperature), unless otherwise stated. Standard deviations on R_{DLS} values have been determined from different transfer reactions.

Sample	Sol (concentration if not 1 wt %)	PA	R_{DLS} (nm)	σ
1	LS101 aqueous sol	-	24±3	0.5
2	PC aqueous sol	-	10±1	0.6
3	LS101	$C_{12}PA$	21±2	0.5
4	LS101 (5 wt%)	$C_{12}PA$	33±3	0.5
5	LS101 (23 wt%)	$C_{12}PA$	39±4	0.5
6	LS101	C_5PA	≈ 100±20	0.5
7	LS101	C_8PA	18±1	0.7
8	LS101 20°C (initial)	$C_{18}PA$	48±8	0.5
	40°C (heating)		19±2	0.6
	12°C (cooling)		46±10	0.4
9	PC	$C_{12}PA$	12±1	0.6
10	PC	$C_{18}PA$	52±19	0.7

For the LS101 sol transferred under standard conditions (1 wt% aqueous sol) with $C_{12}PA$ (sample 3 in table 6.1), R_{DLS} in the organosol (21 nm) is similar to that found in the starting aqueous sol (24 nm), indicating that transfer occurred under these conditions without any significant aggregation or de-aggregation. When the transfer was done starting from more concentrated aqueous sols (samples 4 and 5), R_{DLS} increased by a factor of less than two, suggesting minor aggregation in the final organosols. Next, the size of the aggregates strongly depends on the nature of the PA used for the transfer. The largest aggregates are observed for the smallest molecule (C_5PA, sample 6), which may be related to the short pentyl chain unable to provide sufficient steric repulsion to stabilize the NPs, although the transfer was complete. The hydrodynamic radii found for the sols transferred with C_8PA (sample 5) and $C_{12}PA$ (sample 3) were similar. The R_{DLS} values observed in the sols transferred with $C_{18}PA$ (sample 8) were higher, indicating that some aggregation occured during the transfer. However, when the DLS was performed at 40°C, R_{DLS} decreased to the value of the bare NPs, and increased again to its original value after cooling down the solution below room temperature (12 °C).

We also investigated this thermoreversible aggregation at higher resolution by SANS and the results are discussed in next paragraph.

For comparison, DLS measurements have also been performed with the TiO_2 sol from Plasmachem (PC). An analogous behavior was observed: R_{DLS} for the PC sol transferred with $C_{12}PA$ (sample 9) was close to R_{DLS} in the starting sol (sample 2), whereas the transfer by $C_{18}PA$ led to grafted NPs aggregated in chloroform (sample 10).

We have shown in paragraph II that the aggregated nanoparticles in aqueous suspensions of TiO_2 P25 could be transferred to $CHCl_3$ using $C_{12}PA$. Under our conditions, the average hydrodynamic radius of the clusters in the aqueous sol was ≈ 155 nm, with a very high polydispersity, characteristic of aggregated NPs. After transfer, R_{DLS} of the particles in the $CHCl_3$ phase was ≈ 135 nm, showing that the transfer did not significantly modify the degree of aggregation of the NPs. This is consistent with the fact that the TiO_2 P25 powder is manufactured by hydrolysis of $TiCl_4$ in an oxy-hydrogen flame, which leads to aggregates of strongly bonded primary NPs of about 25 – 30 nm in size. Similar results were obtained for the transfer of Al_2O_3 C: the R_{DLS} of the particles in the aqueous and organic phases were close, ≈ 140 nm and ≈ 135 nm, respectively.

2 - SANS study of the dispersion of nanoparticles in organosols

The structure of organosols obtained from both LS101 and PC sols after transfer under standard conditions with C_8PA, $C_{12}PA$, and $C_{18}PA$, respectively, has been studied by SANS in both protonated and deuterated chloroform, $CHCl_3$ and $CDCl_3$. The difference in scattering length densities between $CHCl_3$ and $CDCl_3$ is not very high, but it allows highlighting the grafted (hydrogenated) phosphonate monolayer with two independent experiments, and thereby checking quantitative intensity models. The bare NPs in water have been investigated by SAXS and the result has been presented in the chapter II: LS101 NPs are made up of small NPs which build up a cluster of approximate dimension of ca. 64 nm, and a fractal dimension describing the internal structure of ca. 1.8. In figure 6.12, the SANS intensities measured in $CDCl_3$ and corresponding to LS101 TiO_2-sols transferred with C_8PA, $C_{12}PA$, and $C_{18}PA$, respectively, are shown.

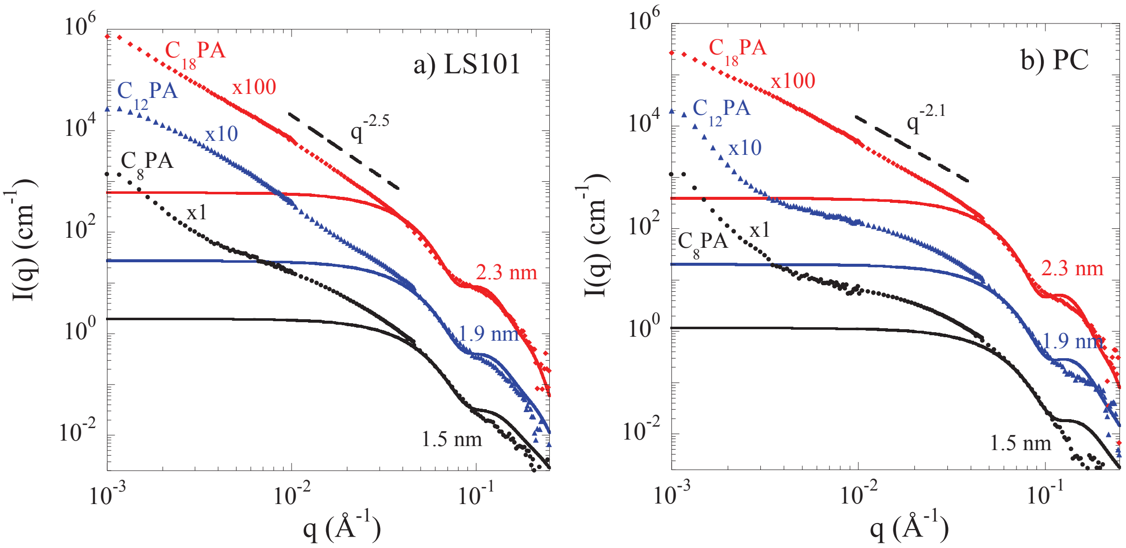

Figure 6.12: Structure analysis with SANS of TiO_2-NP sols transferred with C_8PA (resp. $C_{12}PA$ and $C_{18}PA$) into $CDCl_3$ **a)** LS101 and **b)** PC (TiO_2 volume fraction about 0.4 vol%). The theoretical scattering curves (solid lines) correspond to core-shell fits as explained in the text.

Given the scattering length densities of the different components (cf. chapter 2), these intensities reflect to a large extent the structure of the PA-layer on the nanoparticles, which are a factor of 75 more visible (in $\Delta\rho^2$) than the NP itself (the core) under these contrast conditions. Unlike the bare NPs, there is no low-q Guinier regime indicative of a finite size in figure 6.12. The NPs thus aggregate on scales larger than what can be measured in this scattering experiment, with a self-similar structure described by a fractal law as the internal structure of the clusters. For the C_8PA-sample, the upturn at low q indicates that these particles aggregate in rather dense clusters, whereas the high-q oscillation is reminiscent of the PA-shell around the NPs. In the other two cases, LS101 modified with C_{12}PA or C_{18}PA, the intensities show a high-q oscillation which is better defined, and a stronger fractal power law in the intermediate regime, reaching $q^{-2.5}$ for the C_{18}PA-sample. This power law extends well below 0.005 $Å^{-1}$, i.e., it characterizes objects which are bigger than the original 64 nm clusters (see chapter II), and thus also indicates aggregation. While the exponent for the clusters in the aqueous sol (1.8) is in the typical range of diffusion limited aggregation[197], the values found here for the organosols (up to 2.5) have been reported for thermoreversible aggregation of silica NPs modified by octadecyl chains.[198-202] As higher exponents correspond to denser fractals, this high value suggests that aggregates are reassembled in a denser manner during the transfer. A more plausible explanation is that the fractal aggregates of the PA-coated NPs appear to be denser than those of the un-modified NPs due to the partial filling of the voids between primary particles by the organic layer.

As said previously, all SANS measurements have been performed in deuterated and hydrogenated solvent. Figure 6.13 represents the measurements in $CHCl_3$. Although the scattering length density of the solvent changes only slightly, it becomes smaller than the one of the NP core, and thus approaches the one of the grafted corona. This results in a weakening of the corona signal with respect to the core, and fitting all data sets simultaneously as done here gives a convincing cross-check of our analysis. The same conclusions about fractal dimensions and aggregation can be drawn from the complementary measurement in H-chloroform then in D-chloroform.

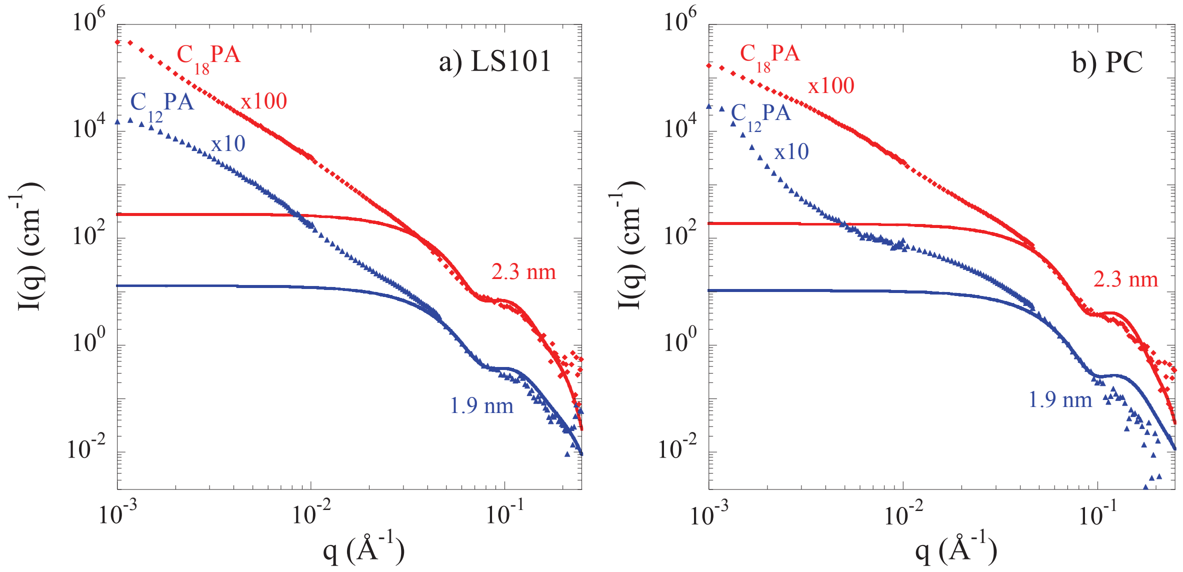

Figure 6.13: Structure analysis by SANS of TiO_2-NP sols transferred with C_{12}PA (resp. C_{18}PA) into $CHCl_3$: **a)** LS101 and **b)** PC sols (TiO_2 volume fraction about 0.4 vol%). The theoretical scattering curves (solid lines) correspond to core-shell fits as explained in the text.

It is noteworthy that no such large scale aggregation was observed by DLS (see table 6.1). This may be ascribed to the higher concentration of the solutions used for SANS experiments, and to the limited stability of the organosols: DLS was performed on fresh and highly diluted samples, whereas SANS measurements were necessarily done on more concentrated samples (≈ 0.4 vol%) aged 3 – 4 days. The aggregation in chloroform is probably due to the moderate quality of the solvent (as shown by the thermoreversible aggregation observed for the sols transferred with C_{18}PA, see next paragraph), and the decrease of electrostatic repulsions due to OH-consumption through grafting and to the low dielectric constant of the solvent (ε = 4.81), implying low dissociation of TiOH groups.

We now turn to a quantitative description of the prominent shoulder observed around $q \approx 0.1$ Å^{-1} in figure 6.12. The form factor oscillation can be described with the scattering law of a homogeneous spherical shell surrounding the polydisperse primary NPs. The bare NPs are analyzed with either Guinier laws describing only the small-angle scattering, or with an expression for polydisperse spheres following a log-normal distribution. The Guinier law reads:

$$I(q) = I_0 \exp\left(-\frac{q^2 R_G^2}{5}\right) \quad \text{(eq6.1)}$$

where the prefactor 1/5th in the exponent is used in order to deduce directly the equivalent sphere radius. For monodisperse core-shell particles, the following expression can be used:

$$I(q) = \frac{N}{V}\left[(\rho_c - \rho_s)F(R,q) + (\rho_{shell} - \rho_s)(F(R+d,q) - F(R,q))\right]^2 \quad \text{(eq6.2)}$$

where N/V is the NP number density, and ρ_c, ρ_s, and ρ_{shell} are the scattering length densities of the core, the solvent, and the shell, respectively. F(R, q) denotes the amplitude of the scattering function of a sphere of radius R, and d is the shell thickness. As (eq6.2) gives the contribution of a population of core radius R, its generalization to polydisperse cores is straightforward.

All scattering length densities were fixed based on the values given in the methods and materials chapter. For the core made of the primary nanoparticles, the same log-normal size distribution as for the bare NPs was used, plus in addition an adjustable monodisperse thickness of a homogeneous grafted layer stemming from the grafting of phosphonic acids. The maximum contrast of the layer is fixed to the one of the phosphonic acids, with a prefactor accounting for solvation, i.e. a reduced layer density. If we define ϕ as the volume fraction of PA in the shell, the remaining fraction (1 – ϕ) being occupied by the solvent of scattering length density ρ_s (i.e., either ρ_H or ρ_D), then the average scattering length density of the shell reads:

$$\rho_{shell} = \rho_s + \varphi(\rho_{grafts} - \rho_s) \quad \text{(eq6.3)}$$

and obviously the shell contrast reduces to $\rho_{shell} = \phi(\rho_{grafts} - \rho_s)$.

Table 6.2 sums up the fit parameters used for modeling the data.

Table 6.2: Fit parameters of core-shell modeling of SANS data: nanoparticles volume fraction, number of NPs per unit volume (N/V), PA volume fraction in the shell (ϕ), and shell thickness (d).

			C8	**C12**	**C18**
LS101	CDCl$_3$	NP volume fraction (%)	0.466	0.388	0.428
		N/V (cm^{-3})	$5.368\ 10^{16}$	$4.469\ 10^{16}$	$4.930\ 10^{16}$
		PA volume fraction ϕ	0.78	0.70	0.73
		Thickness d (nm)	1.5	1.9	2.3
	CHCl$_3$	NP volume fraction (%)		0.407	0.434
		N/V (cm^{-3})		$4.688\ 10^{16}$	$5.000\ 10^{16}$
		PA volume fraction ϕ		0.73	0.73
		Thickness d (nm)		1.9	2.3
PC	CDCl$_3$	NP volume fraction (%)	0.325	0.310	0.331
		N/V (cm^{-3})	$8.873\ 10^{16}$	$8.464\ 10^{16}$	$9.037\ 10^{16}$
		PA volume fraction ϕ	0.75	0.68	0.65
		Thickness d (nm)	1.5	1.9	2.3
	CHCl$_3$	NP volume fraction (%)		0.381	0.334
		N/V (cm^{-3})		$1.040\ 10^{17}$	$9.119\ 10^{16}$
		PA volume fraction ϕ		0.66	0.64
		thickness d (nm)		1.9	2.3

Concerning the four parameters given for each fit in table 6.2, the first two are derived from the particle concentration determined by weighting. The PA volume fraction is proportional to the particle concentration and the signal height, and a typical error of 15% is commonly admitted for the latter, superior to any error introduced by weighting. Finally, the thickness is related to the position in q-space, with a typical error bar of ca. 2%.

Several conclusions can be drawn from the quantitative analysis of the data in figure 6.12 using this core-shell model. First, it is possible to describe the grafted NPs as assemblies of bare primary particles (R_0 = 2.4 nm, σ = 30%) surrounded by the grafted shells, with remarkable agreement around the form factor oscillation, particularly for the longer PAs. Secondly, the comparison of experiments carried out under different contrast conditions (figure 6.12a and figure 6.13a) shows that both contrasts yield identical results, giving additional credit to the analysis in terms of the core-shell model. Thirdly, the variation of the shell thickness with the number of C atoms of the PA is plausible, longer alkyl chains giving rise to thicker shells as indicated in the legend: the thickness increases from 1.5 nm for C_8PA to 1.9 nm for C_{12}PA, and 2.3 nm for C_{18}PA. These values can also be compared to the calculation of the extended length of the pure PA molecules obtained with Chem3D Pro 14.0, which gives 1.1 nm, 1.6 nm, and 2.4 nm, respectively for C_8PA, C_{12}PA, and C_{18}PA.

Finally, by adjusting the absolute intensity prefactor in the fits in figure 6.12 a, one can estimate the volume fraction of grafted phosphonic acids in the shell, or equivalently the degree of solvation of the shell. From the fit parameters and the intensity of the signal given in figure 6.13a, the PA fraction in the shell was found to be about 75% (Φ = 78%, 70%, and 73% for C_8PA, C_{12}PA, and C_{18}PA shells, respectively). Similar values are found for H-chloroform for C_{12}PA and C_{18}PA shells (see table 6.2). Incidentally, the average total volume of PA calculated from the shell volume and ϕ is found to increase with the molecular mass of the PA, which is to be expected given that the quantity of phosphonic acid has been defined by the number of grafted molecules per nm^2.

For comparison, one can also estimate the PA fraction in the shell from the shell thickness d and the known quantities of NPs and grafts. In this way, the PA fraction is found to be only 40%, which remains reasonable given experimental errors. In any case, these estimations show that the PA shell is solvated.

The same core-shell analysis was performed with the grafted PC nanoparticles, and the resulting intensities are shown in figure 6.12b (figure 6.13b for intensities and models in H-chloroform). First, the fractal dimensions (up to 2.1 for C_{18}PA) are also higher than for the pure NPs (1.7, cf. chapter II), with the fractal domain extending to small q which indicates aggregate formation and densification. For the PC-C_{12}PA and C_8PA-samples, the shape of the scattering function exhibit the same low-q upturn as observed for LS101-C_8PA in figure 6.12a. Secondly, the core-shell thicknesses found with LS101 lead to convincing fits of the PC data (see figure 6.12b), and are thus independent of the nanoparticle (figure 6.12a VS 6.12b) as well as the deuteration of the solvent (see table 6.2). The error on the thickness is reasonably small (typically 0.1 nm), and only in the case of grafting of the smallest molecule (C_8PA) is the core-shell description less accurate. Also, the overall intensity prefactors are very close for all fits including H- and D-chloroform, giving the same PA-volume fraction ϕ in the shell (65% to 75%), and thus a solvation of ≈ 30%. Again, this agreement underlines the coherence of our approach.

3 - SANS study of the temperature-dependant nanoparticle dispersion in organosols

By visual inspection the dispersion state of the TiO_2 NPs grafted with C_{18}PA was found to depend reversibly on temperature. Indeed, the samples become less turbid upon heating, and turbidity increases again after cooling down to room temperature. For a more quantitative measurement, the dispersion and microstructure of TiO_2 NPs grafted with C_{18}PA has been investigated by SANS at 20 °C (initial state), then at 40 °C, and again at 20 °C. In figure 6.14 a, the results for a LS101-C_{18}PA sol in $CDCl_3$ are shown.

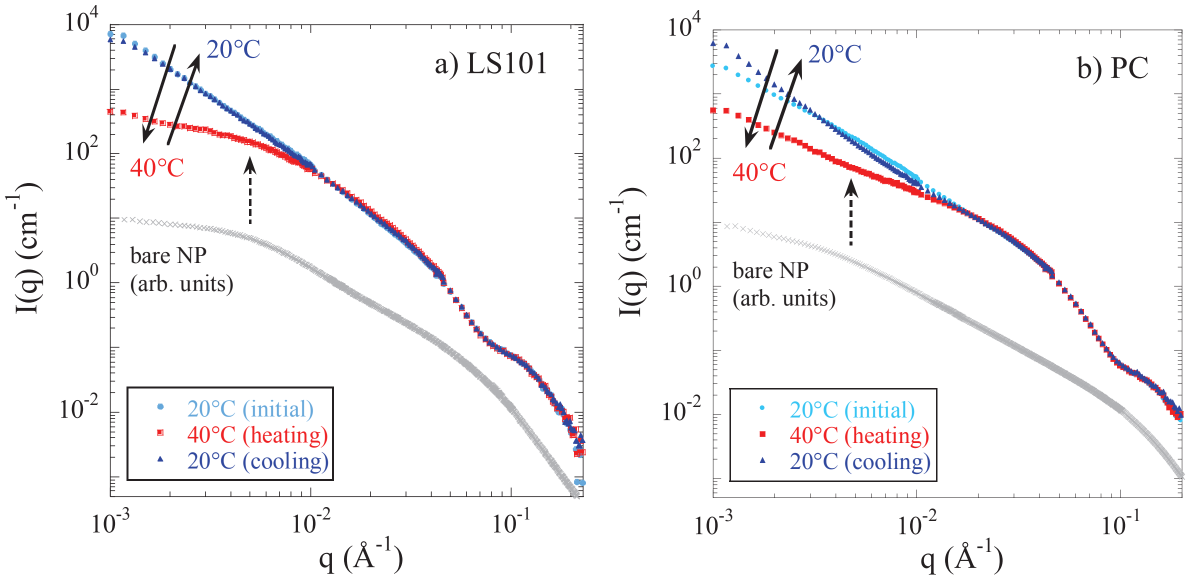

Figure 6.14: Influence of the temperature on the dispersion in $CDCl_3$ of $C_{18}PA$ grafted NPs as seen by SANS. **a)** LS101, **b)** PC (TiO_2 volume fraction about 0.4 vol%).

The result is striking. Whatever the temperature, the high-q part of the data (q > 0.01 $Å^{-1}$) superimposes perfectly, both in D- and H-chloroform (see figures 6.14a and 6.15a). This part of the data has been described successfully in the previous section by the layer of grafted PA on the primary particles. The superposition indicates that the local shell structure does not change measurably, and the same thickness and solvation parameters (see previous paragraph 2) are found. At low angles, the 20°C results follow the same fractal power law ($q^{-2.5}$). The decrease of the low-q scattering by about a factor of ten on heating at 40°C shows that aggregates are broken up into smaller pieces, the radius of which is comparable to the one of the original NPs measured in water: the structural similarity is demonstrated by comparing the intensity curves to the one of the bare NP in figure 6.14a. When the sample is cooled down to 20°C again, however, aggregation leading to exactly the same structure as before is found, the phenomenon is fully reversible. For comparison, the same sequence of experiments has been performed in H-chloroform (cf. figure 6.15), confirming these findings.

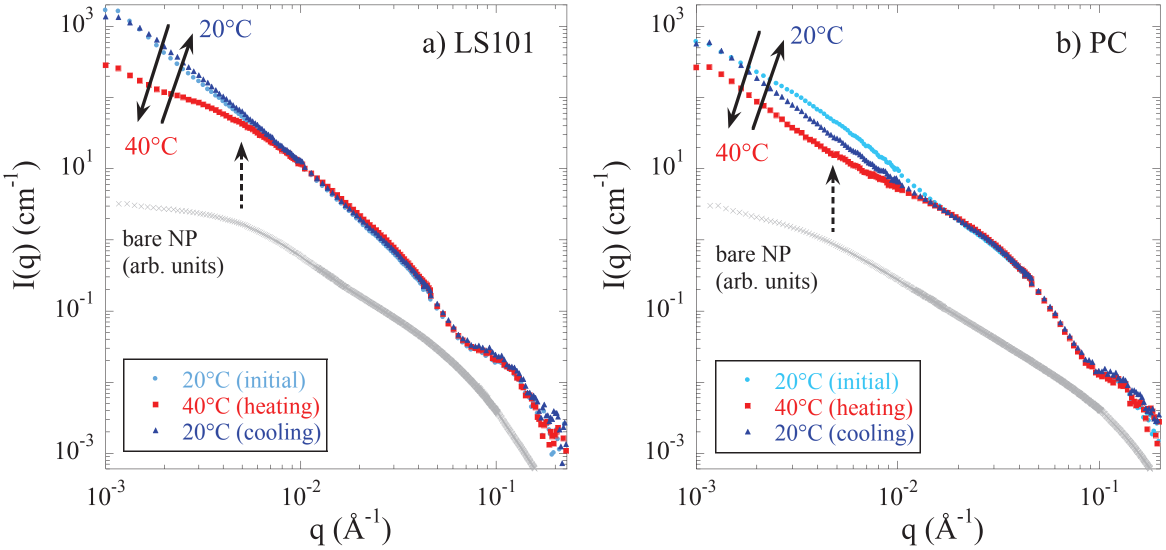

Figure 6.15: Influence of the temperature on the dispersion in $CHCl_3$ of $C_{18}PA$ grafted NPs as seen by SANS. **a)** LS101, **b)** PC (TiO_2 volume fraction about 0.4 vol%).

In figures 6.14 b and 6.15 b, finally, the results for the PC-$C_{18}PA$ organosol are shown. The observations are similar: superposition of intensities in the high-q part, and reversible evolution with temperature in the low-q part. The structure obtained at 40°C in chloroform resembles the one of the bare NPs in water. As for LS101, these results show that the aggregates formed in the organic solvent at 20°C can be broken-up by heating, and rebuilt at least partially upon cooling down, defining thermally reversible aggregation.

Thermoreversible aggregation of silica particles modified by octadecyl chains in various organic solvents has been extensively studied.[198-200, 203] Eberle et al show small-angle data as a function of concentration and temperature.[198] At low concentrations relevant to the present study, the same thermoreversible aggregation was found. This phenomenon is ascribed to a temperature-induced change of the solvent quality, leading on cooling to a modification of the brush layer resulting in short-range attraction between the particles. Two different mechanisms have been proposed in the literature, depending on the nature of the solvent. In solvents having a molecular structure similar to octadecyl groups (e.g. tetradecane), cooling leads to a crystallization of the octadecyl layer by interdigitation of the solvent.[199, 203] In other solvents (e.g., benzene, toluene, or CCl_4), the decrease in solvent quality leads to the collapse of the stabilizing brush.[204] In our case, the thermoreversible aggregation observed in $CHCl_3$ or $CDCl_3$ is likely due to the latter mechanism.

V - Redispersion in organic solvents

After transfer of the LS101 sol to $CHCl_3$ phase under standard conditions, the aqueous phase was eliminated by decantation, and the NP organosol was dried by evaporation of $CHCl_3$ under vacuum at room temperature. Then the dry NPs were redispersed in different organic solvents: $CHCl_3$, toluene, and methyl-ethyl ketone (MEK). The photographs are shown in figure 6.16.

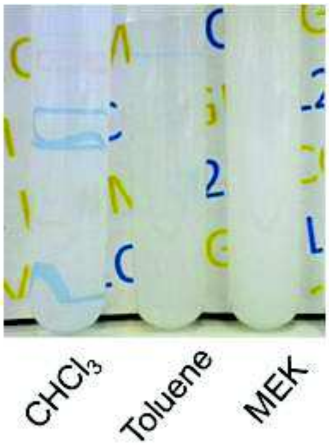

Figure 6.16: Redispersion in various organic solvents of the dry hydrophobic TiO_2 NPs obtained by phase transfer of LS101 under standard conditions, decantation, and drying.

The turbidity of the organosols indicated that the redispersion efficiency varies in the order $CHCl_3$ > toluene > MEK. In the case of toluene and MEK, small deposits were observed after 24h, whereas the redispersion in $CHCl_3$ remains transparent and homogeneous. To confirm these results, we made DLS measurements. The hydrodynamic radii of the NPs in the different solvents were 42 nm (CHCl3), 60 nm (toluene), and 65 nm (MEK), which confirms the results obtained by visual inspection of the redispersions.

VI - Conclusion

In this chapter, we have presented an original, highly efficient method to graft alkylphosphonic acid molecules onto different types of TiO_2 nanoparticles and simultaneously transfer them into a non miscible organic solvent. The conditions for full transfer have been identified, and the dispersion of the NPs in the organosols has been investigated by DLS and SANS.

A rather dense layer of linear alkyl chains is needed to obtain complete transfer, and the dispersion of the NPs in the organic phase is governed by the nature of the PA. Only partial transfer occurred with tBuPA and PPA. The best dispersion in the organosols was observed for C_8PA- and C_{12}PA-modified NPS. After transfer, the thickness (1 – 2 nm) and solvation of the phosphonate shell could be measured by SANS using protonated and deuterated solvents, and the corresponding structural parameters were found to be compatible with both molecular constraints and nominal concentrations. A thermoreversible aggregation was observed for the sols transferred with C_{18}PA, with particles in the organosol of size similar to the native bare NPs in water as temperature was increased. When the phase transfer was performed on pre-agglomerated aqueous sols (obtained by decreasing the electrostatic repulsions between NPs), complete de-aggregation was observed in the organic phase.

The simultaneous phase transfer and surface modification by reaction with PAs was found to work even at very high concentration of the aqueous sol, and for different TiO_2 sols. It could also be applied to water dispersions of fumed TiO_2 and Al_2O_3 powders. This method should thus be quite general, considering the wide variety of metal oxide particles that can be modified by phosphonate monolayers (see chapter I).

Moreover, this method allows obtaining NP sols in organic solvent, without drying or washing steps. By direct mixing with a solution of polymer solubilized in the same solvent, this allows NPs incorporation in a polymer matrix. Note that it is possible to tune the aggregate sizes by varying the alkylphosphonic acid chain length. As for the surface modified NPs obtained in chapter III, it opens the way of controlling the state of aggregation of NPs, and thereby it may be possible to control their structure in the final NC, thus the rheological properties of the obtained material.

General conclusion

The purpose of this PhD work was first to functionalize oxide nanoparticles in aqueous colloidal sols in order to control the dispersion of nanoparticles in the sols and in polymer nanocomposites derived from these sols, and in a second step to evaluate this dispersion using advanced characterization methods.

We successfully modified alumina-coated silica nanoparticles dispersed in water with different phosphonic acids, and characterized the grafted nanoparticles by FTIR, elemental analysis, TGA, and ^{31}P MAS NMR. This surface modification offers a convenient way to modify the interactions in solution, thus to tune the nanoparticle aggregation state, which was monitored by TEM, DLS, and SAS measurements. We found that both the nature of the graft and the grafting density impact the aggregation state of the nanoparticles, through a modification of electrostatic repulsions and of attractive hydrophobic interactions between nanoparticles.

The impact of the C_8PA grafting density on the structure of nanoparticles in the dried state was evidenced by SAXS. And the different relaxation processes of the raw and grafted nanoparticles were studied. In particular, four different processes linked to the surface hydroxyl groups (process 1) and to the adsorbed water (process 2, 3, and 4) were detected. In the case of DEPA, the impact of grafting the DEPA-molecule on the surface of the nanoparticles was investigated: the α-process seems not to be impacted by the grafting, but the β-processes could not be detected for DEPA-grafted nanoparticles, it was assumed that grafting suppressed the β-relaxation process.

The surface-modified nanoparticles were then incorporated in a PEA polymer matrix by an aqueous latex route. The nanoparticle structure in the resulting nanocomposites was investigated by SANS measurements as a function of nanoparticle volume fraction, nature of the grafted phosphonic acid, and grafting density. In particular, the aggregates density was shown to decrease with the amount of grafted phosphonic acid at the nanoparticle surface, whatever the grafted phosphonic acid. Note that this tendency is opposed with what was observed in the case of NPs sols, in which the nature of the grafted PA clearly impacted the NP aggregation state. Moreover, TEM images of the nanocomposites were difficult to obtain, because of the low glass transition temperature of the matrix. TEM images had permitted to go further with the data interpretations.

We also performed the simultaneous phase transfer and surface modification of TiO_2 (and Al_2O_3) nanoparticles using the same type of surface modification with phosphonic acids. The transfer parameters were investigated to deduce the limits of the method. The surface-modified nanoparticles were characterized by FTIR and ^{31}P MAS NMR, and redispersed in different organic solvents. The nanoparticle dispersion state in colloidal suspensions (obtained after phase transfer) was studied by DLS and SANS, and an estimation of the thickness of the grafted layers was obtained. A thermo-reversible aggregation was also evidenced in the case of C_{18}PA-modified nanoparticles.

In both surface modification methods, supplementary washing or drying steps are not necessary, thus avoiding the manipulation of dried nanoparticles. Moreover, this method offers the possibility to modify the surface of nanoparticles with various grafts, and they can be incorporated in hydrophobic polymer matrixes. For the first method, the nanocomposites are obtained via an aqueous route. For the second method, the surface modified nanoparticles were successfully incorporated in PMMA and PS matrixes by direct mixing with a polymer solution. The nanoparticle structure in the nanocomposite was investigated by SAXS, but the elaboration of nanocomposites and the SAXS results are not shown in this dissertation, because the data treatment was not completed.

To complete our study, it would be interesting to study the structure of surface modified L200S/PEA nanocomposites with higher grafting densities: up to 4 P/nm² for C_3PA, C_5PA, and C_8PA. The incorporation of CAPA-grafted nanoparticles could also be interesting, as the CAPA seems to graft with both ends. The resulting nanoparticles should be more hydrophobic, i.e. more compatible with the polymer matrix. Unfortunately, grafting phosphonic acids with longer alkyl chains or more hydrophobic is not possible in water with our protocol, because of the solubility of the phosphonic acid.

Moreover, the study of nanoparticles at dried state by SAXS and BDS could be completed with a study on CAPA-grafted nanoparticles and by complementary measurements, for instance measurements of the dielectric response and scattered intensity of intermediate grafting densities for C_3PA- and C_5PA-modified nanoparticles (1 or 2 P/nm²) could allow confirming our hypothesis on the evolution of process 2. BDS measurements of CAPA-grafted nanoparticles in the whole temperature and frequency range should also provide information on the nature of carboxylic acid binding on the surface (i.e. ionic or covalent binding).

The incorporation of surface-modified TiO_2 nanoparticles in different polymer matrixes (PMMA and PS) was successful. The SAXS data treatment is in progress to study the impact of different parameters (e.g. chain length and tacticity of the polymer) on the nanoparticle structure in the obtained nanocomposites.

Appendix 1: Small Angle Scattering configurations

The scattering cross section per unit sample volume dΣ/dΩ (in cm^{-1}) – which we term scattered intensity I(q) – was obtained by using standard procedures including background subtraction and calibration given by the different facilities.

SANS@LLB

Small-angle neutron scattering measurements on alumina-covered silica NPs solutions was completed on beamline PACE at Laboratoire Léon Brillouin (LLB, Saclay FR) using three configurations, defined by:

- Wave length = 6 Å, sample-detector distance = 1 m
- Wave length = 6 Å, sample-detector distance = 4.7 m
- Wave length = 17 Å, sample-detector distance = 4.7 m

The total q-range was 2.4 10^{-3} – 0.35 $Å^{-1}$. For each sample, the transmission was measured during 2 min. The scattered intensity was measured during 3, 5, or 10 min for high values of q, 60 min for medium values of q and between 120 and 150 minutes for small values of q. The NPs dispersions were measured in 1 mm Hellma cuvettes.

The measurements of surface-modified NPs/PEA nanocomposites were achieved on the same beamline, using the same configurations. The scattered intensity was measured during 2 or 3 min for high values of q, between 10 and 30 min for medium values of q and between 20 and 60 minutes for small values of q. The transmission was measured during 2 min for each sample.

SANS@MLZ

SANS on colloidal TiO_2 nanoparticle dispersions was completed on beamline KWS-2 at Heinz Maier-Leibnitz Zentrum (MLZ) facility in München (Germany) using three configurations, defined by D = 20 m, λ = 10 Å, D = 8 m, λ = 5 Å, and D = 2 m, λ = 5 Å (total q-range: 2.4 10^{-3} – 0.35 $Å^{-1}$). Colloidal dispersions in H-chloroform were measured in 1 mm Hellma cuvettes, respectively in 2 mm for deuterated samples.

For neutron constrat calculations in solvents, scattering length densities of H- and D-chloroform were ρ_H = 2.36 10^{10} cm^{-2} and ρ_D = 3.16 10^{10} cm^{-2}, the one of LS101 NPs ρ_{NP} = 2.8 10^{10} cm^{-2} (measured by contrast variation in H_2O/D_2O), and for all grafts ρ_{graft} = (0.04±0.10) 10^{10} cm^{-2} (calculated from chemical structure).

SAXS@ESRF

Small-angle X-ray scattering on alumina-covered silica nanoparticles solutions (L200S) was performed on beamline ID02 at the European Synchrotron Radiation Facility (ESRF) in Grenoble (France) at a wavelength λ = 1 Å with a sample to detector distance D = 2.48 m, yielding a q-range from 3.8 10^{-3} to 0.15 $Å^{-1}$.

SAXS@Soleil

SAXS measurements of TiO_2 nanoparticles form factors in solution were done on beamline Swing at Synchrotron Soleil in Saclay (France). Note that the X-rays scattering length of TiO_2 is $\rho_{TiO2} = 2.8\ 10^{11}$ cm^{-2} and the contrast between TiO_2 NPs and water is $\Delta\rho = 1.85\ 10^{11}$ cm^{-2}. These values were used for calculation.

Appendix 2: SANS contrast variations

Principle and sample preparation

The principle is explained in details in chapter II. The contrast variation consists in varying the density of scattering length of the solvent (ρ), in order to determine those of the sample, in our case: the nanoparticles one.

For each colloidal dispersion of NPs, four diluted solutions of NPs, with different amount of H_2O and D_2O are prepared. As the scattering length of ^1H (b_{1H} = -3.74 fm) and of ^2H (b_{2H} = 6.67 fm) are very different, the density of scattering length are very different, too: -0.56 $10^{10}cm^{-2}$ for H_2O and 6.34 $10^{10}cm^{-2}$ for D_2O. In this way, the constrast between the solvent and the NPs, Δρ, is varied. The relation, which linked the scattered intensity to the contrast is (in the case of hard spheres):

$$I(q) = \phi.\Delta\rho^2.V.P(q).S(q) \qquad \text{(eq.A2.1)}$$

P(q) and V depends on the NPs, thus they are not modified by varying the H_2O/D_2O ratio. Moreover, by keeping the volume fraction of NPs ϕ fixed, S(q) is also unchanged. Consequently, if $\rho_{solvent}$ is known, one can deduced ρ_{NPs}, because, for a given q value, the scattered intensity is directly proportional to $\Delta\rho^2$.

The most commonly way to determine ρ_{NPs} is to plot $\sqrt{I} = f(\rho_{solvent})$, for a given q value. The obtained curve is a line, which zero value corresponds to $\rho_{solvent} = \rho_{NPs}$.

For our NPs, we chose q = 0.007258 $Å^{-1}$. With the line equation, we deduced ρ_{NPs}. We also plotted the lines for two others q values (q = 0.015322 $Å^{-1}$ and q = 0.040306 $Å^{-1}$) to estimate an error bar for the values. The contrast variation values and the lines for our nanoparticles - L200S, LS101, and PC - are given in the following figures.

L200S

Obtained value: ρ = 3.7 10^{10} ± 0.2 10^{10} cm^{-2}

Note that theorically: ρ_{silica} = 3.5 $10^{10}cm^{-2}$ and $\rho_{alumina}$ = 5.7 10^{10} cm^{-2}.

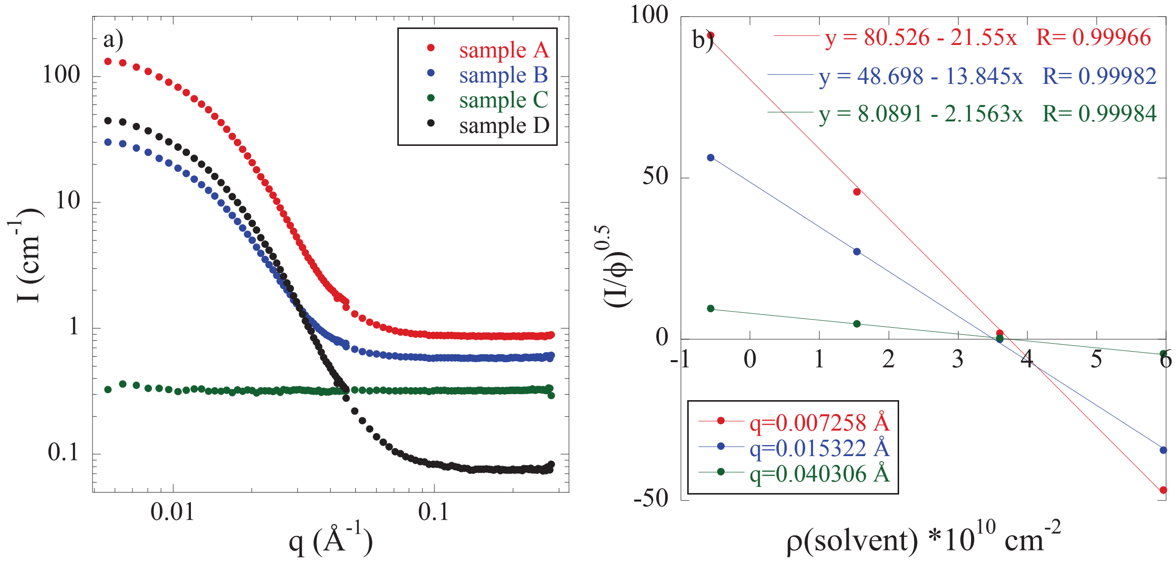

Figure A2.1: **a)** Scattered intensities of L200S dispersed in four different H_2O/D_2O ratios. **b)** Square root of the scattered intensities at fixed q values normalized by the volume fraction as a function of the solvent scattering length.

LS101

Obtained value: ρ = 2.8 10^{10} ± 0.1 10^{10} cm^{-2}

Note that theorically: ρ_{TiO2} = 2.5 10^{10} cm^{-2}

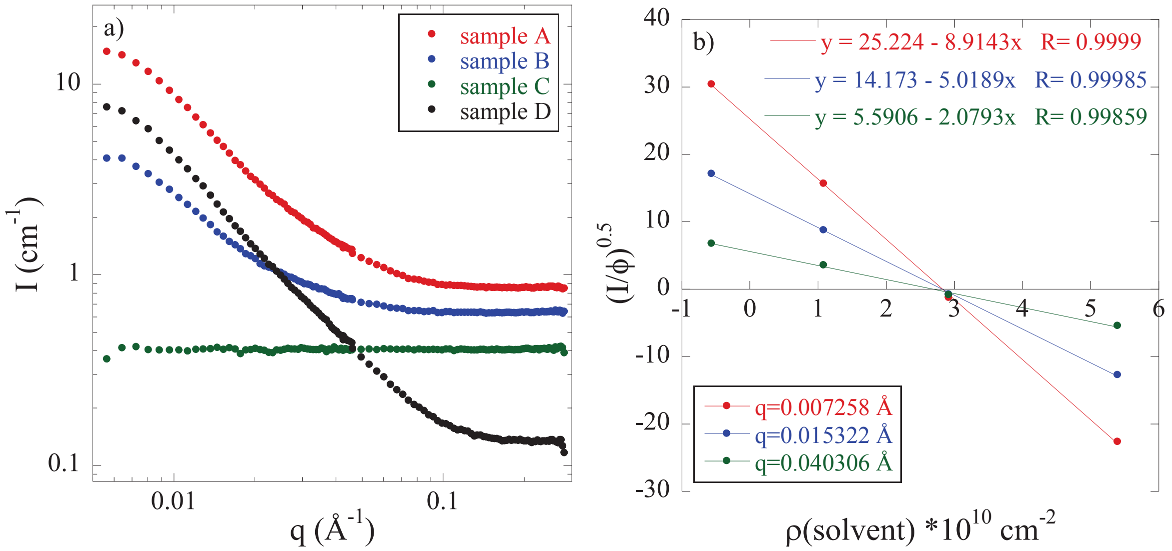

Figure A2.2: **a)** Scattered intensities of LS101 dispersed in four different H_2O/D_2O ratios. **b)** Square root of the scattered intensities at fixed q values normalized by the volume fraction as a function of the solvent scattering length.

PC

Obtained value: ρ = 2.9 10^{10} ± 0.1 10^{10} cm^{-2}

Note that theorically: ρ_{TiO2} = 2.5 10^{10} cm^{-2}

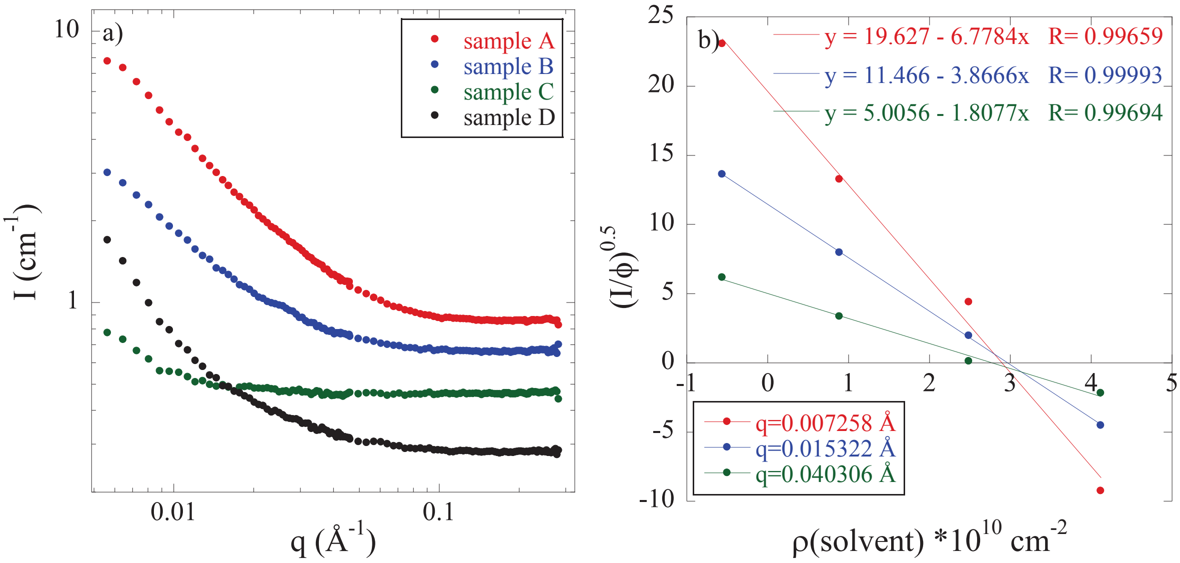

Figure A2.3: **a)** Scattered intensities of PC dispersed in four different H_2O/D_2O ratios. **b)** Square root of the scattered intensities at fixed q values normalized by the volume fraction as a function of the solvent scattering length.

Appendix 3: Refractive index of powders measurements

The refractive index of powders is one of the parameters needed in the chosen BDS model (for the data normalization, see appendix 4). The measurement method and the obtained results are given in this appendix.

Method

For one powder, 6 samples are prepared as follow: 5 ± 0.05 mg of powder are dispersed in 1500 µL of different ratios of MEK/toluene. Each sample is agitated by vortex during 10 seconds before measurement. The scattered light intensity at 90° is collected during one minute with following parameters: power of the laser = 180 mW and pinhole = 1 mm. The average value of intensity and the temperature are collected.

For each mix of solvent, the refractive index is performed at the same temperature than the associated light scattering measure. The intensity (in kcps) is plotted as a function of the solvent refractive index. The relation linking the intensity with the refractive index of the powder, n_{powder}, is:

$$\text{Intensity} = A\,(n_{powder})^2 + B\,n_{powder} + C \qquad \text{(eq.A3.1)}$$

Results

One example of curve is given in figure A3.1 for DEPA-grafted L200S NPs (ρ = 3.5 P/nm²).

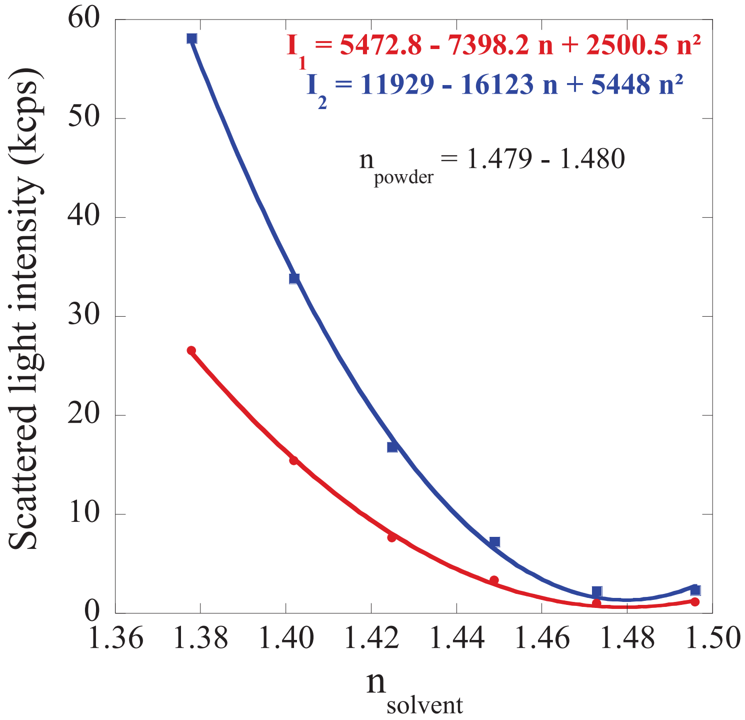

Figure A3.1: Scattered light intensity measurements as a function of the solvent refractive index for DEPA-grafted NPs (ρ = 3.5 P/nm²).

The obtained powder refractive indexes are given in table A3.1.

Table A3.1: Measured refractive indexes.

Sample	Relative humidity of storage box	Refractive index
L200S	Not controlled	1.48
	11%	1.47
	75%	1.47
C_8PA-grafted L200S ρ = 3.5 P/nm²	Not controlled	1.47
C_8PA-grafted L200S ρ = 4.0 P/nm²	33%	1.47
DEPA-grafted L200S ρ = 3.5 P/nm²	Not controlled	1.48
DEPA-grafted L200S ρ = 4.0 P/nm²	33%	1.47

One can conclude that, with the precision of our method, the refractive index is neither varying with the hydration level nor the surface modified of the NPs (grafting density and type of graft).

To normalize our data, we fixed the value at n = 1.48.

Appendix 4: Model used for samples description in Broadband Dielectric Spectroscopy

In order to extract quantitative information about our samples in chapter IV, we need to normalize the measured data. Two simple models can be considered. The first consist in two capacitors in series and the second in two capacitors in parallel. Different values are needed, e.g. the weight or the thickness of the powder, the real capacity of the sample at low temperature (that we fixed at T = 100 K or the lowest measured temperature), and the diameter of the cells. Both models will be detailed in next parts.

First model: two capacitors in series

The simplest model consists in describing the sample with two capacitors in series: one for the air (which is localized between the grains of powder) and another one for the mix {NPs+water} (see figure A4.1). Both capacitors have the same surface, but different thicknesses.

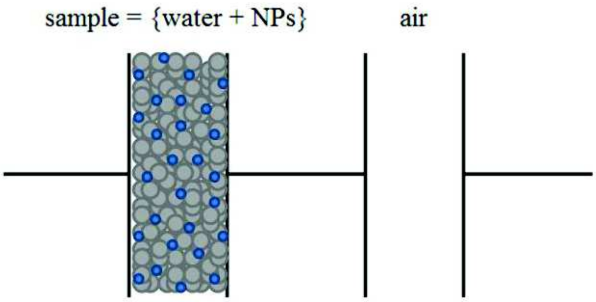

Figure A4.1: Schematization of our samples in the first model.

The total capacity is given by the relation:

$$\frac{1}{C_{\text{measured}}} = \frac{1}{C_{\text{sample}}} + \frac{1}{C_{\text{air}}} \qquad \text{(eq.A4.1)}$$

The capacity is defined by:

$$C_x = \varepsilon.\varepsilon_0.S/e_x \qquad \text{(eq.A4.2)}$$

Where ε is the relative permittivity of the capacitor (= 1 for the air), ε_0 the vacuum permittivity, S the area of the capacitor, and e_x the thickness of the capacitor.

By combining (eq.A4.1) and (eq.A4.2), one can deduce the relation:

$$e_{\text{sample}} = \left(\frac{1-1/\varepsilon_{\text{measured}}}{1-1/\varepsilon_{\text{sample}}}\right) e_{\text{total}} \qquad \text{(eq.A4.3)}$$

The value of the vacuum permittivity is: ε_0 = 8.85418782 10^{-12} F/m. The relative permittivity of the sample can be estimated with $\varepsilon \approx n^2$, i.e. to the square of the refractive index.

To check the validity of this model, we tested it on a given sample by comparing the volume obtained with the density of the powder, $V_{density}$, and those obtained by this model, V_{model}.

$\varepsilon_{measured} = 1.683$
$\varepsilon_{sample} \approx n^2 = 1.48^2 = 2.19$
$e_{sample} = 0.75\ e_{total}$
$V_{model} = 0.75\pi D^2 e/4 = 0.15\ cm^3$
$V_{density} = m/\rho = 0.05\ cm^3$

This model is not adapted for our samples !

Second model: two capacitors in parallel

We are testing here a second model, in which the sample can be assimilated to two capacitors in parallel: one for the air, the other for the water and the NPs. Both capacitors are assumed to have the same thickness, but different surfaces. The total capacity of the system is the sum of both capacities:

$$C_{measured} = C_{air} + C_{sample} \qquad \text{(eq.A4.4)}$$

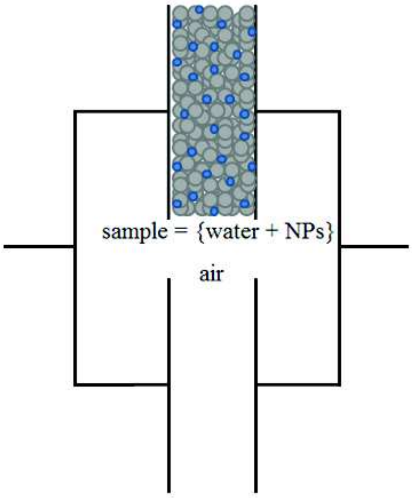

Figure A4.2: Schematization of our samples in the second model.

By combining (eq.A4.2) and (eq.A4.4), we obtain:

$$S_{sample} = \left(\frac{C_{measured}\ e}{\varepsilon_0} - S_{total}\right)\frac{1}{\varepsilon - 1} \qquad \text{(eq.A4.5)}$$

with e the thickness of the capacitors, ε_0 the vacuum permittivity, S_{total} the total area, i.e. the area of the cell, and ε the relative permittivity of the capacitor {NPs+water}.

To check the validity of this model, we tested it again on a given sample by comparing the volume obtained with the density of the powder, $V_{density}$, and those obtained by this model, V_{model}.

$\varepsilon_{measured} = 1.683$
$\varepsilon_{sample} \approx n^2 = 1.48^2 = 2.19$
$S_{sample} = 0.57\ S_{total}$

$V_{model} = 0.57\pi D^2 e/4 = 0.11\ cm^3$
$V_{density} = m/\rho = 0.05\ cm^3$

The error is a bit lower. The calculs were done with the measured thickness of the sample. To decrease the gap between theorical and “model” value, we will use the mass of the sample instead of the thickness, because this value is more accurate. In this case, we obtain: $S_{sample} = 0.32\ S_{total} = 0.06\ cm^3$.

To conclude, we choose to modelize our sample as two capacitors in parallel. The normalization will be done using the mass of the sample (not the thickness) to obtain S_{sample}. The relation between the measured permittivities and those of the sample are:

$$\varepsilon''_{sample} = \frac{C''_{measured}\ e}{\varepsilon_0\ S_{sample}} = \frac{\varepsilon''_{measured}\ S_{total}}{S_{sample}} \qquad \text{(eq.A4.6a)}$$

$$\varepsilon'_{sample} = \frac{C'_{measured}\ e}{\varepsilon_0\ S_{sample}} + \left(1 - \frac{S_{total}}{S_{sample}}\right) = \frac{\varepsilon'_{measured}\ S_{total}}{S_{sample}} + \left(1 - \frac{S_{total}}{S_{sample}}\right) \qquad \text{(eq.A4.6b)}$$

Experimental method

The BDS measurements were done on a Novocontrol Alpha Analyzer system in a frequency range between 10^{-2} and 10^{7} Hz. The samples - approximately 130 mg of washed and dried powders - were placed between two gold-coated electrodes of diameter 3 cm. The electrodes were surrounded by a Teflon ring in order to minimize dehydration. The thickness (in order to control the calculated value) and mass (for data normalization) of the sample were measured previous each analysis.

The electrodes containing the hydrated powders were incorporated at T = 100 K under nitrogen flow to avoid changes in the water content of the samples. The dried powders were incorporated under nitrogen flow and heated 4 hours at T = 393 K previous analysis in the BDS apparatus. The stabilization of the temperature was fixed to ± 0.15°C.

Appendix 5: supporting information about chapter IV

Dipolar moment of hexylphosphonic acid

To have an approximation on the value of the dipolar moment of C_8PA, we give the value for an other alkyl phosphonic acid: hexylphosphonic acid. According to Paniagua et al., the dipolar moment of $C_6H_{13}PO(OH)_2$, grafted on a metal oxide surface is 1.77 D (as illustrated on figure A5.1), which is a value comparable with the one of water.[166]

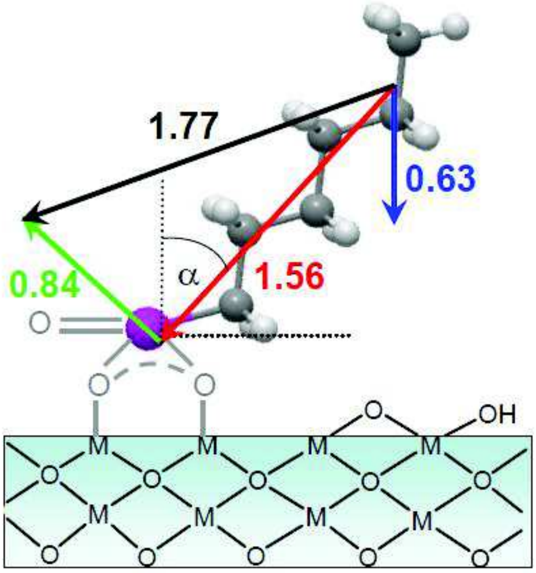

Figure A5.1: Schematic view of the calculation of the dipolar moment of $C_6H_{13}PO(OH)_2$ according to reference [166]. The red arrow is the dipole component along the molecular axis, the green arrow is the dipole component along the perpendicular axis, and the black arrow is the total dipole moment vector. The blue arrow represents the projection of the dipole along the surface normal.

DSC measurements on powders

As described in the bibliographic part and in chapter IV, crystallized water has a different behavior than "free" water molecules adsorbed at the NPs surface. DSC measurements allow evidencing the presence of such a crystallized phase. They were done with 20°C/min heating and cooling temperature ramps from -120 to +25°C. The presence of a crystallization peak at T = -45°C = 228 K was observed for two samples. One obtained DSC measure is shown in figure A5.2a. Respectively, the measurement of a non-crystallized sample is given in figure A5.2b.

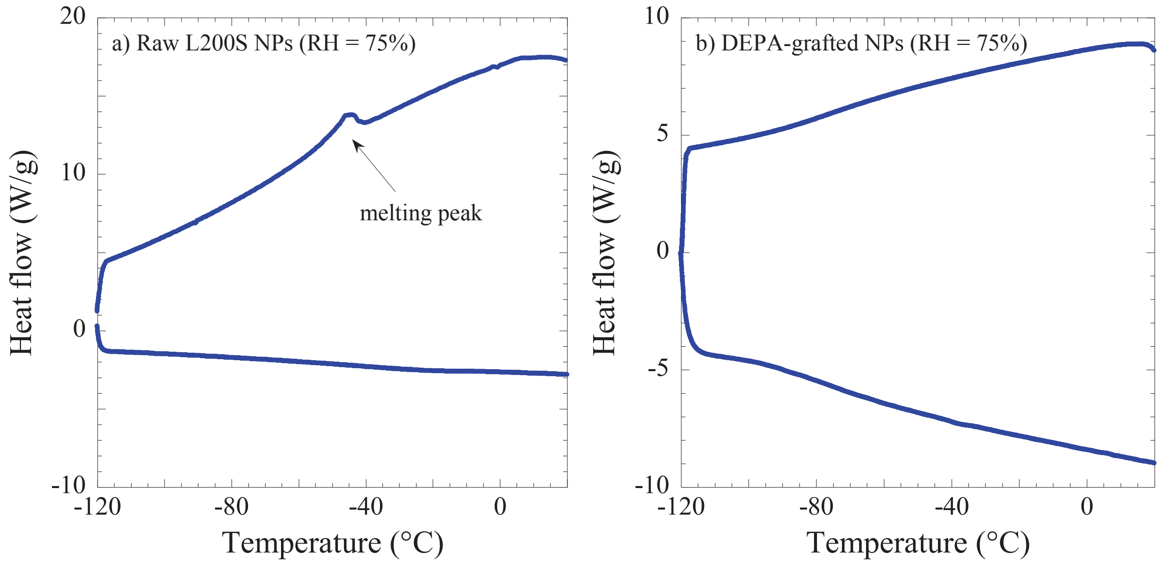

Figure A5.2: DSC measurements on hydrated powders (RH = 75%) for **a)** raw L200S NPs, and **b)** DEPA-grafted NPs.

TGA measurements on powders

The evaluation of the water content is obtained by TGA measurements: under nitrogen flow, from 20 to 120°C with a heating rate of 5°C/min, followed by an isotherm at 120°C. Figure A5.3 shows the weight loss during the heating ramp and the isotherm at 120°C. The aim is to evaluate the optimal isotherm duration. The water content decreases quickly during the heating ramp and stabilized at ca. t = 100 min. We chose an isotherm duration of 120 min, which corresponds to t = 140 min on the graph.

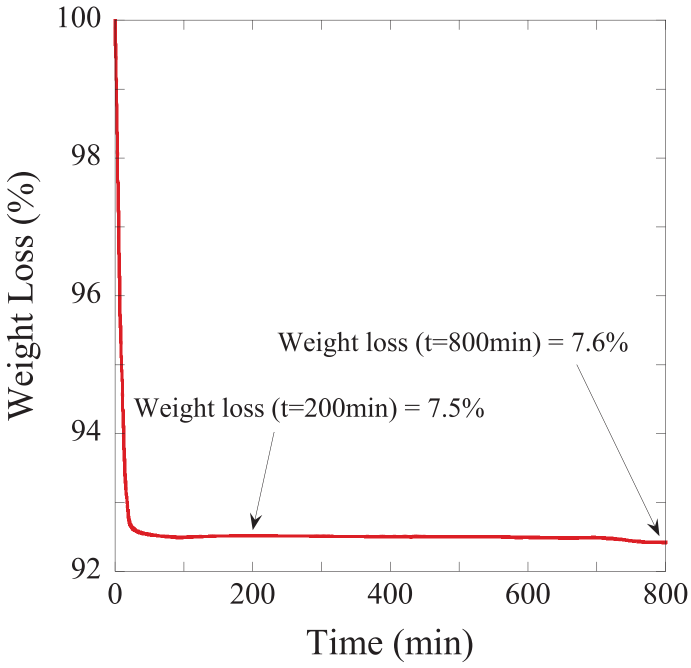

Figure A5.3: Weight loss of hydrated (RH = 75%) raw L200S NPs during the isotherm at 120°C.

Appendix 6: Law-q power law fit for nanocomposite SANS data treatment

In chapter V, the nanocomposite scattered intensities presents a low-q increase (with the decrease of q) following a power law: $I = A\ q^{-B}$. This power law parameters, prefactor A and exposant B, were used for subtraction to obtain S(q) and are grouped in table A6.1.

Table A6.1: Low-q power law parameters: $A\ q^{-B}$.

Nature of the graft	Volume fraction of NPs	Grafting density (in P/nm²)			
		0,5 P/nm²	1,0 P/nm²	1,5 P/nm²	4,0 P/nm²
None	ϕ = 1%	A = 0,06 ; B = 2,3			
	ϕ = 5%	A = 0,4 ; B = 1,8			
	ϕ = 10%	A = 0,04 ; B = 2,1			
DEPA	ϕ = 1%		A = 0,03 ; B = 2,4	A = 0,2 ; B = 2,1	A = 0,05 ; B = 2,3
	ϕ = 5%		A = 0,2 ; B = 1,9	A = 0,1 ; B = 2,1	
	ϕ = 10%		A = 0,06 ; B = 2,1	A = 0,01 ; B = 2,5	A = 0,001 ; B = 2,9
C3PA	ϕ = 1%		A = 0,2 ; B = 2,0		
	ϕ = 5%		A = 0,4 ; B = 1,8		
	ϕ = 10%		A = 0,1 ; B = 1,9		
C5PA	ϕ = 1%				
	ϕ = 5%	A = 1,3 ; B = 1,6	A = 0,2 ; B = 1,9		
	ϕ = 10%	A = 0,05 ; B = 2,2	A = 0,1 ; B = 2,0		
C8PA	ϕ = 1%	A = 2,9 ; B = 1,5	A = 0,02 ; B = 2,5	A = 0,01 ; B = 2,8	
	ϕ = 5%	A = 0,4 ; B = 1,8	A = 0,5 ; B = 1,8	A = 0,9 ; B = 1,7	
	ϕ = 10%	A = 0,2 ; B = 1,9	A = 0,3 ; B = 1,8	A = 0,3 ; B = 1,8	

Both factors, A and B, seem to vary randomly, no tendency or generality can be deduced concerning the fractal dimension of the aggregates, which varies around 2.

Appendix 7: Complementary methods

Thermogravimetric Analysis

In chapter III, to characterize the grafting density on alumina-coated silica NPs, the quantity of grafted phosphonic acid was determined by TGA, under air (flow: 50 mL/min) from 20 to 800°C with a heating rate of 5°C/min on a Netzsch STA 409 PC Luxx thermoanalyzer.

In chapter IV, the water content of phosphonic acids and hydrated powders for BDS measurements were done on a TA Q500 under nitrogen (flow: 50 mL/min), from 20 to 120°C with a heating rate of 5°C/min, followed by an isotherm at 120°C during 120 min.

In the case of nanocomposites studied in chapter V, the NP volume fraction was determined by measuring the residual mass at 800°C of the obtained NCs latex. The measurements were done on a Netzsch STA 409 PC Luxx thermoanalyzer, under air flow (50 mL/min) from 40 to 800°C with a temperature ramp of 20°C/min.

Differential Scanning Calorimetry

The latex Tg measurements were performed on a Netzsch DSC 204 F1 apparatus with 10°C/min cooling and heating temperature ramps, in the temperature range from -40 to +120°C.

In chapter IV, the determination of DEPA glass transition temperature and the characterization of powders were done on a TA Q2000 apparatus with 20°C/min cooling and heating temperature ramps, in the temperature range from -120 to +25°C.

Zeta potential measurements

Electric surface potential measurements of NPs were done with a Zetasizer 3000 HAS after dilution of colloidal suspensions with ultra-pure water to 1 wt%. The pH was adjusted with NaOH and HCl 0.1 M solutions.

Inductively Coupled Plasma - Optical Emission Spectroscopy

Inductively Coupled Plasma Optical Emission Spectroscopy (ICP-OES) was used to determine Al and P contents. About 7 mg of dried NPs were mineralized by adding 1 mL of HNO_3 (70%), 1 mL of H_2SO_4 (95%) and 1 mL of HF (40%). This solution was heated for 1h30 at 170°C, then for 1h at 270°C on a slab in a PTFE beaker, completed with distilled water to 50 mL and injected in a Perkin Elmer Optima 2100 DV Optical Emission Spectrometer apparatus.

NMR

^{1}H and ^{31}P liquid state NMR were recorded with a Brucker DRX 300 spectrometer at room temperature.

Solid state ^{31}P Magic Angle Spinning (MAS) NMR experiments were performed on a Varian VNMRS 400 MHz (9.4 T) spectrometer using a 3.2 mm Varian T3 HXY MAS probe. Single pulse experiments were carried out with a spinning rate of 20 kHz, a 90° excitation pulse of 3 µs, a recycle delay of 30 sec (which ensure a complete relaxation of all the ^{31}P signals) and 100 kHz spinal-64 ^{1}H decoupling. For the most grafted NPs (1 P/nm² of phosphonic acid introduced or more), 400 transients were recorded. The ^{31}P chemical shift was determined using an external reference: hydroxyapatite $Ca_{10}(PO_4)_6(OH)_2$ at 2.8 ppm (with respect to H_3PO_4, 85 wt% in water)

Solid state CP MAS ^{13}C NMR experiments were performed on a Varian VNMRS 300 MHz spectrometer using a 3.2 mm T3 MAS probe. The experiments were carried out with a spinning rate of 6000 Hz, a contact time of 3 ms, a 90° excitation pulse of 5 µs, and a recycle delay of 5 sec. About 14600 scans were recorded for each sample. The spectra were referenced using adamantine as a secondary reference.

FT-IR

Infrared spectra were recorded using an Avatar 320 FT-IR spectrometer. Measurements were done in transmission mode on pellets composed of 2-3 mg of dried nanoparticles dispersed in 100 mg of KBr, also used for background subtraction.

Specific surface area measurements

The specific surfaces of raw nanoparticles were determined by nitrogen physisorption at 77 K on a Micromeritics Tristar sorptometer. Prior to analysis, dried nanoparticles were degassed under vacuum (2 Pa) at 120°C overnight. The specific surface area was determined via the BET method,[205] assuming an area of 0.162 nm^2 per N_2 molecule.

Density measurements

The density of the nanoparticles was determined by helium measurement with a Micromeritics AccuPyc 1330 apparatus. The powder were pounded and degassed under vacuum about 12h before measurements.

Size Exclusion Chromatography

SEC measurements were done on a PL-GPC 50 Plus Polymer Laboratories apparatus. These measurements allowed determining the molecular weight (M_w) and polydispersity (PD) of the polymer chains using PS calibration for PS samples and PMMA standards in THF for PEA and PMMA samples.

Transmission Electron Microscopy

Transmission Electron Microscopy (TEM) pictures were recorded with a JEOL 1200 EXII apparatus at 100 kV.

References

1. Schmitt Pauly, C.; Genix, A.-C.; Alauzun, J. G.; Sztucki, M.; Oberdisse, J.; Mutin, P. H., Surface modification of alumina-coated silica nanoparticles in aqueous sols with phosphonic acids and impact on nanoparticle interactions. *Physical Chemistry Chemical Physics* **2015,** *17* (29), 19173-19182.
2. Schmitt Pauly, C.; Genix, A.-C.; Alauzun, J. G.; Guerrero, G.; Appavou, M.-S.; Pérez, J.; Oberdisse, J.; Mutin, P. H., Simultaneous phase transfer and surface modification of TiO2 nanoparticles using alkylphosphonic acids: optimization and structure of the organosols. *Langmuir* **2015**.
3. Vert, M.; Doi, Y.; Hellwich, K.-H.; Hess, M.; Hodge, P.; Kubisa, P.; Rinaudo, M.; Schue, F., Terminology for biorelated polymers and applications (IUPAC recommendations 2012). *Pure Appl. Chem.* **2012,** *84* (2), 377-410.
4. Arzt, E., Size effects in materials due to microstructural and dimensional constraints: A comparative review. *Acta Mater.* **1998,** *46* (16), 5611-5626.
5. Forrest, J.; Dalnoki-Veress, K.; Stevens, J.; Dutcher, J., Effect of free surfaces on the glass transition temperature of thin polymer films. *Physical review letters* **1996,** *77* (10), 2002.
6. Pankhurst, Q. A.; Connolly, J.; Jones, S.; Dobson, J., Applications of magnetic nanoparticles in biomedicine. *Journal of physics D: Applied physics* **2003,** *36* (13), R167.
7. Steinhögl, W.; Schindler, G.; Steinlesberger, G.; Engelhardt, M., Size-dependent resistivity of metallic wires in the mesoscopic range. *Physical Review B* **2002,** *66* (7), 075414.
8. Kelly, K. L.; Coronado, E.; Zhao, L. L.; Schatz, G. C., The optical properties of metal nanoparticles: the influence of size, shape, and dielectric environment. *The Journal of Physical Chemistry B* **2003,** *107* (3), 668-677.
9. Patzke, G. R.; Zhou, Y.; Kontic, R.; Conrad, F., Oxide nanomaterials: synthetic developments, mechanistic studies, and technological innovations. *Angewandte Chemie International Edition* **2011,** *50* (4), 826-859.
10. Rodriguez, J. A.; Fernandez-Garcia, M., *Synthesis, properties, and applications of oxide nanomaterials*. John Wiley & Sons: 2007.
11. Iler, R. K., *The Chemistry of Silica: Solubility, Polymerization, Colloid and Surface Properties and Biochemistry*. John Wiley and Son: 1979; p 892 pp.
12. Branda, F.; Silvestri, B.; Luciani, G.; Costantini, A.; Tescione, F., Synthesis structure and stability of amino functionalized PEGylated silica nanoparticles. *Colloids and Surfaces, A: Physicochemical and Engineering Aspects* **2010,** *367* (1-3), 12-16.
13. Payne, C., C., Applications of Colloidal Silica: Past, Present, and Future. In *The Colloid Chemistry of Silica*, American Chemical Society: 1994; Vol. 234, pp 581-594.
14. Ulrich, G. D., Theory of particle formation and growth in oxide synthesis flames. *Combust. Sci. Technol.* **1971,** *4* (2), 47-57.
15. Pratsinis, S. E., Flame aerosol synthesis of ceramic powders. *Progress in Energy and Combustion Science* **1998,** *24* (3), 197-219.
16. Burns, A.; Ow, H.; Wiesner, U., Fluorescent core-shell silica nanoparticles: towards "Lab on a Particle" architectures for nanobiotechnology. *Chemical Society Reviews* **2006,** *35* (11), 1028-1042.
17. Stöber, W.; Fink, A.; Bohn, E., Controlled growth of monodisperse silica spheres in the micron size range. *Journal of Colloid and Interface Science* **1968,** *26* (1), 62-69.
18. Arriagada, F. J.; Osseo-Asare, K., Synthesis of nanometer-sized silica by controlled hydrolysis in reverse micellar systems. *Surfactant Sci. Ser.* **2006,** *131* (Colloidal Silica), 81-89.
19. Sang, L.; Zhao, Y.; Burda, C., TiO2 Nanoparticles as Functional Building Blocks. *Chem. Rev.* **2014,** *114* (19), 9283-9318.

20. Winkler, J. In *Nano-scaled titanium dioxide - properties and use in coatings with special functionality*, Macromolecular Symposia, Wiley Online Library: 2002; pp 317-324.

21. Bachinger, A.; Kickelbick, G., Photocatalytic stability of organic phosphonates and phosphates on TiO2 nanoparticles. *Appl. Catal., A* **2011,** *409-410*, 122-132.

22. Howe, R. F.; Gratzel, M., EPR study of hydrated anatase under UV irradiation. *Journal of Physical Chemistry* **1987,** *91* (14), 3906-3909.

23. Formenti, M.; Juillet, F.; Meriaudeau, P.; Teichner, S.; Vergnon, P., Preparation in a hydrogen-oxygen flame of ultrafine metal oxide particles. Oxidative properties toward hydrocarbons in the presence of ultraviolet radiation. *Journal of Colloid and Interface Science* **1972,** *39* (1), 79-89.

24. Chen, X.; Mao, S. S., Titanium dioxide nanomaterials: synthesis, properties, modifications, and applications. *Chemical reviews* **2007,** *107* (7), 2891-2959.

25. Yoldas, B. E., Hydrolysis of titanium alkoxide and effects of hydrolytic polycondensation parameters. *J. Mater. Sci.* **1986,** *21* (3), 1087-92.

26. Livage, J.; Henry, M.; Sanchez, C., Sol-gel chemistry of transition metal oxides. *Prog. Solid State Chem.* **1988,** *18* (4), 259-341.

27. http://www.mvt.ovgu.de/mvt_media/Vorlesungen/VO_ENAP/Folien_ENAP_3.pdf.

28. Kosmulski, M., *Chemical properties of material surfaces*. CRC press: 2001; Vol. 102.

29. Russel, W. B.; Saville, D. A.; Schowalter, W. R., *Colloidal dispersions*. Cambridge university press: 1992.

30. Derjaguin, B.; Landau, L., The theory of stability of highly charged lyophobic sols and coalescence of highly charged particles in electrolyte solutions. *Acta Physicochim. URSS* **1941,** *14*, 633-52.

31. Verwey, E.; Overbeek, J. T. G., Theory of lyophobic colloids. Elsevier, Amsterdam: 1948.

32. Davies, J. T., *A quantitative kinetic theory of emulsion type I. Physical chemistry of the emulsifying agent. Gas/Liquid and Liquid/Liquid Interfaces. Proceedings of the International Congress of Surface Activity*. Butterworths: London, 1957; p 426-438.

33. Verdinelli, V.; Messina, P. V.; Schulz, P. C.; Vuano, B., Hydrophile-lipophile balance (HLB) of n-alkane phosphonic acids and theirs salts. *Colloids and Surfaces, A: Physicochemical and Engineering Aspects* **2008,** *316* (1-3), 131-135.

34. Daniel, M.-C.; Astruc, D., Gold Nanoparticles: Assembly, Supramolecular Chemistry, Quantum-Size-Related Properties, and Applications toward Biology, Catalysis, and Nanotechnology. *Chem. Rev.* **2004,** *104* (1), 293-346.

35. Giersig, M.; Mulvaney, P., Preparation of ordered colloid monolayers by electrophoretic deposition. *Langmuir* **1993,** *9* (12), 3408-13.

36. Pujari, S. P.; Scheres, L.; Marcelis, A. T. M.; Zuilhof, H., Covalent Surface Modification of Oxide Surfaces. *Angewandte Chemie International Edition* **2014,** *53* (25), 6322-6356.

37. Pukanszky, B.; Fekete, E., Adhesion and surface modification. *Adv. Polym. Sci.* **1999,** *139* (Mineral Fillers in Thermoplastics I), 109-153.

38. Kickelbick, G.; Schubert, U. In *Organic functionalization of metal oxide nanoparticles*, American Scientific Publishers: 2003; pp 91-102.

39. Neouze, M.-A.; Schubert, U., Surface Modification and Functionalization of Metal and Metal Oxide Nanoparticles by Organic Ligands. *Monatsh. Chem.* **2008,** *139* (3), 183-195.

40. Ojamae, L.; Aulin, C.; Pedersen, H.; Kall, P.-O., IR and quantum-chemical studies of carboxylic acid and glycine adsorption on rutile TiO2 nanoparticles. *J Colloid Interface Sci* **2006,** *296* (1), 71-8.

41. Ulman, A., Formation and Structure of Self-Assembled Monolayers
Chem. Rev **1996,** *96* (4), 1533-1554.

42. Ye, Q.; Zhou, F.; Liu, W., Bioinspired catecholic chemistry for surface modification. *Chemical Society Reviews* **2011,** *40* (7), 4244-4258.

43. Li, S.-C.; Wang, J.-g.; Jacobson, P.; Gong, X. Q.; Selloni, A.; Diebold, U., Correlation between Bonding Geometry and Band Gap States at Organic-Inorganic Interfaces: Catechol on Rutile TiO2(110). *J. Am. Chem. Soc.* **2009,** *131* (3), 980-984.

44. Nakayama, N.; Hayashi, T., Preparation of TiO2 nanoparticles surface-modified by both carboxylic acid and amine: Dispersibility and stabilization in organic solvents. *Colloids and Surfaces, A: Physicochemical and Engineering Aspects* **2008,** *317* (1-3), 543-550.

45. Raza, M.; Bachinger, A.; Zahn, N.; Kickelbick, G., Interaction and UV-stability of various organic capping agents on the surface of anatase nanoparticles. *Materials* **2014,** *7* (4), 2890-2912, 23 pp.

46. Ramakrishna, G.; Ghosh, H. N., Optical and Photochemical Properties of Sodium Dodecylbenzenesulfonate (DBS)-Capped TiO2 Nanoparticles Dispersed in Nonaqueous Solvents. *Langmuir* **2003,** *19* (3), 505-508.

47. Plueddemann, E., *Silane coupling agents*. 1982.

48. Silberzan, P.; Leger, L.; Ausserre, D.; Benattar, J., Silanation of silica surfaces. A new method of constructing pure or mixed monolayers. *Langmuir* **1991,** *7* (8), 1647-1651.

49. Glaser, A.; Foisner, J.; Hoffmann, H.; Friedbacher, G., Investigation of the Role of the Interplay between Water and Temperature on the Growth of Alkylsiloxane Submonolayers on Silicon. *Langmuir* **2004,** *20* (13), 5599-5604.

50. Fadeev, A. Y.; McCarthy, T. J., Self-Assembly Is Not the Only Reaction Possible between Alkyltrichlorosilanes and Surfaces: Monomolecular and Oligomeric Covalently Attached Layers of Dichloro- and Trichloroalkylsilanes on Silicon. *Langmuir* **2000,** *16* (18), 7268-7274.

51. Sugahara, Y.; Okada, S.; Sato, S.; Kuroda, K.; Kato, C., 29Si-NMR study of hydrolysis and initial polycondensation processes of organoalkoxysilanes. II. Methyltriethoxysilane. *J. Non-Cryst. Solids* **1994,** *167* (1-2), 21-8.

52. Mutin, P. H.; Guerrero, G.; Vioux, A., Hybrid materials from organophosphorus coupling molecules. *Journal of Materials Chemistry* **2005,** *15*, 3761 - 3768.

53. McGovern, M. E.; Kallury, K. M. R.; Thompson, M., Role of Solvent on the Silanization of Glass with Octadecyltrichlorosilane. *Langmuir* **1994,** *10* (10), 3607-14.

54. Choi, J. Y.; Kim, C. H.; Kim, D. K., Formation and characterization of monodisperse, spherical organo-silica powders from organo-alkoxysilane-water system. *J. Am. Ceram. Soc.* **1998,** *81* (5), 1184-1188.

55. Greenwood, P.; Gevert, B., Aqueous silane modified silica sols: theory and preparation. *Pigm. Resin Technol.* **2011,** *40* (5), 275-284.

56. Queffelec, C.; Petit, M.; Janvier, P.; Knight, D. A.; Bujoli, B., Surface Modification Using Phosphonic Acids and Esters. *Chem. Rev.* **2012,** *112* (7), 3777-3807.

57. Guerrero, G.; Alauzun, J. G.; Granier, M.; Laurencin, D.; Mutin, P. H., Phosphonate coupling molecules for the control of surface/interface properties and the synthesis of nanomaterials. *Dalton Transactions* **2013,** *42* (35), 12569-12585.

58. Popov, K.; Ronkkomaki, H.; Lajunen, L. H. J., Critical evaluation of stability constants of phosphonic acids. *Pure Appl. Chem.* **2001,** *73* (10), 1641-1677.

59. Guerrero, G.; Mutin, P. H.; Vioux, A., Anchoring of Phosphonate and Phosphinate Coupling Molecules on Titania Particles. *Chemistry of Materials* **2001,** *13* (11), 4367-4373.

60. Randon, J.; Blanc, P.; Paterson, R., Modification of ceramic membrane surfaces using phosphoric acid and alkyl phosphonic acids and its effects on ultrafiltration of BSA protein. *J. Membr. Sci.* **1995,** *98* (1+2), 119-29.

61. Guerrero, G.; Mutin, P. H.; Vioux, A., Mixed Nonhydrolytic/Hydrolytic Sol-Gel Routes to Novel Metal Oxide/Phosphonate Hybrids. *Chemistry of Materials* **2000,** *12* (5), 1268-1272.

62. Guerrero, G.; Mutin, P. H.; Vioux, A., Organically modified aluminas by grafting and sol-gel processes involving phosphonate derivatives. *J. Mater.Chem.* **2001,** *11* (12), 3161-3165.

63. Gao, W.; Dickinson, L.; Grozinger, C.; Morin, F. G.; Reven, L., Self-Assembled Monolayers of Alkylphosphonic Acids on Metal Oxides. *Langmuir* **1996,** *12* (26), 6429-6435.

64. Lafond, V.; Gervais, C.; Maquet, J.; Prochnow, D.; Babonneau, F.; Mutin, P. H., 17O MAS NMR Study of the Bonding Mode of Phosphonate Coupling Molecules in a Titanium Oxo-Alkoxo-Phosphonate and in Titania-Based Hybrid Materials. *Chemistry of Materials* **2003,** *15* (21), 4098-4103.

65. Brodard-Severac, F.; Guerrero, G.; Maquet, J.; Florian, P.; Gervais, C.; Mutin, P. H., High-Field 17O MAS NMR Investigation of Phosphonic Acid Monolayers on Titania. *Chemistry of Materials* **2008,** *20* (16), 5191-5196.

66. Van Alsten, J. G., Self-Assembled Monolayers on Engineering Metals: Structure, Derivatization, and Utility. *Langmuir* **1999,** *15* (22), 7605-7614.

67. Gao, W.; Reven, L., Solid-State NMR Studies of Self-Assembled Monolayers. *Langmuir* **1995,** *11* (6), 1860-3.

68. Woodward, J. T.; Ulman, A.; Schwartz, D. K., Self-Assembled Monolayer Growth of Octadecylphosphonic Acid on Mica. *Langmuir* **1996,** *12* (15), 3626-3629.

69. Brukman, M. J.; Marco, G. O.; Dunbar, T. D.; Boardman, L. D.; Carpick, R. W., Nanotribological Properties of Alkanephosphonic Acid Self-Assembled Monolayers on Aluminum Oxide: Effects of Fluorination and Substrate Crystallinity. *Langmuir* **2006,** *22* (9), 3988-3998.

70. Adden, N.; Gamble, L. J.; Castner, D. G.; Hoffmann, A.; Gross, G.; Menzel, H., Phosphonic Acid Monolayers for Binding of Bioactive Molecules to Titanium Surfaces. *Langmuir* **2006,** *22* (19), 8197-8204.

71. Gawalt, E. S.; Avaltroni, M. J.; Koch, N.; Schwartz, J., Self-Assembly and Bonding of Alkanephosphonic Acids on the Native Oxide Surface of Titanium. *Langmuir* **2001,** *17* (19), 5736-5738.

72. Marcinko, S.; Fadeev, A. Y., Hydrolytic Stability of Organic Monolayers Supported on TiO2 and ZrO2. *Langmuir* **2004,** *20* (6), 2270-2273.

73. Pawsey, S.; McCormick, M.; De Paul, S.; Graf, R.; Lee, Y.; Reven, L.; Spiess, H. W., 1H fast MAS NMR studies of hydrogen-bonding interactions in self-assembled monolayers. *Journal of the American Chemical Society* **2003,** *125* (14), 4174-4184.

74. Pawsey, S.; Yach, K.; Reven, L., Self-Assembly of Carboxyalkylphosphonic Acids on Metal Oxide Powders. *Langmuir* **2002,** *18* (13), 5205-5212.

75. Mutin, P. H.; Lafond, V.; Popa, A. F.; Granier, M.; Markey, L.; Dereux, A., Selective surface modification of SiO2-TiO2 supports with phosphonic acids. *Chemistry of Materials* **2004,** *16*, 5670-5675.

76. Lassiaz, S.; Labarre, D.; Galarneau, A.; Brunel, D.; Mutin, P. H., Modification of Silica by an Organic Monolayer in Aqueous Medium Using Octylphosphonic Acid and Aluminum Species. *Journal of Materials Chemistry* **2011,** *21*, 8199-8205.

77. Pautrot-d'Alencon, L.; Barboux, P.; Boilot, J. P., Synthesis and acid functionalization of cerium oxide nanoparticles. *J. Sol-Gel Sci. Technol.* **2006,** *39* (3), 261-267.

78. Rehor, I.; Kubicek, V.; Kotek, J.; Hermann, P.; Szakova, J.; Lukes, I., Modification of Nanocrystalline TiO2 with Phosphonate- and Bis(phosphonate)-Bearing Macrocyclic Complexes: Sorption and Stability Studies. *Eur. J. Inorg. Chem.* **2011,** (12), 1981-1989.

79. Keller, A. A.; Wang, H.; Zhou, D.; Lenihan, H. S.; Cherr, G.; Cardinale, B. J.; Miller, R.; Ji, Z., Stability and aggregation of metal oxide nanoparticles in natural aqueous matrices. *Environmental science & technology* **2010,** *44* (6), 1962-1967.

80. Mandelbrot, B. B., *The fractal geometry of nature (Revised and enlarged edition)*. 1983; Vol. 1.

81. Behrens, S.; Borkovec, M.; Schurtenberger, P., Aggregation in charge-stabilized colloidal suspensions revisited. *Langmuir* **1998,** *14* (8), 1951-1954.

82. Wijnen, P. W. J. G.; Beelen, T. P. M.; Rummens, K. P. J.; Saeijs, H. C. P. L.; Van Santen, R. A., Silica gel from water glass: a SAXS study of the formation and aging of fractal aggregates. *J. Appl. Crystallogr.* **1991,** *24* (5), 759-64.

83. Knoblich, B.; Gerber, T., Aggregation in SiO2 sols from sodium silicate solutions. *J. Non-Cryst. Solids* **2001,** *283* (1-3), 109-113.

84. French, R. A.; Jacobson, A. R.; Kim, B.; Isley, S. L.; Penn, R. L.; Baveye, P. C., Influence of ionic strength, pH, and cation valence on aggregation kinetics of titanium dioxide nanoparticles. *Environmental science & technology* **2009,** *43* (5), 1354-1359.

85. Jiang, J.; Oberdorster, G.; Biswas, P., Characterization of size, surface charge, and agglomeration state of nanoparticle dispersions for toxicological studies. *J. Nanopart. Res.* **2009,** *11* (1), 77-89.
86. Bridger, K.; Vincent, B., The terminal grafting of poly(ethylene oxide) chains to silica surfaces. *Eur. Polym. J.* **1980,** *16* (10), 1017-21.
87. Joubert, M.; Delaite, C.; Bourgeat-Lami, E.; Dumas, P., Hairy PEO-silica nanoparticles through surface-initiated polymerization of ethylene oxide. *Macromol. Rapid Commun.* **2005,** *26* (8), 602-607.
88. Zhang, Z.; Berns, A. E.; Willbold, S.; Buitenhuis, J., Synthesis of poly(ethylene glycol) (PEG)-grafted colloidal silica particles with improved stability in aqueous solvents. *Journal of Colloid and Interface Science* **2007,** *310* (2), 446-455.
89. Napper, D.; Netschey, A., Studies of the steric stabilization of colloidal particles. *Journal of Colloid and Interface Science* **1971,** *37* (3), 528-535.
90. Deiss, J. L.; Anizan, P.; El Hadigui, S.; Wecker, C., Steric stability of TiO2 nanoparticles in aqueous dispersions. *Colloids and Surfaces, A: Physicochemical and Engineering Aspects* **1996,** *106* (1), 59-62.
91. Auroy, P.; Auvray, L.; Leger, L., Silica particles stabilized by long grafted polymer chains: from electrostatic to steric repulsion. *Journal of Colloid and Interface Science* **1992,** *150* (1), 187-194.
92. El Harrak, A.; Carrot, G.; Oberdisse, J.; Eychenne-Baron, C.; Boue, F., Surface-Atom Transfer Radical Polymerization from Silica Nanoparticles with Controlled Colloidal Stability. *Macromolecules* **2004,** *37* (17), 6376-6384.
93. Bagwe, R. P.; Hilliard, L. R.; Tan, W., Surface Modification of Silica Nanoparticles to Reduce Aggregation and Nonspecific Binding. *Langmuir* **2006,** *22* (9), 4357-4362.
94. Starck, P.; Ducker, W. A., Simple Method for Controlled Association of Colloidal-Particle Mixtures using pH-Dependent Hydrogen Bonding. *Langmuir* **2009,** *25* (4), 2114-2120.
95. Iijima, M.; Kobayakawa, M.; Kamiya, H., Tuning the stability of TiO2 nanoparticles in various solvents by mixed silane alkoxides. *Journal of Colloid and Interface Science* **2009,** *337* (1), 61-65.
96. Herman, D.; Walz, J. Y., Stabilization of Weakly Charged Microparticles Using Highly Charged Nanoparticles. *Langmuir* **2013,** *29* (20), 5982-5994.
97. Aleman, J.; Chadwick, A. V.; He, J.; Hess, M.; Horie, K.; Jones, R. G.; Kratochal, P.; Meisel, I.; Mita, I.; Moad, G., Definitions of terms relating to the structure and processing of sols, gels, networks, and inorganic-organic hybrid materials (IUPAC Recommendations 2007). *Pure and Applied Chemistry* **2007,** *79* (10), 1801-1829.
98. Pavlidou, S.; Papaspyrides, C. D., A review on polymer-layered silicate nanocomposites. *Prog. Polym. Sci.* **2008,** *33* (12), 1119-1198.
99. Winey, K. I.; Vaia, R. A., Polymer nanocomposites. *MRS bulletin* **2007,** *32* (04), 314-322.
100. Winnik, M. A.; Yekta, A., Associative polymers in aqueous solution. *Curr. Opin. Colloid Interface Sci.* **1997,** *2* (4), 424-436.
101. Fawaz, J.; Mittal, V., Synthesis of Polymer Nanocomposites: Review of Various Techniques. *Synthesis Techniques for Polymer Nanocomposites* **2014**, 1-30.
102. Zhu, L.; Xanthos, M., Effects of process conditions and mixing protocols on structure of extruded polypropylene nanocomposites. *Journal of Applied Polymer Science* **2004,** *93* (4), 1891-1899.
103. Wahba, L.; D'Arienzo, M.; Dire, S.; Donetti, R.; Hanel, T.; Morazzoni, F.; Niederberger, M.; Santo, N.; Tadiello, L.; Scotti, R., A novel non-aqueous sol-gel route for the in situ synthesis of high loaded silica-rubber nanocomposites. *Soft Matter* **2014,** *10* (13), 2234-2244.
104. Park, S. J.; Cho, M. S.; Lim, S. T.; Choi, H. J.; Jhon, M. S., Synthesis and dispersion characteristics of multi-walled carbon nanotube composites with poly(methyl methacrylate) prepared by in-situ bulk polymerization. *Macromol. Rapid Commun.* **2003,** *24* (18), 1070-1073.
105. Yang, F.; Ou, Y.; Yu, Z., Polyamide 6/silica nanocomposites prepared by in situ polymerization. *Journal of Applied Polymer Science* **1998,** *69* (2), 355-361.
106. Tuteja, A.; Duxbury, P. M.; Mackay, M. E., Multifunctional nanocomposites with reduced viscosity. *Macromolecules* **2007,** *40* (26), 9427-9434.

107. Carrot, G.; El Harrak, A.; Oberdisse, J.; Jestin, J.; Boue, F., Polymer grafting from 10-nm individual particles: proving control by neutron scattering. *Soft Matter* **2006,** *2* (12), 1043-1047.

108. Kickelbick, G., Concepts for the incorporation of inorganic building blocks into organic polymers on a nanoscale. *Progress in Polymer Science* **2003,** *28* (1), 83-114.

109. Zou, H.; Wu, S.; Shen, J., Polymer/Silica Nanocomposites: Preparation, Characterization, Properties, and Applications. *Chem. Rev.* **2008,** *108* (9), 3893-3957.

110. Palimi, M. J.; Rostami, M.; Mahdavian, M.; Ramezanzadeh, B., Surface modification of Fe2O3 nanoparticles with 3-aminopropyltrimethoxysilane (APTMS): An attempt to investigate surface treatment on surface chemistry and mechanical properties of polyurethane/Fe2O3 nanocomposites. *Appl. Surf. Sci.* **2014,** *320*, 60-72.

111. Kango, S.; Kalia, S.; Celli, A.; Njuguna, J.; Habibi, Y.; Kumar, R., Surface modification of inorganic nanoparticles for development of organic-inorganic nanocomposites-A review. *Prog. Polym. Sci.* **2013,** *38* (8), 1232-1261.

112. Nakayama, N.; Hayashi, T., Preparation and characterization of poly (l-lactic acid)/TiO 2 nanoparticle nanocomposite films with high transparency and efficient photodegradability. *Polymer degradation and stability* **2007,** *92* (7), 1255-1264.

113. Rharbi, Y.; Cabane, B.; Vacher, A.; Joanicot, M.; Boue, F., Modes of deformation in a soft/hard nanocomposite: a SANS study. *Europhys. Lett.* **1999,** *46* (4), 472-478.

114. Oberdisse, J.; El Harrak, A.; Carrot, G.; Jestin, J.; Boue, F., Structure and rheological properties of soft-hard nanocomposites: influence of aggregation and interfacial modification. *Polymer* **2005,** *46* (17), 6695-6705.

115. Oberdisse, J., Aggregation of colloidal nanoparticles in polymer matrices. *Soft Matter* **2006,** *2* (1), 29-36.

116. Oberdisse, J.; Demé, B., Structure of latex-silica nanocomposite films: A small-angle neutron scattering study. *Macromolecules* **2002,** *35* (11), 4397-4405.

117. Chevalier, Y.; Pichot, C.; Graillat, C.; Joanicot, M.; Wong, K.; Maquet, J.; Lindner, P.; Cabane, B., Film formation with latex particles. *Colloid and Polymer Science* **1992,** *270* (8), 806-21.

118. Rieger, J.; Haedicke, E.; Ley, G.; Lindner, P., Crystals made of close-packed polymeric spheres: a neutron scattering study on latex films. *Phys. Rev. Lett.* **1992,** *68* (18), 2782-5.

119. Joanicot, M.; Wong, K.; Cabane, B., Interdiffusion in Cellular Latex Films. *Macromolecules* **1996,** *29* (14), 4976-4984.

120. Dingenouts, N.; Ballauff, M., First Stage of Film Formation by Latexes Investigated by Small-Angle X-ray Scattering. *Langmuir* **1999,** *15* (9), 3283-3288.

121. Genix, A.-C.; Tatou, M.; Imaz, A.; Forcada, J.; Schweins, R.; Grillo, I.; Oberdisse, J., Modeling of Intermediate Structures and Chain Conformation in Silica-Latex Nanocomposites Observed by SANS During Annealing. *Macromolecules* **2012,** *45* (3), 1663-1675.

122. Dalmas, F.; Genevaz, N.; Roth, M.; Jestin, J.; Leroy, E., 3D Dispersion of Spherical Silica Nanoparticles in Polymer Nanocomposites: A Quantitative Study by Electron Tomography. *Macromolecules* **2014,** *47* (6), 2044-2051.

123. Richards, J. J.; Whittle, C. L.; Shao, G.; Pozzo, L. D., Correlating structure and photocurrent for composite semiconducting nanoparticles with contrast variation small-angle neutron scattering and photoconductive atomic force microscopy. *ACS nano* **2014,** *8* (5), 4313-4324.

124. Kim, D.; Lee, J. S.; Barry, C. M.; Mead, J. L., Microscopic measurement of the degree of mixing for nanoparticles in polymer nanocomposites by TEM images. *Microscopy research and technique* **2007,** *70* (6), 539-546.

125. Jouault, N.; Dalmas, F.; Boue, F.; Jestin, J., Multiscale characterization of filler dispersion and origins of mechanical reinforcement in model nanocomposites. *Polymer* **2012,** *53* (3), 761-775.

126. Janes, D. W.; Moll, J. F.; Harton, S. E.; Durning, C. J., Dispersion Morphology of Poly(methyl acrylate)/Silica Nanocomposites. *Macromolecules* **2011,** *44* (12), 4920-4927.

127. Banc, A.; Genix, A.-C.; Chirat, M.; Dupas, C.; Caillol, S.; Sztucki, M.; Oberdisse, J., Tuning Structure and Rheology of Silica–Latex Nanocomposites with the Molecular Weight of Matrix Chains: A Coupled SAXS–TEM–Simulation Approach. *Macromolecules* **2014,** *47* (9), 3219-3230.

128. Tatou, M.; Genix, A.-C.; Imaz, A.; Forcada, J.; Banc, A.; Schweins, R.; Grillo, I.; Oberdisse, J., Reinforcement and Polymer Mobility in Silica-Latex Nanocomposites with Controlled Aggregation. *Macromolecules* **2011,** *44* (22), 9029-9039.
129. Kumar, S. K.; Jouault, N.; Benicewicz, B.; Neely, T., Nanocomposites with Polymer Grafted Nanoparticles. *Macromolecules* **2013,** *46* (9), 3199-3214.
130. Baeza, G. P.; Genix, A.-C.; Degrandcourt, C.; Petitjean, L.; Gummel, J.; Schweins, R.; Couty, M.; Oberdisse, J., Effect of Grafting on Rheology and Structure of a Simplified Industrial Nanocomposite Silica/SBR. *Macromolecules* **2013,** *46* (16), 6621-6633.
131. Baeza, G. P.; Genix, A.-C.; Degrandcourt, C.; Gummel, J. r. m.; Mujtaba, A.; Saalwächter, K.; Thurn-Albrecht, T.; Couty, M.; Oberdisse, J., Studying Twin Samples Provides Evidence for a Unique Structure-Determining Parameter in Simplifed Industrial Nanocomposites. *ACS Macro Letters* **2014,** *3* (5), 448-452.
132. Chevigny, C.; Dalmas, F.; Di Cola, E.; Gigmes, D.; Bertin, D.; Boue, F.; Jestin, J., Polymer-Grafted-Nanoparticles Nanocomposites: Dispersion, Grafted Chain Conformation, and Rheological Behavior. *Macromolecules* **2011,** *44* (1), 122-133.
133. Zemb, T.; Lindner, P., *Neutrons, X-rays and light: scattering methods applied to soft condensed matter*. North-Holland: 2002.
134. Delaittre, G. Polymerisation radicalaire contrôlée en émulsion et dispersion sans tensioactif. Synthèse de nanoparticules thermo- et/ou pH-sensibles. Université Paris IV - Pierre et Marie Curie, Paris, 2008.
135. Petit, T. Modifications de surface des nanodiamants : compréhension des mécanismes d'échanges électroniques et mise en évidence d'un effet thérapeutique. Ecole Normale Supérieure de Cachan, Saclay, 2013.
136. Wang, B.; Seabrook, S. A.; Nedumpully-Govindan, P.; Chen, P.; Yin, H.; Waddington, L.; Epa, V. C.; Winkler, D. A.; Kirby, J. K.; Ding, F.; Ke, P. C., Thermostability and reversibility of silver nanoparticle-protein binding. *Physical Chemistry Chemical Physics* **2015,** *17* (3), 1728-1739.
137. Miller, C. C., The Stokes-Einstein law for diffusion in solution. *Proceedings of the Royal Society of London. Series A, Containing Papers of a Mathematical and Physical Character* **1924**, 724-749.
138. Cousin, F.; Genix, C.; Grillo, I.; Jestin, J.; Oberdisse, J., Neutrons et Matière Molle. *EDP Sciences*.
139. Baeza, G. P. Nanocomposites industriels simplifiés : analyse structurale et propriétés mécaniques. Université de Montpellier 2, Montpellier, 2013.
140. Dingenouts, N.; Seelenmeyer, S.; Deike, I.; Rosenfeldt, S.; Ballauff, M.; Lindner, P.; Narayanan, T., Analysis of thermosensitive core-shell colloids by small-angle neutron scattering including contrast variation. *Physical Chemistry Chemical Physics* **2001,** *3* (7), 1169-1174.
141. McGreevy, R. L., Reverse Monte Carlo modelling. *J. Phys.: Condens. Matter* **2001,** *13* (46), R877-R913.
142. Mile, V.; Gereben, O.; Kohara, S.; Pusztai, L., On the Structure of Aqueous Cesium Fluoride and Cesium Iodide Solutions: Diffraction Experiments, Molecular Dynamics Simulations, and Reverse Monte Carlo Modeling. *Journal of Physical Chemistry B* **2012,** *116* (32), 9758-9767.
143. Oberdisse, J.; Hine, P.; Pyckhout-Hintzen, W., Structure of interacting aggregates of silica nanoparticles in a polymer matrix: small-angle scattering and reverse Monte Carlo simulations. *Soft Matter* **2007,** *3* (4), 476-485.
144. Pothoczki, S.; Temleitner, L.; Pusztai, L., The structure of PX3 (X = Cl, Br, I) molecular liquids from X-ray diffraction, molecular dynamics simulations, and reverse Monte Carlo modeling. *J. Chem. Phys.* **2014,** *140* (5), 054504/1-054504/9.
145. Baeza, G. P.; Genix, A.-C.; Degrandcourt, C.; Petitjean, L.; Gummel, J.; Couty, M.; Oberdisse, J., Multiscale Filler Structure in Simplified Industrial Nanocomposite Silica/SBR Systems Studied by SAXS and TEM. *Macromolecules* **2013,** *46* (1), 317-329.
146. Papon, A.; Montes, H.; Lequeux, F.; Oberdisse, J.; Saalwaechter, K.; Guy, L., Solid particles in an elastomer matrix: impact of colloid dispersion and polymer mobility modification on the mechanical properties. *Soft Matter* **2012,** *8* (15), 4090-4096.

147. Kremer, F., *Broadband dielectric spectroscopy*. Springer Science & Business Media: 2003.

148. Monasterio Jaqueti, M. On the dielectric properties of water confined in cement-like materials. Universidad del Pais Vasco, Donostia - San Sebastian, 2015.

149. Havriliak, S.; Negami, S., A complex plane representation of dielectric and mechanical relaxation processes in some polymers. *Polymer* **1967,** *8*, 161-210.

150. Fulcher, G. S., Analysis of recent measurements of the viscosity of glasses. *J. Am. Ceram. Soc.* **1925,** *8*, 339-55.

151. Tamman, G.; Hesse, W., The dependence of viscosity upon the temperature of supercooled liquids. *Z. Anorg. Allg. Chem.* **1926,** *156*, 245-57.

152. Vogel, H., Das Temperaturabhängigkeitsgesetz der Viskosität von Flüssigkeiten. *Phys. Z* **1921,** *22*, 645-646.

153. Niederberger, M.; Bartl, M. H.; Stucky, G. D., Benzyl Alcohol and Titanium Tetrachloride-A Versatile Reaction System for the Nonaqueous and Low-Temperature Preparation of Crystalline and Luminescent Titania Nanoparticles. *Chemistry of Materials* **2002,** *14* (10), 4364-4370.

154. Rockland, L. B., Saturated salt solutions for static control of relative humidity between 5 Å and 40 Å
Anal. Chem. **1960,** *32*, 1375-6.

155. Raybaud, P.; Digne, M.; Iftimie, R.; Wellens, W.; Euzen, P.; Toulhoat, H., Morphology and Surface Properties of Boehmite (γ-AlOOH): A Density Functional Theory Study. *Journal of Catalysis* **2001,** *201* (2), 236-246.

156. Zou, D.; Li, X.-f.; Zhu, X.-l.; Kong, X.-z., Preparation of cationic latexes of poly(styrene-co-butyl acrylate) and their properties evolution in latex dilution. *Chinese Journal of Polymer Science* **2012,** *30* (2), 278-286.

157. Acton, B. O.; Ting, G. G.; Shamberger, P. J.; Ohuchi, F. S.; Ma, H.; Jen, A. K. Y., Dielectric Surface-Controlled Low-Voltage Organic Transistors via n-Alkyl Phosphonic Acid Self-Assembled Monolayers on High-k Metal Oxide. *ACS Applied Materials & Interfaces* **2010,** *2* (2), 511-520.

158. Allara, D. L.; Nuzzo, R. G., Spontaneously organized molecular assemblies. 1. Formation, dynamics, and physical properties of n-alkanoic acids adsorbed from solution on an oxidized aluminum surface. *Langmuir* **1985,** *1* (1), 45-52.

159. Fadeev, A. Y.; Helmy, R.; Marcinko, S., Self-Assembled Monolayers of Organosilicon Hydrides Supported on Titanium, Zirconium, and Hafnium Dioxides. *Langmuir* **2002,** *18* (20), 7521-7529.

160. Feichtenschlager, B.; Pabisch, S.; Peterlik, H.; Kickelbick, G., Nanoparticle Assemblies as Probes for Self-Assembled Monolayer Characterization: Correlation between Surface Functionalization and Agglomeration Behavior. *Langmuir* **2011,** *28* (1), 741-750.

161. Mammeri, F.; Le, B. Y.; Daou, T. J.; Gallani, J.-L.; Colis, S.; Pourroy, G.; Donnio, B.; Guillon, D.; Begin-Colin, S., Formation of Ferrimagnetic Films with Functionalized Magnetite Nanoparticles Using the Langmuir-Blodgett Technique. *Journal of Physical Chemistry B* **2009,** *113* (3), 734-738.

162. Verwey, E. J. W.; Overbeek, J. T. G., *Theory of the Stability of Lyophobic Colloids*. Dover Publications: 1948.

163. Hollamby, M. J., Practical applications of small-angle neutron scattering. *Physical Chemistry Chemical Physics* **2013,** *15* (26), 10566-10579.

164. Mehan, S.; Aswal, V. K.; Kohlbrecher, J., Cationic versus Anionic Surfactant in Tuning the Structure and Interaction of Nanoparticle, Protein, and Surfactant Complexes. *Langmuir* **2014,** *30* (33), 9941-9950.

165. Cerveny, S.; Schwartz, G. A.; Otegui, J.; Colmenero, J.; Loichen, J.; Westermann, S., Dielectric Study of Hydration Water in Silica Nanoparticles. *J. Phys. Chem. C* **2012,** *116* (45), 24340-24349.

166. Paniagua, S. A.; Hotchkiss, P. J.; Jones, S. C.; Marder, S. R.; Mudalige, A.; Marrikar, F. S.; Pemberton, J. E.; Armstrong, N. R., Phosphonic acid modification of indium-tin oxide electrodes: Combined xps/ups/contact angle studies *The Journal of Physical Chemistry C* **2008,** *112* (21), 7809-7817.

167. Percus, J. K.; Yevick, G. J., Analysis of classical statistical mechanics by means of collective coordinates. *Physical Review* **1958,** *110* (1), 1.

168. Tielens, F.; De Proft, F.; Geerlings, P., Density functional theory study of the conformation and energetics of silanol and disiloxane. *J. Mol. Struct.: THEOCHEM* **2001,** *542*, 227-237.

169. Middendorf, H. D., Neutron studies of the dynamics of biological water. *Phys. B Condens. Matter* **1996,** *226*, 113-127.

170. Laurati, M.; Sotta, P.; Long, D. R.; Fillot, L. A.; Arbe, A.; Alegria, A.; Embs, J. P.; Unruh, T.; Schneider, G. J.; Colmenero, J., Dynamics of Water Absorbed in Polyamides. *Macromolecules* **2012,** *45* (3), 1676-1687.

171. Tan, H.-S.; Piletic, I. R.; Riter, R. E.; Levinger, N. E.; Fayer, M. D., Dynamics of water confined on a nanometer length scale in reverse micelles: Ultrafast infrared vibrational echo spectroscopy. *Phys. Rev. Lett.* **2005,** *94* (5), 057405/1-057405/4.

172. Vasilyeva, M. A.; Gusev, Y. A.; Shtyrlin, V. G.; Greenbaum, A.; Puzenko, A.; Ben Ishai, P.; Feldman, Y., Dielectric relaxation of water in clay minerals. *Clays Clay Miner.* **2014,** *62* (1-2), 62-73.

173. Monasterio, M.; Gaitero, J. J.; Manzano, H.; Dolado, J. S.; Cerveny, S., Effect of Chemical Environment on the Dynamics of Water Confined in Calcium Silicate Minerals: Natural and Synthetic Tobermorite. *Langmuir* **2015,** *31* (17), 4964-4972.

174. Monasterio, M.; Jansson, H.; Gaitero, J. J.; Dolado, J. S.; Cerveny, S., Cause of the fragile-to-strong transition observed in water confined in C-S-H gel. *J. Chem. Phys.* **2013,** *139* (16), 164714/1-164714/8.

175. Harrach, M. F.; Klameth, F.; Drossel, B.; Vogel, M., Effect of the hydroaffinity and topology of pore walls on the structure and dynamics of confined water. *J. Chem. Phys.* **2015,** *142* (3), 034703/1-034703/8.

176. Faraone, A.; Liu, L.; Mou, C. Y.; Yen, C. W.; Chen, S. H., Fragile-to-strong liquid transition in deeply supercooled confined water. *J. Chem. Phys.* **2004,** *121* (22), 10843-10846.

177. Liu, L.; Chen, S.-H.; Faraone, A.; Yen, C.-W.; Mou, C.-Y., Pressure dependence of fragile-to-strong transition and a possible second critical point in supercooled confined water. *Physical review letters* **2005,** *95* (11), 117802.

178. Mons, S. Surface structure of silica gel, dry and hydrated. https://fr.wikipedia.org/wiki/Gel_de_silice.

179. Hassanali, A. A.; Singer, S. J., Model for the Water-Amorphous Silica Interface: The Undissociated Surface. *Journal of Physical Chemistry B* **2007,** *111* (38), 11181-11193.

180. Mamontov, E., Observation of fragile-to-strong liquid transition in surface water in CeO2. *J. Chem. Phys.* **2005,** *123* (17), 171101/1-171101/4.

181. Mamontov, E., High-resolution neutron-scattering study of slow dynamics of surface water molecules in zirconium oxide. *J. Chem. Phys.* **2005,** *123* (2), 024706/1-024706/9.

182. Mamontov, E.; Vlcek, L.; Wesolowski, D. J.; Cummings, P. T.; Rosenqvist, J.; Wang, W.; Cole, D. R.; Anovitz, L. M.; Gasparovic, G., Suppression of the dynamic transition in surface water at low hydration levels: A study of water on rutile. *Phys. Rev. E: Stat., Nonlinear, Soft Matter Phys.* **2009,** *79* (5-1), 051504/1-051504/6.

183. Mamontov, E.; Vlcek, L.; Wesolowski, D. J.; Cummings, P. T.; Wang, W.; Anovitz, L. M.; Rosenqvist, J.; Brown, C. M.; Garcia Sakai, V., Dynamics and Structure of Hydration Water on Rutile and Cassiterite Nanopowders Studied by Quasielastic Neutron Scattering and Molecular Dynamics Simulations. *J. Phys. Chem. C* **2007,** *111* (11), 4328-4341.

184. Cerveny, S.; Colmenero, J.; Alegria, A., Dielectric properties of water in amorphous mixtures of polymers and other glass forming materials. *J. Non-Cryst. Solids* **2007,** *353* (47-51), 4523-4527.

185. Barroso-Bujans, F.; Cerveny, S.; Alegria, A.; Colmenero, J., Chain Length Effects on the Dynamics of Poly(ethylene oxide) Confined in Graphite Oxide: A Broadband Dielectric Spectroscopy Study. *Macromolecules* **2013,** *46* (19), 7932-7939.

186. Oberdisse, J., Structure and rheological properties of latex-silica nanocomposite films: Stress-strain isotherms. *Macromolecules* **2002,** *35* (25), 9441-9450.

187. Balazs, A. C.; Emrick, T.; Russell, T. P., Nanoparticle polymer composites: where two small worlds meet. *Science* **2006,** *314* (5802), 1107-1110.

188. Ghosh, M.; Lawes, G.; Gayen, A.; Subbanna, G. N.; Reiff, W. M.; Subramanian, M. A.; Ramirez, A. P.; Zhang, J.-P.; Seshadri, R., A Novel Route to Toluene-Soluble Magnetic Oxide Nanoparticles: Aqueous Hydrolysis Followed by Surfactant Exchange. *Chemistry of Materials* **2004,** *16* (1), 118-124.
189. Patil, R. M.; Shete, P. B.; Thorat, N. D.; Otari, S. V.; Barick, K. C.; Prasad, A.; Ningthoujam, R. S.; Tiwale, B. M.; Pawar, S. H., Non-aqueous to aqueous phase transfer of oleic acid coated iron oxide nanoparticles for hyperthermia application. *RSC Adv.* **2014,** *4* (9), 4515-4522.
190. Sastry, M., Phase transfer protocols in nanoparticle synthesis. *Current Science* **2003,** *85* (12), 1735-1745.
191. Karg, M.; Schelero, N.; Oppel, C.; Gradzielski, M.; Hellweg, T.; von Klitzing, R., Versatile Phase Transfer of Gold Nanoparticles from Aqueous Media to Different Organic Media. *Chemistry – A European Journal* **2011,** *17* (16), 4648-4654.
192. Meriguet, G.; Dubois, E.; Perzynski, R., Liquid-liquid phase-transfer of magnetic nanoparticles in organic solvents. *Journal of Colloid and Interface Science* **2003,** *267* (1), 78-85.
193. Machunsky, S.; Grimm, P.; Schmid, H.-J.; Peuker, U. A., Liquid-liquid phase transfer of magnetite nanoparticles. *Colloids and Surfaces, A: Physicochemical and Engineering Aspects* **2009,** *348* (1-3), 186-190.
194. Erler, J.; Machunsky, S.; Grimm, P.; Schmid, H.-J.; Peuker, U. A., Liquid-liquid phase transfer of magnetite nanoparticles - Evaluation of surfactants. *Powder Technol.* **2013,** *247*, 265-269.
195. Zhao, Y.; Wang, B.; Ding, C.; Zhao, X., Nano titanium oxide organosol: synthesis, characterization, and application for electrorheological fluid. *Journal of Applied Polymer Science* **2008,** *110* (6), 3763-3769.
196. Mehring, M.; Guerrero, G.; Dahan, F.; Mutin, P. H.; Vioux, A., Syntheses, Characterizations, and Single-Crystal X-ray Structures of Soluble Titanium Alkoxide Phosphonates. *Inorg. Chem.* **2000,** *39* (15), 3325-3332.
197. Weitz, D.; Oliveria, M., Fractal structures formed by kinetic aggregation of aqueous gold colloids. *Physical review letters* **1984,** *52* (16), 1433.
198. Eberle, A. P. R.; Castaneda-Priego, R.; Kim, J. M.; Wagner, N. J., Dynamical Arrest, Percolation, Gelation, and Glass Formation in Model Nanoparticle Dispersions with Thermoreversible Adhesive Interactions. *Langmuir* **2012,** *28* (3), 1866-1878.
199. Eberle, A. P. R.; Wagner, N. J.; Akgun, B.; Satija, S. K., Temperature-Dependent Nanostructure of an End-Tethered Octadecane Brush in Tetradecane and Nanoparticle Phase Behavior. *Langmuir* **2010,** *26* (5), 3003-3007.
200. Hoekstra, H.; Mewis, J.; Narayanan, T.; Vermant, J., Multi Length Scale Analysis of the Microstructure in Sticky Sphere Dispersions during Shear Flow. *Langmuir* **2005,** *21* (24), 11017-11025.
201. Solomon, M. J.; Varadan, P., Dynamic structure of thermoreversible colloidal gels of adhesive spheres. *Physical Review E* **2001,** *63* (5), 051402.
202. Varadan, P.; Solomon, M. J., Direct visualization of long-range heterogeneous structure in dense colloidal gels. *Langmuir* **2003,** *19* (3), 509-512.
203. Roke, S.; Berg, O.; Buitenhuis, J.; van Blaaderen, A.; Bonn, M., Surface molecular view of colloidal gelation. *Proceedings of the National Academy of Sciences of the United States of America* **2006,** *103* (36), 13310-13314.
204. Roke, S.; Buitenhuis, J.; van Miltenburg, J. C.; Bonn, M.; van Blaaderen, A., Interface-solvent effects during colloidal phase transitions. *Journal of Physics: Condensed Matter* **2005,** *17* (45), S3469.
205. Brunauer, S.; Emmett, P. H.; Teller, E., Adsorption of Gases in Multimolecular Layers. *Journal of the American Chemical Society* **1938,** *60* (2), 309-319.

Résumé en français du travail de thèse

Les dispersions colloïdales sont très répandues dans le milieu industriel, aussi bien dans les peintures que dans les cosmétiques. Même si ces systèmes ont déjà fait l'objet de nombreuses études et sont relativement bien connus, la compréhension et le contrôle des interactions entre les objets dispersés et le milieu dispersant sont encore d'actualité. La modulation de ces interactions, par exemple en changeant les interactions électrostatiques ou en modifiant la surface des objets par adsorption de molécules ou macromolécules organiques, peut permettre de contrôler l'état d'agrégation des objets dispersés.

Certaines nanoparticules (NPs) d'oxydes peuvent être synthétisées par hydrolyse en milieu aqueux. Dans de nombreux cas, l'agrégation peut être évitée - même en l'absence de tensioactifs - en jouant sur les répulsions électrostatiques entre les particules. Par conséquent, la production de sols aqueux de NPs de concentration élevée est possible à grande échelle et à faible coût. Dans le cas des nanoparticules, l'utilisation de sols colloïdaux constitue un avantage majeur, la manipulation de NPs sèches étant très controversée pour des raisons de toxicité. Par conséquent, le développement de nouvelles méthodes permettant la modification de surface directement en milieu dispersé est nécessaire. De plus, depuis quelques décennies, les nanocomposites NP-polymère se sont révélés prometteurs pour une large gamme d'applications, comme par exemple les pneumatiques. Les propriétés des nanocomposites dépendent étroitement à la fois de la taille et de l'état de dispersion des nanoparticules dans la matrice polymère, d'où la nécessité de contrôler cet état de dispersion. L'utilisation de sols pourrait ainsi présenter une voie d'incorporation avantageuse des NPs dans la matrice polymère.

Le premier objectif de ce travail de thèse est donc le développement de méthodes de modification de surface de NPs d'oxyde (SiO_2/Al_2O_3 et TiO_2) en dispersion colloïdale, tout en contrôlant leur état de dispersion dans les sols et dans les nanocomposites issus de ces sols. Puis, le second consiste à évaluer cet état de dispersion par des méthodes de caractérisation avancées, notamment par diffusion aux petits angles (SAXS et SANS). Dans le but de moduler les interactions entre les NPs, et ainsi leur état de dispersion, leurs surfaces ont été modifiées par des acides phosphoniques. Ces molécules peuvent être greffées sur une large variété de NPs d'oxyde, directement en dispersion dans l'eau. A noter que la modification de surface via des organosilanes, très largement répandue, n'est pas applicable en milieu aqueux.

Deux méthodes de modification de surface ont ainsi été développées afin d'obtenir des sols aqueux ou organiques de NPs fonctionnalisées. La première méthode implique le greffage d'acides phosphoniques, d'hydrophobie et de charge variables, sur des NPs de silice recouvertes d'alumine en dispersion dans l'eau. La seconde met en jeu le greffage d'acides alkylphosphoniques sur des NPs de TiO_2 et leur transfert d'une phase aqueuse à une phase chloroforme. Les nanoparticules modifiées par ces deux voies de greffage ont été caractérisées par diverses méthodes, notamment par FTIR et par RMN du ^{31}P en phase solide. L'étude de leur état de dispersion a ensuite été menée par DLS et diffusion aux petits angles.

De plus, dans le cas des nanoparticules de silice-alumine, l'impact de la densité de greffage de l'acide octylphosphonique (noté C_8PA) sur la structure des NPs modifiées - à l'état sec - a été mis en évidence par SAXS et différent processus de relaxation ont été étudiés par spectroscopie diélectrique (BDS) dans le cas des NPs nues et modifiées.

Enfin, les NPs de silice-alumine modifiées en surface ont été incorporées dans une matrice polymère de polyacrylate d'éthyle (PEA) par voie aqueuse via l'utilisation de latex. Leur état de dispersion dans les nanocomposites a été mesuré par SANS.

I - Impact du greffage d'acides phosphoniques sur les interactions et la stabilité de nanoparticules en dispersion dans l'eau

La surface de nanoparticules de silice recouvertes d'une couche d'alumine (L200S) en dispersion dans l'eau a été modifiée par des acides phosphoniques (PAs) comportant des chaînes organiques différentes, donc d'hydrophobie et de charge variables. Cette modification de surface a été menée directement sur des sols aqueux de NPs. A noter que les liaisons Si-O-P sont sensibles à l'hydrolyse, d'où la nécessité d'utiliser des NPs de silice recouvertes d'alumine, puisque les liaisons Al-O-P formées sont, quant à elles, relativement stables à l'hydrolyse. L'utilisation, très répandue, d'organosilanes est également inenvisageable en milieu aqueux.

1 - Caractérisation des nanoparticules greffées

Les nanoparticules modifiées en surface et lavées ont été caractérisées par FTIR, ATG et RMN du ^{31}P en phase solide. Dans le cas du greffage par le CAPA, l'absence de la bande d'élongation des C=O à environ 1710 cm^{-1} (caractéristique des groupements COOH) sur le spectre infrarouge nous a permis de déduire au bouclage du groupement carboxylate à la surface des NPs, situation favorisée par les faibles densités de greffage. La RMN du ^{31}P en phase solide nous a permis de conclure à la formation d'espèces phosphonates greffées. De plus, l'absence de pics fins sur ces spectres nous laisse penser à l'absence d'acides phosphoniques physisorbés ou de formation de phases cristallines par dissolution-précipitation.

La quantification de la densité de greffage est couramment faite par ATG dans l'air dans le cas de monocouches auto-assemblées. Cependant, dans le cas de greffages d'acides phosphoniques, elle est délicate, car la dégradation des chaînes organiques greffées se fait dans la même gamme de température que la condensation des groupements hydroxyles de surface et du fait que cette dégradation mène à la formation de P_2O_5. Nous avons donc évalué la densité de greffage effective en PA par analyse élémentaire (ICP-OES).

Les résultats de ces analyses nous ont permis de dégager une tendance générale des données : nous avons conclu à une relation linéaire entre la densité de greffage nominale (ρ_{nom}, liée à la quantité de PA introduite) et la densité effectivement greffée à la surface des NPs (notée ρ) : $\rho = 0.82\ \rho_{\mathrm{nom}}$.

2 - Stabilité des solutions colloïdales de NPs modifiées

La stabilité colloïdale des sols de départ est due aux répulsions électrostatiques entre les NPs, chargées positivement. Par conséquent, la modification de surface de ces NPs par des acides phosphoniques a entraîné une modification des interactions entre NPs (notamment électrostatiques et interactions entre chaînes greffées) et avec le milieu de dispersion. Afin d'étudier l'impact de la nature et de la densité de greffage en PA sur l'état de dispersion des NPs modifiées dans l'eau, il est nécessaire de connaître l'échelle de temps au cours de laquelle les sols sont stables. Cette étude, menée par DLS, a permis de mettre en évidence une première étape d'agrégation des sols pendant le greffage des PAs ou directement dans l'heure suivant le greffage. La mesure des rayons hydrodynamiques et de la polydispersité apparente des agrégats de NPs au cours du temps nous a indiqué qu'il n'y avait plus d'évolution significative de l'état d'agrégation des NPs entre 1 heure et 6 jours après la fin de la réaction de greffage. Ainsi, nous avons pu mettre en parallèle les mesures faites par différentes techniques (mesure de potentiel zêta, DLS, diffusion aux petits angles) conduites après différents laps de temps (entre 1h et 6 jours après la modification de surface).

3 - Etat de dispersion des nanoparticules dans l'eau

Comme énoncé précédemment, la modification de surface des NPs entraîne un changement des interactions entre les NPs de différentes manières. La première est une diminution des répulsions électrostatiques entre les NPs. La diminution des répulsions électrostatiques entre les NPs résulte à la fois de la diminution des charges de surface des NPs par consommation des groupements OH de surface au cours du greffage, à la présence possible de groupements P-OH résiduels et, dans le cas du CAPA, à la présence de groupements COOH. Ces changements ont été évalués par des mesures de potentiel zêta.

La seconde modification des interactions avec le milieu dispersant (dans notre cas l'eau) et entre les NPs provient de la modification de l'hydrophilie de surface des NPs. En effet, au départ les nanoparticules nues sont hydrophiles et le greffage des acides phosphoniques peut modifier cette caractéristique. Le caractère hydrophile des acides phosphoniques greffés décroit selon l'ordre : DEPA > CAPA > C_3PA > C_5PA > C_8PA.

Le but de notre étude a donc été de voir comment l'évolution de la balance entre les répulsions électrostatiques et les attractions entre groupements hydrophobes impacte l'agrégation des NPs en dispersion dans l'eau, mesurée par microscopie électronique en transmission (TEM), DLS et diffusion aux petits angles.

Le potentiel zêta décroît progressivement avec l'augmentation de la densité de greffage des acides phosphoniques. Cette diminution s'est avérée plus rapide dans le cas du CAPA que des acides alkylphosphoniques et du DEPA. Nous avons pu expliquer cette diminution accélérée soit par une dissociation partielle des groupements COOH libres, soit par la complexation de ces groupements avec la surface des NPs, menant à une consommation supplémentaire de groupements Al-OH de surface.

Puis nous avons étudié l'évolution de la taille des agrégats formés en solution. Dans un premier temps, cette étude a été menée par DLS : la taille des agrégats formés, ainsi que leur polydispersité, augmente avec la densité de greffage en acide phosphonique, quelque soit le type d'acide phosphonique utilisé. De plus, cette augmentation se fait à plus forte densité de greffage dans l'ordre suivant : DEPA > C_3PA > C_5PA > C_8PA > CAPA. Des clichés TEM ont montré une évolution similaire avec la densité de greffage en C_8PA. Enfin, l'étude par diffusion aux petits angles (neutrons et rayons X) nous a permis de suivre l'évolution du facteur de structure des NPs (lié à leur arrangement spatial en solution). Ainsi, les mêmes tendances ont pu être mises en évidence, comme le montre la figure R.1.

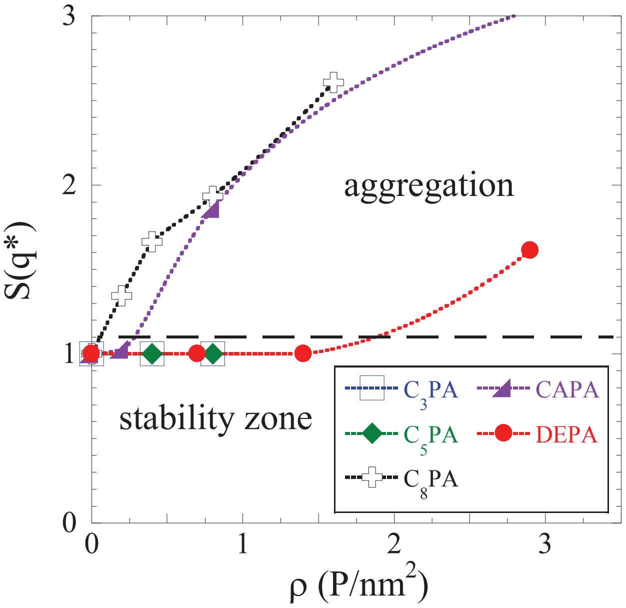

Figure R.1 : Evolution de l'état d'agrégation des NPs greffées en fonction de la nature de l'acide phosphonique et de sa densité de greffage, notée ρ. S(q* = 4x10^{-3} Å^{-1}) représente la force de l'augmentation de l'intensité diffusée aux petits q, mesuré par diffusion aux petits angles. Une limite arbitraire a été tracée pour S(q*) = 1.1, délimitant la zone d'agrégation avec la zone de stabilité des sols colloïdaux.

Ainsi la méthode de modification de surface étudiée dans cette partie offre la possibilité de greffer des acides phosphoniques à la surface de NPs d'oxyde en dispersion dans l'eau, tout en modifiant leur état d'agrégation dans les sols.

II - Arrangement spatial des NPs sèches modifiées par C_8PA

L'impact de la modification de surface des NPs de silice couvertes d'alumine (L200S) par l'acide octylphosphonique, C_8PA, sur l'arrangement des NPs lavées et séchées a été étudié par SAXS. Comme le montre la figure R.2, l'intensité diffusée par ces poudres dépend de la densité de greffage.

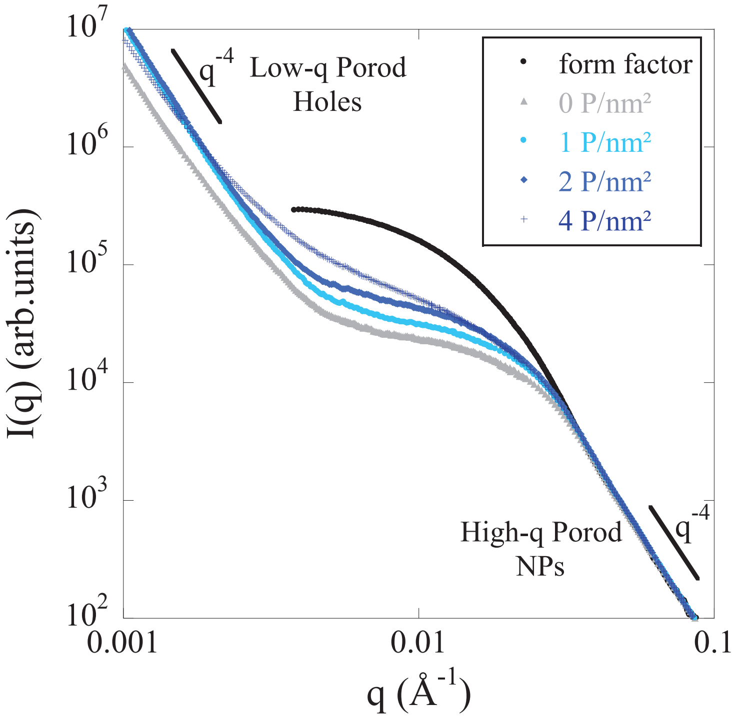

Figure R.2 : Intensité diffusée par les NPs sèches modifiées par C_8PA à différentes densité de greffage. La courbe noire représente le facteur de forme des NPs nues en solution diluée.

Nous avons donc pu conclure sur l'évolution de l'arrangement spatial de ces NPs avec la densité de greffage en C_8PA et proposer un modèle pour décrire nos poudres.

En effet, celles-ci peuvent être vues comme un système biphasique composé de trous d'air d'une part, et de phases denses de nanoparticules, contenant elles-aussi de l'air. Nous avons évalué les fractions volumiques respectives de ces phases et déduit le rayon moyen des trous d'air. Il s'est avéré que le rayon de ces poches d'air décroît fortement avec la densité de greffage de C_8PA.

III - Etude BDS de la dynamique interfaciale des nanoparticules à différents taux d'hydratation

1 - Nanoparticules nues de L200S

L'étude par spectroscopie diélectrique (BDS) des nanoparticules de silice recouvertes d'alumine non modifiées en surface (à l'état sec) a permis de mettre en évidence l'existence de 4 procédés de relaxation, notés procédés 1, 2, 3 et 4, du plus rapide au plus lent, qui suivent un comportement Arrhénien.

Le premier procédé, noté procédé 1, est lié aux groupements hydroxyles de surface des nanoparticules, et plus particulièrement à la réorientation des groupements Al-OH de surface. Il a pu être observé à basse température, T = 77 K (son maximum étant à une fréquence d'environ 10^5 Hz pour cette température).

Le second procédé a été attribué à la relaxation des molécules d'eau adsorbées dans la couche d'hydratation externe. La force diélectrique de ce procédé augmente avec la concentration en eau dans les poudres.

Le procédé 3 s'est avéré être du à la relaxation des molécules d'eau dans la couche d'hydratation interne, c'est-à-dire dans la couche d'hydratation au contact de la surface des nanoparticules et en interaction avec les OH de surface.

Malheureusement, l'origine du procédé 4 n'a pas encore pu être expliquée, bien que ce procédé semble également être lié à l'eau d'hydratation des NPs, puisqu'il évolue avec le taux d'hydratation des poudres.

La figure R.3 est la « carte de relaxation » des différents procédés observés dans le cas des nanoparticules de silice couverte d'alumine (L200S) non modifiées.

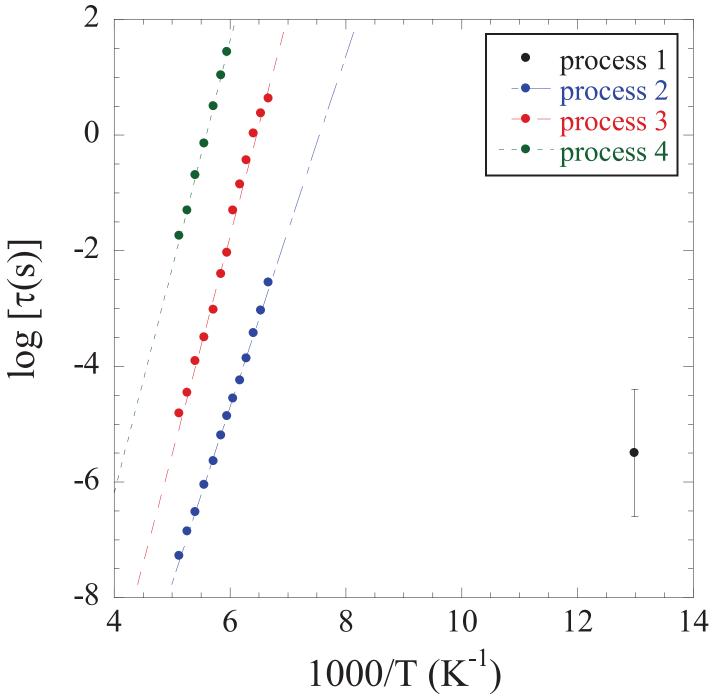

Figure R.3 : « Carte de relaxation » des nanoparticules de L200S nues au taux d'hydratation le plus élevé parmi ceux étudiés (RH = 75%). Les pointillés représentent le comportement Arrhénien de ces procédés. A noter que le procédé 1 n'a été mesuré que sur la poudre sèche, i.e. non hydratée a posteriori.

Nous avons également pu calculer les énergies d'activation de ces différents procédés et leurs échelles de temps associées (log τ_0). Ces valeurs ont été comparées avec celles obtenues dans la littérature pour des NPs de silice précipitée (Zeosil).

2 - Nanoparticules greffées

Nous sommes ensuite passés à l'étude des nanoparticules modifiées en surface par différents acides phosphoniques : notamment le C_8PA et le DEPA. Nous avons dans un premier temps suivi l'évolution de la force diélectrique du procédé 1 avec la densité de greffage de différents acides phosphoniques. En effet, ce procédé ayant été attribué à la relaxation des groupements Al-OH de surface, l'augmentation de la densité de greffage des PAs à la surface des NPs a pour conséquence d'accroître la consommation des groupements

Al-OH et, par conséquent, de réduire le nombre de dipôles à l'origine du procédé 1. Nous avons pu faire un suivi de la densité de greffage par mesure de force diélectrique et confirmer l'attribution de ce procédé. De plus, dans le cas du CAPA, la diminution accrue de la force diélectrique de ce procédé semblait confirmer le bouclage de ces greffons à la surface des NPs, comme annoncé précédemment.

Pour les NPs modifiées par C_8PA, les mêmes procédés de relaxation que pour les NPs non modifiées ont été observés. L'évolution du procédé 2 avec le taux d'hydratation des poudres a été étudiée. Nous avons pu constater que le procédé 3, lié à la relaxation des molécules d'eau dans la couche d'hydratation interne, s'est avéré moins intense d'environ 50% en comparaison aux NPs non modifiées. Nous avons expliqué ce fait par la consommation des Al-OH de surface au cours du greffage, menant à la diminution du nombre de molécules d'eau en interactions avec ces groupements. Toutefois, les procédés de relaxation des acides phosphoniques greffés n'ont pas été détectés dans la gamme de fréquence et de température étudiée.

Dans le cas des nanoparticules modifiées par le DEPA, le procédé de relaxation β, lié à des changements conformationnels des chaînes du DEPA a été mis en évidence sur les nanoparticules greffées. De plus, le greffage des chaînes n'a pas impacté l'énergie d'activation et l'échelle de temps caractéristiques de ce procédé. Le procédé de relaxation α, lié à la transition vitreuse du DEPA n'a quant à lui pas pu être détecté dans le cas des NPs greffées, ni par DSC, ni par BDS, alors qu'il avait été mis en évidence par ces deux techniques pour le DEPA pur.

La figure R.4 ci-dessous représente l'évolution de la force de ces procédés pour le DEPA pur et pour les NPs modifiées avec le DEPA.

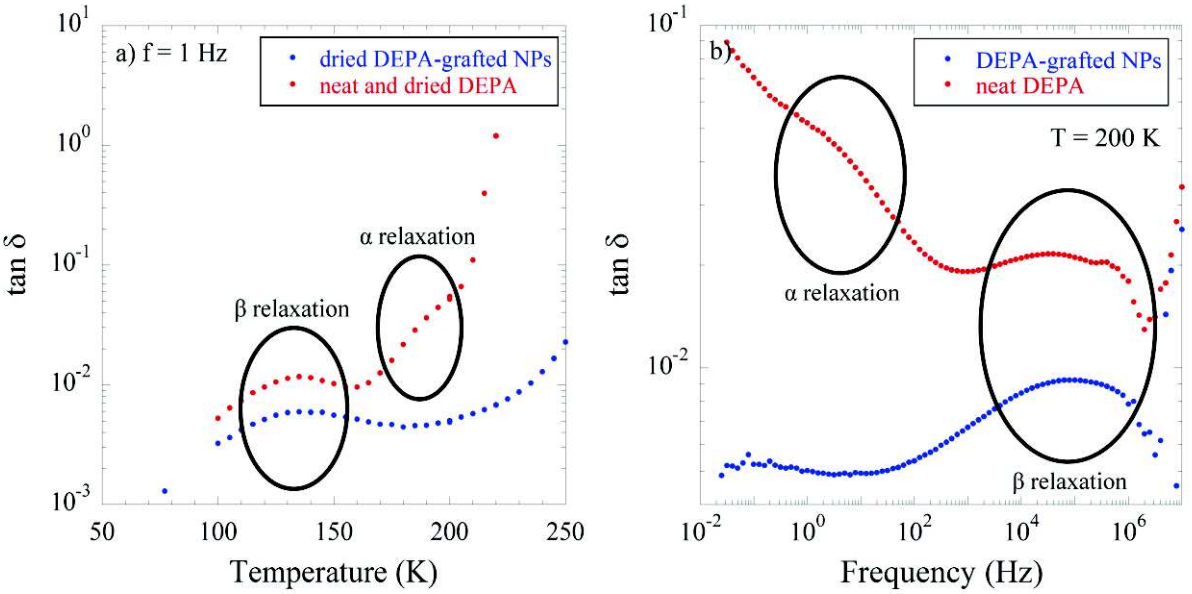

Figure R.4 : Evolution de tan δ **a)** avec la température à fréquence fixe (f = 1 Hz), et **b)** avec la fréquence à température fixe (T = 200 K) pour le DEPA pur et pour les nanoparticules modifiées avec le DEPA (densité de greffage = 4 P/nm²).

IV - Nanocomposites PEA/nanoparticules modifiées

Les nanoparticules nues et modifiées décrites ci-dessus ont ensuite été incorporées dans une matrice de polyacrylate d'éthyle (PEA) par voie aqueuse en mélangeant les sols aqueux de NPs modifiées avec un latex. A noter que les sols colloïdaux de NPs ont été utilisés tels quels, directement après le greffage des PAs. Cette méthode d'élaboration de nanocomposites présente plusieurs avantages : elle permet notamment d'éviter la manipulation de NPs sèches et l'utilisation de solvants organiques. L'état de dispersion des NPs dans les nanocomposites obtenus a ensuite été mesuré par SANS. Nous avons en particulier calculé la compacité des agrégats, κ, grâce à une équation de Percus-Yevick modifiée, prenant en compte la polydispersité des NPs nues, et suivi l'évolution de la taille des agrégats grâce à l'intensité diffusée aux petits q des échantillons les plus dilués (pour une fraction volumique en NPs de 1%).

Le but de cette étude était de voir si le greffage d'acides phosphoniques hydrophobes menait à une meilleure compatibilisation avec le polymère (hydrophobe également) ou si l'état d'agrégation des NPs dans les sols aqueux était maintenu dans les nanocomposites, c'est-à-dire une augmentation de la taille des agrégats avec la densité de greffage et en faisant varier la nature de l'acide phosphonique du plus hydrophile (DEPA) au plus hydrophobe (C_8PA).

Le premier paramètre étudié est la fraction volumique de NPs dans le polymère, Φ : nous avons pu constater que l'augmentation de cette fraction volumique mène à la fois à une augmentation de la masse des agrégats (pour les échantillons à Φ = 1%) et à la formation d'agrégats plus denses dans le cas de nanoparticules nues, et celles modifiées par le C_8PA et le DEPA.

De plus, nous avons pu suivre l'impact de la densité de greffage sur la masse des agrégats dans les nanocomposites peu chargés : un greffage plus dense du C_8PA induit une augmentation de la masse des agrégats, alors que ce paramètre reste inchangé pour les agrégats composés par les NPs modifiées par le DEPA.

Concernant l'évolution de la compacité des agrégats avec la densité de greffage, nous avons mis en évidence que celle-ci reste à peu près constante pour les échantillons peu chargés quelque soit la nature de l'acide phosphonique étudiée (C_3PA, C_5PA, C_8PA et DEPA) : κ ≈ 5 - 6% pour les échantillons à Φ = 1% et κ ≈ 11 - 12% pour les échantillons à Φ = 5%. Dans le cas des nanocomposites plus chargés (Φ = 10%), la compacité des agrégats diminue avec l'augmentation de la densité de greffage en PA, comme le montre la figure R.5.

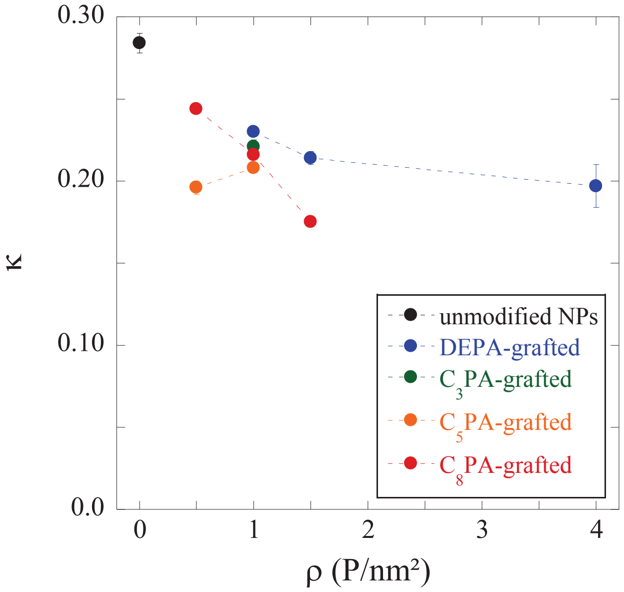

Figure R.5 : Evolution de la compacité des agrégats, κ, avec la densité de greffage de différents acides phosphoniques pour une fraction volumique en nanoparticules de 10%.

Pour continuer cette étude sur les nanocomposites, des clichés TEM auraient permis de conclure sur la forme des agrégats au sein de la matrice polymère (réseau de nanoparticules agrégées ou dispersion de gros agrégats). De plus, l'intensité diffusée n'a pas pu être mesurée à des plus petits angles, nous n'avons donc pas pu observer de plateau aux petits angles, ce qui nous aurait permis de déterminer la taille des agrégats de NPs dans les nanocomposites.

V - Modification de surface et transfert simultanés de nanoparticules de TiO_2 par des acides alkylphosphoniques

Nous avons également mis au point une méthode de modification de surface de nanoparticules de TiO_2 par des acides alkylphosphoniques et le transfert simultané des nanoparticules modifiées de la phase aqueuse de départ vers une phase organique de chloroforme.

Cette méthode mono-étape, dont le principe est illustré en figure R.6, nous a permis d'obtenir des sols de nanoparticules modifiées en phase organique, qui peuvent être utilisés - sans étapes de purification ou de lavage supplémentaires - pour l'élaboration de nanocomposites, tout en évitant la manipulation de poudres de NPs sèches.

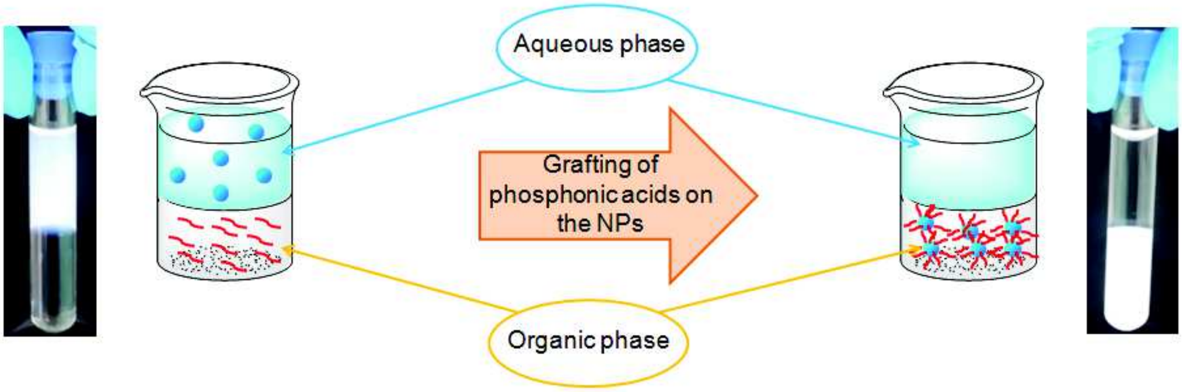

Figure R.6 : Principe de la modification de surface des NPs de TiO_2 et transfert de phase simultané de la phase aqueuse vers la phase chloroforme.

Nous avons étudié l'impact de différents paramètres sur la méthode de transfert de phase pour en déterminer les limites. Ainsi, nous avons réussi à transférer en milieu organique des sols aqueux de NPs :

- de concentration en NPs de 1 à 23% massiques ;
- avec différents acides phosphoniques : C_5PA, C_8PA, C_{12}PA et C_{18}PA ;
- avec différentes nanoparticules : LS101 et PC (sols de TiO_2), TiO_2 Degussa et Al_2O_3 C ;
- pré-agrégées en phase aqueuse par variation de pH ou de teneur en sel.

Cependant, la variation de la quantité d'acide phosphonique mène à un transfert partiel des NPs : en défaut de PA, la modification de surface est seulement partielle et ne suffit pas à rendre les NPs suffisamment organophiles et, en excès de PA, nous avons supposé la formation de bicouches à la surface des nanoparticules, menant à nouveau à des NPs trop peu organophiles pour assurer un transfert complet.

A noter que cette méthode de transfert ne peut pas être appliquée pour les acides tertio butyl- et phényl-phosphoniques.

Les nanoparticules modifiées ont ensuite été caractérisées par FTIR et RMN du ^{31}P en phase solide.

Les nanoparticules modifiées ont également été séchées et redispersées avec succès dans différents solvants organiques : le chloroforme, la butanone et le toluène.

Nous avons également étudié l'état de dispersion des NPs dans les sols organiques obtenus. La DLS nous a permis de suivre l'évolution du rayon hydrodynamique et de la polydispersité des agrégats.

Par ailleurs, des mesures de diffusion de neutrons aux petits angles ont été effectuées sur des sols de nanoparticules dans $CHCl_3$ et $CDCl_3$. En appliquant un modèle cœur-coquille, nous avons donc estimé l'épaisseur de la couche formée par les acides phosphoniques greffés : elle varie de 1.5 nm pour C_8PA, 1.9 nm pour C_{12}PA, à 2.3 nm pour C_{18}PA.

Concernant la modification de surface par le C_{18}PA, nous avons également mis en évidence une agrégation thermo-réversible des nanoparticules dans les dispersion en phase chloroforme.

Surface modification of oxide nanoparticles using phosphonic acids: characterization, surface dynamics, and dispersion in sols and nanocomposites

Colloidal nanoparticles (NPs) dispersions are largely used in the industry, and avoid the use of dried NPs, which is controversial due to safety concerns. The key point in such systems remains the control of the interactions with the dispersed medium and between the NPs. Mastering these interactions allows controlling the NPs' state of dispersion. Moreover, as polymer-NPs nanocomposites have been found promising for a wide variety of applications, the use of colloidal sols could thus be an advantageous way of NPs' incorporation in the polymer, with a possible control of the NPs state of dispersion, and finally on the properties of the material, as they are linked to the NPs' dispersion. The purpose of this PhD work is to develop surface-functionalization methods of oxide NPs in colloidal sols in order to control the dispersion of NPs in the sols and in polymer nanocomposites derived from these sols, and to evaluate this dispersion using SAXS. Two surface modification methods have been developed to obtain aqueous or organic sols of functionalized NPs. The first one concerns the reaction in water of alumina-coated silica NPs with phosphonic acids (PAs), and the second one involves the simultaneous grafting and phase transfer of TiO_2 NPs from an aqueous to a $CHCl_3$ phase using PAs. The resulting NPs were characterized and their state of dispersion was monitored by DLS and SAS measurements. The impact of the C_8PA grafting density on the structure of modified alumina-coated silica NPs in the dried state was evidenced by SAXS. The different relaxation processes of bare and grafted NPs were studied by BDS. These NPs were then incorporated in a PEA polymer by an aqueous latex route, and their structure in the nanocomposites was investigated by SANS.

TiO_2 nanoparticles, alumina coated silica nanoparticles, sols, phosphonic acids, dielectric spectroscopy, SAXS

Modification de surface de nanoparticules d'oxyde par des acides phosphoniques : caractérisation, dynamique de surface et dispersion dans des sols et des nanocomposites

Les dispersions colloïdales de nanoparticules (NPs) sont très répandues dans l'industrie, et permettent d'éviter l'utilisation de NPs sèches, controversée pour des raisons de toxicité. Le contrôle des interactions entre les NPs et le milieu dispersant reste le point clé de ces systèmes. La modulation de ces interactions permet de contrôler l'état de dispersion des NPs dans les sols. De plus, les nanocomposites NPs-polymère se sont avérés prometteurs pour une large gamme d'applications, ainsi l'utilisation de sols pourrait présenter une voie avantageuse d'incorporation des NPs dans le polymère, tout en offrant la possibilité de contrôler leur état de dispersion, et *in fine* les propriétés du matériau, celles-ci étant liées à l'état de dispersion des NPs. L'objectif de ce travail de thèse est le développement de méthodes de modification de surface de NPs d'oxyde en dispersion colloïdale, tout en contrôlant la dispersion des NPs dans les sols et dans les nanocomposites issus de ces sols. Puis, l'évaluation de cet état de dispersion par SAXS. Deux méthodes de modification de surface ont ainsi été développées : la première implique le greffage d'acides phosphoniques sur des NPs de silice recouvertes d'alumine en dispersion dans l'eau, et la seconde met en jeu le greffage d'acides phosphoniques sur des NPs de TiO_2 et leur transfert d'une phase aqueuse à une phase $CHCl_3$. Les NPs modifiées ont été caractérisées par diverses méthodes. Leur état de dispersion a été étudié par DLS et SAS. De plus, pour les NPs de silice-amine, l'impact de la densité de greffage du C_8PA sur la structure des NPs (à l'état sec) a été mis en évidence par SAXS et différents processus de relaxation ont été étudiés par BDS pour les NPs nues et modifiées. Enfin, ces NPs ont été incorporées dans un polymère de PEA par voie aqueuse via des latex et leur état de dispersion dans les composites a été mesuré par SANS.

Nanoparticules de TiO_2, nanoparticules de silice recouvertes d'alumine, sols, acides phosphoniques, spectroscopie diélectrique, SAXS